



Universiteit  
Leiden  
The Netherlands

## Bioorthogonal labeling tools to study pathogenic intracellular bacteria

Bakkum, T.

### Citation

Bakkum, T. (2021, November 17). *Bioorthogonal labeling tools to study pathogenic intracellular bacteria*. Retrieved from <https://hdl.handle.net/1887/3240088>

Version: Publisher's Version

License: [Licence agreement concerning inclusion of doctoral thesis in the Institutional Repository of the University of Leiden](#)

Downloaded from: <https://hdl.handle.net/1887/3240088>

**Note:** To cite this publication please use the final published version (if applicable).

# **Bioorthogonal Labeling Tools to Study Pathogenic Intracellular Bacteria**

Proefschrift

ter verkrijging van

de graad van doctor aan de Universiteit Leiden,

op gezag van rector magnificus prof. dr. ir. H. Bijl,

volgens besluit van het college voor promoties

te verdedigen op woensdag 17 november 2021

klokke 13:45 uur

door

**Thomas Bakkum**

geboren te Delft in 1991



# Promotiecommissie

Promotor: Dr. S.I. van Kasteren

Promotor: Prof. dr. H.S. Overkleeft

Promotiecommissie: Voorzitter: Prof. dr. Jaap Brouwer

Secretaris: Prof. dr. Mario van der Stelt

Overige commissieleden: Prof. dr. Paul Verkade (Bristol University)

Prof. dr. Ariane Briegel

Dr. Lorenzo Albertazzi (TU-Eindhoven)

Dr. Daniel Rozen

Cover by: Berg designs & T. Bakkum

Printed by: Ipskamp Printing

ISBN: 978-94-6421-493-2

All rights reserved. No part of this book may be reproduced in any manner or by any means without permission.

“Failure is only the opportunity to begin again.”

- Iroh (Avatar The Last Airbender)

# Table of Contents

<b>List of Abbreviations</b>	<b>6</b>
<b>Chapter 1</b>	<b>9</b>
General Introduction and Aim of This Thesis	
<b>Chapter 2</b>	<b>21</b>
Metabolic Labeling Probes for Interrogation of the Host-Pathogen Interaction	
<b>Chapter 3</b>	<b>53</b>
Quantification of Bioorthogonal Stability in Immune Phagocytes Using Flow Cytometry Reveals Rapid Degradation of Strained Alkynes	
<b>Chapter 4</b>	<b>121</b>
Ultrastructural Imaging of <i>Salmonella</i> -Host Interactions Using Super-Resolution Correlative Light-Electron Microscopy of Bioorthogonal Pathogens	

<b>Chapter 5</b>	<b>163</b>
Bioorthogonal Correlative Light-Electron Microscopy of <i>Mycobacterium tuberculosis</i> in Macrophages Reveals the Effect of Anti-Tuberculosis Drugs on Subcellular Bacterial Distribution	
<b>Chapter 6</b>	<b>215</b>
Summary and Future Prospects	
<b>Nederlandse Samenvatting</b>	<b>250</b>
<b>List of Publications – First Authorships</b>	<b>254</b>
<b>List of Publications – Co-authorships</b>	<b>255</b>
<b>Curriculum Vitae – English</b>	<b>256</b>
<b>Curriculum Vitae – Nederlands</b>	<b>258</b>
<b>Dankwoord</b>	<b>260</b>

# List of Abbreviations

ABP	Activity-Based Probe
ABPP	Activity-Based Protein Profiling
Ac4ManNAz	1,3,4,6-Tetra- <i>O</i> -acetyl- <i>N</i> -azidoacetylmannosamine
AG	Arabinogalactan
AGM	Arabinogalactan mycolate
Ag85	Mycolyltransferase complex antigen 85
Aha	Azidohomoalanine
alkDala	Alkyne-modified D-alanine (= D-propargylglycine)
ANL	Azidonorleucine
AOA	2-Aminooctynoic acid
APC	Antigen-Presenting Cell
azDala	Azide-modified D-alanine (= 2-amino-3-azidopropanoic acid)
B-CLEM	Bioorthogonal Correlative Light-Electron Microscopy
BCN	Bicyclo[6.1.0]nonyne
bcnDala	BCN-modified D-alanine
BMDC	Bone marrow-derived dendritic cell
BONCAT	Bioorthogonal Non-Canonical Amino acid Tagging
BSA	Bovine serum albumin
CatS	Cathepsin S
ccHc	Copper catalyzed Huisgen cycloaddition (= CuAAC)
CLEM	Correlative Light-Electron Microscopy
CuAAC	Cu-catalyzed Azide-Alkyne Cycloaddition (= ccHc)
DAA	D-amino acid
DABCYL	4-(Dimethylaminoazo)benzene-4-carboxylic acid
DAPI	4',6-Diamidino-2-phenylindole
DBCO	Dibenzocyclooctyne
DC	Dendritic cell
DMN	4- <i>N,N</i> -Dimethylamino-1,8-naphthalimide
DMN-Tre	DMN-modified trehalose
<i>E. coli</i>	<i>Escherichia coli</i>
EdU	5-Ethynyl-2'-deoxyuridine
EM	Electron microscopy
EMB	Ethambutol
FACS	Fluorescence-Activated Cell Sorting
FITC	Fluorescein isothiocyanate

FITC-Tre	FITC-modified trehalose
FDAA	Fluorescent D-amino acid
FDL	Fluorescein-modified D-lysine
FM	Fluorescence microscopy
FRAP	Fluorescence Recovery After Photobleaching
GEN	Gentamycin
GILT	Gamma Interferon-inducible Lysosomal Thioeductase
GM-CSF	Granulocyte-Macrophage Colony-Stimulating Factor
GSH	Glutathione
HADA	HCC-amino-D-alanine
HCC	7-Hydroxycoumarin-3-carboxylic acid
HOCl	Hypochlorous acid
Hpg	Homopropargylglycine
IEDDA	Inverse Electron-Demand Diels-Alder
INH	Isoniazid
LAMP1	Lysosomal-Associated Membrane Protein 1
LPS	Lipopolysaccharide
ManNAc	<i>N</i> -Acetylmannosamine
ManNAI	Alkyne-modified <i>N</i> -acetylmannosamine
ManNAz	Azide-modified <i>N</i> -acetylmannosamine
ManLev	Levulinoyl-modified <i>N</i> -acetylmannosamine
MDR	Multi-drug resistant
Met	Methionine
MetRS	Methionyl-tRNA synthetase
MHC I/II	Major Histocompatibility Complex class I/II
MM	Mycomembrane
MPO	Myeloperoxidase
<i>Mtb</i>	<i>Mycobacterium tuberculosis</i>
MurNAc	<i>N</i> -Acetyl muramic acid
MurNAI	Alkyne-modified <i>N</i> -acetyl muramic acid
MurNAz	Azide-modified <i>N</i> -acetyl muramic acid
NADA	NBD-amino-D-alanine
NBD	4-Chloro-7-nitrobenzofurazan
ncAA	Non-canonical amino acid
NIR	Near-infrared
nitroneDala	Nitrone-modified D-alanine
NLL-MetRS	L13N/Y260L/H301L mutant form of the <i>E. coli</i> MetRS

NOX2	NADPH oxidase-2 complex
O-AlkTMM	<i>O</i> -alkyne-trehalose (6-heptynoyl trehalose analogue)
PALM	Photoactivated Localization Microscopy
pAz	<i>p</i> -Azidophenylalanine
pBPA	<i>p</i> -Benzoyl-L-phenylalanine
PDR	Pan-drug resistant
PET	Positron Emission Tomography
PFA	Paraformaldehyde
PG	Peptidoglycan
QTF	Quencher-Trehalose-Fluorophore
RADA	TAMRA-amino-D-alanine
RIF	Rifampicin
ROS	Reactive Oxygen Species
RPI	Free radical photoinitiator
SDS-PAGE	Sodium Dodecyl Sulfate-Polyacrylamide Gel Electrophoresis
SEM	Scanning Electron Microscopy
SNak	Alkyne-modified short <i>N</i> -acetyl cysteamine (acetyl-CoA analogue)
SNAz	Azide-modified short <i>N</i> -acetyl cysteamine (acetyl-CoA analogue)
SPAAC	Strain-Promoted Azide-Alkyne Cycloaddition (= spHc)
SPANC	Strain-Promoted Alkyne-Nitrone Cycloaddition
spHc	Strain-promoted Huisgen cycloaddition (= SPAAC)
StA	Sterculic acid
STED	Stimulated Emission Depletion
<i>Stm</i>	<i>Salmonella enterica</i> serovar Typhimurium
STORM	Stochastic Optical Reconstruction Microscopy
TAMRA	Carboxy-tetramethylrhodamine
TB	Tuberculosis
TCO	Trans-cyclooctene
TDL	TAMRA-modified D-lysine
TDM	Trehalose dimycolate
TEM	Transmission Electron Microscopy
TMM	Trehalose monomycolate
TreAz	Azide-modified trehalose
XDR	Extensive drug resistant
3HC	3-Hydroxychromone
3HC-Tre	3HC-modified trehalose

# Chapter 1

## **General Introduction**



## **Abstract**

Over the years, the field of bioorthogonal chemistry has developed many biocompatible ligation reactions or 'click reactions', that are highly suitable for detection of biomolecules of interest by fluorescence-based analysis techniques. Click reactions are very interesting for the visualization of intracellular bacteria, due to the various challenges that are encountered when studying these organisms *in situ*. This chapter describes the basics of applying bioorthogonal chemistry to the study of intracellular bacteria.

## 1.1 The biochemistry of a cell

At the smallest level of organization, all life is built from cells. Cells are tiny compartments that exist to seclude the internal processes, that are essential to life, from the outside, that is considered lifeless. Life is fundamentally driven by chemistry, primarily used to metabolize fuel into energy (catabolism) and build new biomolecules (anabolism).<sup>1</sup> A cell consists of four major types of biological macromolecules; proteins, carbohydrates, lipids and nucleic acids. These macromolecules themselves are made from smaller biological building blocks, such as amino acids, sugars, fatty acids and nitrogenous bases.<sup>2</sup> The biochemistry of a cell is highly complex, and it has been estimated that around a billion reactions occur per cell per second. There are six major classes of biochemical reactions; oxidation/reduction, hydrolysis/condensation, ligation/cleavage, functional group transfer, isomerization and the formation/removal of carbon-carbon double bonds.<sup>3</sup> Due to their high activation energy and the relatively low temperature in a living cell, most biochemical reactions must be sped up by biological catalysts, called enzymes. Enzymes are usually proteins but in some cases RNA can function as an enzyme (ribozyme).<sup>4</sup> Compartmentalization of biochemical reactions inside cells and subcellular compartments is thought to have been crucial for life to evolve to the complexity of multicellular organisms such as humans.<sup>5</sup>

## 1.2 Bioorthogonal chemistry & click chemistry

Bioorthogonal chemistry refers to chemical reactions that can be selectively performed within the complex environment of a living cell, without interacting or interfering with the biological system.<sup>1</sup> The term bioorthogonal was coined by Bertozzi in 2003 and refers to orthogonality between the artificially introduced reaction and all biochemical reactions that occur within a living system (i.e. the cell).<sup>2,3</sup> True bioorthogonality requires high selectivity, fast kinetics, biocompatibility of the reaction, biological and chemical inertness of the introduced functional group and the resulting product, as well as accessible engineering of the biomolecule.<sup>1,3,4</sup> The first bioorthogonal reaction is arguably the Staudinger ligation, in which an organic azide is irreversibly ligated to a triphenylphosphine moiety to form an amide group (**Figure 1A**).<sup>5-7</sup> Historically, various attempts were made to obtain bioorthogonality already in 1990 by the group of McCarthy<sup>8</sup>, with a condensation reaction between hydrazine and aldehyde moieties and in 1997 by the group of Bertozzi<sup>9</sup>, with a condensation reaction between hydrazide and levulinoyl moieties. However, since the functional groups used in these reactions are not unique in nature and the products of these reactions are instable, they cannot be considered truly bioorthogonal.

Although fundamentally different in nature, the terms bioorthogonal chemistry and click chemistry are often used interchangeably. The term click chemistry was coined by Sharpless in 1998 and refers to ligation reactions in which two functional groups can be joined selectively, quickly and with high yield in aqueous solution, producing a physiologically stable product without toxic byproducts.<sup>10</sup> Although some click reactions can be performed in live cells, biocompatibility is not a requirement. Click reactions are ideally suited for the production of biologically active molecules in organic synthesis, as well as for biochemical ligation reactions, in which a reporter moiety is connected to a 'click handle'-containing biomolecule of interest, to facilitate the analysis of said biomolecule.<sup>11</sup> In practice, the reporter is usually a fluorophore for fluorescent measurements or a biotin for enrichment of the tagged biomolecule (e.g., for mass spectrometry analysis).<sup>12</sup> Bioorthogonal reactions can be considered the ideal click reactions for ligations in living cells, due to their biocompatibility and bio-inertness of their click handles.

The first reported click reaction was the Cu(I)-catalyzed azide-alkyne cycloaddition (CuAAC; **Figure 1B**), also known as the copper-catalyzed Huisgen cycloaddition (ccHc), discovered simultaneously but independently by the group of Sharpless<sup>13</sup> and the group of Meldal<sup>14</sup>. Although this reaction can be performed successfully in fixed cells (and live cells under special conditions<sup>15,16</sup>), this reaction cannot be considered as a true bioorthogonal reaction, due to cytotoxicity of the Cu(I)-catalyst.<sup>17</sup> To avoid this toxicity, Bertozzi and coworkers then went on to develop a copper-free click reaction, using the intrinsic ring-strain of cyclooctynes to overcome the activation energy of the azide-alkyne cycloaddition.<sup>18,19</sup> This reaction is known as the Strain-Promoted Azide-Alkyne Cycloaddition (SPAAC; **Figure 1C**) or strain-promoted Huisgen cycloaddition (spHc). In order to overcome the suboptimal reaction kinetics of these cycloadditions, another copper-free click reaction was then developed, combining the ring-strain of a cyclooctyne with the stereoelectronic tunability of a nitron moiety. This reaction was termed the Strain-Promoted Alkyne-Nitron Cycloaddition (SPANC; **Figure 1D**).<sup>20</sup>

Although many other bioorthogonal reactions have been developed to date<sup>21,22</sup>, the most notable recent addition is the inverse electron demand Diels-Alder (IEDDA) reaction, due to its excellent reaction kinetics, chemical orthogonality and biocompatibility.<sup>23</sup> The IEDDA reaction involves a cycloaddition between a 1,2,4,5-tetrazine and a (strained) alkene group, and is often referred to as the tetrazine ligation reaction (**Figure 1E**).<sup>24,25</sup> Both reaction partners of this reaction can be extensively tuned to optimize the reaction in terms of speed, selectivity and stability of the product. Several different strained alkenes have been developed,

including norbornene<sup>26</sup>, cyclopropene<sup>27</sup>, spirohexene<sup>28</sup> and trans-cyclooctene (TCO)<sup>25,29</sup>.

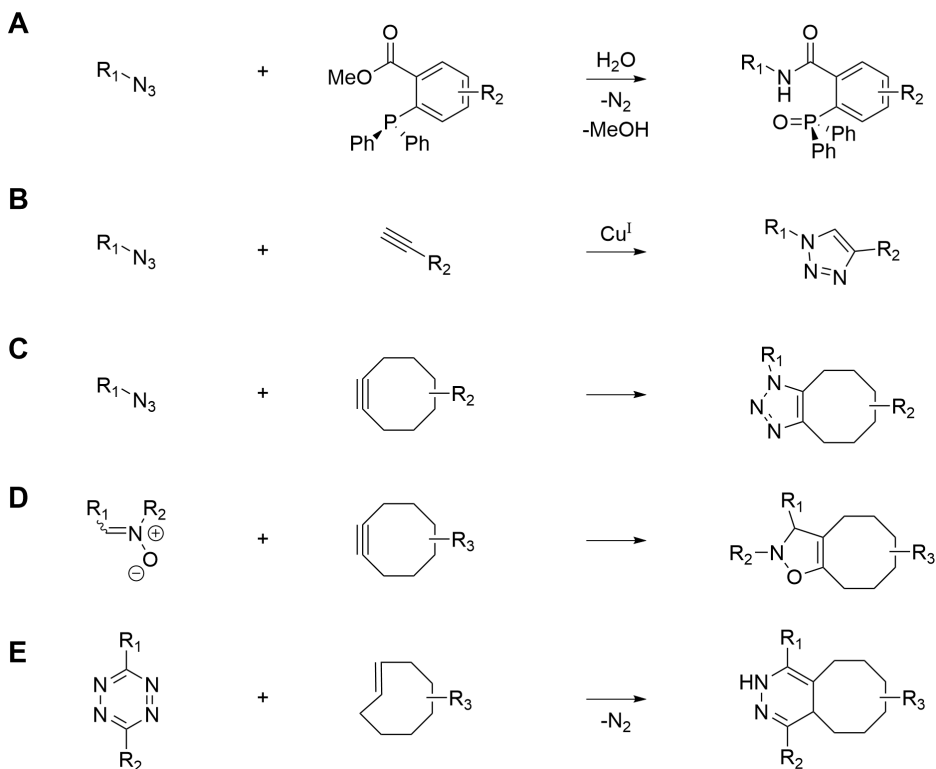


**Figure 1.** Overview of the most common bioorthogonal (click) reactions. **(A)** Staudinger ligation (a.k.a. Staudinger-Bertozzi ligation). **(B)** Cu(I)-catalyzed Azide-Alkyne Cycloaddition (CuAAC, a.k.a. copper-click reaction). **(C)** Strain-Promoted Azide-Alkyne Cycloaddition (SPAAC, a.k.a. copper-free click reaction). **(D)** Strain-Promoted Alkyne-Nitrone Cycloaddition (SPANC). **(E)** Inverse Electron-Demand Diels-Alder reaction (IEDDA), here showing the reaction between a tetrazine and a TCO (tetrazine ligation).

### 1.3 Bioorthogonal metabolic labeling

Metabolic labeling (also known as metabolic engineering) involves the incorporation of a detectable chemical label into a biomolecule of interest, using the native metabolism of the organism.<sup>30</sup> This is achieved by creating a synthetic analogue of a building block (e.g., an amino acid) that can be incorporated into larger biomolecules by the organism. The synthetic analogue needs to be sufficiently similar to the original, in order to be accepted by the cellular machinery, while containing a detectable label. Metabolic labeling can be achieved either by one-step labeling, in which the initial label can be detected directly (e.g. fluorophore or radioactive isotope), or two-step (direct) labeling, in which the initial label can be selectively ligated to a reporter molecule for detection (e.g. click handle), also known as bioorthogonal metabolic labeling.<sup>30</sup> The main advantage of bioorthogonal metabolic labeling is its broad compatibility with common analysis methods such as fluorescence microscopy, flow cytometry and proteomics<sup>31</sup> without interfering with the cellular processes<sup>32</sup>, which is often observed for one-step labeling approaches<sup>33</sup>.

Bioorthogonal metabolic labeling was originally developed by the group of Bertozzi, in order to selectively label and modify cell surface glycans.<sup>9,34,35</sup> In this study, a levulinoyl-analogue of *N*-acetylmannosamine (ManLev) was incorporated by the cells into the cell surface associated sialic acids. A hydrazide-functionalized biotin moiety could then be selectively ligated to the levulinoyl-modified sialic acids and subsequently visualized using a fluorophore-modified avidin moiety (which selectively binds to biotin).<sup>9</sup> Switching to an azide-analogue of *N*-acetylmannosamine (ManNAz), in combination with the more biocompatible Staudinger ligation, eventually made it possible to study cell surface glycans in living animals.<sup>36</sup> Bertozzi then continued to modify this strategy, using SPAAC to visualize the azide-modified sialic acid, which proved possible in living animals as well.<sup>37</sup> Although CuAAC is insufficiently biocompatible to be performed in live cells, it proved possible to metabolically incorporate an alkyne-analogue of *N*-acetylmannosamine (ManNAI) into living animals and perform the click reaction *ex vivo* after harvesting the organs.<sup>38</sup>

At present, bioorthogonal metabolic labeling has been successfully achieved for virtually all biomolecules<sup>33</sup>, including carbohydrates<sup>39</sup> as described above, but also proteins<sup>40</sup>, lipids<sup>41–43</sup>, nucleic acids<sup>44–46</sup> and bacterial cell wall components<sup>47–49</sup>. Although the method originated with carbohydrates, bioorthogonal labeling of proteins has gained a lot of attention over the years.<sup>40</sup> Some bioorthogonal

analogues of amino acids can be directly incorporated by an organism, when they are recognized by the native translational machinery (i.e. aminoacyl-tRNA synthetase).<sup>50</sup> This technique was termed Bioorthogonal Non-Canonical Amino acid Tagging (BONCAT) and provides both an azide and an alkyne analogue of L-methionine, that are readily incorporated into newly synthesized proteins.<sup>50,51</sup> BONCAT has been successfully applied to many different organisms including bacteria<sup>52,53</sup>, mammalian cells<sup>51,54</sup>, whole animals<sup>55–58</sup>, plants<sup>59</sup>, parasites<sup>60</sup> and viruses<sup>61,62</sup>.

#### 1.4 Bioorthogonal metabolic labeling of intracellular bacteria

One research field in which bioorthogonal metabolic labeling can be applied is the study of intracellular pathogenic bacteria and their interaction with the host cell. Both the extracellular and intracellular life cycle of pathogenic bacteria can be studied using bioorthogonal labeling to visualize the newly synthesized bacterial components, such as the membranes, cell wall or cytoplasmic content under various conditions. For example, the effect of antibiotics on peptidoglycan synthesis can be studied using D-alanine analogues<sup>63</sup> or the effect of nutrient limitation on mycomembrane remodeling using trehalose analogues<sup>64</sup>. Another possibility is to study the metabolic activity of viable bacteria using BONCAT.<sup>65</sup> Finally, various bioorthogonal analogues can be used to label bacteria of interest and study their intracellular fate, after uptake by phagocytic immune cells such as macrophages or dendritic cells. This approach has previously been used to visualize degradation of non-pathogenic *Escherichia coli* (*E. coli*)<sup>66</sup> and survival and proliferation of *Salmonella enterica* serovar Typhimurium (*Stm*)<sup>67</sup>. Additionally, this approach could be used to study more dangerous pathogenic intracellular bacteria such as *Mycobacterium tuberculosis* (*Mtb*) and the effect of antibiotics on the intracellular survival of those bacteria.

The broad compatibility of bioorthogonal metabolic labeling allows for many fluorescence-based analysis methods to be used. For example, when using BONCAT, the incorporation of bioorthogonal amino acids into the bacterial proteins can be assessed using SDS-PAGE, followed by in-gel fluorescence analysis. Additionally, the average labeling efficiency per bacterium can be assessed using flow cytometry. Finally, several microscopy techniques can be used to visualize the fluorescently labeled bacteria, including confocal fluorescence microscopy, Stochastic Optical Reconstruction Microscopy (STORM) and Correlative Light-Electron Microscopy (CLEM). Since STORM provides the best spatial resolution in terms of fluorescence and CLEM can provide the ultrastructural context of the host

cell, a combination of the two (STORM-CLEM) would provide the most detailed information on the intracellular bacterium, *in situ*.

### 1.5 Aim of this thesis

The aim of this thesis is to expand on the previously developed bioorthogonal CLEM technique for the study of intracellular bacteria. In **chapter 2**, the principle of bioorthogonal metabolic labeling for the study of intracellular bacteria is discussed in more detail and recent developments in the field are reviewed. In **chapter 3**, the stability of several commonly used click handles is tested within the chemically harsh intracellular environment of phagocytic immune cells, to confirm that they can be used to study the degradation or survival of intracellular bacteria. In **chapter 4**, bioorthogonal metabolic labeling of *Stm* is optimized for the development of STORM-CLEM, to study intracellular pathogenic bacteria in more detail. In **chapter 5**, dual bioorthogonal metabolic labeling of *Mtb* is presented and combined with a fluorescent protein. The resulting triple-label *Mtb* are studied using CLEM, and the effect of various first line antibiotics on the intracellular distribution and shape of *Mtb* is quantified. Additionally, the bioorthogonal label retention of intracellular *Mtb* is measured by flow cytometry, after retrieval of the bacteria by selective host cell lysis. In **chapter 6**, a summary of the previous chapters is provided, along with several future prospects which can be pursued, following the findings of this thesis.

## 1.6 References

- (1) Cox, M.; Nelson, D. L. *Lehninger Principles of Biochemistry*, 5th edition; **2008**.
- (2) Abozenadah, H.; Bishop, A.; Bittner, S.; Flatt, P. M. Chapter 8: The Major Macromolecules. **2018**, available from: <https://wou.edu/chemistry/chapter-11-introduction-major-macromolecules/> (accessed Jul 2, 2021).
- (3) Abozenadah, H.; Bishop, A.; Bittner, S.; Flatt, P. M. Chapter 7: Chemical Reactions in Biological Systems. **2018**, available from: <https://wou.edu/chemistry/courses/online-chemistry-textbooks/ch103-allied-health-chemistry/ch103-chapter-6-introduction-to-organic-chemistry-and-biological-molecules/> (accessed Jul 2, 2021).
- (4) Tanner, N. K. Ribozymes: The Characteristics and Properties of Catalytic RNAs. *FEMS Microbiol. Rev.* **1999**, 23 (3), 257–275.
- (5) Evolution Towards Complexity. *New Compr. Biochem.* **1999**, 34, 333–352.
- (6) Sletten, E. M.; Bertozzi, C. R. Bioorthogonal Chemistry: Fishing for Selectivity in a Sea of Functionality. *Angew. Chemie - Int. Ed.* **2009**, 48 (38), 6974–6998.
- (7) Hang, H. C.; Yu, C.; Kato, D. L.; Bertozzi, C. R. A Metabolic Labeling Approach toward Proteomic Analysis of Mucin-Type O-Linked Glycosylation. *Proc. Natl. Acad. Sci. U. S. A.* **2003**, 100 (25), 14846–14851.
- (8) Sletten, E. M.; Bertozzi, C. R. From Mechanism to Mouse; A Tale of Two Bioorthogonal Reactions. *Acc. Chem. Res.* **2011**, 44 (9), 666–676.
- (9) Prescher, J. a; Bertozzi, C. R. Chemistry in Living Systems. *Nat. Chem. Biol.* **2005**, 1 (1), 13–21.
- (10) Nilsson, B. L.; Kiessling, L. L.; Raines, R. T. Staudinger Ligation: A Peptide from a Thioester and Azide. *Org. Lett.* **2000**, 2 (13), 1939–1941.
- (11) Saxon, E.; Armstrong, J. I.; Bertozzi, C. R. A “Traceless” Staudinger Ligation for the Chemoselective Synthesis of Amide Bonds. *Org. Lett.* **2000**, 2 (14), 2141–2143.
- (12) Saxon, E.; Bertozzi, C. R. Cell Surface Engineering by a Modified Staudinger Reaction. *Science* **2000**, 287 (5460), 2007–2010.
- (13) Rideout, D.; Calogeropoulou, T.; Jaworski, J.; McCarthy, M. Synergism through Direct Covalent Bonding between Agents: A Strategy for Rational Design of Chemotherapeutic Combinations. *Biopolymers* **1990**, 29 (1), 247–262.
- (14) Mahal, L. K.; Yarema, K. J.; Bertozzi, C. R. Engineering Chemical Reactivity on Cell Surfaces through Oligosaccharide Biosynthesis. *Science*. **1997**, 276 (5315), 1125–1128.
- (15) Kolb, H. C.; Finn, M. G.; Sharpless, K. B. Click Chemistry: Diverse Chemical Function from a Few Good Reactions. *Angew. Chemie - Int. Ed.* **2001**, 40 (11), 2004–2021.
- (16) Nwe, K.; Brechbiel, M. W. Growing Applications of “Click Chemistry” for Bioconjugation in Contemporary Biomedical Research. *Cancer Biotherapy and Radiopharmaceuticals*. Mary Ann Liebert, Inc. 140 Huguenot Street, 3rd Floor New Rochelle, NY 10801 USA June 1, **2009**, pp 289–302.
- (17) Martell, J.; Weerapana, E. Applications of Copper-Catalyzed Click Chemistry in Activity-Based Protein Profiling. *Molecules* **2014**, 19 (2), 1378–1393.
- (18) Rostovtsev, V. V.; Green, L. G.; Fokin, V. V.; Sharpless, K. B. A Stepwise Huisgen Cycloaddition Process: Copper(I)-Catalyzed Regioselective “Ligation” of Azides and Terminal Alkynes. *Angew. Chemie - Int. Ed.* **2002**, 41 (14), 2596–2599.
- (19) Tornøe, C. W.; Christensen, C.; Meldal, M. Peptidotriazoles on Solid Phase: [1,2,3]-Triazoles by Regiospecific Copper(I)-Catalyzed 1,3-Dipolar Cycloadditions of Terminal Alkynes to Azides. *J. Org. Chem.* **2002**, 67 (9), 3057–3064.
- (20) Hong, V.; Steinmetz, N. F.; Manchester, M.; Finn, M. G. Labeling Live Cells by Copper-Catalyzed Alkyne - Azide Click Chemistry. *Bioconjugate chem.* **2010**, 21 (10), 1912–1916.
- (21) Yang, M.; Jalloh, A. S.; Wei, W.; Zhao, J.; Wu, P.; Chen, P. R. Biocompatible Click



- Chemistry Enabled Compartment-Specific PH Measurement inside E. Coli. *Nat. Commun.* **2014**, *5*, 1–10.
- (22) Yang, M.; Li, J.; Chen, P. R. Transition Metal-Mediated Bioorthogonal Protein Chemistry in Living Cells. *Chem. Soc. Rev.* **2014**, *43* (18), 6511.
- (23) Agard, N. J.; Prescher, J. A.; Bertozzi, C. R. A Strain-Promoted [3 + 2] Azide-Alkyne Cycloaddition for Covalent Modification of Biomolecules in Living Systems. *J. Am. Chem. Soc.* **2004**, *126* (46), 15046–15047.
- (24) Agard, N. J.; Baskin, J. M.; Prescher, J. A.; Lo, A.; Bertozzi, C. R. A Comparative Study of Bioorthogonal Reactions with Azides. *JACS Chem. Biol.* **2006**, *1* (10), 644–648.
- (25) MacKenzie, D. A.; Sherratt, A. R.; Chigrinova, M.; Cheung, L. L. W.; Pezacki, J. P. Strain-Promoted Cycloadditions Involving Nitrones and Alkynes-Rapid Tunable Reactions for Bioorthogonal Labeling. *Curr. Opin. Chem. Biol.* **2014**, *21*, 81–88.
- (26) Patterson, D. M.; Nazarova, L. A.; Prescher, J. A. Finding the Right (Bioorthogonal) Chemistry. *ACS Chem. Biol.* **2014**, *9* (3), 592–605.
- (27) Nguyen, S. S.; Prescher, J. A. Developing Bioorthogonal Probes to Span a Spectrum of Reactivities. *Nat. Rev. Chem.* **2020**, *4* (9), 476–489.
- (28) Oliveira, B. L.; Guo, Z.; Bernardes, G. J. L. Inverse Electron Demand Diels–Alder Reactions in Chemical Biology. *Chem. Soc. Rev.* **2017**, *46* (16), 4895–4950.
- (29) Knall, A. C.; Slugovc, C. Inverse Electron Demand Diels–Alder (IEDDA)-Initiated Conjugation: A (High) Potential Click Chemistry Scheme. *Chem. Soc. Rev.* **2013**, *42* (12), 5131–5142.
- (30) Blackman, M. L.; Royzen, M.; Fox, J. M. Tetrazine Ligation: Fast Bioconjugation Based on Inverse-Electron-Demand Diels–Alder Reactivity. *J. Am. Chem. Soc.* **2008**, *130* (41), 13518–13519.
- (31) Hansell, C. F.; Espeel, P.; Stamenović, M. M.; Barker, I. A.; Dove, A. P.; Du Prez, F. E.; O'Reilly, R. K. Additive-Free Clicking for Polymer Functionalization and Coupling by Tetrazine–Norbornene Chemistry. *J. Am. Chem. Soc.* **2011**, *133* (35), 13828–13831.
- (32) Yang, J.; Liang, Y.; Šečkute, J.; Houk, K. N.; Devaraj, N. K. Synthesis and Reactivity Comparisons of 1-Methyl-3-Substituted Cyclopropene Mini-Tags for Tetrazine Bioorthogonal Reactions. *Chem. – A Eur. J.* **2014**, *20* (12), 3365–3375.
- (33) Ramil, C. P.; Dong, M.; An, P.; Lewandowski, T. M.; Yu, Z.; Miller, L. J.; Lin, Q. Spirohexene–Tetrazine Ligation Enables Bioorthogonal Labeling of Class B G Protein-Coupled Receptors in Live Cells. *J. Am. Chem. Soc.* **2017**, *139* (38), 13376–13386.
- (34) Devaraj, N. K.; Weissleder, R.; Hilderbrand, S. A. Tetrazine-Based Cycloadditions: Application to Pretargeted Live Cell Imaging. *Bioconjug. Chem.* **2008**, *19* (12), 2297–2299.
- (35) Siegrist, M. S.; Swarts, B. M.; Fox, D. M.; Lim, S. A.; Bertozzi, C. R. Illumination of Growth, Division and Secretion by Metabolic Labeling of the Bacterial Cell Surface. *FEMS Microbiology Reviews*. Oxford University Press March 1, **2015**, pp 184–202.
- (36) Cañeque, T.; Müller, S.; Rodriguez, R. Visualizing Biologically Active Small Molecules in Cells Using Click Chemistry. *Nat. Rev. Chem.* **2018**, *2* (9), 202–215.
- (37) Steward, K. F.; Eilers, B.; Tripet, B.; Fuchs, A.; Dorle, M.; Rawle, R.; Soriano, B.; Balasubramanian, N.; Copié, V.; Bothner, B.; Hatzenpichler, R. Metabolic Implications of Using BioOrthogonal Non-Canonical Amino Acid Tagging (BONCAT) for Tracking Protein Synthesis. *Front. Microbiol.* **2020**, *11* (February), 197.
- (38) Grammel, M.; Hang, H. C. Chemical Reporters for Biological Discovery. *Nat. Chem. Biol.* **2013**, *9* (8), 475–484.
- (39) Yarema, K. J.; Mahal, L. K.; Bruehl, R. E.; Rodriguez, E. C.; Bertozzi, C. R. Metabolic Delivery of Ketone Groups to Sialic Acid Residues. Application to Cell Surface Glycoform Engineering. *J. Biol. Chem.* **1998**, *273* (47), 31168–31179.
- (40) Lee, J. H.; Baker, T. J.; Mahal, L. K.; Zabner, J.; Bertozzi, C. R.; Wiemer, D. F.; Welsh, M. J.

- Engineering Novel Cell Surface Receptors for Virus-Mediated Gene Transfer. *J. Biol. Chem.* **1999**, *274* (31), 21878–21884.
- (41) Prescher, J. A.; Dube, D. H.; Bertozzi, C. R. Chemical Remodelling of Cell Surfaces in Living Animals. *Nature* **2004**, *430* (7002), 873–877.
- (42) Chang, P. V.; Prescher, J. A.; Sletten, E. M.; Baskin, J. M.; Miller, I. A.; Agard, N. J.; Lo, A.; Bertozzi, C. R. Copper-Free Click Chemistry in Living Animals. *Proc. Natl. Acad. Sci. U. S. A.* **2010**, *107* (5), 1821–1826.
- (43) Chang, P. V.; Chen, X.; Smyrniotis, C.; Xenakis, A. Metabolic Labeling of Sialic Acids in Living Animals with Alkynyl Sugars. *Angew. Chem. Int. Ed. Engl.* **2009**, *48* (22), 4030–4033.
- (44) Sminia, T. J.; Zuilhof, H.; Wennekes, T. Getting a Grip on Glycans: A Current Overview of the Metabolic Oligosaccharide Engineering Toolbox. *Carbohydrate Research*. **2016**, pp 121–141.
- (45) Lang, K.; Chin, J. W. Bioorthogonal Reactions for Labeling Proteins. *ACS Chem. Biol.* **2014**, *9* (1), 16–20.
- (46) Neef, A. B.; Schultz, C. Selective Fluorescence Labeling of Lipids in Living Cells. *Angew. Chemie - Int. Ed.* **2009**, *48* (8), 1498–1500.
- (47) Bumpus, T. W.; Baskin, J. M. Greasing the Wheels of Lipid Biology with Chemical Tools. *Trends Biochem. Sci.* **2018**, *43* (12), 970–983.
- (48) Ancajas, C. F.; Ricks, T. J.; Best, M. D. Metabolic Labeling of Glycerophospholipids via Clickable Analogs Derivatized at the Lipid Headgroup. *Chem. Phys. Lipids* **2020**, *232* (July), 104971.
- (49) Neef, A. B.; Luedtke, N. W. An Azide-Modified Nucleoside for Metabolic Labeling of DNA. *ChemBioChem* **2014**, *15* (6), 789–793.
- (50) Nguyen, K.; Fazio, M.; Kubota, M.; Nainar, S.; Feng, C.; Li, X.; Atwood, S. X.; Bredy, T. W.; Spitale, R. C. Cell-Selective Bioorthogonal Metabolic Labeling of RNA. *J. Am. Chem. Soc.* **2017**, *139* (6), 2148–2151.
- (51) Klöcker, N.; Weissenboeck, F. P.; Rentmeister, A. Covalent Labeling of Nucleic Acids. *Chem. Soc. Rev.* **2020**.
- (52) Backus, K. M.; Boshoff, H. I.; Barry, C. E. C. S.; Boutureira, O.; Patel, M. K.; D'Hooge, F.; Lee, S. S.; Via, L. E.; Tahlan, K.; Barry, C. E. C. S.; Davis, B. G. Uptake of Unnatural Trehalose Analogs as a Reporter for Mycobacterium Tuberculosis. *Nat. Chem. Biol.* **2011**, *7* (4), 228–235.
- (53) Siegrist, M. S.; Whiteside, S.; Jewett, J. C.; Aditham, A.; Cava, F.; Bertozzi, C. R. D-Amino Acid Chemical Reporters Reveal Peptidoglycan Dynamics of an Intracellular Pathogen. *ACS Chem. Biol.* **2013**, *8* (3), 500–505.
- (54) Liang, H.; DeMeester, K. E.; Hou, C. W.; Parent, M. A.; Caplan, J. L.; Grimes, C. L. Metabolic Labelling of the Carbohydrate Core in Bacterial Peptidoglycan and Its Applications. *Nat. Commun.* **2017**, *8*, 1–11.
- (55) Kiick, K. L.; Saxon, E.; Tirrell, D. a; Bertozzi, C. R. Incorporation of Azides into Recombinant Proteins for Chemoselective Modification by the Staudinger Ligation. *Proc. Natl. Acad. Sci. U. S. A.* **2002**, *99* (1), 19–24.
- (56) Dieterich, D. C.; Link, A. J.; Graumann, J.; Tirrell, D. A.; Schuman, E. M. Selective Identification of Newly Synthesized Proteins in Mammalian Cells Using Bioorthogonal Noncanonical Amino Acid Tagging (BONCAT). *Proc. Natl. Acad. Sci.* **2006**, *103* (25), 9482–9487.
- (57) Wang, J.; Zhao, L.-Y.; Uyama, T.; Tsuboi, K.; Wu, X.-X.; Kakehi, Y.; Ueda, N. Expression and Secretion of N-Acylethanolamine-Hydrolysing Acid Amidase in Human Prostate Cancer Cells. *J. Biochem.* **2008**, *144* (5), 685–690.
- (58) Reichart, N. J.; Jay, Z. J.; Krukenberg, V.; Parker, A. E.; Spietz, R. L.; Hatzenpichler, R. Activity-Based Cell Sorting Reveals Responses of Uncultured Archaea and Bacteria to

- Substrate Amendment. *ISME J.* **2020**, 1–11.
- (59) Howden, A. J. M.; Geoghegan, V.; Katsch, K.; Efstathiou, G.; Bhushan, B.; Boutureira, O.; Thomas, B.; Trudgian, D. C.; Kessler, B. M.; Dieterich, D. C.; Davis, B. G.; Acuto, O. QuanCAT: Quantitating Proteome Dynamics in Primary Cells. *Nat. Methods* **2013**, *10* (4), 343–346.
  - (60) Hinz, F. I.; Dieterich, D. C.; Tirrell, D. A.; Schuman, E. M. Noncanonical Amino Acid Labeling in Vivo to Visualize and Affinity Purify Newly Synthesized Proteins in Larval Zebrafish. *ACS Chem. Neurosci.* **2012**, *3* (1), 40–49.
  - (61) Ullrich, M.; Liang, V.; Chew, Y. L.; Banister, S.; Song, X.; Zaw, T.; Lam, H.; Berber, S.; Kassiou, M.; Nicholas, H. R.; Götz, J. Bio-Orthogonal Labeling as a Tool to Visualize and Identify Newly Synthesized Proteins in *Caenorhabditis Elegans*. *Nature Protocols*. Nature Publishing Group August 28, **2014**, pp 2237–2255.
  - (62) Erdmann, I.; Marter, K.; Kobler, O.; Niehues, S.; Abele, J.; Müller, A.; Bussmann, J.; Storkebaum, E.; Ziv, T.; Thomas, U.; Dieterich, D. C. Cell-Selective Labelling of Proteomes in *Drosophila Melanogaster*. *Nat. Commun.* **2015**, *6* (1), 1–11.
  - (63) Evans, H. T.; Bodea, L. G.; Götz, J. Cell-Specific Non-Canonical Amino Acid Labelling Identifies Changes in the de Novo Proteome during Memory Formation. *Elife* **2020**, *9*, 1–19.
  - (64) Glenn, W. S.; Stone, S. E.; Ho, S. H.; Sweredoski, M. J.; Moradian, A.; Hess, S.; Bailey-Serres, J.; Tirrell, D. A. Bioorthogonal Noncanonical Amino Acid Tagging (BONCAT) Enables Time-Resolved Analysis of Protein Synthesis in Native Plant Tissue. *Plant Physiol.* **2017**, *173* (3), 1543–1553.
  - (65) Kalesh, K.; Denny, P. W. A BONCAT-ITRAQ Method Enables Temporally Resolved Quantitative Profiling of Newly Synthesised Proteins in *Leishmania Mexicana* Parasites during Starvation. *PLoS Negl. Trop. Dis.* **2019**, 1–26.
  - (66) Pasulka, A. L.; Thamatrakoln, K.; Kopf, S. H.; Guan, Y.; Poulos, B.; Moradian, A.; Sweredoski, M. J.; Hess, S.; Sullivan, M. B.; Bidle, K. D.; Orphan, V. J. Interrogating Marine Virus-Host Interactions and Elemental Transfer with BONCAT and NanoSIMS-Based Methods. *Environ. Microbiol.* **2018**, *20* (2), 671–692.
  - (67) Berjón-Otero, M.; Duponchel, S.; Hackl, T.; Fischer, M. Visualization of Giant Virus Particles Using BONCAT Labeling and STED Microscopy. *bioRxiv* **2020**, 2020.07.14.202192.
  - (68) García-Heredia, A.; Pohane, A. A.; Melzer, E. S.; Carr, C. R.; Fiolek, T. J.; Rundell, S. R.; Lim, H. C.; Wagner, J. C.; Morita, Y. S.; Swarts, B. M.; Siegrist, M. S. Peptidoglycan Precursor Synthesis along the Sidewall of Pole-Growing Mycobacteria. *Elife* **2018**, *7*, 1–22.
  - (69) Pohane, A. A.; Carr, C. R.; Garhyan, J.; Swarts, B. M.; Siegrist, M. S. Trehalose Recycling Promotes Energy-Efficient Biosynthesis of the Mycobacterial Cell Envelope. *MBio* **2021**, *12* (1), 1–19.
  - (70) Sherratt, A. R.; Rouleau, Y.; Luebbert, C.; Strmiskova, M.; Veres, T.; Bidawid, S.; Corneau, N.; Pezacki, J. P. Rapid Screening and Identification of Living Pathogenic Organisms via Optimized Bioorthogonal Non-Canonical Amino Acid Tagging. *Cell Chem. Biol.* **2017**, *24* (8), 1048–1055.e3.
  - (71) van Elsland, D. M.; Bos, E.; de Boer, W.; Overkleeft, H. S.; Koster, A. J.; van Kasteren, S. I. Detection of Bioorthogonal Groups by Correlative Light and Electron Microscopy Allows Imaging of Degraded Bacteria in Phagocytes. *Chem. Sci.* **2016**, *7* (1), 752–758.
  - (72) van Elsland, D. M.; Pujals, S.; Bakkum, T.; Bos, E.; Oikonomias-Koppas, N.; Berlin, I.; Neefjes, J.; Meijer, A. H.; Koster, A. J.; Albertazzi, L.; van Kasteren, S. I. Ultrastructural Imaging of Salmonella–Host Interactions Using Super-Resolution Correlative Light-Electron Microscopy of Bioorthogonal Pathogens. *ChemBioChem* **2018**, *19* (16), 1766–1770.

# Chapter 2

## Metabolic Labeling Probes for Interrogation of the Host-Pathogen Interaction

Published as:

Bob J. Ignacio\*, Thomas Bakkum\*, Kimberly M. Bonger, Nathaniel I. Martin, and Sander I. van Kasteren. *Organic & Biomolecular Chemistry*, **2021**; 19: 2856-2870 (\*Authors contributed equally).



## **Abstract**

Bacterial infections are still one of the leading causes of death worldwide; despite the near-ubiquitous availability of antibiotics. With antibiotic resistance on the rise, there is an urgent need for novel classes of antibiotic drugs. One particularly troublesome class of bacteria are those that have evolved highly efficacious mechanisms for surviving inside the host. These contribute to their virulence by immune evasion, and make them harder to treat with antibiotics due to their residence inside intracellular membrane-limited compartments. This has sparked the development of new chemical reporter molecules and bioorthogonal probes that can be metabolically incorporated into bacteria to provide insights into their activity status. This chapter provides an overview of several classes of metabolic labeling probes capable of targeting either the peptidoglycan cell wall, the mycomembrane of mycobacteria and corynebacteria, or specific bacterial proteins. In addition, several important insights that have been made using these metabolic labeling probes are highlighted.

## 2.1 Introduction

Despite the near-ubiquity of antibiotics in modern times, bacterial infections are still among the leading causes of death globally.<sup>1</sup> Overuse of antibiotics in high-income countries has contributed to an evolutionary selection pressure that is driving antibiotic resistance.<sup>2</sup> New antibiotic resistance mechanisms are rapidly emerging<sup>3</sup>, resulting in a staggering increase in multi-drug resistant (MDR), extensive drug resistant (XDR), and pan-drug resistant (PDR) strains.<sup>4</sup> At the same time, the development of novel classes of antibiotics has been extremely slow, with only two new classes of broad-spectrum antibiotics introduced to the clinic since 1962.<sup>5,6</sup> Development of antibiotics for a certain class of pathogenic bacteria has been particularly difficult: the intracellular bacteria. Intracellular bacteria reside inside host cells, where they can evade immune detection and persist for months or even years in a dormant state.<sup>7,8</sup> In order for an antibiotic to be active against infections caused by intracellular bacteria, the drug not only has to cross the bacterial cell envelope but also the host cell membrane. The study of (obligate) intracellular pathogens is further complicated by the fact that they are often difficult to culture *in vitro*.<sup>9,10</sup> In light of these challenges, novel antibiotics against intracellular bacteria are much needed, as the disease burden from these species is very high.

The deadliest bacterial species is arguably *Mycobacterium tuberculosis* (*Mtb*), a facultative intracellular bacterium that is the major cause of tuberculosis (TB). This pathogen is responsible for approximately 2 million deaths annually<sup>11</sup> and antibiotic-resistant strains are continually emerging. Treating infections due to *Mtb* is made difficult by the heterogeneity in its intracellular life cycle: after infecting macrophages it diverges into fast and very slow-growing forms.<sup>12,13</sup> The slow growing form is generally hard to treat with conventional antibiotics such as those that target the nascent cell wall of the dividing bacteria.<sup>14–20</sup> As a result, TB is typically treated with a complex cocktails of antibiotics that need to be taken for long periods of time. Addressing infections due to MDR *Mtb* is even more challenging requiring antibiotic treatment courses of up to 2 years (often with severe side-effects).<sup>21</sup> One new therapy – the first in many years – was recently approved for drug-resistant forms of *Mtb*: pretomanid in combination with bedaquiline and linezolid. Whilst this is laudable – as is the clinical development of other *Mtb* active agents – the demand for new treatments for *Mtb* and other intracellular pathogens currently far outstrips supply.<sup>22</sup> *Mtb* is not the only intracellular pathogen causative of high-mortality/morbidity disease. Other intracellular pathogens of clinical concern include *Salmonella enterica*, *Yersinia*

*pestis*, *Chlamydia trachomatis*, *Listeria monocytogenes* and *Coxiella burnetii* to name but a few.<sup>23</sup> Whilst not displaying quite the same nefariousness as *Mtb*, these organisms are associated with a host of pathologies ranging from infertility to increased risk of bowel cancer.<sup>24,25</sup> While these pathogens can largely still be controlled with available antibiotics, the increased emergence of resistance threatens our continued ability to do so and paints a bleak future.<sup>26</sup>

Bacterial pathogens have acquired highly effective mechanisms for infecting- and surviving inside hosts. These mechanisms lead to increased virulence and persistence within the host environment, along with suppression of the host immune system.<sup>27</sup> Due to their importance for bacterial cell viability and infectivity inside the host, bacterial defense mechanisms at the host-pathogen interface are a promising target for novel antibiotics.<sup>28,29</sup> Thus, effective chemical tools to study the host-pathogen interface at the molecular level are of paramount importance in the fight against antibiotic resistance. To provide clinically significant data, these chemical tools must be useable *in vivo* in pathogenic bacteria. Moreover, the cellular processes they report on must be relevant to bacterial cell survival and/or virulence.

Recently, novel chemical probes and approaches have been developed that allow for the profiling of various metabolic processes, as well as *in vivo* cell wall and protein labeling. In metabolic profiling a chemical probe is exogenously supplied to an organism, which subsequently incorporates the chemical probe into its cellular architecture by means of endogenous enzymes. Novel chemical probes have been developed that carry fluorescent dyes allowing for facile, one-step metabolic labeling of bacterial structures of interest such as the peptidoglycan (PG) of the cell wall<sup>30,31</sup>, or the mycomembrane (MM) of corynebacteria.<sup>32,33</sup> Moreover, the introduction of bioorthogonal chemistry has furthered the field by allowing for chemical reactions to be performed inside the crowded environment of the bacterial cell.<sup>34</sup> Bioorthogonal groups are by definition non-reactive, or orthogonal, to their biological environment, but highly reactive towards their bioorthogonal reaction partner.<sup>35</sup> Moreover, bioorthogonal groups such azides or alkynes can be readily introduced into common bacterial metabolites with minimal perturbation of biological function. After metabolic incorporation into bacteria, bioorthogonal probes can be reacted with reporter molecules carrying a complimentary bioorthogonal group. Such reporters include fluorophores that allow for the visualization of bacterial biomolecules of interest or affinity tags to facilitate their enrichment. As such, bioorthogonal chemistry has driven advancements in two-step metabolic labeling approaches for host-pathogen interaction studies. As a

whole, metabolic labeling in bacteria, in one step or two steps, has shed a light on previously uncharacterized bacterial cell processes, making it a valuable tool in the search for novel targets for antibiotic drug development.

In this chapter, recent developments in the field of metabolic labeling are reviewed in the context of the host-pathogen interface. The initial discoveries of several chemical probes and labeling strategies are covered, as well as the subsequent improvements made to these probes and labeling strategies while also highlighting several examples of important findings achieved using these methods. Specifically, the use of D-amino acids (DAAs) for metabolic labeling of PG in the bacterial cell wall and the labeling of the MM of corynebacteria using trehalose-analogues are discussed. Moreover, the use of Bioorthogonal Non-Canonical Amino acid Tagging (BONCAT) for the labeling of new protein synthesis in bacteria and the application of so-called activity based probes that target enzyme activities specific to the bacterial pathogen of interest are covered. The principle of labeling intracellular bacteria is illustrated in **Figure 1A**.

## 2.2 Metabolic labeling of peptidoglycan

Peptidoglycan (PG) is the major constituent of the bacterial cell wall. PG consists of linear glycan strands that are cross-linked through short peptides, creating a dense macromolecular network that is vital to bacterial survival. The bacterial cell wall provides structural integrity for the cell and protects it against the osmotic pressure established by high intracellular concentrations of proteins and other biomolecules.<sup>36</sup> The PG cell wall also functions as an anchor for important macromolecules of the cell envelope, such as teichoic acids<sup>37</sup>, and Braun's lipoprotein.<sup>38</sup> Due to its vital role in bacterial survival, relative accessibility at the outside of the cell, and absence in eukaryotic cells, PG biosynthesis is a prime target for antibiotics.<sup>39</sup> Many widely used antibiotics including the  $\beta$ -lactams exemplified by penicillin,<sup>40</sup> glycopeptides such as vancomycin<sup>41</sup>, and the lipopeptide bacitracin<sup>42</sup> function by inhibiting various aspects of bacterial cell wall biosynthesis. However, due to misuse and overuse, bacteria are acquiring resistance against these antibiotics at an alarming rate.<sup>5,43</sup> Nonetheless, the bacterial cell wall remains a very promising target for the development of novel antibiotics.

PG metabolism has been studied using various methods, such as metabolic labeling with radioprobes.<sup>44</sup> Other methods include labeling of the bacterial cell wall using fluorescently tagged antibiotics<sup>45,46</sup> as well as by the incorporation of a fluorescently labeled tripeptide into the cell wall by exploiting the PG recycling machinery of *Escherichia coli* (*E. coli*).<sup>47</sup> These techniques have multiple limitations:



1) labeling techniques that are dependent on the PG recycling pathway of *E. coli* can only be used to study this specific organism; 2) Radiolabeling of PG is known to be a very laborious and technically complex technique; 3) Labeling the bacterial cell wall using fluorescently tagged antibiotics is limited to bacterial species with an accessible cell wall and enzyme machinery tolerant to these large pendant fluorophores; and 4) The use of fluorescently tagged antibiotics has an inhibitory effect on bacterial cell growth, thereby limiting their use for *in vivo* applications.

Recently, metabolic labeling of PG using new D-amino acid (DAA) analogues has led to significant advancements in the understanding of cell wall biosynthesis and recycling of PG. Whereas nearly all life forms use exclusively L-amino acids, most bacteria also use DAAs, which are incorporated into the PG cell wall.<sup>48</sup> D-alanine and D-glutamic acid are the DAAs that are most often incorporated into PG and can thus be found in the cell wall of nearly all bacteria.<sup>48</sup> Interestingly, studies have shown that the biosynthetic machinery involved in PG synthesis is highly tolerant to a variety of different DAAs.<sup>49,50</sup> This phenomenon has been exploited to incorporate DAAs and analogues thereof, to act as reporter molecules (one-step metabolic PG labeling) or as chemical handles for the conjugation of reporter molecules (two-step metabolic PG labeling). Kuru et al.<sup>16</sup> were the first to employ fluorescent D-amino acids (FDAAs) for one-step PG labeling and imaging of bacterial cell walls in live cells. Starting from the D-amino acids 3-amino-D-alanine and D-lysine, they reacted reporter molecules 7-hydroxycoumarin-3-carboxylic acid (HCC), 4-chloro-7-nitrobenzofurazan (NBD), fluorescein and carboxy-tetramethylrhodamine (TAMRA) to synthesize a variety of fluorescent amino acids, such as HADA, NADA, FDL and TDL (**Figure 1B**).<sup>30</sup> Subsequently, they succeeded in labeling a wide range of Gram-negative and Gram-positive bacteria, including, but not limited to, *E. coli*, *Staphylococcus aureus* and *Bacillus subtilis*, and showed that these FDAAs were selectively incorporated into the bacterial cell wall. In *B. subtilis*, they showed that these FDAAs were incorporated exclusively into PG and not into teichoic acids; which also contain D-alanine residues.<sup>30</sup> Because of their broad species applicability and excellent selectivity for PG, FDAAs have been used to study cell wall synthesis and its role in pathogenesis<sup>51–59</sup>, and to establish the presence of PG in many bacterial species.<sup>60–62</sup> An interesting application of FDAAs is the construction of so-called ‘virtual time-lapse’ images of PG synthesis in individual organisms. By sequentially adding FDAAs with different spectral properties, the growing PG layer can be sequentially labeled with multiple, differently colored FDAAs. This creates a multi-colored image where each color represents the location and amount of PG that is synthesized during the time in which FDAA was added.<sup>30,63</sup>

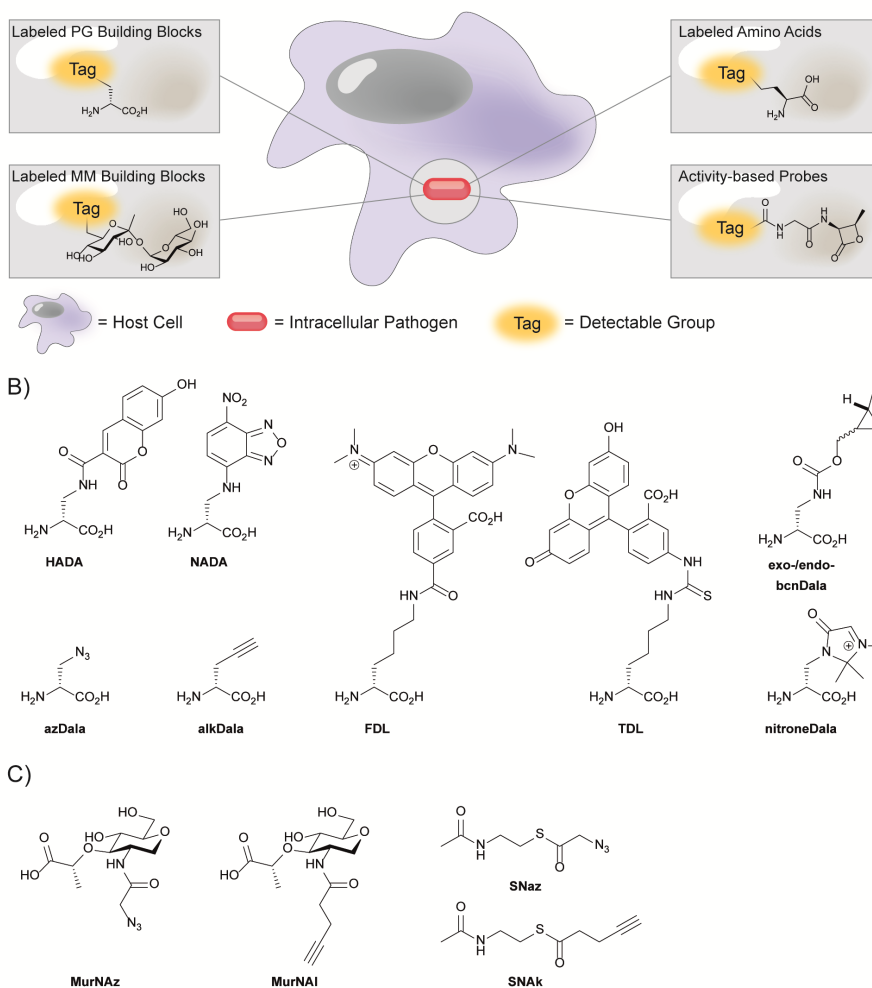


**Figure 1.** (A) Schematic overview of the bioorthogonal metabolic labeling approaches discussed here. (B) D-amino acid analogues for metabolic labeling of PG. (C) Click-reactive muramic acid for selective labeling of newly synthesized PG and acetyl-CoA analogues for post-synthetic labeling of existing PG through O-acetylation.

FDAAs owe their broad applicability partially to their low molecular weight; labeling of the Gram-negative bacterial cell wall requires passage through the outer membrane, which is markedly less permeable to molecules over a molecular weight of ~600 Da, such as antibiotics.<sup>64</sup> Indeed, when Hsu et al.<sup>65</sup> compared the labeling of *E. coli* with FDAAs with molecular weights between 300-700 Da, they found that FDAAs over a molecular weight of ~500 Da have reduced access to the *E. coli*

periplasm and cytoplasm and label the cell wall less efficiently. Today, the available toolkit of FDAAs covers the whole visible spectrum, from violet to far-red, providing many options for PG imaging in real time. Amongst these are FDAAs that are compatible with Stochastic Optical Reconstruction Microscopy (STORM), such as Cy3B and Atto 488, allowing imaging of PG nanostructures with far better spatial resolution.<sup>65</sup> Improvements to other FDAAs include increased water solubility, increased photostability, and the possibility to excite with far-red light, reducing the phototoxic burden on the bacteria that is being probed. In conclusion, FDAA labeling is an excellent analysis technique to study the bacterial cell wall because of its selectivity for bacterial PG, its relative experimental simplicity, and the ubiquity of DAAs in the cell walls of all bacterial taxa. Moreover, FDAAs only label nascent PG and are therefore an ideal tool to study spatial and temporal aspects of PG synthesis. The expansion of the FDAA toolkit into probes that are suitable for STORM has improved the spatial resolution that can be attained with FDAA labeling and cements the relevance of this technique for the study of the bacterial cell wall.<sup>65</sup> Notably, however, FDAAs have not yet been applied to the imaging of intracellular pathogenic bacteria.

One downside of the FDAA-approach is that these probes are only incorporated into PG via the extracellular pathways reliant on the D,D- and L,D-transpeptidases, and are therefore not tolerated by the D-alanine racemase (Alr) and the UDP-*N*-acetylmuramoyl-tripeptide-D-alanyl-D-alanine ligase (MurF).<sup>62,66</sup> These steps of the pathway in most species can, however, be labeled using a two-step labeling approach. The approach is based on metabolic incorporation of a D-amino acid equipped with a specific chemical handle, which, once incorporated into the PG network, can be labeled using a reporter molecule that is reactive to the handle. Two-step PG labeling has a lower risk of causing biological perturbation than one-step PG labeling, as the chemical handle is usually much smaller than the probes used in one-step PG labeling. Presently, bioorthogonal groups are commonly used as chemical handles in two-step PG labeling, because of their high reactivity towards their bioorthogonal reaction partners and their inertness towards biomolecules.<sup>34</sup> PG labeling has been performed using D-cysteine as a chemical handle, effectively incorporating thiol groups into the cell wall for coupling to thiol-reactive reporter molecules.<sup>67</sup> But, reporter molecules that target D-cysteine do not selectively label PG, as they are also reactive to L-cysteine residues in cellular proteins. To overcome such limitations, the introduction of D-amino acids containing bioorthogonal groups such as azides, alkynes, and nitrones allows for highly selective two-step metabolic labeling of PG.<sup>68</sup>

Kuru et al.<sup>30</sup> and Siegrist et al.<sup>31</sup> independently reported the use of DAAs containing bioorthogonal groups for PG labeling: D-propargylglycine (alkDala; alkyne analogue of D-alanine), and 2-amino-3-azidopropanoic acid (azDala; azide-analogue of D-alanine) (**Figure 1B**). Kuru et al. validated the concept of bioorthogonal two-step metabolic PG labeling by labeling both *B. subtilis* and *E. coli* cells *in vitro* with alkDala and azDala.<sup>68</sup> Expanding on this work, Siegrist et al. showed that *Listeria monocytogenes* and *Mtb* could be efficiently labeled by alkDala and azDala, both *in vitro* and *in vivo*, inside infected J774 macrophages. Notably, this work also demonstrated that macrophages take up sufficient alkDala for effective labeling of intracellular bacteria without any apparent toxicity to either the macrophages or bacteria, highlighting the potential of two-step metabolic DAA labeling for *in vivo* applications.<sup>17</sup> Combining the promiscuity of alkDala labeling with the selectivity of RADA labeling, Garcia-Heredia et al. showed that PG repair also occurs away from the sites of *de novo* PG synthesis in various mycobacterial species.<sup>66</sup> Since then, Pidgeon et al. also reported probes specific for the L,D-transpeptidase to provide further tools to study bacterial cell wall synthesis. The possibility of applying these probes to the study of the intracellular lifecycle of pathogens offers a tantalizing opportunity as a tool in the development of drugs against such pathogens.<sup>69</sup>

The bioorthogonal toolkit for *in vivo* metabolic labeling of PG was further expanded by Shieh et al.<sup>70</sup> They synthesized D-amino acids equipped with the strained cyclooctyne and bicyclononyne (BCN) moieties (**Figure 1B**), for copper-free, strain-promoted alkyne-azide “click” (SPAAC) reactions. Furthermore, they synthesized near-infrared (NIR) azide-functionalized fluorogenic Si-rhodamine dyes whose fluorescence quantum yield greatly increases upon reaction with alkynes. These NIR fluorogenic dyes are optimal for *in vivo* imaging as near infrared light penetrates deeper through tissue than higher wavelength light and no washing of excess dye is required as the dye becomes vastly more fluorescent upon reaction. The Pezacki group added an additional bioorthogonal reaction to the labeling repertoire by designing nitron D-amino acids that readily undergo reactions with strained alkynes in a Strain-Promoted Alkyne-Nitron Cycloaddition (SPANC) reaction (**Figure 1B**).<sup>68,71</sup>

Metabolic incorporation of D-amino acid probes is well tolerated in most bacteria, with notable exceptions. For instance, the intracellular bacterium *Chlamydia trachomatis* required additional reagents to enable PG labeling. While circumstantial evidence for the existence of a PG containing cell wall in *C. trachomatis* had existed for decades,<sup>72,73</sup> until recently no one had conclusively isolated or characterized PG from this bacterium.<sup>74,75</sup> This resulted in a discrepancy

called the 'Chlamydial Anomaly', where no PG was observed, yet the pathogen was sensitive to PG-targeting antibiotics.<sup>76,77</sup> To address the matter Liechti et al. set out to conclusively establish the presence of PG in *C. trachomatis* by labeling with the D-amino acid probe alkDala, but found that alkDala failed to label the bacteria.<sup>62</sup> They hypothesized that this was because chlamydial PG synthesis enzymes could not accommodate alkDala, but that they might accommodate modified D-alanine dimers wherein one of the two amino acids was alkDala (alkDala-DA). Indeed, after incubating the bacteria with the alkyne containing alkDala-DA dipeptide, they were subsequently able to label *C. trachomatis* with Alexa Fluor 488 azide. Interestingly, no labeling was detected when using the dipeptide analogue bearing the bioorthogonal modification on the C-terminal D-alanine residue (i.e. DA-alkDala). The authors reasoned that the lack of labeling was due to removal of the C-terminal D-alanine residue in either transpeptidation or carboxypeptidation reactions. The work of Liechti et al. shows that labeling of PG in some bacteria may require modified D-amino acid probes, but also highlights the versatility of D-amino acid labeling for the detection and study of bacterial PG.

In addition to the use of unnatural D-amino acids, strategies based on other building blocks have been developed to probe PG assembly in bacteria. In this regard, Grimes and coworkers designed metabolic probes based on *N*-acetyl muramic acid (MurNAc) that allowed for labeling of the carbohydrate moiety of PG.<sup>78,79</sup> Although labeling of PG with D-amino acids analogues is a powerful and versatile method, there are several benefits to labeling this carbohydrate moiety: firstly, D-alanine residues of the PG stem peptide can be removed by transpeptidation and carboxypeptidation reactions, which may decrease the probe's lifetime, whereas the carbohydrate backbone of PG is not subject to remodeling. Secondly, MurNAc is a superior probe for *de novo* PG synthesis, as it is only incorporated in newly synthesized PG, while D-alanine probes can also be incorporated into mature PG by exchange reactions.<sup>50,80,81</sup> Finally, MurNAc binding to Nod-like receptors (NLRs) is involved in innate immune activation<sup>82</sup>, while D-alanine residues are not involved in immune activation, making MurNAc analogues more suitable for probing immune activation by PG. Metabolic labeling of the carbohydrate moiety in PG was first achieved by Liang et al. using MurNAc analogues with azido- and alkyne modifications at the 2-*N* acetyl position (**Figure 1C**).<sup>78</sup> In some Gram-negative bacteria, including, amongst others, *Pseudomonas putida*, MurNAc can be recycled to uridine diphosphate-MurNAc (UDP-MurNAc) by enzymes AmgK and MurU and subsequently incorporated into newly synthesized PG.<sup>83</sup> Interestingly, Liang et al showed that both *E. coli* and *B. subtilis* could

incorporate MurNAc analogues into *de novo* synthesized PG after transfection with a vector for *P. putida* AmgK and MurU.<sup>78</sup> Their results suggest that metabolic MurNAc labeling could be applied to a wide range of bacteria, both Gram-negative and Gram-positive, if transfected with *amgK* and *murU*. Metabolic MurNAc labeling of most bacteria does, however, require genetic modification of the bacteria and is limited to bacteria in which *amgK* and *murU* can be introduced, limiting the practical use of this particular metabolic labeling technique.

Building upon these approaches, Wang et al. recently reported an elegant method for post-synthetic, metabolic labeling of the PG carbohydrate backbone.<sup>79</sup> Their technique exploits the function of the bacterial enzyme peptidoglycan *O*-acetyltransferase B (PatB), which uses acetyl-CoA as an acetyl donor to *O*-acetylate the 6' hydroxyl group of MurNAc residues in the carbohydrate moiety of PG.<sup>84</sup> Post-synthetic *O*-acetylation of PG occurs in many intracellular pathogenic bacteria, such as *Neisseria meningitidis*, *Neisseria gonorrhoeae* and *Staphylococcus aureus*<sup>85–87</sup>, where it contributes to bacterial virulence by providing resistance against PG degradation by the antimicrobial enzyme lysozyme.<sup>88</sup> Wang et al. hypothesized that bioorthogonal groups could be introduced into PG post-synthetically by feeding azide- (SNAz) or alkyne- (SNAk) functionalized acetyl-CoA analogues (**Figure 1C**). They found that PatB efficiently *O*-acetylates PG in *B. subtilis* when supplied with SNAz or SNAk and in doing so enabled visualization of the incorporated probes by reaction with fluorescent dyes carrying complementary bioorthogonal groups.<sup>79</sup> Interestingly, they also showed that the artificially *O*-acylated *B. subtilis* was, at least partially, protected from degradation by lysozyme.

### 2.3 Metabolic labeling of the mycomembrane

The mycobacterial cell wall contains an outer membrane – the mycomembrane (MM) – that lends itself well to selective labeling. It consists of long chain (C<sub>60</sub>–C<sub>90</sub>) mycolic acids that are covalently linked to the cell wall's PG layer through highly branched polysaccharides called arabinogalactan (AG).<sup>89,90</sup> Components of the MM are important for mycobacterial cell survival; for example, blocking the biosynthesis of the nonmammalian disaccharide trehalose, a key component of the MM glycolipids trehalose dimycolate (TDM) and trehalose monomycolate (TMM), reduces cell viability and induces growth defects.<sup>91,92</sup> TMM is a modulator of MM biosynthesis<sup>84</sup> and a precursor to TDM, which promotes virulence and survival in host macrophages.<sup>93</sup> Since trehalose metabolism is vital for mycobacterial cell viability and is not found in mammalian cells, its biosynthetic pathway makes an excellent target for the development of novel antibiotics against *Mtb*. Moreover,

since trehalose is exclusively found in members of the suborder of *Corynebacterineae*, which does not include canonical Gram-negative or Gram-positive bacteria, it opens up the possibility to use metabolic labeling with trehalose-probes for clinical diagnosis of *Mtb*.

Clinical diagnosis of *Mtb* in high-burden, developing countries is currently performed using either the Ziehl-Neelsen test or the Auramine Truant stain, both of which are only moderately reliable.<sup>86</sup> Furthermore, these diagnostic tests also do not discriminate between live or dead *Mtb* cells and thus cannot be used by physicians to determine treatment efficacy.<sup>94</sup> Thus, novel, *Mtb*-specific diagnostic tools are required to improve TB diagnosis efficacy. Metabolic labeling with trehalose analogues has shown promise as a novel diagnostic approach for the rapid detection of *Mtb* infection. Trehalose, in the form of TMM and TDM, is anchored non-covalently to the mycobacterial cell wall. Trehalose is synthesized and esterified to form TMM in the cytosol, after which TMM is transported to the periplasm.<sup>95</sup> Once in the periplasm, the mycolyltransferase complex antigen 85 (Ag85) transfers mycolate from TMM to AG, to form a network of covalent mycolates that form the foundation of the MM, or to another molecule of TMM, forming TDM.<sup>96–98</sup> In both cases, a molecule of trehalose is regained, which is recycled by active transport into the cytosol by the trehalose-specific transporter SugABCLpqY.<sup>99</sup>

Based on analysis of the trehalose/Ag85 co-crystal structure, Backus et al.<sup>32</sup> hypothesized that trehalose could be modified with functional groups without affecting substrate activity for Ag85, exploiting a promiscuity that is similar to that of D-alanine metabolism. They synthesized various trehalose-analogues, including fluorescein isothiocyanate (FITC)-trehalose (FITC-Tre, **Figure 2**), and tested their ability to label pathogenic *Mtb* using a one-step labeling method. FITC-trehalose was efficiently incorporated into the growing *Mtb* mycomembrane by Ag85 *in vitro* and exclusively labeled live *Mtb* cells; heat-killed *Mtb* cells were not labeled, nor were cells of the Gram-negative pathogens *Pseudomonas aeruginosa* and *Haemophilus influenza* or Gram-positive *Staphylococcus aureus*.<sup>32</sup> FITC-Tre could even be incorporated into *Mtb* inside macrophages; macrophages were infected with *Mtb* and successfully labeled with FITC-Tre. This has opened up possibilities for *in vivo* metabolic trehalose-labeling studies.

Backus et al. also demonstrated that Ag85 enzymes tolerate a surprisingly wide range of substrate modifications. Moreover, their work demonstrates that the Ag85 pathway can be hijacked to incorporate exogenous trehalose into TMM and,

subsequently, into the MM. They also speculate that, given the conserved nature of Ag85 amongst mycobacteria, the FITC-trehalose probe could presumably label other mycobacterial species equally as well as *Mtb*. However, Rodriguez-Rivera et al.<sup>100</sup> found that FITC-trehalose labels other mycobacteria with poor efficiency and does not label corynebacteria at a detectable level at all. SAR studies showed that removal of an anomeric methyl group significantly increased labeling efficiency amongst myco- and corynebacteria, as did repositioning of the FITC functionality on the trehalose scaffold. Rodriguez-Rivera et al. applied metabolic trehalose labeling to assess the influence of ethambutol treatment on MM fluidity using Fluorescence Recovery After Photobleaching (FRAP) experiments. They showed that ethambutol can increase MM fluidity at sub-inhibitory concentrations, thereby enhancing antibiotic drug accessibility.<sup>100</sup>

One-step metabolic labeling is an excellent method for metabolic incorporation of trehalose analogues into the MM via extracellular incorporation by the Ag85 complex. However, an important aspect of trehalose metabolism occurs intracellularly, where trehalose is formed and subsequently incorporated into various metabolites, which together constitute the 'trehalome'.<sup>33</sup> The importance of trehalose for bacterial survival calls for chemical probes that can provide insight into intracellular trehalose metabolism. Swarts et al.<sup>33</sup> hypothesized that the trehalose-recycling pathway could be hijacked to actively transport azido-trehalose analogues into the mycobacterial cytosol through the trehalose-specific transporter SugABCLpqY, after which the trehalose-analogue would be incorporated into the 'trehalome' and subsequently labeled with azide-reactive reporter molecules. Trehalose-analogues with azido-groups (TreAz analogues) at the 2-, 3-, 4- or 6-position (**Figure 2**) were added to a culture of *Mycobacterium smegmatis*, a non-pathogenic *Mycobacterium* that is frequently used as a model organism for *Mtb*, and then exposed to a fluorescent dye coupled to a cyclooctyne group leading to labeling via a strain-promoted [3+2] cycloaddition. They found that the TreAz analogues labeled *M. smegmatis* efficiently and that the route of trehalose incorporation was dependent on the structure of the TreAz analogue; 2-, 4- and 6-TreAz were incorporated via the recycling pathway, while 3-TreAz was incorporated only extracellularly by Ag85. This incorporation was also possible for pathogenic *Mtb* and *Mycobacterium bovis*. The recent development of chemoenzymatic routes towards unnatural trehalose analogues is expected to expand the application of this method by facilitating access to the new analogues.<sup>101</sup>



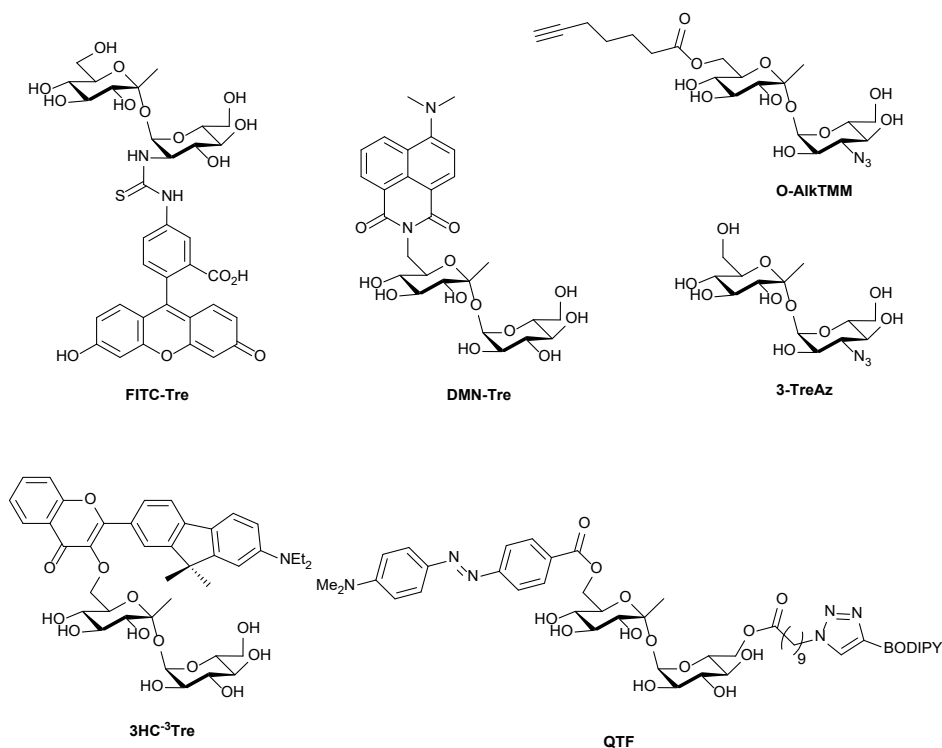


**Figure 2.** Fluorescent and fluorogenic trehalose analogues for labeling of the MM.

Two-step metabolic labeling with trehalose analogues has also been applied to study mycolation of AG and *O*-mycolated proteins that are found in the MM. The Swarts group hypothesized that the substrate specificity of Ag85 as a mycolyltransferase would extend to a 6-heptynoyl trehalose analogue (*O*-AlkTMM, **Figure 2**), based on previously reported Ag85 activity studies.<sup>32,102</sup> They hypothesized that *O*-AlkTMM could be taken up into the periplasm, where Ag85 would transfer the 6-heptynoyl group to mycolyl acceptors such as AG and *O*-mycolated proteins.<sup>103,104</sup> Subsequent reaction with alkyne-reactive reporter molecules would allow for enrichment or visualization of mycolated targets. Foley et al.<sup>103</sup> reported on the synthesis of *O*-AlkTMM and showed that *O*-AlkTMM effectively labels mycobacterial AG. Similar to TreAz analogues, *O*-AlkTMM selectively labels cell walls of mycobacteria and corynebacteria without labeling canonical Gram-negative and Gram-positive bacteria. In contrast to TreAz analogues, metabolic labeling with *O*-AlkTMM also provides the means to directly incorporate labels during the synthesis of AG mycolate (AGM), which is an essential

component of the mycobacterial cell wall. *O*-mycolation of proteins has only recently been discovered as a post-translational protein modification in corynebacteria.<sup>105</sup> Notably, *O*-acylation of bacterial proteins was unheard of prior to the discovery of *O*-mycolated proteins, making it an intriguing phenomenon and worthy of further study. Using the *O*-AlkTMM probe, Kavunja et al.<sup>104</sup> were able to label multiple *O*-mycolation target proteins in *Corynebacterium glutamicum*. Next, they visualized them with an in-gel fluorescence assay, by means of the well-established copper(I)-catalyzed Azide-Alkyne Cycloaddition (CuAAC) click reaction with Alexa Fluor 488 azide. Their study uncovered multiple novel *O*-mycolated proteins and revealed that proteins can carry more than one *O*-mycolate group, highlighting the utility of the *O*-AlkTMM probe for studies into the 'O-mycoloylome'. Much remains to be discovered about bacterial protein *O*-mycolation and the *O*-AlkTMM probe has proven to be a highly valuable tool for such *O*-mycolation studies. Taken together, the aforementioned investigations show the potential of trehalose analogues for studies into trehalose- and mycoloyl-metabolism. The same group recently expanded the bioorthogonal TMM library to include *trans*-cyclooctene TMM analogues reactive in an Inverse Electron-Demand Diels-Alder (IEDDA) ligation reaction.<sup>106</sup>

Recently, various trehalose analogues have emerged as novel potential point-of-care diagnostic tools for *Mtb*. This is a large unmet clinical need, as the current diagnostic methods are notoriously unreliable.<sup>107</sup> Rundell et al.<sup>108</sup> took the first steps towards synthesis of an <sup>18</sup>F-labeled trehalose analogue that would facilitate targeted Positron Emission Tomography (PET) imaging of patients lungs for quick diagnosis of TB infections. However, this approach requires advanced equipment for diagnosis – infrastructure often absent at remote diagnostic sites. To provide a facile low-tech *Mtb*-detection test, Kamariza et al.<sup>109</sup> developed a solvatochromic trehalose probe (DMN-Tre), consisting of a trehalose-conjugated fluorescent dye, 4-*N,N*-dimethylamino-1,8-naphthalimide (DMN) (**Figure 2**), that dramatically increases in fluorescence upon transition from a hydrophilic to a hydrophobic environment. The authors showed that the solvatochromic nature of DMN allowed for no-wash labeling of *Mtb*, since DMN-Tre should only become fluorescent once incorporated into the hydrophobic environment of the MM. DMN-Tre could indeed be used for efficient no-wash labeling of *Mtb* cells, even in sputum samples from TB-positive patients. This probe was further used for high-content image-based screening of the effect of various drugs on intracellular *Mtb*.<sup>110</sup> Recently, new solvatochromic trehalose probes based on 3-hydroxychromone fluorophores (3HC, **Figure 2**) were reported that show a 10-fold increase in fluorescence enhancement

compared to DMN. This allowed the detection of *Mtb* cells within 10 minutes of treatment and may well represent a major step towards on-site testing for *Mtb* infection.<sup>111</sup>

Hodges et al. recently reported the use of a different strategy for fluorogenic *Mtb* cell wall detection. Their approach employs a trehalose variant dubbed “Quencher-Trehalose-Fluorophore” (QTF, **Figure 2**) consisting of a lipid-BODIPY construct and a DABCYL quencher attached to a trehalose scaffold. Esterase Ag85 cleaves the lipid-fluorophore from the quencher-trehalose, leading to enhancement (turn-on) of fluorescence (**Figure 2**).<sup>112</sup> Finally, the Swarts-group recently reported a similar approach, in which cleavage of a quencher group from a construct containing fluorescein and a DABCYL quencher by the MM remodeling hydrolase Tdmh, led to a the enhancement of green fluorescence.<sup>113</sup> One downside to all these probes is that they exclusively label metabolically active cells. As such, they can only be used to diagnose dividing *Mtb* and monitor treatment efficacy. The metabolically dormant forms of *Mtb*, however, remain undetected by these technologies. There remains an urgent and unmet need for the development of probes for this subclass of *Mtb*.

## 2.4 Proteome labeling with bioorthogonal amino acids

The methionine tRNA/tRNA synthetase pair of many species are rather promiscuous. At the turn of the millennium, the Tirrell and Bertozzi groups were the first to exploit this promiscuity to introduce bioorthogonal groups into bacterially expressed proteins and label these using click reactions.<sup>114</sup> This technique was later applied by the Tirrell-lab to the pan-proteome Met-labeling of whole cells. The approach, latter dubbed Bioorthogonal Non-Canonical Amino acid Tagging (BONCAT)<sup>115</sup>, has subsequently been used for the enrichment, identification, and visualization of exclusively nascent proteins, thus reducing the complexity of proteomic analysis of a given sample<sup>116</sup>. Moreover, pulse-labeling with bioorthogonal amino acid analogues allows for analysis of changes in protein production in response to internal and external cues.<sup>115</sup> With regards to the study of intracellular pathogens, two BONCAT-based approaches have been taken. Those reliant on the hijacking of existing tRNA/synthase pairs, and those that genetically incorporate new tRNA/synthase pairs. Both approaches have been used extensively to interrogate pathogen’s protein expression at the host-pathogen interface.

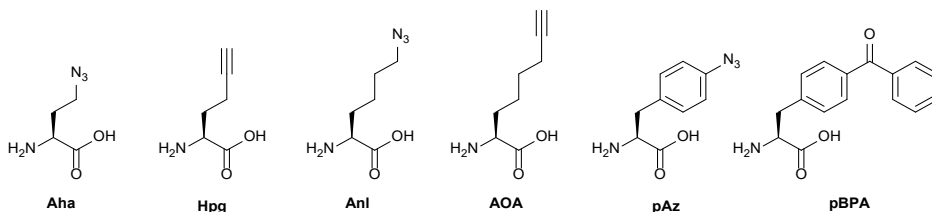


**Figure 3.** Bioorthogonal amino acid analogues for metabolic labeling of proteins.

The first approach, which relies on the promiscuity of the methionine tRNA and its synthase, have shown that methionine analogues containing alkene-<sup>117–120</sup>, alkyne-<sup>114,117</sup> and azido-<sup>114</sup> functionalities can be accepted substrates by the methionyl-tRNA synthetase (MetRS) in a variety of pro- and eukaryotes<sup>121</sup>. Care has to be taken when incorporating these amino acids into new species, as the speed of protein synthesis and cell division can be altered by the presence of such unnatural amino acids, as demonstrated by homopropargylglycine (Hpg, **Figure 3**) which shows toxicity towards certain bacteria at higher incubation rates, whereas azidohomoalanine does not (Aha, **Figure 3**).<sup>122</sup> The advantage of this approach is that it provides a facile way to image only the proteome of an intracellular pathogen after uptake by a host cell, without any need for further genetic modification of the species. Reacting these proteins with a clickable biotin or FLAG-tag can also enable the enrichment of these target proteins for mass spectrometry.<sup>116</sup> This strategy has previously been used to incorporate Aha or Hpg into *E. coli* *ex vivo* and then co-incubated these bacteria with mouse bone marrow-derived dendritic cells (BMDCs) to visualize bacterial cell degradation *in situ*.<sup>123</sup> In order to provide ultrastructural content of the degrading *E. coli* cells within BMDC phagosomes, Correlative Light-Electron Microscopy (CLEM) imaging was used. Chapter 3 of this thesis confirms that the bioorthogonal groups used in these studies are resistant to the harsh conditions encountered in the lysosomal pathway.<sup>124</sup> Chapter 4 describes the development of this technique to include super-resolution fluorescence, by combining Stochastic Optical Reconstruction Microscopy and CLEM (STORM-CLEM). This technique is applied to the study of *Salmonella* bacteria in BMDCs to show the durability of these pathogenic bacteria inside the host cell vacuole.<sup>122</sup> Chapter 5 illustrates how BONCAT labeling of the *Mtb* proteome can be combined with labeling of the *Mtb* PG layer through the use of alkDala-labeling with correlative imaging, showing that multiple click reactions can be performed on pathogens simultaneously. This approach to assess the heterogeneous effect of various antibiotics on intracellular *Mtb* (See **Figure 4** for an example image).<sup>125</sup>

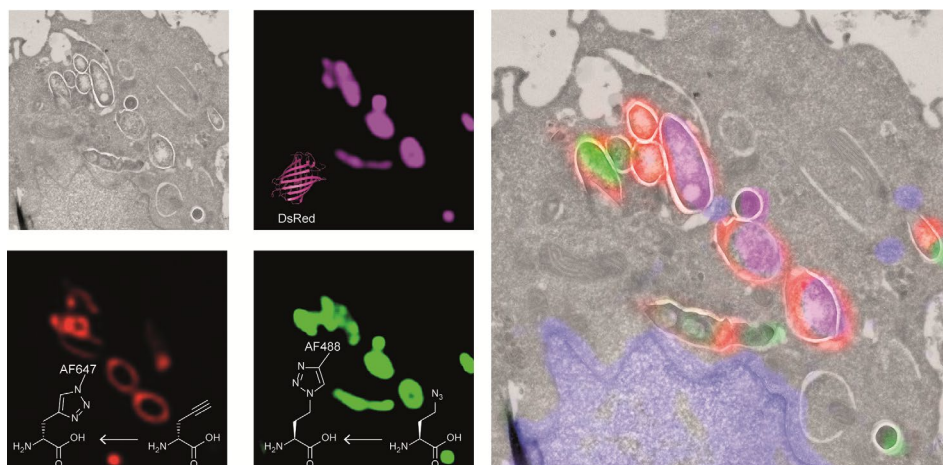


**Figure 4.** CLEM of triple labeled *Mtb*.<sup>125</sup> Green: Alexa Fluor 488 (AF488)-alkyne reacted to Aha in the proteome; Red: Alexa Fluor 647 (AF647)-azide reacted to alkDala; Magenta: Expressed DsRed signal. Grey: electron micrograph indicating the subcellular environment in which the bacteria reside.

Approaches that allow expansion of the genetic code of pathogens have also become powerful tools to study host-pathogen interactions. For example, Ngo et al.<sup>126</sup> devised a new BONCAT-like strategy that involved genetically modifying the cell type of interest to enable incorporation of a non-canonical amino acid (ncAA) for this cell type only. For this strategy, a mutant MetRS (NLL-MetRS) was developed that can append the ncAA azidonorleucine (ANL; **Figure 3**) to endogenous tRNA.<sup>127</sup> To achieve cell type selective protein labeling with bioorthogonal handles, the cell type of interest is transfected with the NLL-MetRS gene, enabling this cell type to incorporate ANL into newly synthesized proteins. ANL is not compatible with endogenous MetRS, leading the ncAA to be exclusively incorporated into proteins from the pathogen and not the host. Because of these features, BONCAT using NLL-MetRS is highly suited for analyzing pathogen's nascent protein expression at the host-pathogen interface. The potential of this approach was further demonstrated in the interrogation of host-pathogen interactions by infecting murine macrophages with *E. coli* that constitutively expressed NLL-MetRS and visualizing the bacteria selectively within the macrophage.

Using this cell selective BONCAT method, Mahdavi et al. were able to enrich and identify several key secreted *Yersinia* outer proteins (Yops) and other secreted factors in an infection model.<sup>128</sup> To enrich Yops that were secreted into the host cytosol, HeLa cells were infected with NLL-MetRS-expressing *Yersinia* cells and subsequently lysed using digitonin, preserving the integrity of the *Yersinia* cells.

Subsequent reaction to TAMRA-alkyne allowed for facile identification of fluorescent Yops in host cytosol fractions. Moreover, by applying BONCAT in a pulse-labeling manner at specific times after infections, the authors were able to determine the order of Yop secretion, demonstrating the potential of BONCAT for elucidating the temporal aspects of virulence factor secretion. The Hang group also reported a similar strategy for the labeling of intracellular salmonella with 2-aminooctynoic acid (AOA, **Figure 3**) and showed that the bacterial proteome of intracellular *Salmonella enterica* could be labeled and imaged with a high degree of selectivity inside RAW-macrophages<sup>129</sup>. In addition, this approach also enabled for the enrichment and proteomic analysis of endogenously expressed *Salmonella* proteins from infected mammalian cells.

Amber codon suppression – the approach whereby a tRNA/tRNA synthetase pair reactive to the amber stop codon are introduced in a species have also been applied to the study of pathogenic species. Wang et al. reported the application of this strategy to incorporate *para*-iodophenylalanine into GFP expressed in the *Mtb*-strain H37Ra inside RAW-macrophages.<sup>130</sup> The same approach was later exploited by Touchette et al. for the incorporation of the photo-crosslinkable amino acid *p*-benzoyl-L-phenylalanine (pBPA, **Figure 3**) into the mycobacterial outer cell wall of *M. smegmatis* to identify the interaction partners of this protein.<sup>131</sup> It is likely that the application of such techniques to study *Mtb* interactions with the host proteome will deliver new insights. The expanded genetic code variant of *Salmonella* was also recently reported and used to incorporate *p*-azidophenylalanine (pAz, **Figure 3**) into the bacterial proteome. However, no intracellular labeling was attempted yet by this approach.<sup>132</sup> Intracellular labeling was achieved for the facultative intracellular pathogen *Neisseria meningitidis*. Takahashi et al. also incorporated pBPA into the bacterium and used it to elucidate the role of NMB1345 in the infection pathway.<sup>133</sup>

## 2.5 ABPP CLEM of bacterial enzymes

A final area which is providing tantalizing new insights into the intracellular biology of the host-pathogen interaction is the use of probes to visualize the activity of specific pathogenic enzymes inside the host, so-called Activity-Based Protein Profiling (ABPP).<sup>134</sup> The combination of ABPP and CLEM has previously been used to image host cell alterations upon bacterial infection<sup>123,135,136</sup>, but the imaging of pathogenic enzymes – particularly those involved in virulence – is an exciting new area.<sup>134</sup> An early example involved the use of the broad spectrum serine hydrolase probe FP-TAMRA (**Figure 5**) to identify the secreted serine hydrolases of *Mtb*<sup>137,138</sup>

and *V. cholera*.<sup>139</sup> In a later study, all four *V. cholera* serine hydrolases were identified using a proteomic approach in an infection model of this pathogen. FP-TAMRA was also used to identify 8 new serine hydrolases in the facultative<sup>140</sup> intracellular pathogen *Staphylococcus aureus*.<sup>141</sup> Lentz et al. used FP-TAMRA to develop Activity-Based Probes (ABPs) for two of these hydrolases FphB and FphF. Using these inhibitors/probes the authors could delineate a role for FphB in the infection of liver and heart cells, although an exact mechanism for this role remains elusive. The recently resolved crystal structure of FphF in complex with the inhibitor may help in elucidating these roles.<sup>142</sup> Perhaps this relates to the potential for intracellular survival of this pathogen under certain conditions. Recently, the group of Bogoy also used this approach to developed a covalent probe that allowed visualization of an *Mtb* hydrolase, namely the hydrolase important for pathogenicity-1 (HIP-1). Using probe CSL173 (**Figure 5**), they could observe its activity when spiked into the host proteome to identify HIP-activity.<sup>143</sup> They have recently described the further development of these types of probes to synthesize a chemiluminescent point-of-care test for *Mtb* that allowed the selective identification of live *Mtb*, providing a useful tool for the study of drug efficacy.<sup>144</sup>

The electrophilic nature of the beta-lactam scaffold has also been used to image penicillin binding protein (PBPs) activities in pathogens.<sup>145</sup> Initial approaches were marred by a poor substrate specificity of these probes for the various PBPs. This was recently solved for another facultative intracellular pathogen, *Streptococcus pneumoniae*.<sup>146</sup> By modifying the beta-lactam core and attaching an L-phenylalanine as well as a fluorescein (Lac(L)-Phe-FL, **Figure 5**) or a TAMRA to these modified lactam-cores, the PBPs 1b and 2x could be selectively labeled and imaged in the dividing bacteria.<sup>147</sup> Interestingly, when a D-phenylalanine was introduced to the probe (Lac(D)-Phe-TAMRA, **Figure 5**), dual labeling of PBP2x and PBP2b could be achieved.<sup>147</sup> With these probes it was found that these PBPs were restricted to a ring surrounding the bacterial division site. What these observations mean in the context of the recently discovered intracellular niche of the pathogen remains to be elucidated.

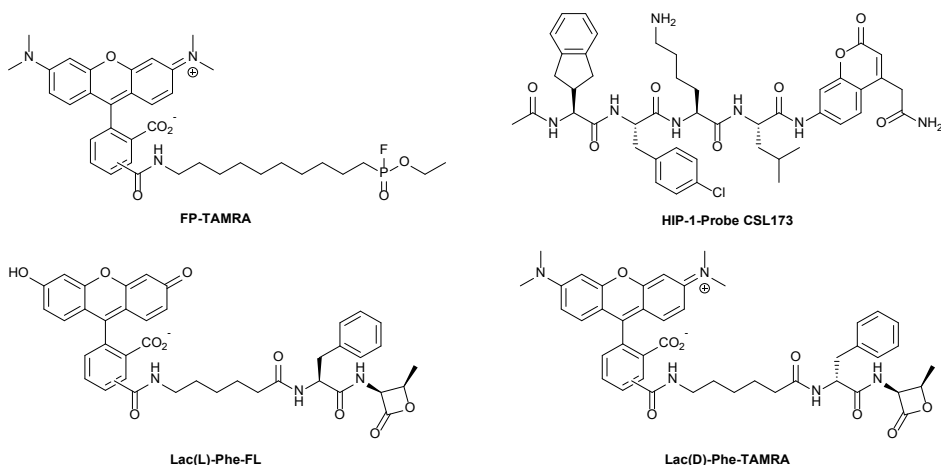


**Figure 5.** Covalent active-based probes used for imaging (active) bacterial enzymes.

## 2.6 Conclusion

As the examples mentioned above clearly demonstrate, the application of novel chemical approaches to imaging is leading to rapid advances in the study of intracellular pathogens. The labeling of cellular components and individual enzyme activities is leading to improved point of care tests, as well as a better understanding of the mechanism of action for both existing and novel antibacterial drugs. For the near future, the currently existing metabolic cell wall probes, D-alanine and trehalose analogues, will likely maintain their relevance, as there are still many lingering questions concerning bacterial cell wall metabolism and growth modes. Moreover, secreted bacterial proteins, many of which are associated with virulence and persistence in the host environment, remain uncharacterized and their mechanisms of action poorly understood. Rationally designed experiments using BONCAT-probes may contribute significantly to further the understanding of these secreted factors. Together, these findings may lead to novel vaccines, antibiotics and other therapies against bacterial infection.



## 2.7 References

- (1) Dye, C. After 2015: Infectious Diseases in a New Era of Health and Development. *Philos. Trans. R. Soc. B Biol. Sci.* **2014**, *369* (1645), 20130426.
- (2) Laxminarayan, R.; Heymann, D. L. Challenges of Drug Resistance in the Developing World. *BMJ* **2012**, *344* (7852).
- (3) Nordmann, P.; Poirel, L.; Toleman, M. A.; Walsh, T. R. Does Broad-Spectrum  $\beta$ -Lactam Resistance Due to NDM-1 Herald the End of the Antibiotic Era for Treatment of Infections Caused by Gram-Negative Bacteria? *J. Antimicrob. Chemother.* **2011**, *66* (4), 689–692.
- (4) Laxminarayan, R.; Duse, A.; Wattal, C.; Zaidi, A. K. M.; Wertheim, H. F. L.; Sumpradit, N.; Vlieghe, E.; Hara, G. L.; Gould, I. M.; Goossens, H.; Greko, C.; So, A. D.; Bigdeli, M.; Tomson, G.; Woodhouse, W.; Ombaka, E.; Peralta, A. Q.; Qamar, F. N.; Mir, F.; Kariuki, S.; Bhutta, Z. A.; Coates, A.; Bergstrom, R.; Wright, G. D.; Brown, E. D.; Cars, O. Antibiotic Resistance-the Need for Global Solutions. *Lancet Infect. Dis.* **2013**, *13* (12), 1057–1098.
- (5) Coates, A. R.; Halls, G.; Hu, Y. Novel Classes of Antibiotics or More of the Same? *Br. J. Pharmacol.* **2011**, *163* (1), 184–194.
- (6) Walsh, C. Opinion – Anti-Infectives: Where Will New Antibiotics Come From? *Nat. Rev. Microbiol.* **2003**, *1* (1), 65–70.
- (7) Byndloss, M. X.; Tsois, R. M. Chronic Bacterial Pathogens: Mechanisms of Persistence. *Microbiol. Spectr.* **2016**, *4* (2).
- (8) Gomez, J. E.; McKinney, J. D. M. Tuberculosis Persistence, Latency, and Drug Tolerance. In *Tuberculosis*; Churchill Livingstone, **2004**; Vol. 84, pp 29–44.
- (9) Omsland, A.; Cockrell, D. C.; Howe, D.; Fischer, E. R.; Virtaneva, K.; Sturdevant, D. E.; Porcella, S. F.; Heinzen, R. A. Host Cell-Free Growth of the Q Fever Bacterium *Coxiella burnetii*. *Proc. Natl. Acad. Sci. U. S. A.* **2009**, *106* (11), 4430–4434.
- (10) Singh, S.; Eldin, C.; Kowalczywska, M.; Raoult, D. Axenic Culture of Fastidious and Intracellular Bacteria. *Trends Microbiol.* **2013**, *21* (2), 92–99.
- (11) Dye, C. Global Epidemiology of Tuberculosis. *Lancet*. Elsevier Limited March 18, **2006**, pp 938–940.
- (12) Mahboub, B.; Vats, M. *Tuberculosis: Current Issues in Diagnosis and Management*; Mahboub, B., Vats, M., Eds.; InTech, **2013**.
- (13) Bald, D.; Villellas, C.; Lu, P.; Koul, A. Targeting Energy Metabolism in Mycobacterium Tuberculosis, a New Paradigm in Antimycobacterial Drug Discovery. *MBio* **2017**, *8* (2), 1–11.
- (14) Sarathy, J. P.; Via, L. E.; Weiner, D.; Blanc, L.; Boshoff, H.; Eugenin, E. A.; Barry, C. E.; Dartois, V. A. Extreme Drug Tolerance of Mycobacterium Tuberculosis in Caseum. *Antimicrob. Agents Chemother.* **2018**, *62* (2), 1–11.
- (15) Evangelopoulos, D.; Fonseca, J. D. da; Waddell, S. J. Understanding Anti-Tuberculosis Drug Efficacy: Rethinking Bacterial Populations and How We Model Them. *Int. J. Infect. Dis.* **2015**, *32*, 76–80.
- (16) Pullan, S. T.; Allnutt, J. C.; Devine, R.; Hatch, K. A.; Jeeves, R. E.; Hendon-Dunn, C. L.; Marsh, P. D.; Bacon, J. The Effect of Growth Rate on Pyrazinamide Activity in Mycobacterium Tuberculosis - Insights for Early Bactericidal Activity? *BMC Infect. Dis.* **2016**, *16* (205), 1–11.
- (17) Daniel, J.; Mamar, H.; Deb, C.; Sirakova, T. D.; Kolattukudy, P. E. Mycobacterium Tuberculosis Uses Host Triacylglycerol to Accumulate Lipid Droplets and Acquires a Dormancy-like Phenotype in Lipid-Loaded Macrophages. *PLoS Pathog.* **2011**, *7* (6), e1002093.
- (18) Baker, J. J.; Abramovitch, R. B. Genetic and Metabolic Regulation of Mycobacterium

- Tuberculosis Acid Growth Arrest. *Sci. Rep.* **2018**, *8* (1), 4168.
- (19) Dutta, N. K.; Karakousis, P. C. Latent Tuberculosis Infection: Myths, Models, and Molecular Mechanisms. *Microbiol. Mol. Biol. Rev.* **2014**, *78* (3), 343–371.
  - (20) Deb, C.; Lee, C.-M. M.; Dubey, V. S.; Daniel, J.; Abomoelak, B.; Sirakova, T. D.; Pawar, S.; Rogers, L.; Kolattukudy, P. E. A Novel in Vitro Multiple-Stress Dormancy Model for Mycobacterium Tuberculosis Generates a Lipid-Loaded, Drug-Tolerant, Dormant Pathogen. *PLoS One* **2009**, *4* (6), e6077.
  - (21) Sarkar, S.; Ganguly, A. Current Overview of Anti-Tuberculosis Drugs: Metabolism and Toxicities. *Mycobact. Dis.* **2016**, *6* (2), 1–6.
  - (22) Hoagland, D. T.; Liu, J.; Lee, R. B.; Lee, R. E. New Agents for the Treatment of Drug-Resistant Mycobacterium Tuberculosis. *Adv. Drug Deliv. Rev.* **2016**, *102*, 55–72.
  - (23) Kamaruzzaman, N. F.; Kendall, S.; Good, L. Targeting the Hard to Reach: Challenges and Novel Strategies in the Treatment of Intracellular Bacterial Infections. *Br. J. Pharmacol.* **2017**, *174* (14), 2225–2236.
  - (24) Mughini-Gras, L.; Schaapveld, M.; Kramers, J.; Mooij, S.; Neefjes-Borst, E. A.; Pelt, W. van; Neefjes, J. Increased Colon Cancer Risk after Severe Salmonella Infection. *PLoS One* **2018**, *13* (1), e0189721.
  - (25) Ahmadi, M. H.; Mirsalehian, A.; Bahador, A. Association of *Chlamydia Trachomatis* with Infertility and Clinical Manifestations: A Systematic Review and Meta-Analysis of Case-Control Studies. *Infect. Dis. (Auckl)*. **2016**, *48* (7), 517–523.
  - (26) Ditchburn, J.-L.; Hodgkins, R. Yersinia Pestis, a Problem of the Past and a Re-Emerging Threat. *Biosaf. Heal.* **2019**, *1* (2), 65–70.
  - (27) Escoll, P.; Mondino, S.; Rolando, M.; Buchrieser, C. Targeting of Host Organelles by Pathogenic Bacteria: A Sophisticated Subversion Strategy. *Nat. Rev. Microbiol.* **2015**, *14* (1), 5–19.
  - (28) Krachler, A. M.; Orth, K. Targeting the Bacteria-Host Interface Strategies in Anti-Adhesion Therapy. *Virulence* **2013**, *4* (4), 284–294.
  - (29) Cambier, C. J.; Falkow, S.; Ramakrishnan, L. Host Evasion and Exploitation Schemes of Mycobacterium Tuberculosis. *Cell* **2014**, *159* (7), 1497–1509.
  - (30) Kuru, E.; Hughes, H. V.; Brown, P. J.; Hall, E.; Tekkam, S.; Cava, F.; De Pedro, M. A.; Brun, Y. V.; Vannieuwenhze, M. S. In Situ Probing of Newly Synthesized Peptidoglycan in Live Bacteria with Fluorescent D-Amino Acids. *Angew. Chemie - Int. Ed.* **2012**, *51* (50), 12519–12523.
  - (31) Siegrist, M. S.; Whiteside, S.; Jewett, J. C.; Aditham, A.; Cava, F.; Bertozzi, C. R. D-Amino Acid Chemical Reporters Reveal Peptidoglycan Dynamics of an Intracellular Pathogen. *ACS Chem. Biol.* **2013**, *8* (3), 500–505.
  - (32) Backus, K. M.; Boshoff, H. I.; Barry, C. E. C. S.; Boutureira, O.; Patel, M. K.; D’Hooge, F.; Lee, S. S.; Via, L. E.; Tahlan, K.; Barry, C. E. C. S.; Davis, B. G. Uptake of Unnatural Trehalose Analogs as a Reporter for Mycobacterium Tuberculosis. *Nat. Chem. Biol.* **2011**, *7* (4), 228–235.
  - (33) Swarts, B. M.; Holsclaw, C. M.; Jewett, J. C.; Alber, M.; Fox, D. M.; Siegrist, M. S.; Leary, J. A.; Kalscheuer, R.; Bertozzi, C. R. Probing the Mycobacterial Trehalome with Bioorthogonal Chemistry. *J. Am. Chem. Soc.* **2012**, *134* (39), 16123–16126.
  - (34) Sletten, E. M.; Bertozzi, C. R. Bioorthogonal Chemistry: Fishing for Selectivity in a Sea of Functionality. *Angew. Chemie - Int. Ed.* **2009**, *48* (38), 6974–6998.
  - (35) Nguyen, S. S.; Prescher, J. A. Developing Bioorthogonal Probes to Span a Spectrum of Reactivities. *Nat. Rev. Chem.* **2020**, *4* (9), 476–489.
  - (36) Typas, A.; Banzhaf, M.; Gross, C. A.; Vollmer, W. From the Regulation of Peptidoglycan Synthesis to Bacterial Growth and Morphology. *Nat. Rev. Microbiol.* **2012**, *10* (2), 123–136.
  - (37) Silhavy, T. J.; Kahne, D.; Walker, S. The Bacterial Cell Envelope. *Cold Spring Harb.*

- Perspect. Biol.* **2010**, 2 (a000414), 1–16.
- (38) Kovacs-Simon, A.; Titball, R. W.; Michell, S. L. Lipoproteins of Bacterial Pathogens. *Infect. Immun.* **2011**, 79 (2), 548–561.
  - (39) Schneider, T.; Sahl, H. G. An Oldie but a Goodie - Cell Wall Biosynthesis as Antibiotic Target Pathway. *Int. J. Med. Microbiol.* **2010**, 300 (2–3), 161–169.
  - (40) Wise, E. M.; Park, J. T. Penicillin: Its Basic Site of Action as an Inhibitor of a Peptide Cross-Linking Reaction in Cell Wall Mucopolysaccharide Synthesis. *Proc. Natl. Acad. Sci. U. S. A.* **1965**, 54 (1), 75–81.
  - (41) Barna, J. C. J.; Williams, D. H. The Structure and Mode of Action of Glycopeptide Antibiotics of the Vancomycin Group. *Annu. Rev. Microbiol.* **1984**, 38 (1), 339–357.
  - (42) Siewert, G.; Strominger, J. L. Bacitracin: An Inhibitor Of The Dephosphorylation Of Lipid Pyrophosphate, An Intermediate In The Biosynthesis Of The Peptidoglycan Of Bacterial Cell Walls. *Proc. Natl. Acad. Sci.* **1967**, 57 (3), 767–773.
  - (43) Draenert, R.; Seybold, U.; Grütznert, E.; Bogner, J. R. Novel Antibiotics: Are We Still in the Pre-Post-Antibiotic Era? *Infection* **2015**, 43 (2), 145–151.
  - (44) Viala, J.; Chaput, C.; Boneca, I. G.; Cardona, A.; Girardin, S. E.; Moran, A. P.; Athman, R.; Mémet, S.; Huerre, M. R.; Coyle, A. J.; DiStefano, P. S.; Sansonetti, P. J.; Labigne, A.; Bertin, J.; Philpott, D. J.; Ferrero, R. L. Nod1 Responds to Peptidoglycan Delivered by the Helicobacter Pylori Cag Pathogenicity Island. *Nat. Immunol.* **2004**, 5 (11), 1166–1174.
  - (45) Tiyanont, K.; Doan, T.; Lazarus, M. B.; Fang, X.; Rudner, D. Z.; Walker, S. Imaging Peptidoglycan Biosynthesis in Bacillus Subtilis with Fluorescent Antibiotics. *Proc. Natl. Acad. Sci. U. S. A.* **2006**, 103 (29), 11033–11038.
  - (46) Daniel, R. A.; Errington, J. Control of Cell Morphogenesis in Bacteria: Two Distinct Ways to Make a Rod-Shaped Cell. *Cell* **2003**, 113 (6), 767–776.
  - (47) Orlachs, N. K.; Aarsman, M. E. G. G.; Verheul, J.; Arnusch, C. J.; Martin, N. I.; Hervé, M.; Vollmer, W.; de Kruijff, B.; Breukink, E.; den Blaauwen, T. A Novel in Vivo Cell-Wall Labeling Approach Sheds New Light on Peptidoglycan Synthesis in Escherichia Coli. *ChemBioChem* **2011**, 12 (7), 1124–1133.
  - (48) Lam, H.; Oh, D. C.; Cava, F.; Takacs, C. N.; Clardy, J.; De Pedro, M. A.; Waldor, M. K. D-Amino Acids Govern Stationary Phase Cell Wall Remodeling in Bacteria. *Science* (80-. ). **2009**, 325 (5947), 1552–1555.
  - (49) Cava, F.; de Pedro, M. A.; Lam, H.; Davis, B. M.; Waldor, M. K. Distinct Pathways for Modification of the Bacterial Cell Wall by Non-Canonical <sc>D</sc>-Amino Acids. *EMBO J.* **2011**, 30 (16), 3442–3453.
  - (50) Lupoli, T. J.; Tsukamoto, H.; Doud, E. H.; Wang, T. S. A.; Walker, S.; Kahne, D. Transpeptidase-Mediated Incorporation of d-Amino Acids into Bacterial Peptidoglycan. *J. Am. Chem. Soc.* **2011**, 133 (28), 10748–10751.
  - (51) Bartlett, T. M.; Bratton, B. P.; Duvshani, A.; Miguel, A.; Sheng, Y.; Martin, N. R.; Nguyen, J. P.; Persat, A.; Desmarais, S. M.; VanNieuwenhze, M. S.; Huang, K. C.; Zhu, J.; Shaevitz, J. W.; Gitai, Z. A Periplasmic Polymer Curves Vibrio Cholerae and Promotes Pathogenesis. *Cell* **2017**, 168 (1–2), 172–185.
  - (52) Bisson-Filho, A. W.; Hsu, Y. P.; Squyres, G. R.; Kuru, E.; Wu, F.; Jukes, C.; Sun, Y.; Dekker, C.; Holden, S.; VanNieuwenhze, M. S.; Brun, Y. V.; Garner, E. C. Treadmilling by FtsZ Filaments Drives Peptidoglycan Synthesis and Bacterial Cell Division. *Science* (80-. ). **2017**, 355 (6326), 739–743.
  - (53) Boersma, M. J.; Kuru, E.; Rittichier, J. T.; VanNieuwenhze, M. S.; Brun, Y. V.; Winkler, M. E. Minimal Peptidoglycan (PG) Turnover in Wild-Type and PG Hydrolase and Cell Division Mutants of Streptococcus Pneumoniae D39 Growing Planktonically and in Host-Relevant Biofilms. *J. Bacteriol.* **2015**, 197 (21), 3472–3485.
  - (54) Morales Angeles, D.; Liu, Y.; Hartman, A. M.; Borisova, M.; de Sousa Borges, A.; de Kok,

- N.; Beilharz, K.; Veening, J.-W. W.; Mayer, C.; Hirsch, A. K. H.; Scheffers, D.-J. J. Pentapeptide-Rich Peptidoglycan at the *Bacillus Subtilis* Cell-Division Site. *Mol. Microbiol.* **2017**, *104* (2), 319–333.
- (55) Cserti, E.; Roskopf, S.; Chang, Y.-W.; Eisheuer, S.; Selter, L.; Shi, J.; Regh, C.; Koert, U.; Jensen, G. J.; Thanbichler, M. Dynamics of the Peptidoglycan Biosynthetic Machinery in the Stalked Budding Bacterium *Hyphomonas Neptunium*. *Mol. Microbiol.* **2017**, *103* (5), 875–895.
- (56) Fenton, A. K.; Mortaji, L. El; Lau, D. T. C.; Rudner, D. Z.; Bernhardt, T. G. CozE Is a Member of the MreCD Complex That Directs Cell Elongation in *Streptococcus Pneumoniae*. *Nat. Microbiol.* **2016**, *2* (3), 1–10.
- (57) Fleurie, A.; Lesterlin, C.; Manuse, S.; Zhao, C.; Cluzel, C.; Lavergne, J. P.; Franz-Wachtel, M.; MacEk, B.; Combet, C.; Kuru, E.; VanNieuwenhze, M. S.; Brun, Y. V.; Sherratt, D.; Grangeasse, C. MapZ Marks the Division Sites and Positions FtsZ Rings in *Streptococcus Pneumoniae*. *Nature* **2014**, *516* (7530), 260–262.
- (58) Monteiro, J. M.; Fernandes, P. B.; Vaz, F.; Pereira, A. R.; Tavares, A. C.; Ferreira, M. T.; Pereira, P. M.; Veiga, H.; Kuru, E.; Vannieuwenhze, M. S.; Brun, Y. V.; Filipe, S. R.; Pinho, M. G. Cell Shape Dynamics during the Staphylococcal Cell Cycle. *Nat. Commun.* **2015**, *6* (1), 1–12.
- (59) Yang, X.; Lyu, Z.; Miguel, A.; McQuillen, R.; Huang, K. C.; Xiao, J. GTPase Activity-Coupled Treadmilling of the Bacterial Tubulin FtsZ Organizes Septal Cell Wall Synthesis. *Science* (80-. ). **2017**, *355* (6326), 744–747.
- (60) Pilhofer, M.; Aistleitner, K.; Biboy, J.; Gray, J.; Kuru, E.; Hall, E.; Brun, Y. V.; VanNieuwenhze, M. S.; Vollmer, W.; Horn, M.; Jensen, G. J. Discovery of Chlamydial Peptidoglycan Reveals Bacteria with Murein Sacculi but without FtsZ. *Nat. Commun.* **2013**, *4* (1), 1–7.
- (61) Van Teeseling, M. C. F.; Mesman, R. J.; Kuru, E.; Espaillet, A.; Cava, F.; Brun, Y. V.; Vannieuwenhze, M. S.; Kartal, B.; Van Niftrik, L. Anammox Planctomycetes Have a Peptidoglycan Cell Wall. *Nat. Commun.* **2015**, *6* (1), 1–6.
- (62) Liechti, G. W.; Kuru, E.; Hall, E.; Kalinda, A.; Brun, Y. V.; Vannieuwenhze, M.; Maurelli, A. T. A New Metabolic Cell-Wall Labelling Method Reveals Peptidoglycan in Chlamydia Trachomatis. *Nature* **2014**, *506* (7489), 507–510.
- (63) Kuru, E.; Tekkam, S.; Hall, E.; Brun, Y. V.; Van Nieuwenhze, M. S. Synthesis of Fluorescent D-Amino Acids and Their Use for Probing Peptidoglycan Synthesis and Bacterial Growth in Situ. *Nat. Protoc.* **2015**, *10* (1), 33–52.
- (64) Yoshimura, F.; Nikaido, H. Diffusion of  $\beta$ -Lactam Antibiotics through the Porin Channels of *Escherichia Coli* K-12. *Antimicrob. Agents Chemother.* **1985**, *27* (1), 84–92.
- (65) Hsu, Y. P.; Rittichier, J.; Kuru, E.; Yablonowski, J.; Pasciak, E.; Tekkam, S.; Hall, E.; Murphy, B.; Lee, T. K.; Garner, E. C.; Huang, K. C.; Brun, Y. V.; VanNieuwenhze, M. S. Full Color Palette of Fluorescent D-Amino Acids for: In Situ Labeling of Bacterial Cell Walls. *Chem. Sci.* **2017**, *8* (9), 6313–6321.
- (66) Garcia-Heredia, A.; Pohane, A. A.; Melzer, E. S.; Carr, C. R.; Fiolek, T. J.; Rundell, S. R.; Lim, H. C.; Wagner, J. C.; Morita, Y. S.; Swarts, B. M.; Siegrist, M. S. Peptidoglycan Precursor Synthesis along the Sidewall of Pole-Growing Mycobacteria. *Elife* **2018**, *7*, 1–22.
- (67) De Pedro, M. A.; Quintela, J. C.; Hölte, J. V.; Schwarz, H. Murein Segregation in *Escherichia Coli*. *J. Bacteriol.* **1997**, *179* (9), 2823–2834.
- (68) Sherratt, A. R.; Chigrinova, M.; Mackenzie, D. A.; Rastogi, N. K.; Ouattara, M. T. M.; Pezacki, A. T.; Pezacki, J. P. Dual Strain-Promoted Alkyne-Nitrone Cycloadditions for Simultaneous Labeling of Bacterial Peptidoglycans. *Bioconjug. Chem.* **2016**, *27* (5), 1222–1226.
- (69) Pidgeon, S. E.; Apostolos, A. J.; Nelson, J. M.; Shaku, M.; Rimal, B.; Islam, M. N.; Crick,

- D. C.; Kim, S. J.; Pavelka, M. S.; Kana, B. D.; Pires, M. M. L, D-Transpeptidase Specific Probe Reveals Spatial Activity of Peptidoglycan Cross-Linking. *ACS Chem. Biol.* **2019**, *14* (10), 2185–2196.
- (70) Shieh, P.; Siegrist, M. S.; Cullen, A. J.; Bertozzi, C. R. Imaging Bacterial Peptidoglycan with Near-Infrared Fluorogenic Azide Probes. *Proc. Natl. Acad. Sci.* **2014**, *111* (15), 5456–5461.
- (71) MacKenzie, D. A.; Sherratt, A. R.; Chigrinova, M.; Kell, A. J.; Pezacki, J. P. Bioorthogonal Labelling of Living Bacteria Using Unnatural Amino Acids Containing Nitrones and a Nitro Derivative of Vancomycin. *Chem. Commun.* **2015**, *51* (62), 12501–12504.
- (72) Stephens, R. S.; Kalman, S.; Lammel, C.; Fan, J.; Marathe, R.; Aravind, L.; Mitchell, W.; Olinger, L.; Tatusov, R. L.; Zhao, Q.; Koonin, E. V.; Davis, R. W. Genome Sequence of an Obligate Intracellular Pathogen of Humans: Chlamydia Trachomatis. *Science* (80-. ). **1998**, *282* (5389), 754–759.
- (73) Tamura, A.; Manire, G. P. Effect of Penicillin on the Multiplication of Meningopneumonitis Organisms (Chlamydia Psittaci). *J. Bacteriol.* **1968**, *96* (4), 875–880.
- (74) Barbour, A. G.; Amano, K. I.; Hackstadt, T.; Perry, L.; Caldwell, H. D. Chlamydia Trachomatis Has Penicillin-Binding Proteins but Not Detectable Muramic Acid. *J. Bacteriol.* **1982**, *151* (1), 420–428.
- (75) Fox, A.; Rogers, J. C.; Gilbert, J.; Morgan, S.; Davis, C. H.; Knight, S.; Wyrick, P. B. Muramic Acid Is Not Detectable in Chlamydia Psittaci or Chlamydia Trachomatis by Gas Chromatography-Mass Spectrometry. *Infect. Immun.* **1990**, *58* (3).
- (76) Moulder, J. W. Why Is Chlamydia Sensitive to Penicillin in the Absence of Peptidoglycan? *Infectious Agents and Disease*. April 1, **1993**, pp 87–99.
- (77) Chopra, I.; Storey, C.; Falla, T. J.; Pearce, J. H. Antibiotics, Peptidoglycan Synthesis and Genomics: The Chlamydial Anomaly Revisited. *Microbiology*. Society for General Microbiology October 1, **1998**, pp 2673–2678.
- (78) Liang, H.; DeMeester, K. E.; Hou, C. W.; Parent, M. A.; Caplan, J. L.; Grimes, C. L. Metabolic Labelling of the Carbohydrate Core in Bacterial Peptidoglycan and Its Applications. *Nat. Commun.* **2017**, *8*, 1–11.
- (79) Wang, Y.; Lazor, K. M.; DeMeester, K. E.; Liang, H.; Heiss, T. K.; Grimes, C. L. Postsynthetic Modification of Bacterial Peptidoglycan Using Bioorthogonal N-Acetylcysteamine Analogs and Peptidoglycan o-Acetyltransferase B. *J. Am. Chem. Soc.* **2017**, *139* (39), 13596–13599.
- (80) Lebar, M. D.; May, J. M.; Meeske, A. J.; Leiman, S. A.; Lupoli, T. J.; Tsukamoto, H.; Losick, R.; Rudner, D. Z.; Walker, S.; Kahne, D. Reconstitution of Peptidoglycan Cross-Linking Leads to Improved Fluorescent Probes of Cell Wall Synthesis. *J. Am. Chem. Soc.* **2014**, *136* (31), 10874–10877.
- (81) Lupoli, T. J.; Lebar, M. D.; Markovski, M.; Bernhardt, T.; Kahne, D.; Walker, S. Lipoprotein Activators Stimulate Escherichia Coli Penicillin-Binding Proteins by Different Mechanisms. *J. Am. Chem. Soc.* **2014**, *136* (1), 52–55.
- (82) Inohara, N.; Ogura, Y.; Fontalba, A.; Gutierrez, O.; Pons, F.; Crespo, J.; Fukase, K.; Inamura, S.; Kusumoto, S.; Hashimoto, M.; Foster, S. J.; Moran, A. P.; Fernandez-Luna, J. L.; Nuñez, G. Host Recognition of Bacterial Muramyl Dipeptide Mediated through NOD2: Implications for Crohn's Disease. *J. Biol. Chem.* **2003**, *278* (8), 5509–5512.
- (83) Borisova, M.; Gisin, J.; Mayer, C. Blocking Peptidoglycan Recycling in Pseudomonas Aeruginosa Attenuates Intrinsic Resistance to Fosfomycin. In *Microbial Drug Resistance*; Mary Ann Liebert Inc., **2014**; Vol. 20, pp 231–237.
- (84) Moynihan, P. J.; Clarke, A. J. O-Acetylated Peptidoglycan: Controlling the Activity of Bacterial Autolysins and Lytic Enzymes of Innate Immune Systems. *Int. J. Biochem. Cell Biol.* **2011**, *43* (12), 1655–1659.

- (85) Blundell, J. K.; Perkins, H. R. Effects of Beta-Lactam Antibiotics on Peptidoglycan Synthesis in Growing *Neisseria Gonorrhoeae*, Including Changes in the Degree of O-Acetylation. *J. Bacteriol.* **1981**, *147* (2).
- (86) Ghuysen, J. M.; Strominger, J. L. Structure of the Cell Wall of *Staphylococcus Aureus*, Strain Copenhagen. II. Separation and Structure of Disaccharides. *Biochemistry* **1963**, *2* (5), 1119–1125.
- (87) Antignac, A.; Rousselle, J. C.; Namane, A.; Labigne, A.; Taha, M. K.; Boneca, I. G. Detailed Structural Analysis of the Peptidoglycan of the Human Pathogen *Neisseria Meningitidis*. *J. Biol. Chem.* **2003**, *278* (34), 31521–31528.
- (88) Brumfitt, W.; Wardlaw, A. C.; Park, J. T. Development of Lysozyme-Resistance in *Micrococcus Lysodieticus* and Its Association with an Increased O-Acetyl Content of the Cell Wall. *Nature* **1958**, *181* (4626), 1783–1784.
- (89) Alderwick, L. J.; Harrison, J.; Lloyd, G. S.; Birch, H. L. The Mycobacterial Cell Wall—Peptidoglycan and Arabinogalactan. *Cold Spring Harb. Perspect. Med.* **2015**, *5* (8), 1–16.
- (90) Brennan, P.; Crick, D. The Cell-Wall Core of *Mycobacterium Tuberculosis* in the Context of Drug Discovery. *Curr. Top. Med. Chem.* **2007**, *7* (5), 475–488.
- (91) Woodruff, P. J.; Carlson, B. L.; Siridechadilok, B.; Pratt, M. R.; Senaratne, R. H.; Mougous, J. D.; Riley, L. W.; Williams, S. J.; Bertozzi, C. R. Trehalose Is Required for Growth of *Mycobacterium Smegmatis*. *J. Biol. Chem.* **2004**, *279* (28), 28835–28843.
- (92) Murphy, H. N.; Stewart, G. R.; Mischenko, V. V.; Apt, A. S.; Harris, R.; McAlister, M. S. B.; Driscoll, P. C.; Young, D. B.; Robertson, B. D. The OtsAB Pathway Is Essential for Trehalose Biosynthesis in *Mycobacterium Tuberculosis*. *J. Biol. Chem.* **2005**, *280* (15), 14524–14529.
- (93) Indrigo, J.; Hunter, R. L.; Actor, J. K. Cord Factor Trehalose 6,6'-Dimycolate (TDM) Mediates Trafficking Events during Mycobacterial Infection of Murine Macrophages. *Microbiology*. Society for General Microbiology August 1, **2003**, pp 2049–2059.
- (94) Datta, S.; Sherman, J. M.; Bravard, M. A.; Valencia, T.; Gilman, R. H.; Evans, C. A. Clinical Evaluation of Tuberculosis Viability Microscopy for Assessing Treatment Response. *Clin. Infect. Dis.* **2015**, *60* (8), 1186–1195.
- (95) Tahlan, K.; Wilson, R.; Kastrinsky, D. B.; Arora, K.; Nair, V.; Fischer, E.; Whitney Barnes, S.; Walker, J. R.; Alland, D.; Barry, C. E.; Boshoff, H. I. SQ109 Targets MmpL3, a Membrane Transporter of Trehalose Monomycolate Involved in Mycolic Acid Donation to the Cell Wall Core of *Mycobacterium Tuberculosis*. *Antimicrob. Agents Chemother.* **2012**, *56* (4), 1797–1809.
- (96) Belisle, J. T.; Vissa, V. D.; Sievert, T.; Takayama, K.; Brennan, P. J.; Besra, G. S. Role of the Major Antigen of *Mycobacterium Tuberculosis* in Cell Wall Biogenesis. *Science* (80-. ). **1997**, *276* (5317), 1420–1422.
- (97) Sathyamoorthy, N.; Takayama, K. Purification and Characterization of a Novel Mycolic Acid Exchange Enzyme from *Mycobacterium Smegmatis*. *J. Biol. Chem.* **1987**, *262* (28), 13417–13423.
- (98) Kilburn, J. O.; Takayama, K.; Armstrong, E. L. Synthesis of Trehalose Dimycolate (Cord Factor) by a Cell-Free System of *Mycobacterium Smegmatis*. *Biochem. Biophys. Res. Commun.* **1982**, *108* (1), 132–139.
- (99) Kalscheuer, R.; Weinrick, B.; Veeraraghavan, U.; Besra, G. S.; Jacobs, W. R. Trehalose-Recycling ABC Transporter LpqY-SugA-SugB-SugC Is Essential for Virulence of *Mycobacterium Tuberculosis*. *Proc. Natl. Acad. Sci. U. S. A.* **2010**, *107* (50), 21761–21766.
- (100) Rodriguez-Rivera, F. P.; Zhou, X.; Theriot, J. A.; Bertozzi, C. R. Visualization of Mycobacterial Membrane Dynamics in Live Cells. *J. Am. Chem. Soc.* **2017**, *139* (9), 3488–3495.
- (101) Urbanek, B. L.; Wing, D. C.; Haislop, K. S.; Hamel, C. J.; Kalscheuer, R.; Woodruff, P. J.;

- Swarts, B. M. Chemoenzymatic Synthesis of Trehalose Analogues: Rapid Access to Chemical Probes for Investigating Mycobacteria. *ChemBioChem* **2014**, *15* (14), 2066–2070.
- (102) Favrot, L.; Grzegorzewicz, A. E.; Lajiness, D. H.; Marvin, R. K.; Boucau, J.; Isailovic, D.; Jackson, M.; Ronning, D. R. Mechanism of Inhibition of Mycobacterium Tuberculosis Antigen 85 by Ebselen. *Nat. Commun.* **2013**, *4* (1), 1–10.
- (103) Foley, H. N.; Stewart, J. A.; Kavunja, H. W.; Rundell, S. R.; Swarts, B. M. Bioorthogonal Chemical Reporters for Selective in Situ Probing of Mycomembrane Components in Mycobacteria. *Angew. Chemie - Int. Ed.* **2016**, *55* (6), 2053–2057.
- (104) Kavunja, H. W.; Piligian, B. F.; Fiolek, T. J.; Foley, H. N.; Nathan, T. O.; Swarts, B. M. A Chemical Reporter Strategy for Detecting and Identifying: O -Mycoloylated Proteins in Corynebacterium. *Chem. Commun.* **2016**, *52* (95), 13795–13798.
- (105) Huc, E.; Meniche, X.; Benz, R.; Bayan, N.; Ghazi, A.; Tropis, M.; Daffé, M. O-Mycoloylated Proteins from Corynebacterium: An Unprecedented Post-Translational Modification in Bacteria. *J. Biol. Chem.* **2010**, *285* (29), 21908–21912.
- (106) Fiolek, T. J.; Banahene, N.; Kavunja, H. W.; Holmes, N. J.; Rylski, A. K.; Pohane, A. A.; Siegrist, M. S.; Swarts, B. M. Engineering the Mycomembrane of Live Mycobacteria with an Expanded Set of Trehalose Monomycolate Analogues. *ChemBioChem* **2019**, *20* (10), 1282–1291.
- (107) Dinnes, J.; Deeks, J.; Kunst, H.; Gibson, A.; Cummins, E.; Waugh, N.; Drobniewski, F.; Lalvani, A. A Systematic Review of Rapid Diagnostic Tests for the Detection of Tuberculosis Infection. *Health Technology Assessment*. National Co-ordinating Centre for HTA January 22, **2007**, pp 1–178.
- (108) Rundell, S. R.; Wagar, Z. L.; Meints, L. M.; Olson, C. D.; O'Neill, M. K.; Piligian, B. F.; Poston, A. W.; Hood, R. J.; Woodruff, P. J.; Swarts, B. M. Deoxyfluoro-d-Trehalose (FDTre) Analogues as Potential PET Probes for Imaging Mycobacterial Infection. *Org. Biomol. Chem.* **2016**, *14* (36), 8598–8609.
- (109) Kamariza, M.; Shieh, P.; Ealand, C. S.; Peters, J. S.; Chu, B.; Rodriguez-Rivera, F. P.; Babu Sait, M. R.; Treuren, W. V.; Martinson, N.; Kalscheuer, R.; Kana, B. D.; Bertozzi, C. R. Rapid Detection of Mycobacterium Tuberculosis in Sputum with a Solvatochromic Trehalose Probe. *Sci. Transl. Med.* **2018**, *10* (430), eaam6310.
- (110) Sahile, H. A.; Rens, C.; Shapira, T.; Andersen, R. J.; Av-Gay, Y. DMN-Tre Labeling for Detection and High-Content Screening of Compounds against Intracellular Mycobacteria. *ACS Omega* **2020**, *5* (7), 3661–3669.
- (111) Kamariza, M.; Keyser, S.; Utz, A.; Knapp, B.; Ahn, G.; Chen, T.; Huang, K. C.; Bertozzi, C. Towards Mycobacterium Tuberculosis Detection at the Point-of-Care: A Brighter Solvatochromic Probe Permits the Detection of Mycobacteria within Minutes. *bioRxiv* **2020**, 2020.05.29.124008.
- (112) Hodges, H. L.; Brown, R. A.; Crooks, J. A.; Weibel, D. B.; Kiessling, L. L. Imaging Mycobacterial Growth and Division with a Fluorogenic Probe. *Proc. Natl. Acad. Sci. U. S. A.* **2018**, *115* (20), 5271–5276.
- (113) Holmes, N. J.; Kavunja, H. W.; Yang, Y.; Vannest, B. D.; Ramsey, C. N.; Gepford, D. M.; Banahene, N.; Poston, A. W.; Piligian, B. F.; Ronning, D. R.; Ojha, A. K.; Swarts, B. M. A FRET-Based Fluorogenic Trehalose Dimycolate Analogue for Probing Mycomembrane-Remodeling Enzymes of Mycobacteria. *ACS Omega* **2019**, *4* (2), 4348–4359.
- (114) Kiick, K. L.; Saxon, E.; Tirrell, D. a; Bertozzi, C. R. Incorporation of Azides into Recombinant Proteins for Chemoselective Modification by the Staudinger Ligation. *Proc. Natl. Acad. Sci. U. S. A.* **2002**, *99* (1), 19–24.
- (115) Dieterich, D. C.; Link, A. J.; Graumann, J.; Tirrell, D. A.; Schuman, E. M. Selective Identification of Newly Synthesized Proteins in Mammalian Cells Using Bioorthogonal Noncanonical Amino Acid Tagging (BONCAT). *Proc. Natl. Acad. Sci.* **2006**, *103* (25),

- 9482–9487.
- (116) Dieterich, D. C.; Lee, J. J.; Link, A. J.; Graumann, J.; Tirrell, D. A.; Schuman, E. M. Labeling, Detection and Identification of Newly Synthesized Proteomes with Bioorthogonal Non-Canonical Amino-Acid Tagging. *Nat. Protoc.* **2007**, 2 (3), 532–540.
  - (117) Van Hest, J. C. M.; Kiick, K. L.; Tirrell, D. A. Efficient Incorporation of Unsaturated Methionine Analogues into Proteins in Vivo. *J. Am. Chem. Soc.* **2000**, 122 (7), 1282–1288.
  - (118) Van Hest, J. C. M.; Tirrell, D. A. Efficient Introduction of Alkene Functionality into Proteins in Vivo. *FEBS Lett.* **1998**, 428 (1–2), 68–70.
  - (119) Saleh, A. M.; Wilding, K. M.; Calve, S.; Bundy, B. C.; Kinzer-Ursem, T. L. Non-Canonical Amino Acid Labeling in Proteomics and Biotechnology. *Journal of Biological Engineering*. BioMed Central Ltd. May 22, **2019**, p 43.
  - (120) Song, W.; Wang, Y.; Yu, Z.; Vera, C. I. R.; Qu, J.; Lin, Q. A Metabolic Alkene Reporter for Spatiotemporally Controlled Imaging of Newly Synthesized Proteins in Mammalian Cells. *ACS Chem. Biol.* **2010**, 5 (9), 875–885.
  - (121) Lang, K.; Chin, J. W. Cellular Incorporation of Unnatural Amino Acids and Bioorthogonal Labeling of Proteins. *Chem. Rev.* **2014**, 114 (9), 4764–4806.
  - (122) van Elsland, D. M.; Pujals, S.; Bakkum, T.; Bos, E.; Oikonomas-Koppas, N.; Berlin, I.; Neefjes, J.; Meijer, A. H.; Koster, A. J.; Albertazzi, L.; van Kasteren, S. I. Ultrastructural Imaging of Salmonella–Host Interactions Using Super-Resolution Correlative Light-Electron Microscopy of Bioorthogonal Pathogens. *ChemBioChem* **2018**, 19 (16), 1766–1770.
  - (123) van Elsland, D. M.; Bos, E.; de Boer, W.; Overkleeft, H. S.; Koster, A. J.; van Kasteren, S. I. Detection of Bioorthogonal Groups by Correlative Light and Electron Microscopy Allows Imaging of Degraded Bacteria in Phagocytes. *Chem. Sci.* **2016**, 7 (1), 752–758.
  - (124) Bakkum, T.; van Leeuwen, T.; Sarris, A. J. C.; van Elsland, D. M.; Poulcharidis, D.; Overkleeft, H. S.; van Kasteren, S. I. Quantification of Bioorthogonal Stability in Immune Phagocytes Using Flow Cytometry Reveals Rapid Degradation of Strained Alkynes. *ACS Chem. Biol.* **2018**, 13 (5), 1173–1179.
  - (125) Bakkum, T.; Heemskerk, M. T.; Bos, E.; Groenewold, M.; Oikonomas-Koppas, N.; Walburg, K. V.; van Veen, S.; van der Lienden, M. J. C.; van Leeuwen, T.; Haks, M. C.; Ottenhoff, T. H. M.; Koster, A. J.; van Kasteren, S. I. Bioorthogonal Correlative Light-Electron Microscopy of Mycobacterium Tuberculosis in Macrophages Reveals the Effect of Antituberculosis Drugs on Subcellular Bacterial Distribution. *ACS Cent. Sci.* **2020**.
  - (126) Ngo, J. T.; Champion, J. A.; Mahdavi, A.; Tanrikulu, I. C.; Beatty, K. E.; Connor, R. E.; Yoo, T. H.; Dieterich, D. C.; Schuman, E. M.; Tirrell, D. A. Cell-Selective Metabolic Labeling of Proteins. *Nat. Chem. Biol.* **2009**, 5 (10), 715–717.
  - (127) Link, A. J.; Vink, M. K. S.; Agard, N. J.; Prescher, J. A.; Bertozzi, C. R.; Tirrell, D. A. Discovery of Aminoacyl-TRNA Synthetase Activity through Cell-Surface Display of Noncanonical Amino Acids. *Proc. Natl. Acad. Sci. U. S. A.* **2006**, 103 (27), 10180–10185.
  - (128) Mahdavi, A.; Szychowski, J.; Ngo, J. T.; Sweredoski, M. J.; Graham, R. L. J.; Hess, S.; Schneewind, O.; Mazmanian, S. K.; Tirrell, D. A. Identification of Secreted Bacterial Proteins by Noncanonical Amino Acid Tagging. *Proc. Natl. Acad. Sci.* **2014**, 111 (1), 433–438.
  - (129) Grammel, M.; Zhang, M. M.; Hang, H. C. Orthogonal Alkynyl Amino Acid Reporter for Selective Labeling of Bacterial Proteomes during Infection. *Angew. Chemie - Int. Ed.* **2010**, 49 (34), 5970–5974.
  - (130) Wang, F.; Robbins, S.; Guo, J.; Shen, W.; Schultz, P. G. Genetic Incorporation of Unnatural Amino Acids into Proteins in Mycobacterium Tuberculosis. *PLoS One* **2010**, 5 (2).



- (131) Touchette, M. H.; Van Vlack, E. R.; Bai, L.; Kim, J.; Cognetta, A. B.; Previti, M. L.; Backus, K. M.; Martin, D. W.; Cravatt, B. F.; Seeliger, J. C. A Screen for Protein-Protein Interactions in Live Mycobacteria Reveals a Functional Link between the Virulence-Associated Lipid Transporter LprG and the Mycolyltransferase Antigen 85A. *ACS Infect. Dis.* **2017**, *3* (5), 336–348.
- (132) Gan, Q.; Lehman, B. P.; Bobik, T. A.; Fan, C. Expanding the Genetic Code of Salmonella with Non-Canonical Amino Acids. *Sci. Rep.* **2016**, *6* (November), 1–7.
- (133) Takahashi, H.; Dohmae, N.; Kim, K. S.; Shimuta, K.; Ohnishi, M.; Yokoyama, S.; Yanagisawa, T. Genetic Incorporation of Non-Canonical Amino Acid Photocrosslinkers in Neisseria Meningitidis: New Method Provides Insights into the Physiological Function of the Function-Unknown NMB1345 Protein. *PLoS One* **2020**, *15* (8 August 2020), e0237883.
- (134) Wright, M. H. Chemical Proteomics of Host–Microbe Interactions. *Proteomics* **2018**, *18* (1700333), 1–10.
- (135) van Meel, E.; Bos, E.; van der Lienden, M. J. C.; Overkleeft, H. S.; van Kasteren, S. I.; Koster, A. J.; Aerts, J. M. F. G. Localization of Active Endogenous and Exogenous  $\beta$ -Glucocerebrosidase by Correlative Light-Electron Microscopy in Human Fibroblasts. *Traffic* **2019**, *20* (5), 346–356.
- (136) van Dalen, F. J.; Bakkum, T.; van Leeuwen, T.; Groenewold, M.; Deu, E.; Koster, A.; Van Kasteren, S. I.; Verdoes, M. Application of a Highly Selective Cathepsin S Two-Step Activity-Based Probe in Multicolour Bio-Orthogonal Correlative Light Electron Microscopy. *Front. Chem.* **2020**, *8* (628433), 1–13.
- (137) Ortega, C.; Anderson, L. N.; Frando, A.; Sadler, N. C.; Brown, R. W.; Smith, R. D.; Wright, A. T.; Grundner, C. Systematic Survey of Serine Hydrolase Activity in Mycobacterium Tuberculosis Defines Changes Associated with Persistence. *Cell Chem. Biol.* **2016**, *23* (2), 290–298.
- (138) Tallman, K. R.; Levine, S. R.; Beatty, K. E. Small-Molecule Probes Reveal Esterases with Persistent Activity in Dormant and Reactivating Mycobacterium Tuberculosis. *ACS Infect. Dis.* **2016**, *2* (12), 936–944.
- (139) Hatzios, S. K.; Abel, S.; Martell, J.; Hubbard, T.; Sasabe, J.; Munera, D.; Clark, L.; Bachovchin, D. A.; Qadri, F.; Ryan, E. T.; Davis, B. M.; Weerapana, E.; Waldor, M. K. Chemoproteomic Profiling of Host and Pathogen Enzymes Active in Cholera. *Nat. Chem. Biol.* **2016**, *12* (4), 268–274.
- (140) Rollin, G.; Tan, X.; Tros, F.; Dupuis, M.; Nassif, X.; Charbit, A.; Coureuil, M. Intracellular Survival of Staphylococcus Aureus in Endothelial Cells: A Matter of Growth or Persistence. *Front. Microbiol.* **2017**, *8* (JUL), 1354.
- (141) Lentz, C. S.; Sheldon, J. R.; Crawford, L. A.; Cooper, R.; Garland, M.; Amieva, M. R.; Weerapana, E.; Skaar, E. P.; Bogyo, M. Identification of a S. Aureus Virulence Factor by Activity-Based Protein Profiling (ABPP) Article. *Nat. Chem. Biol.* **2018**, *14* (6), 609–617.
- (142) Fellner, M.; Lentz, C. S.; Jamieson, S. A.; Brewster, J. L.; Chen, L.; Bogyo, M.; Mace, P. D. Structural Basis for the Inhibitor and Substrate Specificity of the Unique Fph Serine Hydrolases of Staphylococcus Aureus. *ACS Infect. Dis.* **2020**, *6* (10), 2771–2782.
- (143) Lentz, C. S.; Ordonez, A. A.; Kasperkiewicz, P.; La Greca, F.; O'Donoghue, A. J.; Schulze, C. J.; Powers, J. C.; Craik, C. S.; Drag, M.; Jain, S. K.; Bogyo, M. Design of Selective Substrates and Activity-Based Probes for Hydrolase Important for Pathogenesis 1 (HIP1) from Mycobacterium Tuberculosis. *ACS Infect. Dis.* **2016**, *2* (11), 807–815.
- (144) Babin, B. M.; Fernandez-Cuervo, G.; Sheng, J.; Green, O.; Ordonez, A. A.; Turner, M. L.; Keller, L. J.; Jain, S. K.; Shabat, D.; Bogyo, M. A Chemiluminescent Protease Probe for Rapid, Sensitive, and Inexpensive Detection of Live Mycobacterium Tuberculosis. *bioRxiv* **2020**, 2020.09.14.296772.
- (145) Marshall, A. P.; Shirley, J. D.; Carlson, E. E. Enzyme-Targeted Fluorescent Small-

- Molecule Probes for Bacterial Imaging. *Current Opinion in Chemical Biology*. Elsevier Ltd August 1, **2020**, pp 155–165.
- (146) Subramanian, K.; Henriques-Normark, B.; Normark, S. Emerging Concepts in the Pathogenesis of the *Streptococcus Pneumoniae*: From Nasopharyngeal Colonizer to Intracellular Pathogen. *Cellular Microbiology*. Blackwell Publishing Ltd November 1, **2019**.
- (147) Sharifzadeh, S.; Boersma, M. J.; Kocaoglu, O.; Shokri, A.; Brown, C. L.; Shirley, J. D.; Winkler, M. E.; Carlson, E. E. Novel Electrophilic Scaffold for Imaging of Essential Penicillin-Binding Proteins in *Streptococcus Pneumoniae*. *ACS Chem. Biol.* **2017**, *12* (11), 2849–2857.



# Chapter 3

## **Quantification of Bioorthogonal Stability in Immune Phagocytes Using Flow Cytometry Reveals Rapid Degradation of Strained Alkynes**

Published as:

Thomas Bakkum, Tyrza van Leeuwen, Alexi J. C. Sarris, Daphne M. van Elsland, Dimitrios Poulcharidis, Herman S. Overkleeft and Sander I. van Kasteren. *ACS Chemical Biology*, **2018**; 13(5): 1173-1179



## **Abstract**

One of the areas in which bioorthogonal chemistry has become of pivotal importance is in the study of host– pathogen interactions. The incorporation of bioorthogonal groups into the cell wall or proteome of intracellular pathogens has allowed study within the endolysosomal system. However, for the approach to be successful, the incorporated bioorthogonal groups must be stable to chemical conditions found within these organelles, which are some of the harshest found in metazoans: the groups are exposed to oxidizing species, acidic conditions, and reactive thiols. This chapter presents an assay that allows the assessment of the stability of bioorthogonal groups within host cell phagosomes. Using a flow cytometry-based assay, the relative label stability inside dendritic cell phagosomes of strained and unstrained alkynes were quantified. Strained alkynes that displayed stability in other systems, were found to be degraded by as much as 79% after maturation of the phagosome.

### 3.1 Introduction

Bioorthogonal chemistry is the execution of a selective chemical reaction within the complex composition of a biological system.<sup>1</sup> Bioorthogonal chemistry is often used for ligation purposes, whereby a small abiotic chemical functionality is first introduced into a biomolecule (or class of biomolecules) through metabolic engineering.<sup>2</sup> This chemical group is subsequently modified with a large detectable/retrievable group to realize its detection. Bioorthogonal ligation approaches have been used extensively; for example to study the *in vitro*<sup>3,4</sup> and *in vivo*<sup>5</sup> dynamics of glycans, lipids<sup>6</sup>, nucleic acids<sup>7,8</sup>, prokaryotic<sup>9</sup> and eukaryotic proteomes<sup>10</sup>, and peptidoglycan.<sup>11</sup> Bioorthogonal peptidoglycan structures for instance were used to label intracellular pathogens inside a phagocytic host cell to visualize this interaction.<sup>12</sup> The fact that bioorthogonal groups can be incorporated within amino acid sidechains, has even allowed for the visualization of pathogens as they are being degraded by the lysosomal hydrolases in macrophages and dendritic cells (DCs).<sup>13–16</sup> However, to provide unbiased results, the stability of bioorthogonal functionalities to intracellular conditions is essential to prevent label loss during the biological time course. The Antigen-Presenting Cells (APCs) used in the above studies expose their phagosomal content to some of harshest chemistries found in the body (**Figure 1A**).<sup>17,18</sup> When an APC phagocytoses a bacterium, the activity of the NADPH oxidase-2 complex (NOX2) will first result in the intraphagosomal generation of superoxide radicals ( $O_2^{\cdot-}$ ) to concentrations up to 25-100  $\mu M$ <sup>19</sup> (in absence of myeloperoxidase; MPO). These will rapidly be converted to hydrogen peroxide ( $< 30 \mu M$ )<sup>19</sup>, but also NO-radicals ( $< 15 \mu M$ )<sup>20</sup>, and hydroxyl radicals ( $\cdot OH$ ).<sup>21</sup> MPO can further react hydrogen peroxide with chloride anions to yield hypochlorous acid (HOCl).<sup>22,23</sup> This oxidative burst in APCs is followed by acidification of the phagosome down to pH-values as low as 4.8 through the action of the vATPase proton pump.<sup>24</sup> During this process, the phagosome fuses with lysosomes containing a wide range of highly proteolytic and reducing enzymes, including the Gamma Interferon-inducible Lysosomal Thioreductase (GILT)<sup>25</sup>, a wide range of cathepsins<sup>26</sup> and various other types of hydrolases.<sup>27</sup> This sequence of events renders traditional genetic labeling approaches of partial use as they will be degraded by the lysosomal proteases over time and thus rendered invisible. Even small molecule fluorophores can easily become damaged due to their general sensitivity to oxidation, reduction and pH.<sup>28,29</sup>

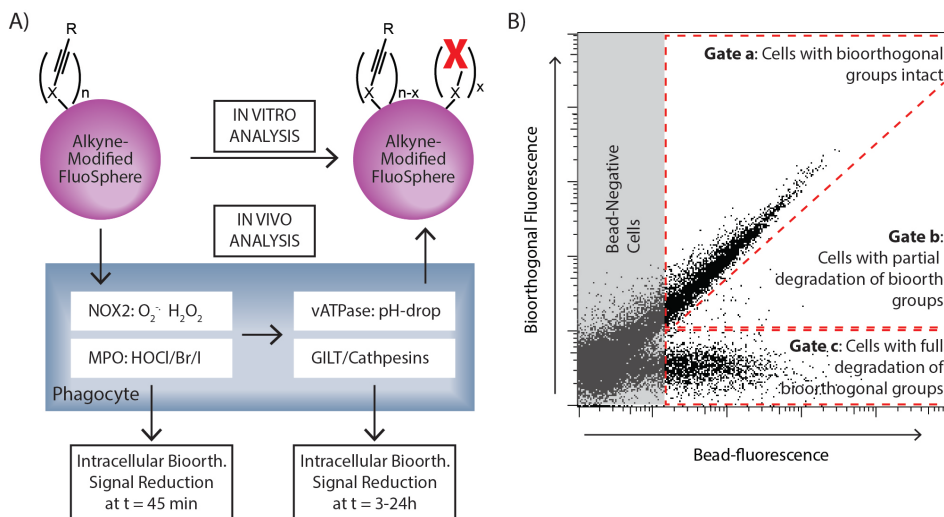


**Figure 1.** Outline of the stability assays and flow cytometric analysis. **(A)** Alkyne-modified fluorescent latex beads were incubated either in vitro or fed to APCs and the reduction in the number of reactive alkynes was assessed either on the naked beads, or of the cells containing the beads. **X** depicts alkynes rendered unreactive. **(B)** Degradation in cells was quantified as the percentage of cells in which all bioorthogonal groups were degraded to avoid ambiguity. Bead fluorescence was used as an internal standard to negate differences in bead uptake between cells.

Copper-catalyzed and strain-promoted Huisgen-type cycloaddition reactions (ccHc and spHc, also known as CuAAC and SPAAC, respectively) are amongst the most widely applied reactions for the study of intraphagosomal events.<sup>11,12,30,31</sup> However, the stability of the reaction partners in this environment has not previously been characterized. It has, for example, been reported that alkynes are sensitive to thiols and/or radical conditions<sup>32–35</sup>, such as these found in phagosomes.<sup>36</sup> Yet, despite this potential stability risk, most stability studies of bioorthogonal groups have been performed in either buffered growth media or cell lysates<sup>35</sup>, or the cytosol of intact target cells.<sup>37,38</sup> None of these conditions recapitulate the chemical harshness of the maturing phagosome. To fill this knowledge gap, the method described here was developed to quantify bioorthogonal group stability inside phagosomes. Fluorescent beads (FluoSpheres™) were modified with terminal alkynes or azides (for ccHc) or strained alkynes (for spHc), and used to quantify their stability against the chemistries encountered during phagosomal maturation, using flow cytometry. Strained alkynes were found to be rapidly degraded under these intraphagosomal conditions. Terminal alkynes on the other hand remained stable to the conditions found during the entire phagosomal maturation pathway. The stability of azides proved more difficult to study due to the high background observed for the alkyne-

fluorophore but seemed to display a similar stability profile as the terminal alkynes. Subsequent *in vitro* analysis revealed that a reaction between the spHc-reagents and HOCl was a likely culprit for the inactivation of the bioorthogonal groups, although additional reactive species could not be excluded.

## 3.2 Results and Discussion

### 3.2.1 Development of a bioorthogonal stability assay in phagocytes

There are three main classes of phagocytes in the immune system, macrophages, dendritic cells (DCs), and neutrophils, of which DCs and macrophages are most important for antigen processing and presentation.<sup>39,40</sup> They are also the main reservoir for intracellular pathogenic bacteria and thus under intense scrutiny to study the host-pathogen interactions. DCs and macrophages – as well as their subsets – display wide heterogeneity regarding their phagocytic capacity and intracellular chemistries.<sup>41,42</sup> In order to develop an assay that would allow the assessment of the stability of bioorthogonal groups after phagocytosis independent of the differences in uptake, an approach was designed where the phagocytes would take up microspheres, that were not only surface modified with the bioorthogonal groups, but that also contained intra-bead fluorophores, not exposed to the phagosomal environment (**Figure 1A**) and thus showing minimal bleaching.<sup>43</sup> These beads would allow the quantification of bioorthogonal handles per bead over time inside a phagocyte, by measuring the change in ratio of fluorescent signal resulting from a bioorthogonal ligation to that of the internal fluorophore. This approach would negate not only differences in uptake between cells, but also signal changes resulting from any potential expulsion of beads through exocytosis<sup>41</sup> (**Figure 1B**). The approach is also facile, as the whole analysis could also be performed in fixed cells, preventing the need for re-isolating the spheres after the biological time course.

Amine-functionalized 0.2  $\mu\text{m}$  polystyrene FluoSpheres (excitation/emission = 580/605 nm, **5**) were modified with various bioorthogonal ligands for the azide-alkyne [3+2] cycloaddition (**Figure 2**) using hydroxysuccinimidyl (**1-4**)-mediated amide/carbamate condensation reactions.<sup>44</sup> The acetylenyl and azido-groups were chosen for their widespread application in the copper-catalyzed<sup>45</sup> or strain-promoted Huisgen cycloaddition<sup>46</sup>, or the Bertozzi-Staudinger ligation.<sup>3</sup> The strained dibenzocyclooctynyl (DBCO, also known as DIBAC; **3**) and bicyclo[6.1.0.]nonyne (BCN; **4**) were chosen for their copper-independency, relatively fast reaction rates ( $0.31\text{ M}^{-1}\text{s}^{-1}$  and  $0.14\text{ M}^{-1}\text{s}^{-1}$  respectively)<sup>47</sup> and widespread use in literature.<sup>48–52</sup> Optimal reaction conditions were found to be



shaking the unmodified beads for two days at 20°C in a 1:5 mixture of DMSO in PBS, containing a large excess of the succinimidyl esters **1-4** to yield acetylenyl- (**6**), azido- (**7**), dibenzocyclooctynyl (**8**), or bicyclo[6.1.0]nonyne (**9**)-modified FluoSpheres.

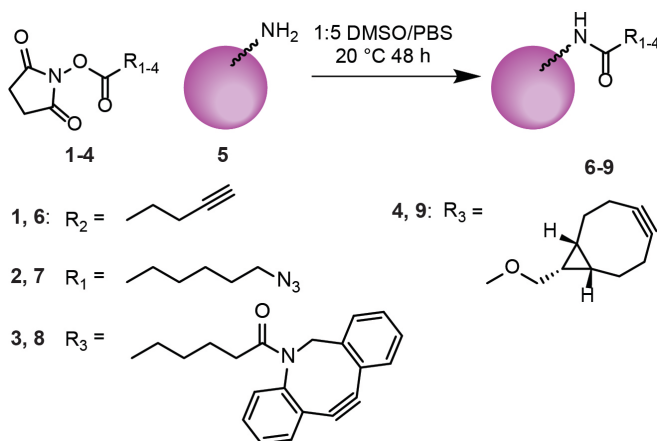


**Figure 2.** Synthesis of bioorthogonal fluorescent polystyrene beads. Amine-functionalized FluoSpheres **5** (200 nm) were modified with hydroxysuccinimidyl esters **1-4** to yield bioorthogonal FluoSpheres **6-9**.

The fluorescence of the beads allowed their assessment by bead-only flow cytometry: using either a copper-catalyzed or copper-free [3+2] cycloaddition reaction (in case of **6** and **7**) with AF488-azide (or alkyne for **7**)<sup>8,53</sup>, followed by flow cytometric analysis of the FluoSpheres (**Figure 3**,  $t = 0$ ) to visualize the introduced alkynes or fluorescamine to visualize the remaining unreacted amines (**Figure S1**).<sup>54</sup> Complete disappearance of the fluorescamine signal was observed for all particles indicating complete consumption of the free amine functionalities in all reactions.

### 3.2.2 Stability of bioorthogonal FluoSpheres in vitro

It was first determined whether this assay could recapitulate previously reported stability properties of the various above bioorthogonal groups (**Figure 3**, **Figure S2-S7**).<sup>37</sup> All groups were previously reported to be stable in PBS and cell lysates, but strained alkynes were reported to react with thiols<sup>32,55</sup>, and thiol radicals.<sup>32</sup> Terminal alkynes were also shown to be reactive towards thiol radicals<sup>32</sup>, as well as to hydroxyl radicals.<sup>56,57</sup>

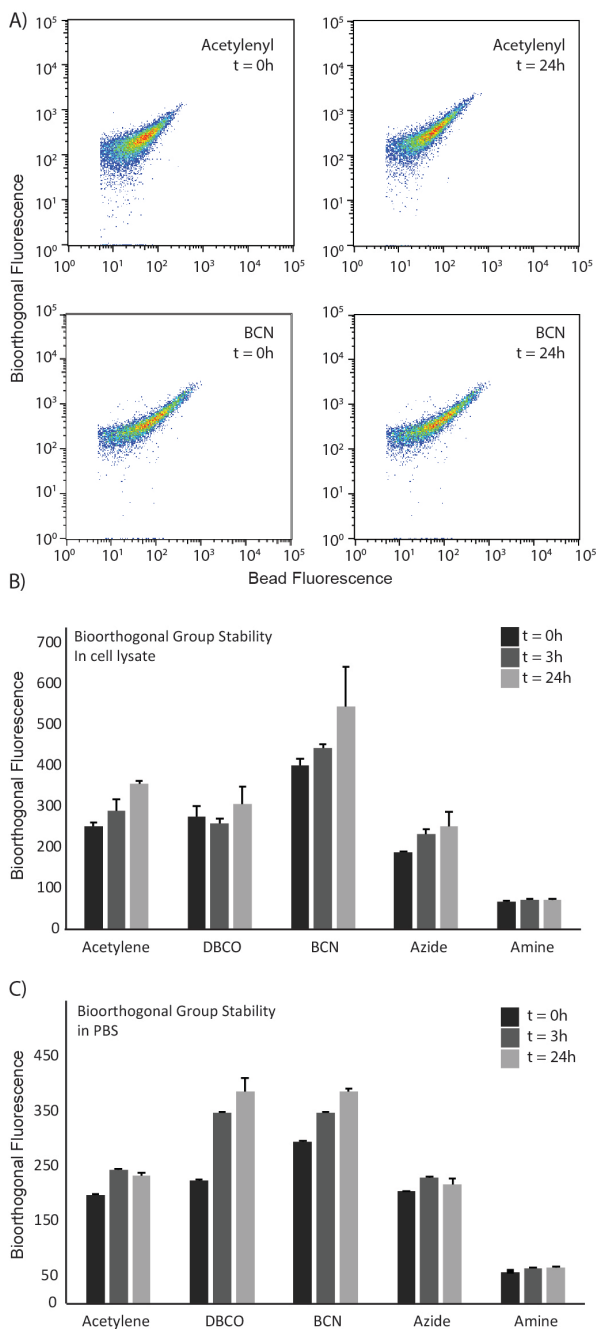


**Figure 3.** Assessment of stability of bioorthogonal groups in cell lysate or PBS. **(A)** plots at t = 0 and t = 24 of an incubation of acetylenyl-FluoSpheres **5** and BCN-FluoSpheres **9** in cell lysate. Y-axis shows the fluorescence stemming from bioorthogonal ligations, x-axis the intrinsic fluorescence of the spheres; **(B)** quantification of the median bioorthogonal fluorescence over time of the modified FluoSpheres **5-9** in cell lysate and **(C)** in PBS. (See also Figure S2-S4). N = 3 for all.

The bioorthogonal FluoSpheres were first incubated (in triplicate) in cell lysate (**Figure S3**) or PBS (**Figure S4**) for up to 24 h and subsequently reacted with AF488-azide or alkyne using the appropriate bioorthogonal ligation conditions (**Figure 3**, **Figure S2**). The beads were then injected directly into the flow cytometer for quantification of both bead-based and bioorthogonal-based fluorescent signal. The internal fluorescent dye could readily be used to discriminate beads from cellular debris of a similar size. Changes in the median fluorescence intensity (MFI) of the bioorthogonally introduced fluorophore allowed quantification of the remaining signal.

None of the bioorthogonal groups showed significant reduction in lysate (**Figure 3B**, **Figure S2/S3**) and PBS (**Figure 3C**, **Figure S2/S4**). An increase in signal over time was even observed, possibly due to de-aggregation of the beads in these media, increasing the available surface area and thus bioorthogonal groups. A similar effect was observed for the amine control beads, although to a much lesser extent, possibly by virtue of the more hydrophilic nature of these beads. When assessing whether the thiol and thiol-reactivity could be recapitulated, it was indeed found that all groups completely degraded, in presence of a high concentration (250 mM) of glutathione (GSH) and the free radical photoinitiator 2-Hydroxy-4'-(2-hydroxyethoxy)-2-methylpropiophenone (25 mM) after 5 or 10 minutes irradiation with UV-light (145  $\mu\text{W}/\text{cm}^2$ ) to generate radicals *in-situ* (**Figure S2/S5**). Even without radicals, all bioorthogonal signal disappeared after incubation with 250 mM GSH for 30 minutes (**Figure S2/S6**). Radicals alone resulted in selective (partial) degradation of BCN, DBCO and azide (**Figure S2/S7**), confirming the suitability of this approach at least *in vitro*.

### 3.2.3 Stability of bioorthogonal FluoSpheres in cells

Next, the stability of bioorthogonal FluoSpheres **6-9** was tested in the endolysosomal environment of phagocytes (*in cellula*). DCs (DC2.4 cell line<sup>58</sup>) and macrophages (RAW264.7 cell line<sup>59,60</sup>) were used, as they are at the opposite ends of the property spectrum of phagocytes.<sup>61</sup> DC2.4 cells phagocytose in a controlled manner and use their oxidative burst to attenuate protease activity leading to improved antigen presentation, either by oxidizing cysteine proteases and decreasing the reductive capacity of the phagosome<sup>62</sup>, or by limiting the acidification of the phagosome.<sup>63,64</sup> RAW264.7 cells are macrophage-like and have a very high phagocytic capacity.<sup>65</sup> They are also capable of producing Reactive Oxygen Species (ROS) in high amounts<sup>66</sup>, as well as secondary ROS-metabolites through the action of MPO.<sup>67</sup>

The assay was designed in the following manner. The APCs were first allowed to take up the bioorthogonal FluoSpheres for 45 minutes ( $t = 0$ ), after which uptake and the initial oxidative burst should be complete, as suggested in literature.<sup>68</sup> The cells were then washed and chased for 3 or 24 hours to determine to what extent the combination of acidification, thioreductase expression<sup>25</sup> and proteolysis<sup>69,70</sup> in the matured phagosome contributes to bioorthogonal handle degradation. Cells were then fixed and permeabilized (allowing free entry of bioorthogonal reagents and neutralization of the phagosomal compartment), ligated with a complementary bioorthogonal fluorophore, before quantification of the two fluorescent signals by flow cytometry (**Figure 4**, **Figure S8/S9**). Fluorescence in the red channel (FluoSpheres) was plotted against the green channel (AF488 coupled to the bioorthogonal groups). Quantification gates were set to exclude cells and debris that had not taken up beads (bead-negative cells). Bioorthogonal degradation was quantified by looking at the percentage of cells in which the bioorthogonal fluorescence had been reduced to the level of unmodified FluoSpheres **5** (**Figure 4A**).

The acetylenyl-groups on FluoSpheres **6** showed a remarkable stability in both DCs and macrophages (**Figure 4A/B** and **Figure S8/S9**) with <6% degradation observed at any time point in either cell types. BCN-groups showed the poorest stability, especially to the intracellular conditions found in macrophages: 79% ( $\pm 2\%$ ) of cells had fully degraded all bioorthogonal groups after 24h). DBCO-groups showed a moderate stability (36%  $\pm 1\%$  degradation after 24h). Azide-modified spheres showed very poor uptake in macrophages preventing the quantification of their degradation in these cells. In DCs, the degradation of azides was minimal (**Figure 4A**, **Figure S8/S9**). Attempts to further enhance degradation by stimulating the oxidative burst by adding LPS or a combination of phorbol-12-myristoyl-13-acetate (PMA)<sup>71</sup> and yeast-derived zymosan particles<sup>72,73</sup> to both cell lines did not yield a further increase in degradation (**Figure S10/S11**). Moreover, these stimuli either resulted in reduced degradation or extensive cell death over the time course of the experiment, again preventing quantification of the degradation.

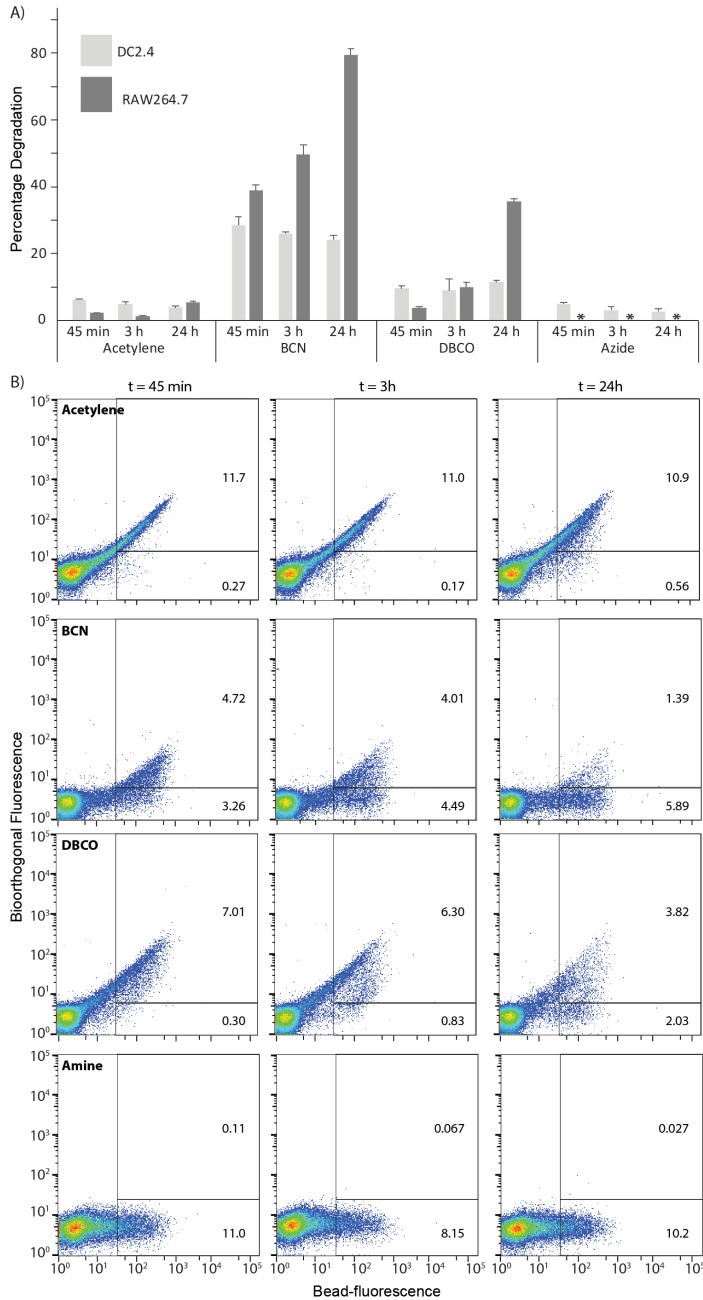


**Figure 4.** Quantification of bioorthogonal group stability. **(A)** Percentage of degraded bioorthogonal groups after incubation in DCs (DC2.4) or macrophages (RAW264.7), as quantified by illustrated gating strategy. Cells that had not taken up beads (bead-negative cells) were excluded from the gated area, cells in which the bioorthogonal signal had fully degraded to background (gate b) were counted, as were the cells still positive for bioorthogonal signal (gate a); **(B)** Quantification of percentage macrophages (RAW264.7) containing degraded beads ( $a/[a+b]$ ) (see also Figure S9). Indicated values are fractions of total cell count.

Since only the strained alkynes showed degradation but not the terminal acetylene or azide groups, it was hypothesized that this might be caused by radicals during the oxidative burst, as extensive degradation was already observed at the earliest time point. It was hypothesized that the potential culprits could be either superoxide, the superoxide metabolite  $\text{H}_2\text{O}_2$ , which can reach levels of 100  $\mu\text{M}$  if MPO is inhibited<sup>74</sup>, or one of the species produced by MPO, such as hypochlorous acid (HOCl). This species is produced by MPO in presence of imported chloride and can reach high  $\mu\text{M}$  concentrations in the phagosome.<sup>18,75</sup> However, HOCl-production is well established in neutrophils but less is known about its intracellular concentrations in DCs and macrophages, due to the interplay between MPO and chloride channels in these cells.<sup>75–78</sup> Other potential reaction partners could be hydroxyl-radicals produced through Fenton chemistry, or thiol oxidation products produced during the oxidative burst.<sup>19</sup>

To determine the responsible species, the *in vitro* system was used once more to assess whether the reactive species in the endosome could degrade bioorthogonal handles at the concentrations found in the phagosome (**Table 1**). **6–9** were incubated with hydrogen peroxide concentrations of 50, 100 or 200  $\mu\text{M}$  at pH 7.4 or 5.0, either in the dark (**Figure S12**) or whilst exposed to UV radiation (145  $\mu\text{W}/\text{cm}^2$  for 5 minutes, **Figure S13**). All particles proved stable under these conditions suggesting that primary products of oxidative burst are not responsible for the in cell-degradation. Incubation with the MPO product HOCl at 50, 100 or 200  $\mu\text{M}$  at pH 7.4 showed a surprisingly similar stability pattern as observed in both macrophages and DCs: **8** and **9** were degraded under these conditions, whereas **5** and **6** remained stable (**Figure S14**). The degradation of BCN and DBCO occurred at neutral pH but not at acidic pH, which is in agreement with the relatively high pH during the oxidative burst<sup>64,79</sup> and the lack of further degradation observed after  $t = 0$  *in cellula*, when acidification occurs. The stability of the bioorthogonal FluoSpheres to GSH (100  $\mu\text{M}$  or 1 mM) in combination with *in situ*-generated radicals was also assessed to investigate the potential role of thiols and thiyl-radicals. Surprisingly, the strained alkynes proved stable to these conditions, whereas the acetylene and azide were degraded under acidic incubation with GSH and radicals (**Figure S15**). This makes the thiyl-radical species an unlikely candidate for the observed degradation *in cellula*.

Alternatively, thiols can be oxidized by ROS-metabolites such as  $\text{H}_2\text{O}_2$  or HOCl to form short-lived sulfenic acids (SOH)<sup>80,81</sup>, which could very well be responsible for the degradation of the strained alkynes, as these have been described as sulfenic acid traps.<sup>82</sup> However, it is not straightforward to reproduce these transient

compounds *in vitro* due to rapid overoxidation. Although HOCl appears to play a part in the observed degradation, the true mechanism may very well be a combination of the above factors, or a set of conditions as yet undescribed.

**Table 1.** Overview of bioorthogonal group stability to degradative conditions *in vitro* and *in cellula*. The relevant conditions are listed and the stability of the corresponding bioorthogonal groups is indicated with green (negligible degradation), red (significant degradation) or grey (unclear due to specified reason). RPI = radical photoinitiator. Asterisk (\*) indicates the formation of radicals during the indicated conditions.

Test conditions	Acetylene	BCN	DBCO	Azide
PBS				
Cell lysate				
1% APS + 0.5% TEMED*				
25 mM RPI				
25 mM RPI + UV*				
200 $\mu$ M H <sub>2</sub> O <sub>2</sub> (pH 7.4)				
200 $\mu$ M H <sub>2</sub> O <sub>2</sub> (pH 7.4) + UV*				
50 $\mu$ M HOCl (pH 7.4)				
200 $\mu$ M HOCl (pH 7.4)				
200 $\mu$ M H <sub>2</sub> O <sub>2</sub> (pH 5) + UV*				
200 $\mu$ M H <sub>2</sub> O <sub>2</sub> (pH 5)				
50 $\mu$ M HOCl (pH 5)				
200 $\mu$ M HOCl (pH 5)				
1 mM GSH (pH 7.4)				
1 mM GSH (pH 7.4) + H <sub>2</sub> O <sub>2</sub>				
1 mM GSH (pH 7.4) + RPI + UV*				
1 mM GSH (pH 5)				
1 mM GSH (pH 5) + H <sub>2</sub> O <sub>2</sub>				
1 mM GSH (pH 5) + RPI + UV*				
2.5 mM GSH (1:3 MeOH/H <sub>2</sub> O)				
250 mM GSH (1:3 MeOH/H <sub>2</sub> O)				
250 mM GSH (1:3 MeOH/H <sub>2</sub> O) + RPI + UV*				
In dendritic cells				Background
In dendritic cells + LPS				Background
In dendritic cells + zymosan/PMA				Background
In macrophages				Background
In macrophages + LPS			Not tested	Not tested
In macrophages + zymosan/PMA	Cell death	Cell death	Cell death	Cell death
In macrophages + NOX2 inhibitor	Not tested		Not tested	Not tested

### 3.3 Conclusion

Using a straightforward bead-based assay to test the stability of bioorthogonal handles within the endolysosomal compartments of dendritic cells, a striking difference was observed in the disappearance of reactivity between strained alkynes and terminal alkynes in phagocytes. These are obviously not the only class of bioorthogonal reactions available to date. Many other bioorthogonal ligation reactions have been developed<sup>83</sup>, such as the Inverse Electron-Demand Diels-Alder (IEDDA) cycloaddition<sup>84,85</sup>, the [4+1] photoclick<sup>86</sup>, diazo-based ligation reactions<sup>87</sup>, and many more. Most of these reactions have been incompletely profiled with regards to their *in cellula* stability and it is thus foreseen that this simple assay could also provide insight into the biochemical stability of these groups and those yet to be discovered.



### 3.4 Experimental

#### Mammalian cell culture and lysate preparation

RAW264.7 cells (Merck) were cultured in DMEM (Sigma-Aldrich) supplemented with 10% heat-inactivated fetal calf serum (FCS), 1% GlutaMAX and 1% penicillin/streptomycin. DC2.4 cells (Merck) were cultured in IMDM (Sigma-Aldrich) supplemented with 10% heat-inactivated fetal calf serum (FCS), 1% GlutaMAX, 1% penicillin/streptomycin, 10 mM HEPES, 1 mM pyruvate and 1x MEM non-essential amino-acids (Life Technologies). 2-Mercaptoethanol (final concentration: 50  $\mu$ M, Life Technologies) was freshly added to the medium every time after splitting the cells. Cells were grown at 37 °C under a humidified atmosphere containing 5% CO<sub>2</sub>. Cell lysates were obtained by harvesting DC2.4 cells at confluence, washing with ice-cold PBS and subsequently resuspending in 10  $\mu$ L lysis buffer (150 mM NaCl, 1% IGEPAL in 50 mM HEPES pH 7.4) per  $1 \times 10^6$  cells. The resulting suspension was subjected to a triple freeze-thaw cycle in liquid nitrogen and subsequently diluted 1:100 in ice-cold PBS and stored in aliquots at -20 °C for until further use.

#### Bioorthogonal group-functionalization and characterization of polystyrene fluorescent beads

FluoSpheres® Amine-Modified Microspheres, 0.2  $\mu$ m, red fluorescent (580/605), 2% solids (Thermo Scientific; F8763) were functionalized with a series of bioorthogonal groups (**Figure 2**) through a *N*-hydroxysuccinimide (NHS) ester coupling to the free amines on the bead surface. 100  $\mu$ L of bead stock suspension was diluted 1:2 in milliQ H<sub>2</sub>O and washed twice by centrifugation (30 min, 30000 rcf, 10 °C). After washing, the beads were resuspended in 160  $\mu$ L PBS after which 0.5  $\mu$ mol NHS-reagents in 40  $\mu$ L DMSO was added to the beads to end up with a final concentration of 20% DMSO. The reaction mixture was shaken for 2 days, 20 °C & 1000 rpm after which the conjugated beads were washed 4x with 200  $\mu$ L 20% DMSO in MilliQ, 1 x with 200  $\mu$ L MilliQ, resuspended in 1 mL milliQ and stored at 4 °C until further use. Control (unmodified amine) beads were treated similarly, omitting only the NHS-modified bioorthogonal groups. The resulting FluoSpheres **5-9** were first characterized by ligating to Alexa Fluor 488 (AF488) by ccHc (1 mM copper sulfate, 10 mM sodium ascorbate, 1 mM THPTA ligand, 10 mM aminoguanidine and 2  $\mu$ M AF488-alkyne or azide in 100 mM HEPES pH 7.4) or spHc (2  $\mu$ M AF488-azide in 100 mM HEPES pH 7.4) for 1 hour at RT in the dark, to determine the relative labeling density. Alternatively, FluoSpheres **5-9** were reacted with fluorescamine (1 mM in PBS) for 30 min at RT in the dark, to determine the relative amount of free amines remaining after ligation of the bioorthogonal groups. The resulting fluorophore-modified beads were further diluted 1:20 in FACS

buffer (1% FCS, 1% BSA, 0.1% NaN<sub>3</sub> and 2 mM EDTA in PBS pH 7.4) and immediately measured by flow cytometry.

### ***In vitro* bioorthogonal group stability assay**

Buffer or cell lysate

1  $\mu$ L bioorthogonal group-functionalized or control bead suspension was diluted 1:100 in PBS buffer or cell lysate and shaken at 37 °C, 600 rpm for the indicated time points (0, 3, 24 h). After the indicated time points, the beads were ligated to AF488 by ccHc or spHc for 1 hour at RT in the dark. The resulting fluorophore-modified beads were further diluted 1:20 in FACS buffer and immediately measured by flow cytometry.

#### *Oxidative conditions (Lo Conte conditions<sup>32</sup>)*

1  $\mu$ L bioorthogonal group-functionalized or control bead suspension was diluted 1:100 in 250 mM glutathione (GSH) and 10% (25 mM) free radical photoinitiator (RPI) 2-Hydroxy-4'-(2-hydroxyethoxy)-2-methylpropiophenone (Sigma-Aldrich; 410896) in 1:3 MeOH/H<sub>2</sub>O in open glass tubes. Samples were exposed to UV-irradiation (280-320 nm, 145  $\mu$ W/cm<sup>2</sup>) for 5 or 10 minutes. After a total incubation of 30 minutes, the beads were ligated to AF488 by ccHc or spHc for 1 hour at RT in the dark. The resulting fluorophore-modified beads were further diluted 1:20 in FACS buffer and immediately measured by flow cytometry. Additional experiments were performed with either 2.5 or 250 mM GSH or 25 mM free radical photoinitiator under the same reaction conditions to observe their individual effects.

#### *Physiological oxidative conditions*

1  $\mu$ L bioorthogonal group-functionalized or control bead suspension was diluted 1:100 in 0.1 M phosphate buffer (pH=7.4) or 0.1 M citrate buffer (pH=5) with 1 mM or 100  $\mu$ M GSH and 10% free radical photoinitiator. Open glass tubes were used for incubation. Samples were exposed to UV- irradiation (280-320 nm, 145  $\mu$ W/cm<sup>2</sup>) for 5 minutes. After total incubation of 30 minutes, the beads were ligated to AF488 by ccHc or spHc and immediately measured by flow cytometry as described before. Additional experiments were performed with 50, 100 and 200  $\mu$ M H<sub>2</sub>O<sub>2</sub> or NaClO in 0.1 M phosphate buffer (pH=7.4) or in 0.1 M citrate buffer (pH=5). Incubation in H<sub>2</sub>O<sub>2</sub> was performed with and without 5 minutes of UV irradiation, while incubation in NaClO was performed only without UV-irradiation.

### ***In cellula* bioorthogonal group stability assay in dendritic cells and macrophages**

DC2.4 or RAW264.7 cells were seeded onto 6-well plates containing  $1 \times 10^6$  cells/well and rested for at least 3 hours. Cells were pulsed with 10  $\mu$ L beads for 45 min, washed with PBS and fresh medium was added for further incubation of indicated time points (0, 3, 24 h). After incubation, all cells were harvested, washed twice with PBS and fixed in suspension in 4% PFA in PBS for 20 min at RT. Next, cells were washed twice with PBS, gently permeabilized with 0.1% IGEPAL in PBS for 20 min at RT and blocked with 3% BSA in PBS twice for 15 minutes. The cells containing bioorthogonal beads were then reacted with a fluorophore by ccHc or spHc for 1 hour at RT in the dark. The resulting cells, containing fluorophore-modified beads were finally washed twice with FACS buffer and resuspended in FACS buffer for flow cytometry measurements.

### ***In cellula* pre-clicked beads stability assay in dendritic cells**

Pre-clicked FluoSpheres were prepared by reacting 100  $\mu$ L acetylenyl-functionalized FluoSpheres with AF488-azide by ccHc for 1 hour at RT in the dark. The reaction was quenched by adding 5 mM EDTA and 5% DMSO and washed with 100  $\mu$ L MilliQ by centrifugation (30 min, 30000 rcf, 10°C). Pre-clicked beads were resuspended in 100  $\mu$ L MilliQ and stored at 4 °C until further use. Cell experiments were performed as described above. After fixation, cells were washed twice with PBS and resuspended in FACS buffer for flow cytometry measurements.

### **Flow cytometry**

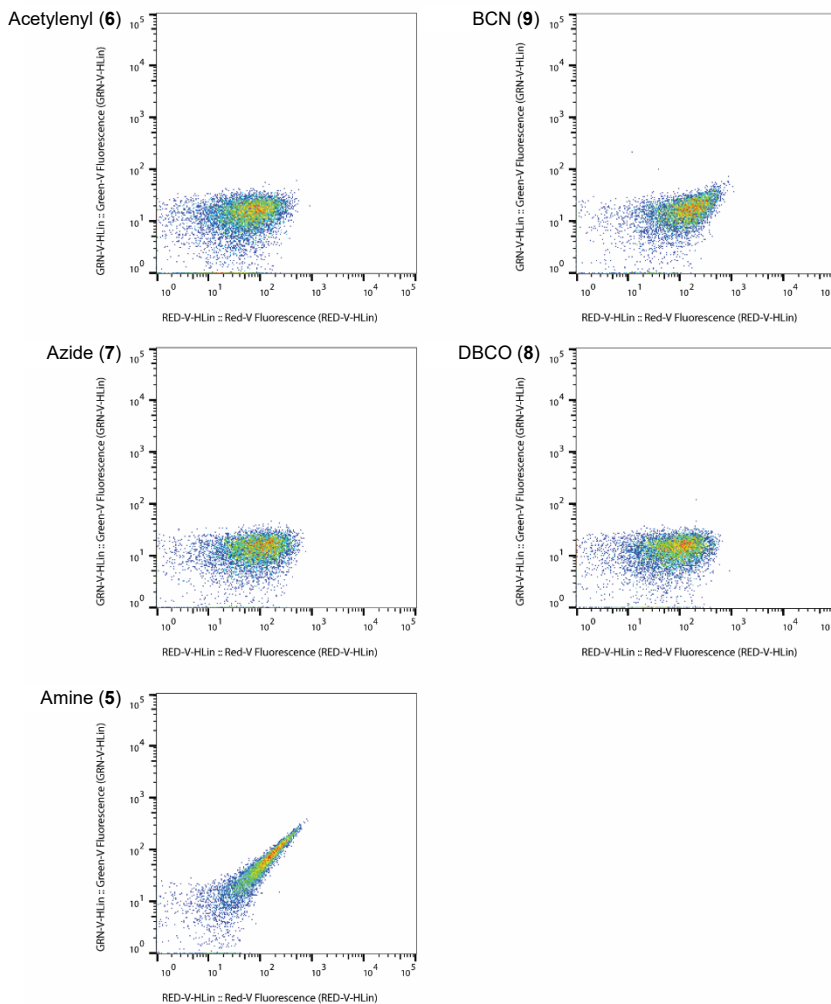
All flow cytometry measurements were performed on a Guava® easyCyte 12 HT Sampling Flow Cytometer and data analysis was performed with FlowJo V10. Beads in suspension were gated manually using internal bead fluorescence (to exclude signal resulting from debris). The resulting data was visualized in pseudocolor dot plots, plotting the internal bead fluorescence (Cytometer Channel RED-V) against the external fluorophore fluorescence (Cytometer Channel GRN-B) to show the correlation between external and internal fluorescence, as a measure for the number of stable bioorthogonal groups per bead.

### **Quantification of degradation**

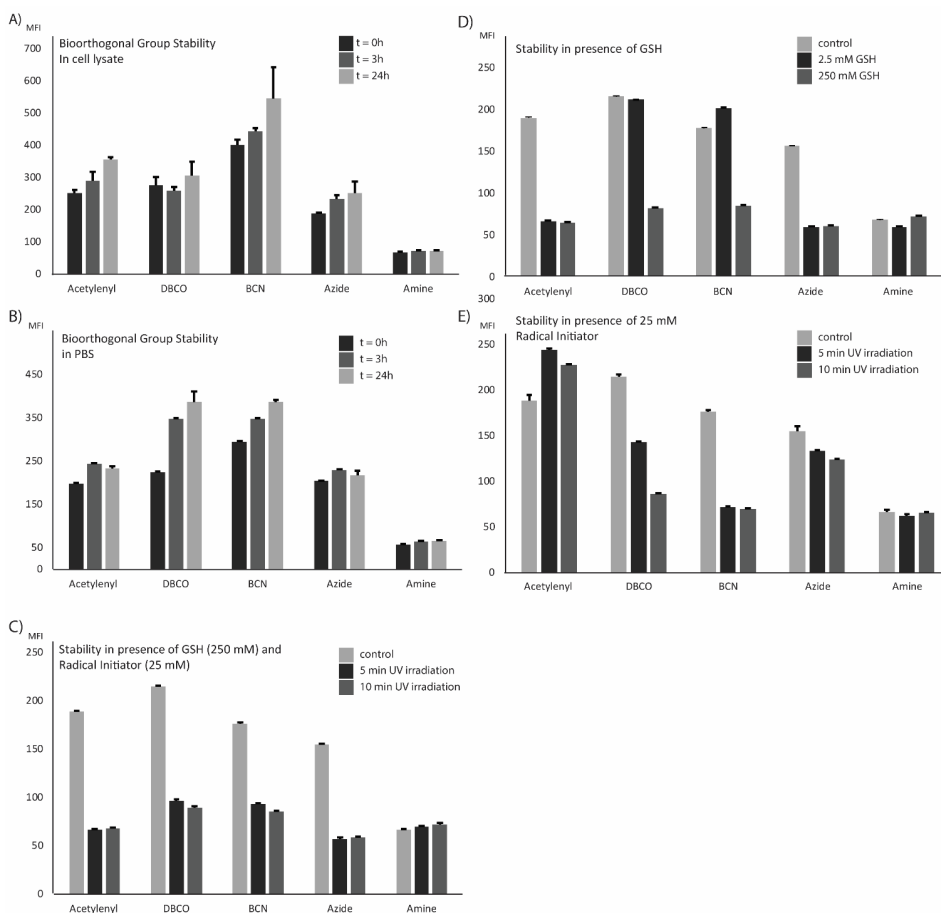
The relative percentage of stable bioorthogonal groups in DC2.4 cells was quantified by first excluding cells containing insufficient beads for accurate differentiation and subsequently dividing the remaining cells into two groups; those containing fully degraded bioorthogonal groups and those containing unaffected or partially degraded bioorthogonal groups. The ratio of cells with fully

degraded bioorthogonal groups to the total cell count (**Figure 4A**;  $b/[a+b]$ ), provided a robust estimate of the percentage of degraded bioorthogonal groups, avoiding subjective interpretation of the data and minimizing false positives.

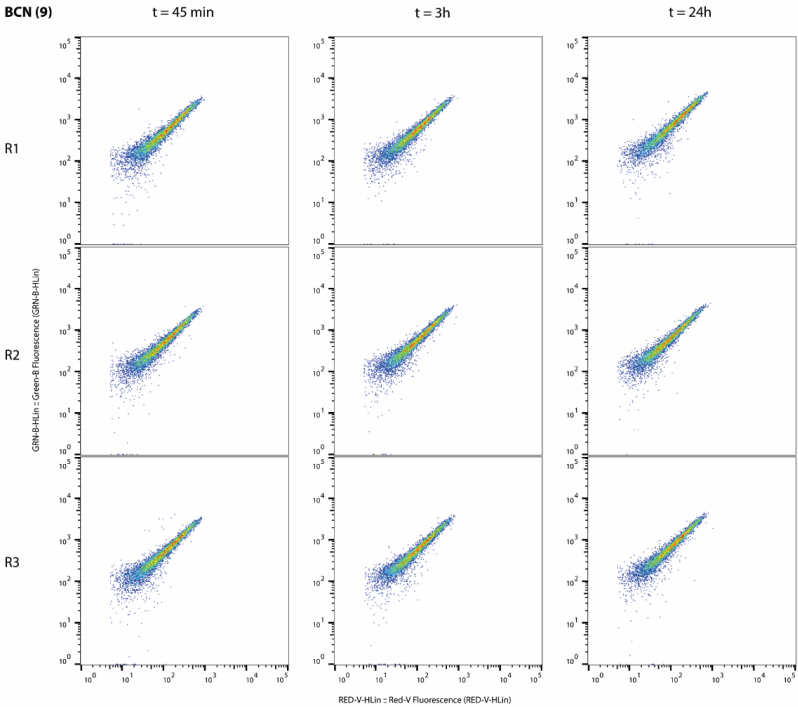
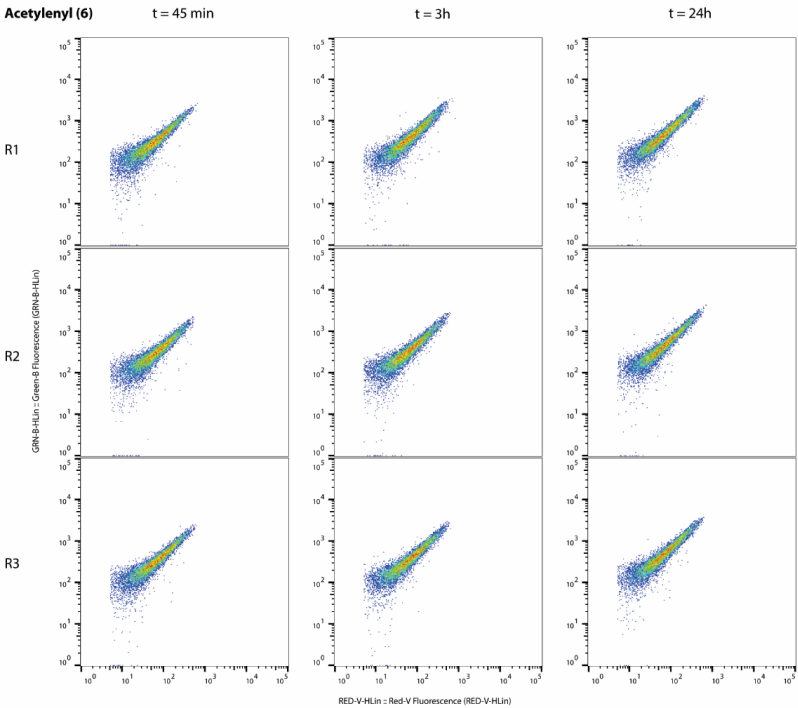
### 3.5 Supplemental Figures

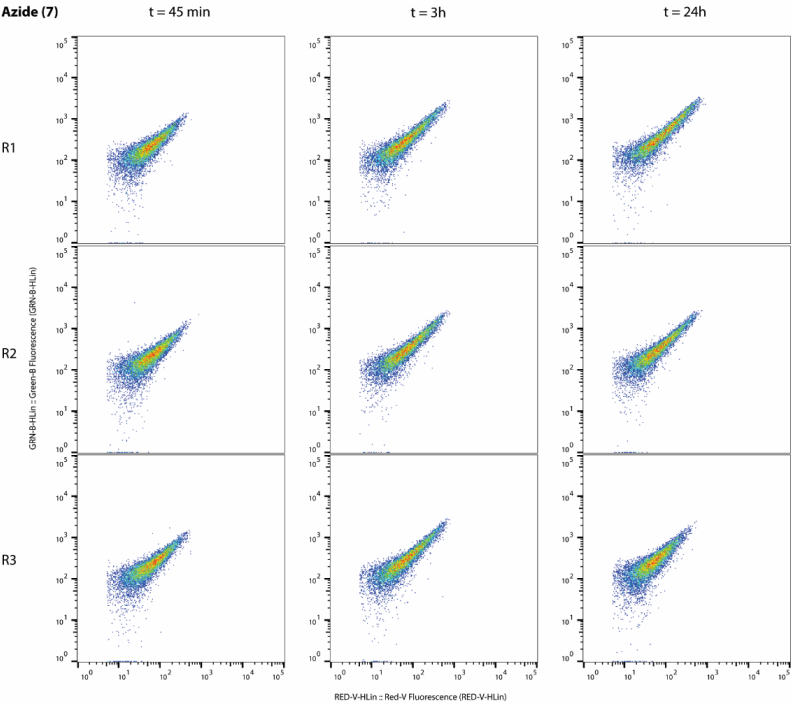
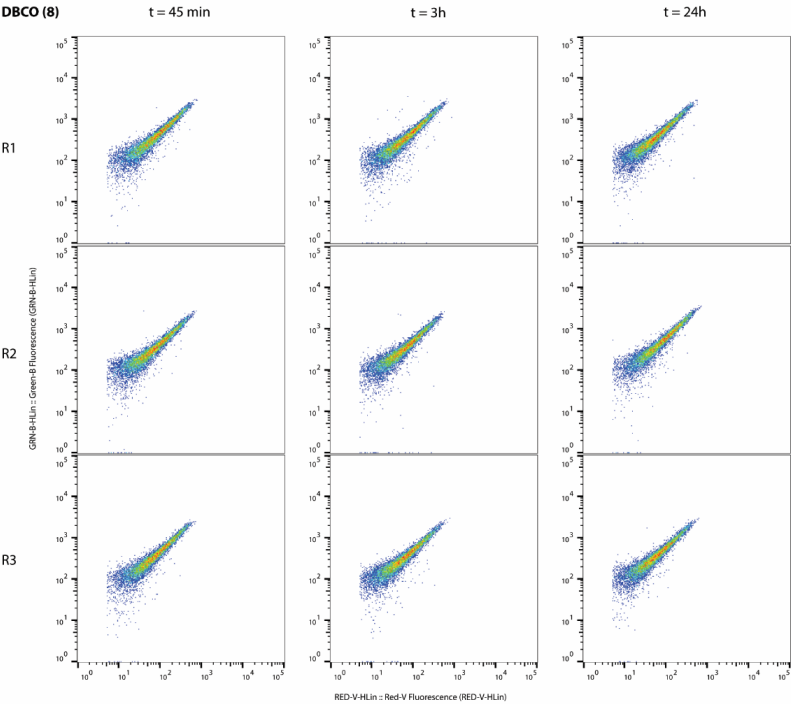


**Figure S1.** Visualization of remaining unreacted amines on FluoSpheres **5-9** with fluorescamine. FluoSpheres, GRN-V: fluorescamine, arbitrary fluorescence units. Intermediate patterns were found for suboptimal modification conditions (data not shown).

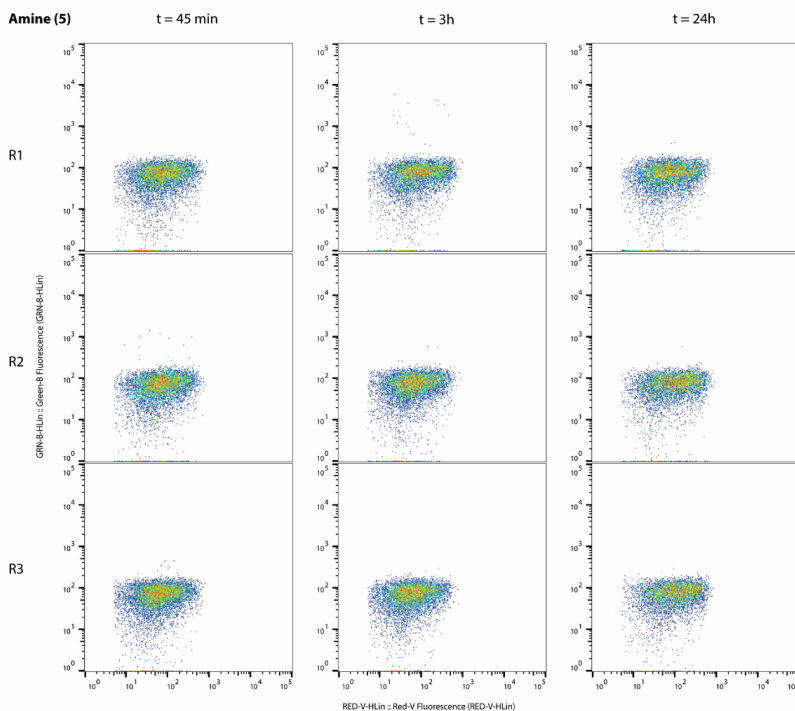


**Figure S2.** Bioorthogonal group stability of FluoSpheres 5-9 in vitro, quantified using the median fluorescence intensity (MFI) of the GRN-B channel (AF488) on the y-axis. **(A)** Stability in cell lysate: no degradation of any groups is observed. **(B)** Stability in PBS; showing no degradation of any groups. **(C)** Stability in the presence of GSH and in situ-generated radicals, after UV irradiation and 30 minutes of total incubation; showing near complete degradation for all groups tested. **(D)** Stability in the presence of GSH alone after 30 minutes of incubation; showing complete degradation for acetylene 6 and azide 7 already at 2.5 mM, while DBCO 8 and BCN 9 are degraded only at 250 mM. **(E)** Stability in the presence of in situ-generated radicals alone, after UV irradiation with a chase totaling 30 minutes of incubation; on-sphere BCN 9 is degraded after 5 minutes irradiation, DBCO 8 becomes increasingly degraded with increased UV-irradiation. Acetylene 6 and azide 7 are degraded by 2.5 mM GSH plus radicals, but are resistant to radicals alone. N=3 for all experiments. Raw data underlying this quantification are presented in Figure S3-S7.

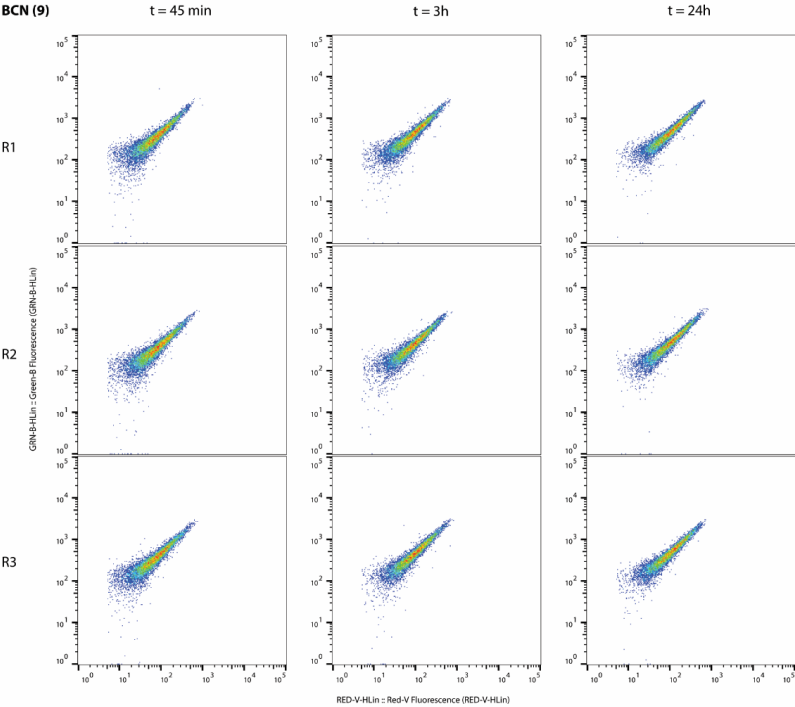
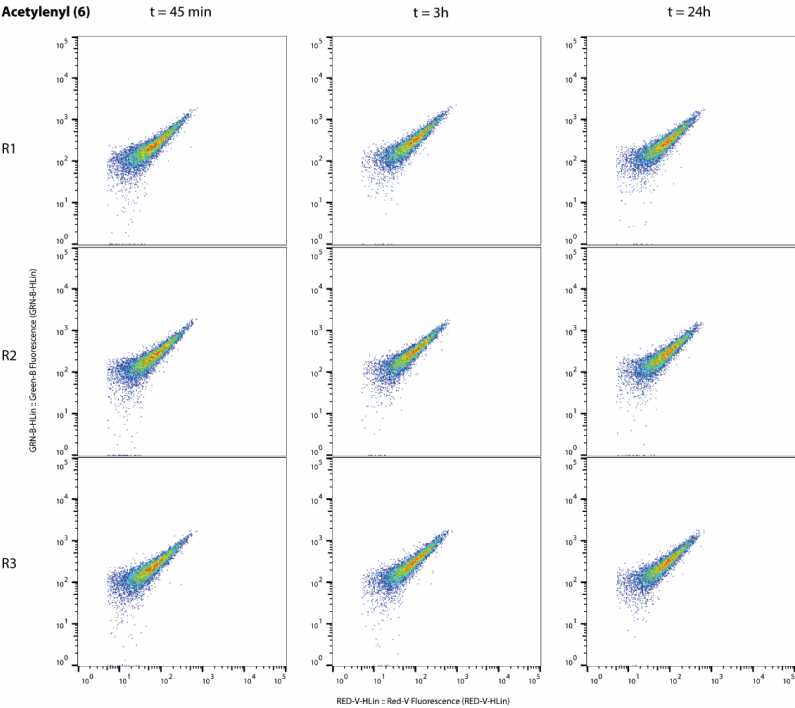


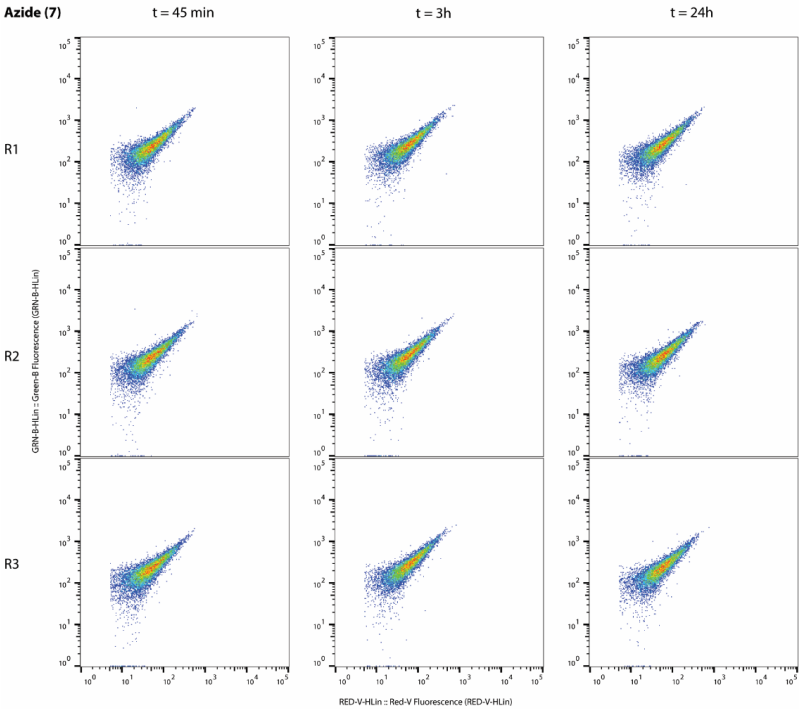
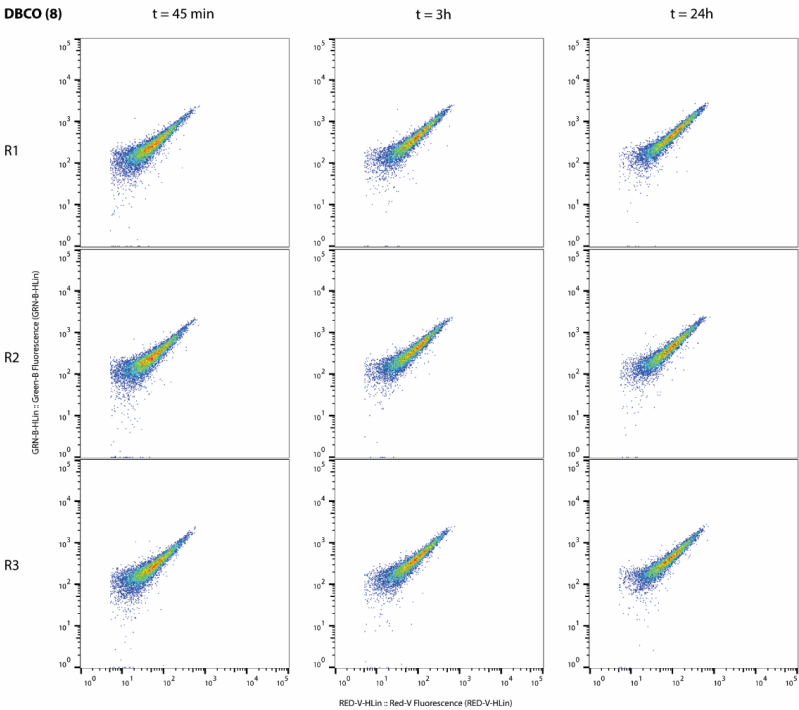


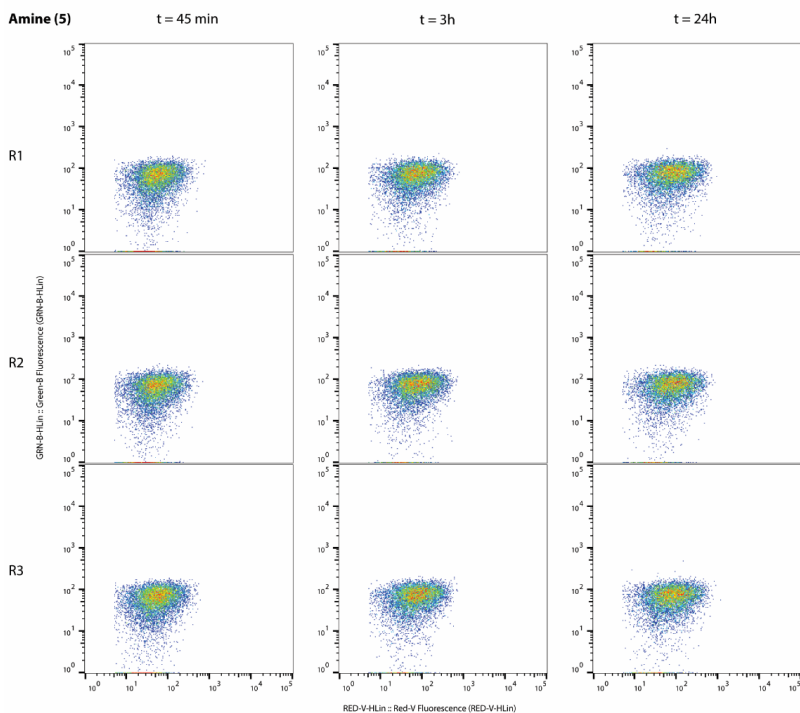




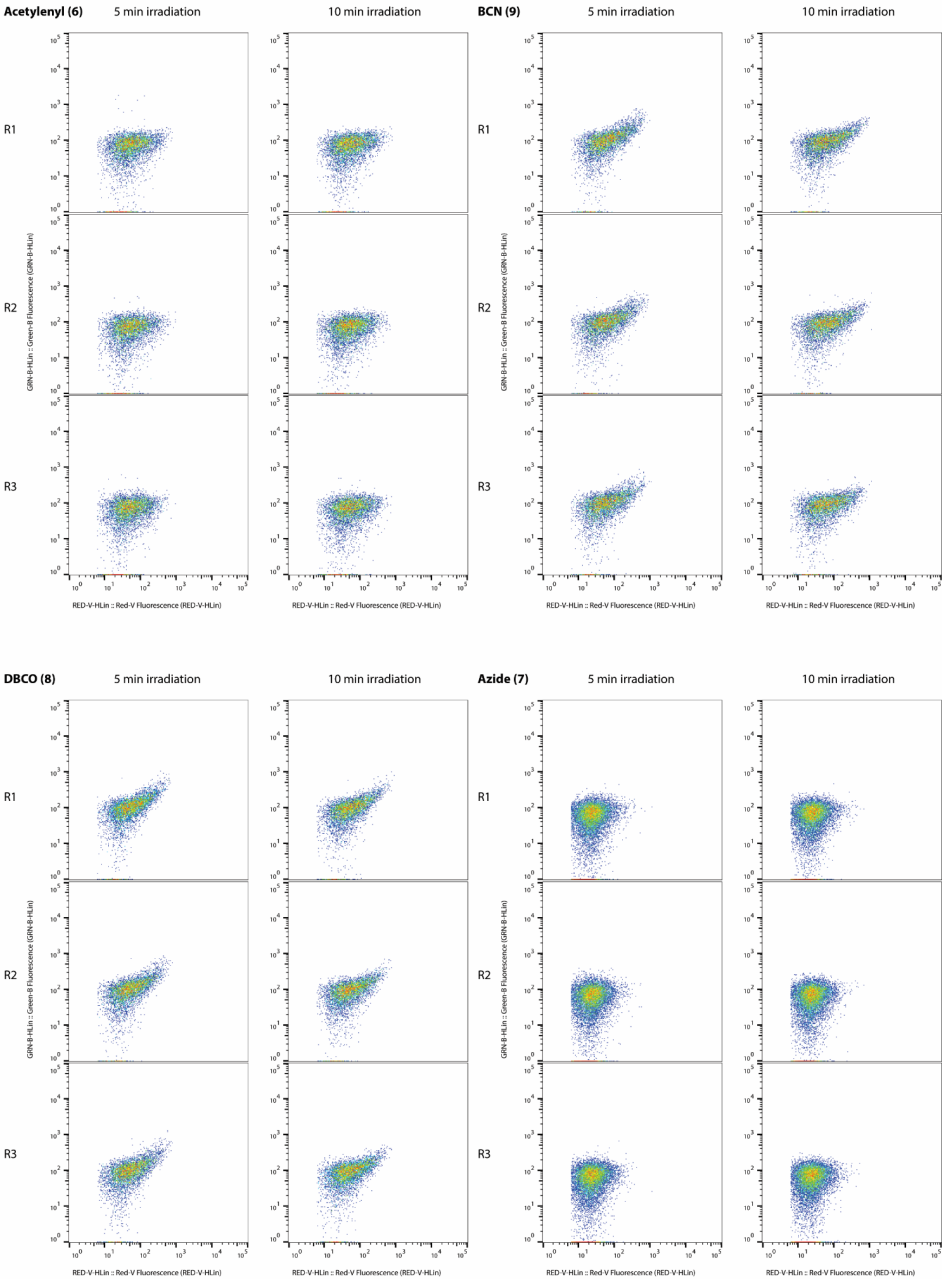
**Figure S3.** Stability assessment of bioorthogonal groups in DC2.4 cell lysate. None of the bioorthogonal groups tested show any degradation over the entire time course of 24h. Amine **5** was included as a control. N=3 for all experiments (R1-3).

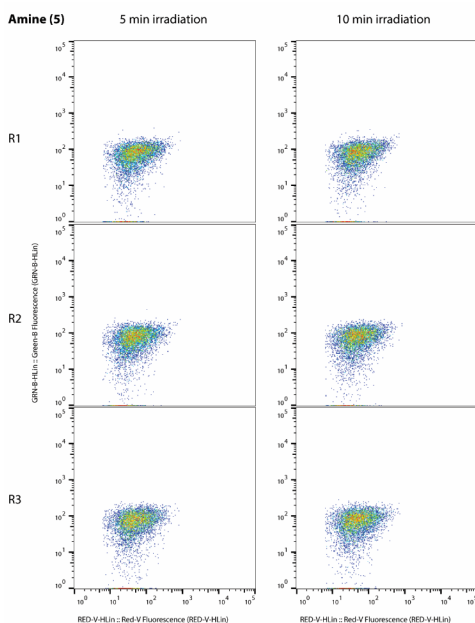




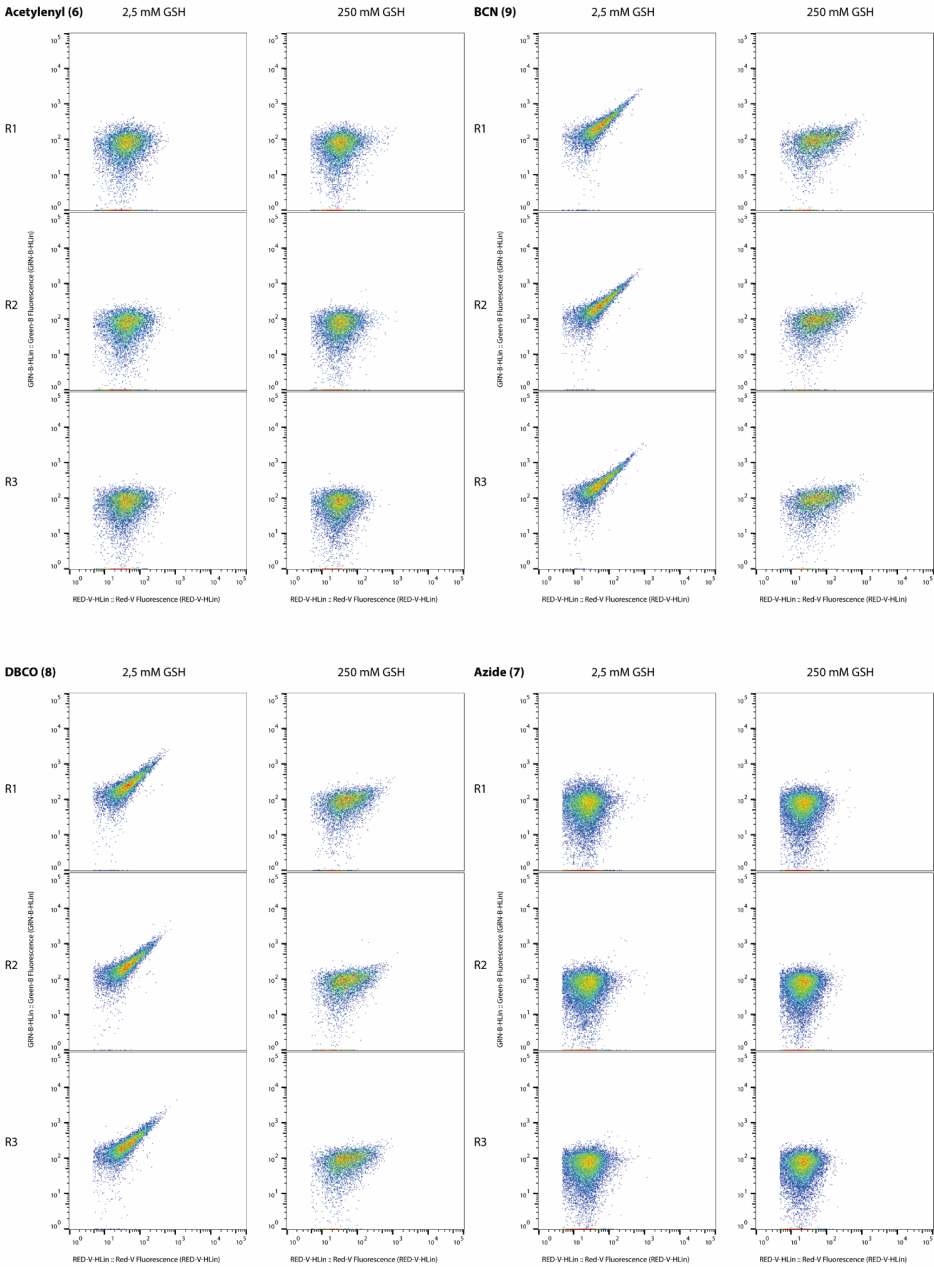


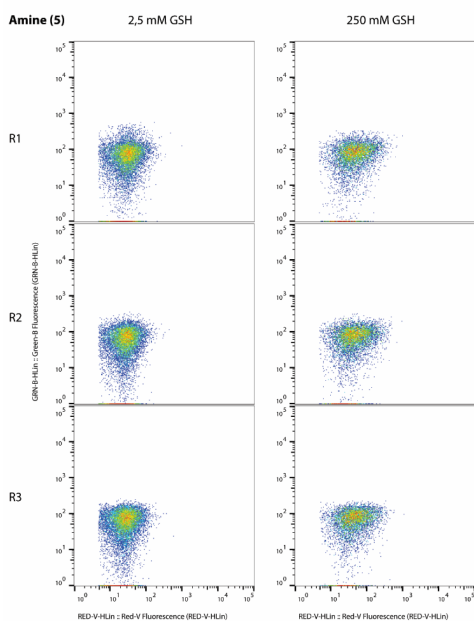
**Figure S4.** Stability assessment of bioorthogonal groups in PBS. None of the bioorthogonal groups tested show any degradation over the entire time course of 24h. N=3 for all experiments (R1-3) shown.





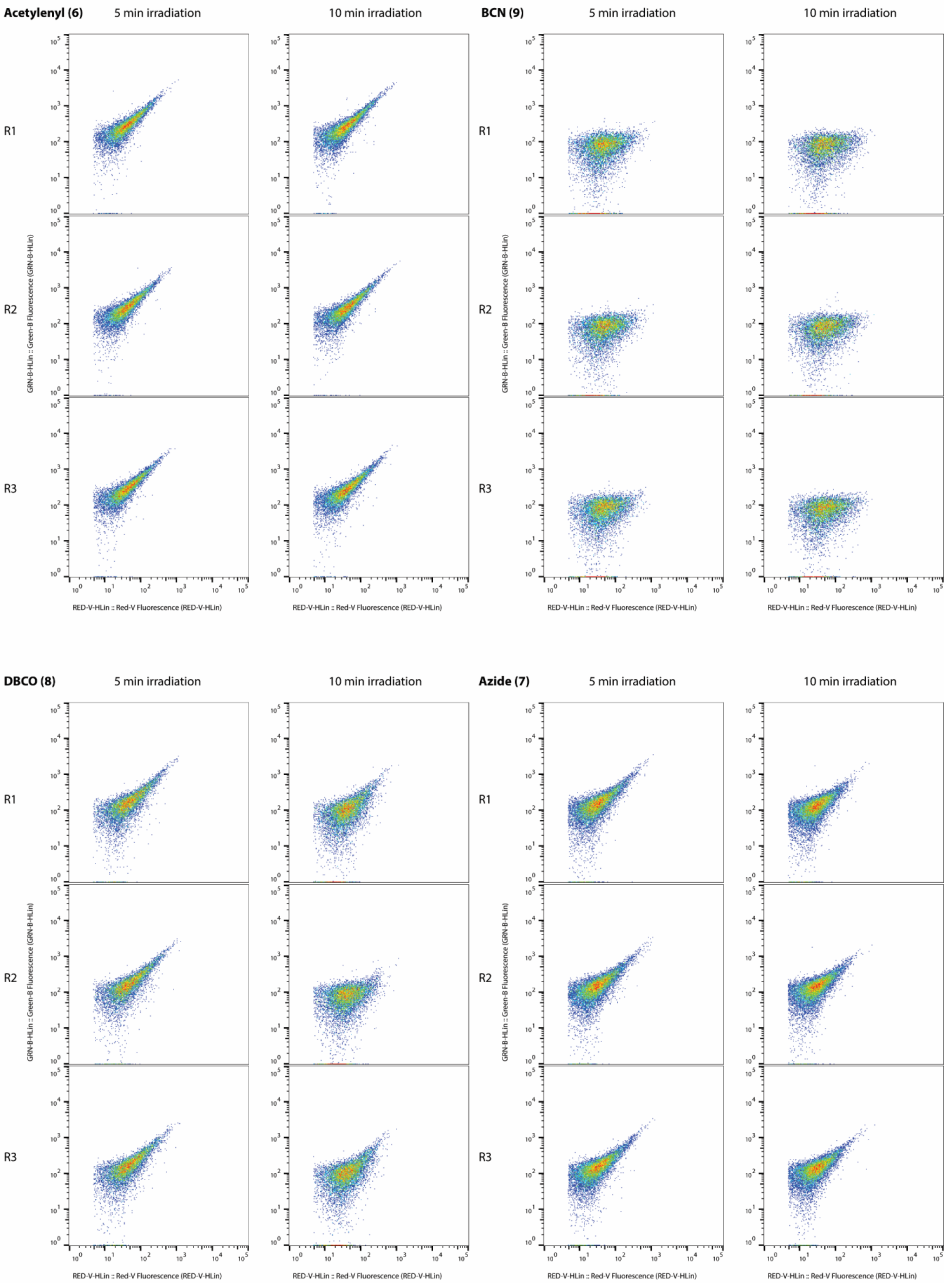
**Figure S5.** Stability assessment of bioorthogonal groups in 250 mM GSH and 25 mM light-activated radical initiator in MeOH/H<sub>2</sub>O (1:3). Samples were exposed for 5 or 10 minutes to UV-irradiation (280-320 nm, 145  $\mu$ W/cm<sup>2</sup>), followed by incubation to a total time of 30 minutes. N=3 for all experiments (R1-3) shown.

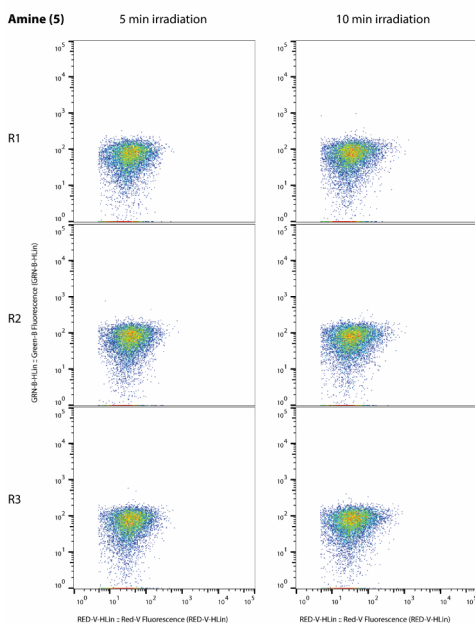




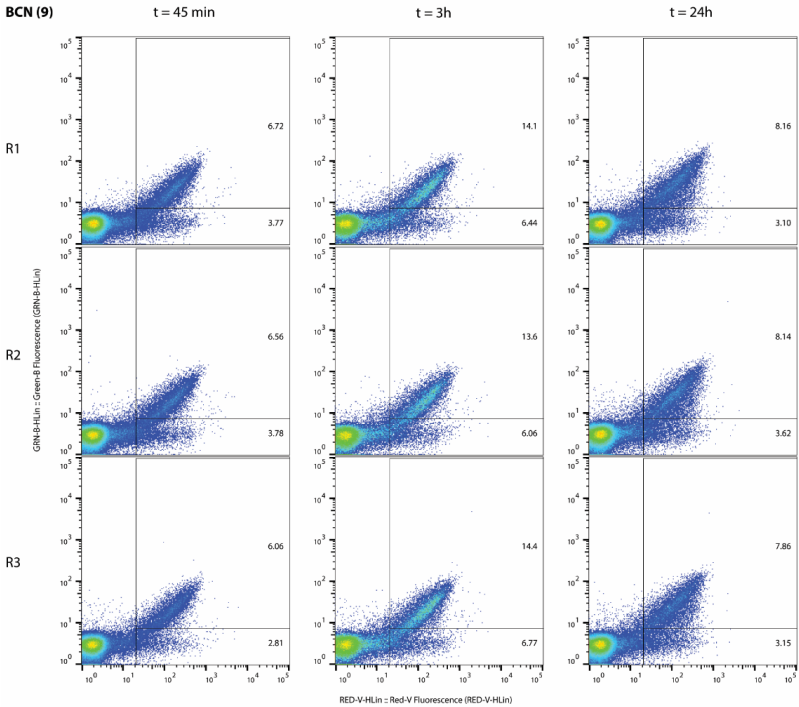
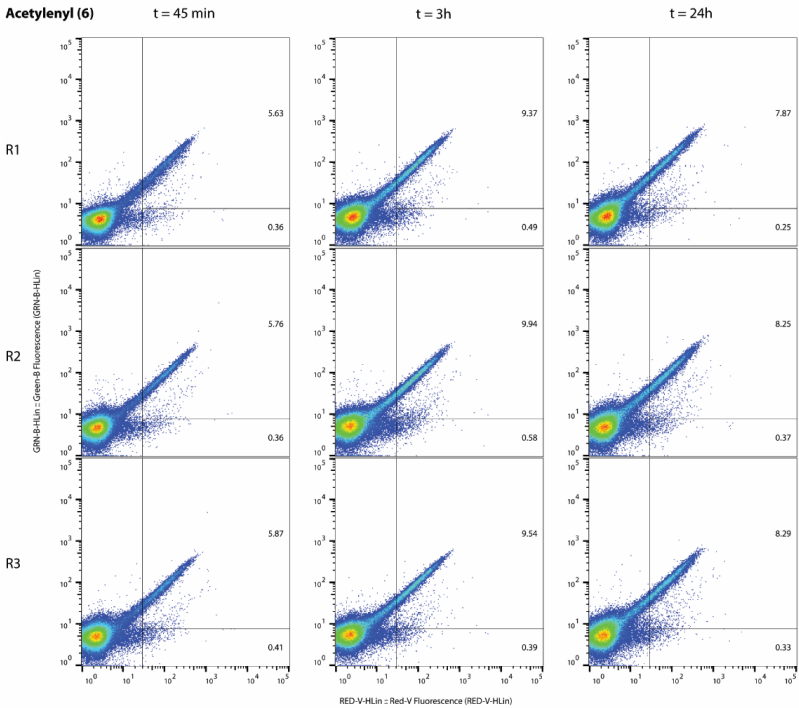
**Figure S6.** Stability assessment of bioorthogonal groups in 2.5 or 250 mM GSH. N=3 for all experiments (R1-3) shown.

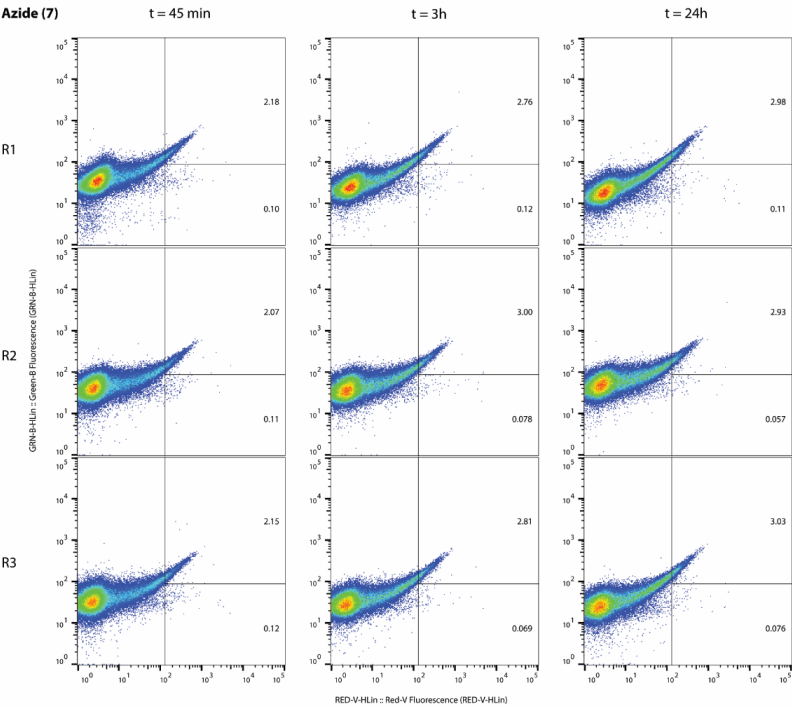
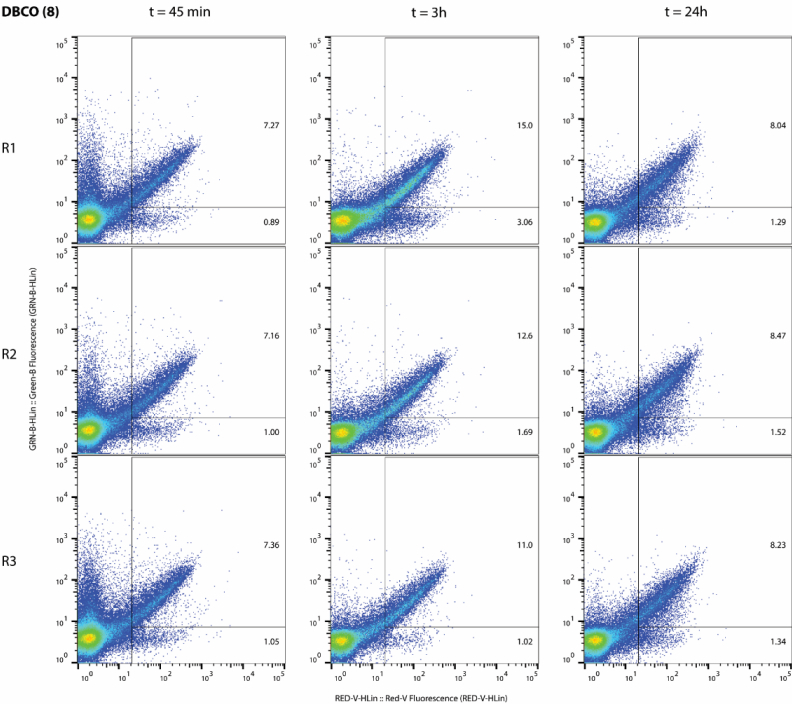


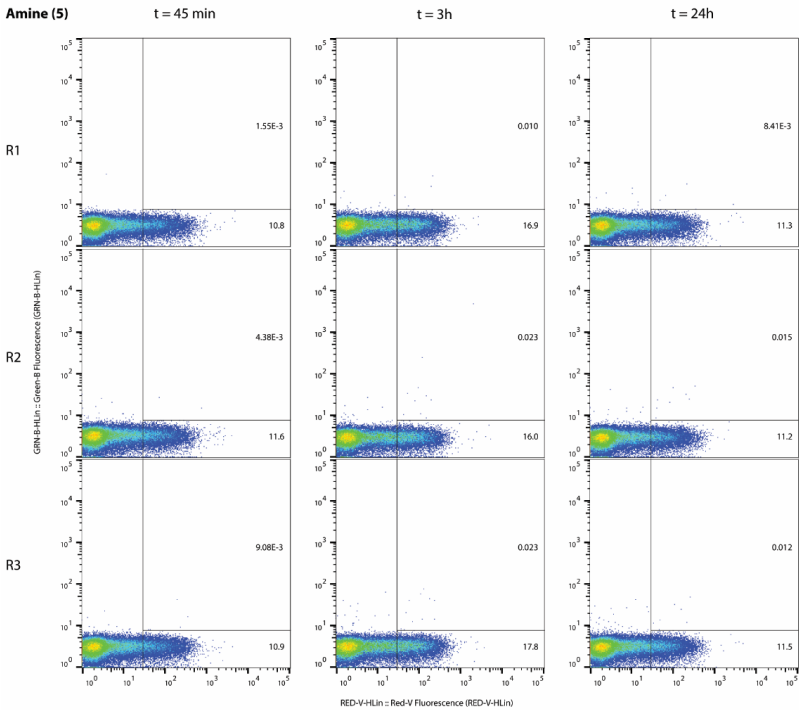




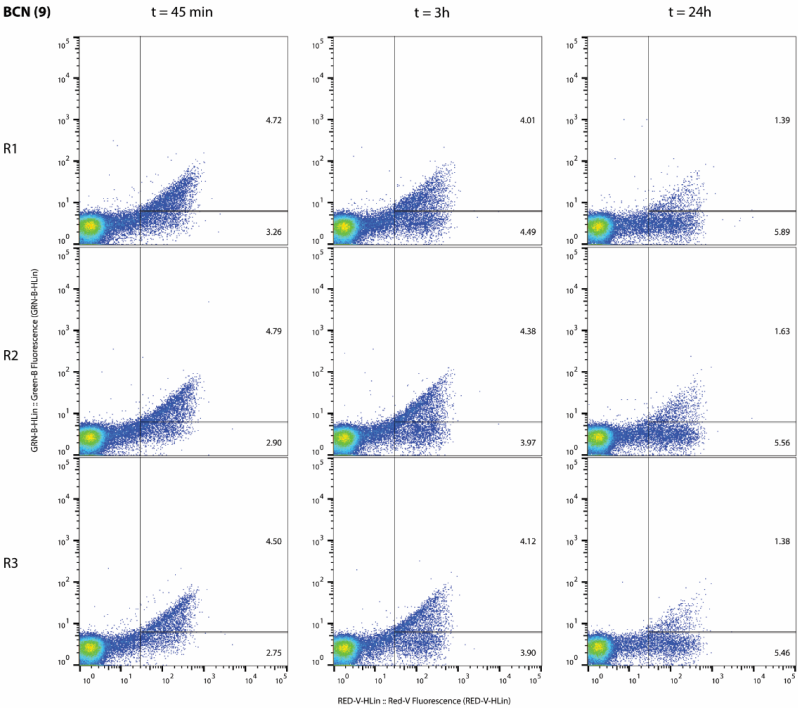
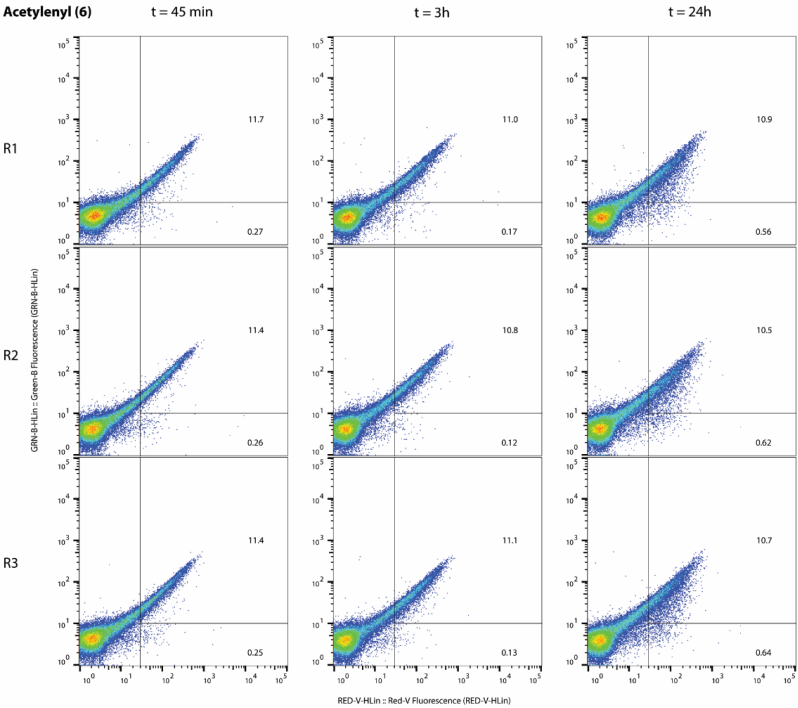
**Figure S7.** Stability assessment of bioorthogonal groups incubated in 25 mM light-activated radical initiator in MeOH/H<sub>2</sub>O (1:3). Samples were exposed to UV-irradiation (280-320 nm, 145  $\mu$ W/cm<sup>2</sup>) for 5 or 10 minutes, followed by incubation totalling 30 minutes including irradiation time N=3 for all experiments shown (R1-3).

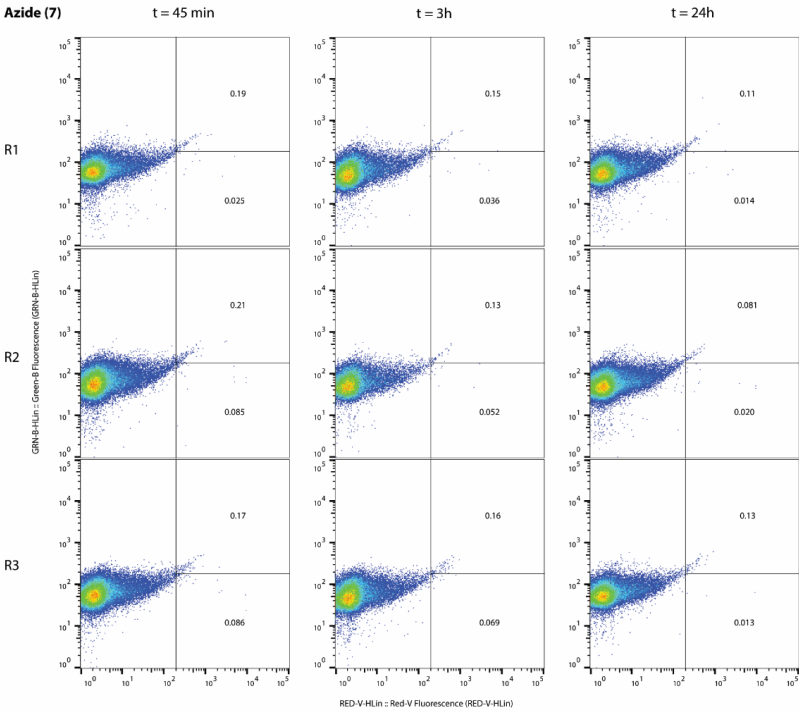
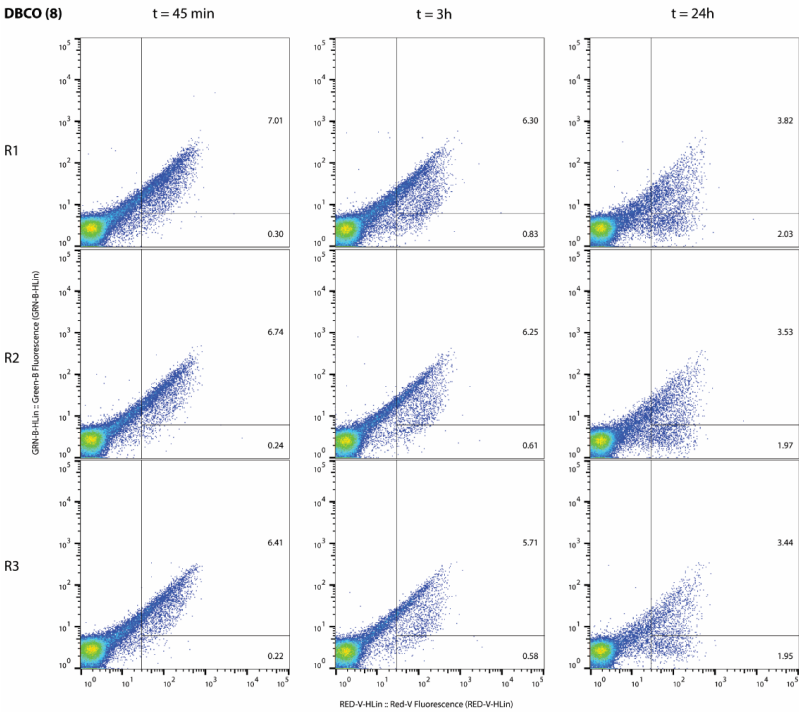


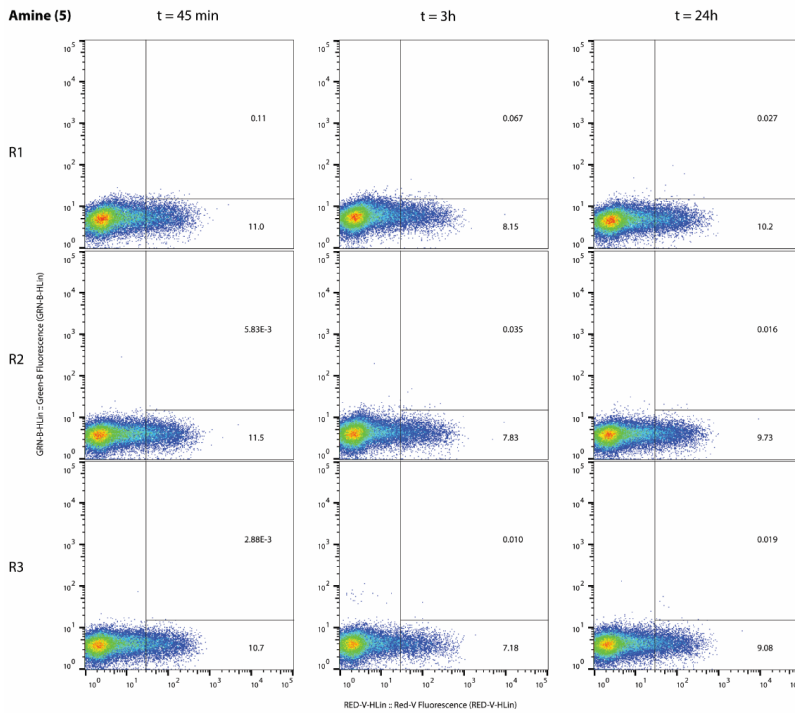




**Figure S8.** Stability assessment of bioorthogonal groups in DC2.4 phagocytic cells. Cells were allowed to take up the bioorthogonal FluoSpheres for 45 minutes ( $t = 45 \text{ min}$ ) followed by a 3 or 24h chase. Two quantification gates were set to exclude cells and debris that had not taken up beads.  $N=3$  for all experiments shown (R1-3).

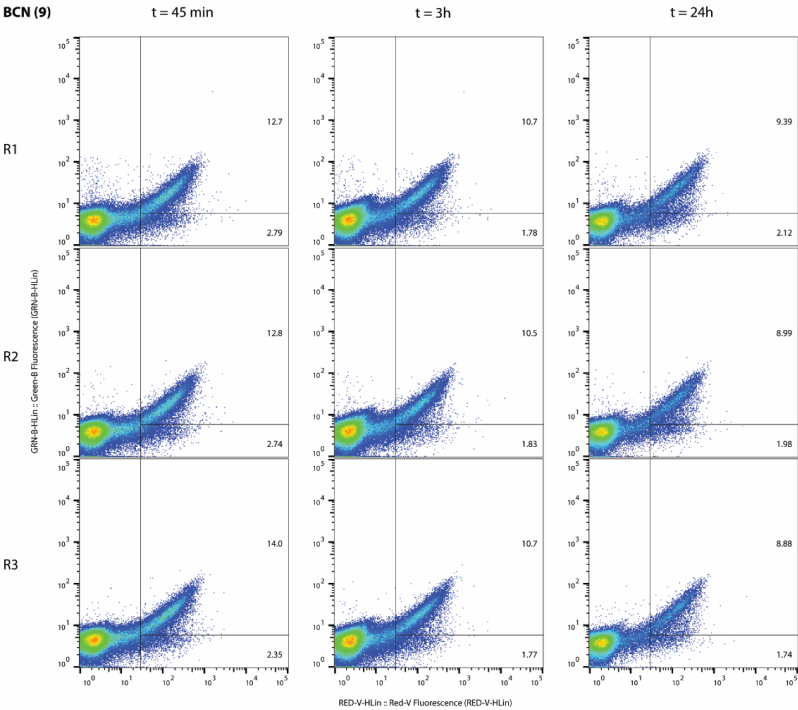
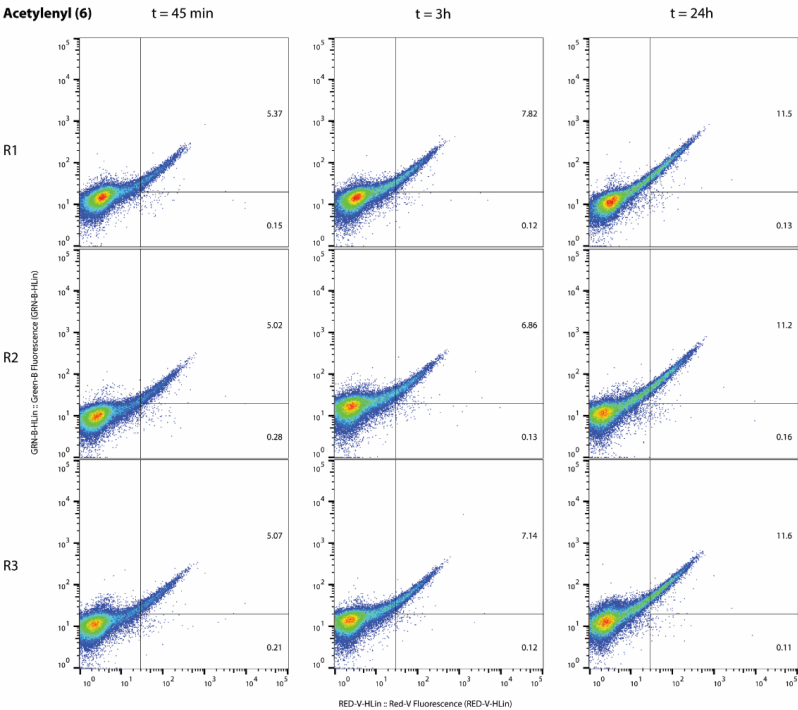


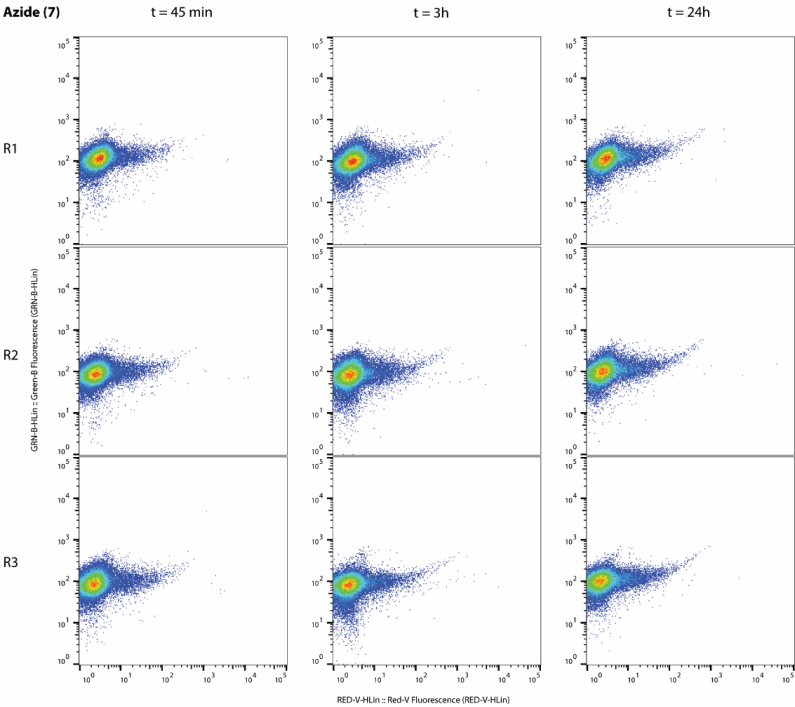
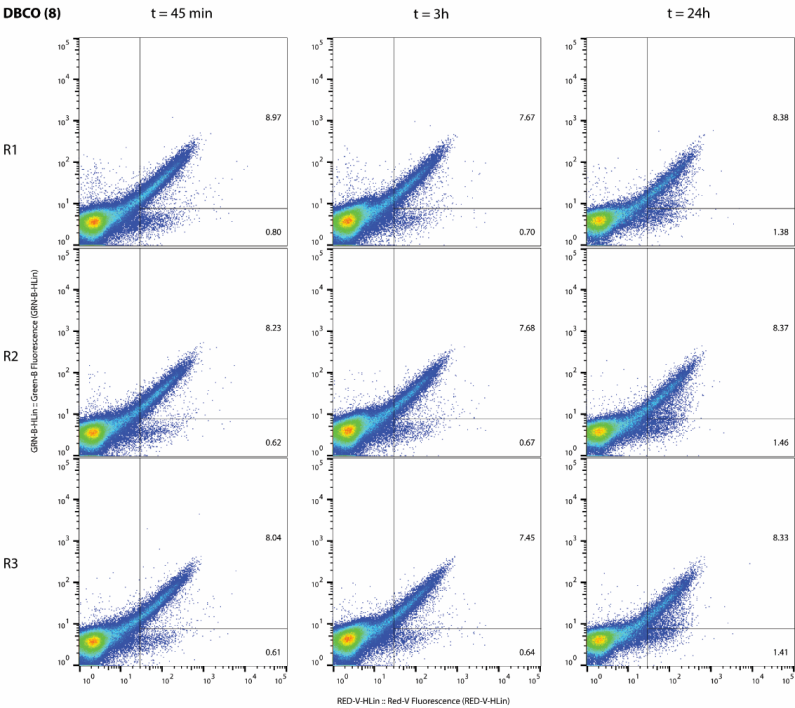


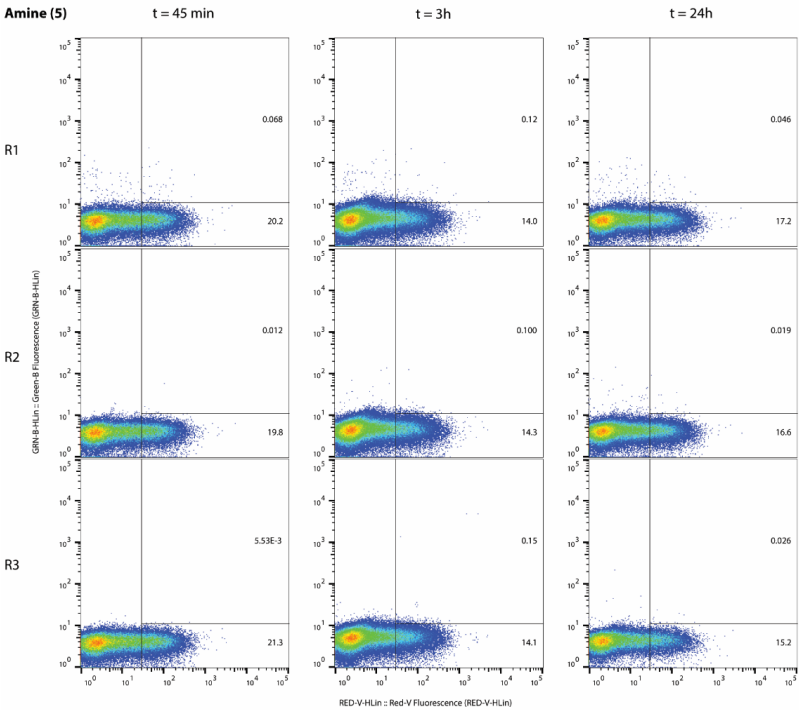


**Figure S9.** Stability assessment of bioorthogonal groups in RAW 264.7 phagocytic cells. Cells were first allowed to take up the bioorthogonal FluoSpheres for 45 minutes ( $t = 45$  min). Cells were then washed and chased 3 or 24 hours. Two quantification gates were set to exclude cells and debris that had not taken up beads.  $N=3$  shown for all experiments (R1-3).

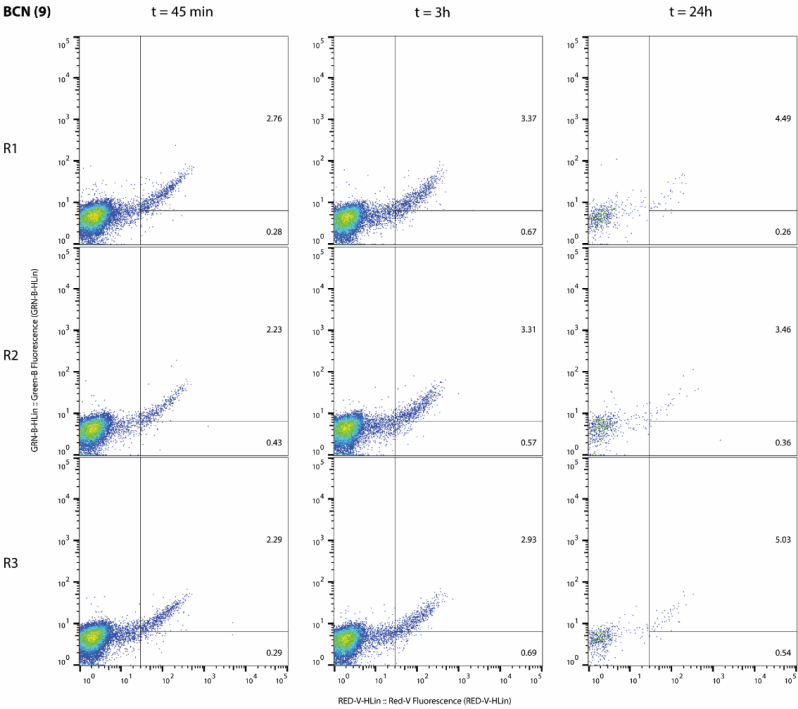
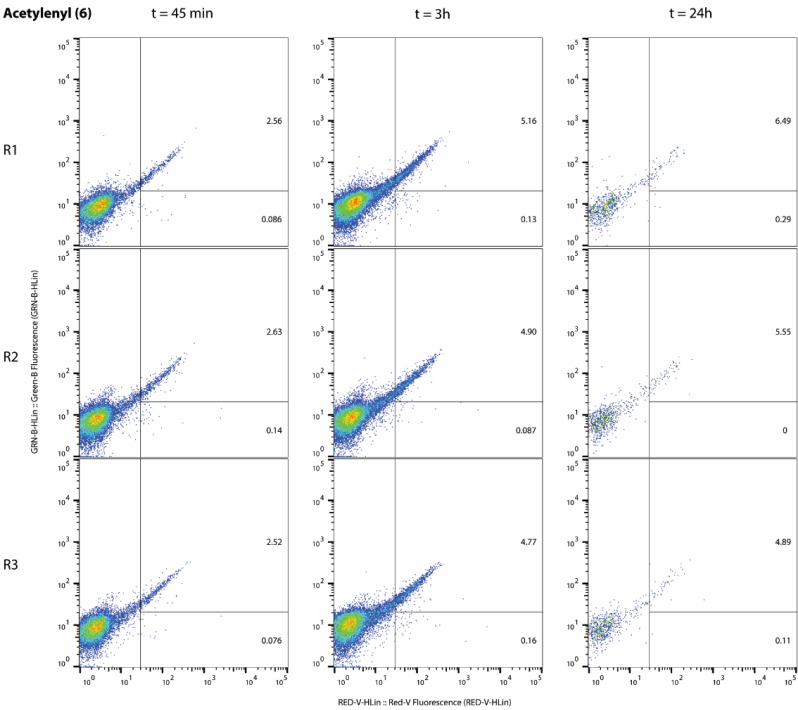


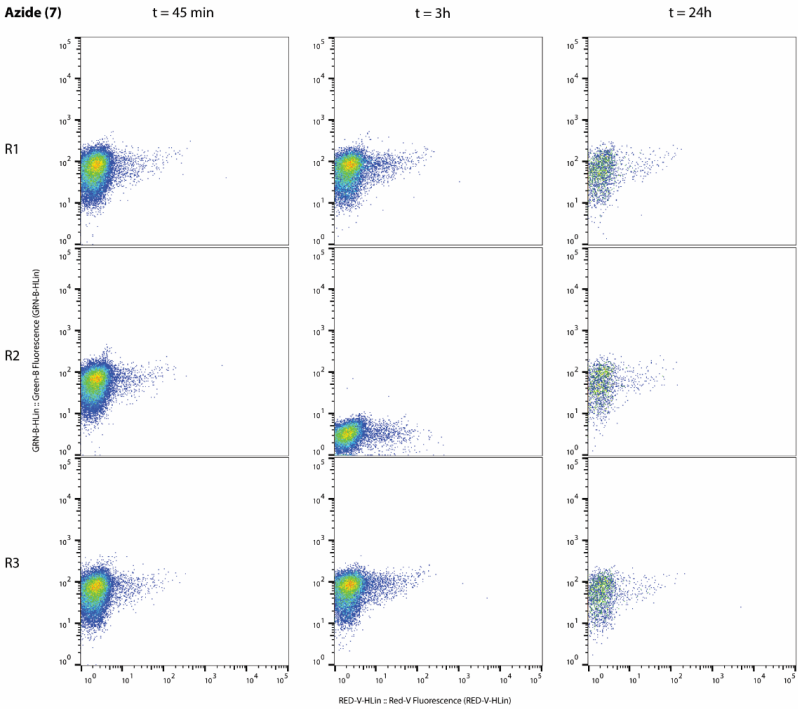
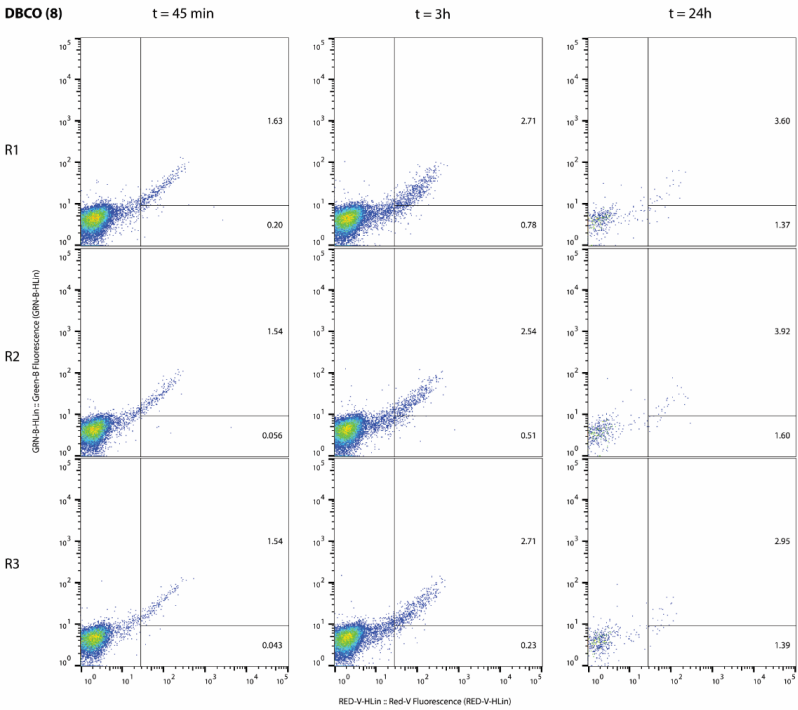


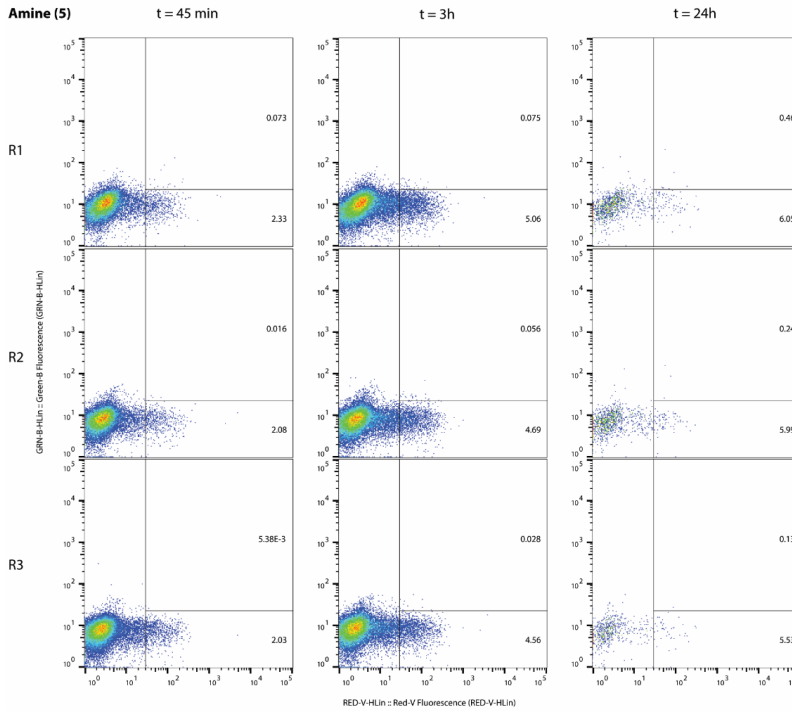




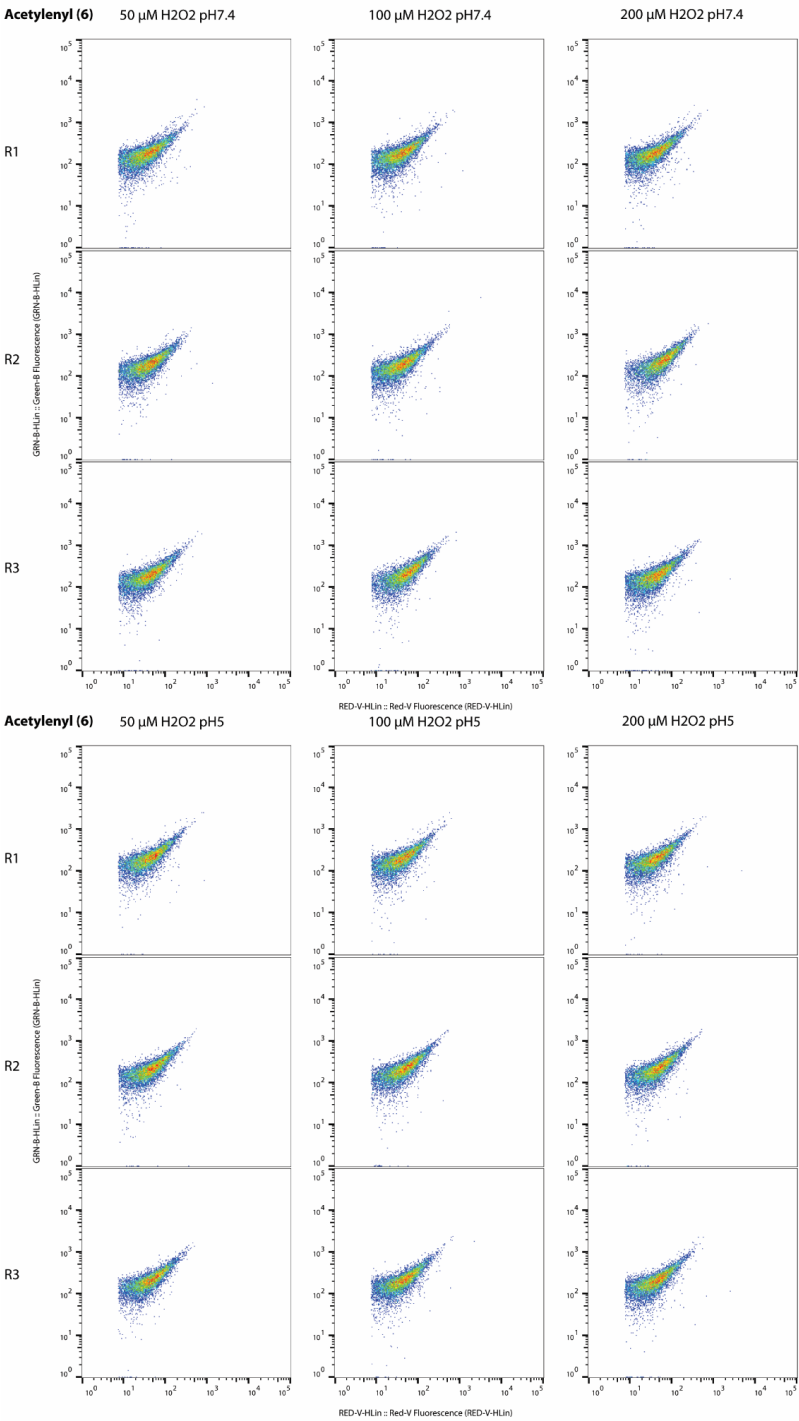
**Figure S10.** Stability assessment of bioorthogonal groups in DC2.4 phagocytic cells stimulated with zymosan and PMA. Cells were pre-stimulated with zymosan and PMA 24 hours before adding the bioorthogonal FluoSpheres as in Figure S8. N=3 shown for all experiments (R1-3).

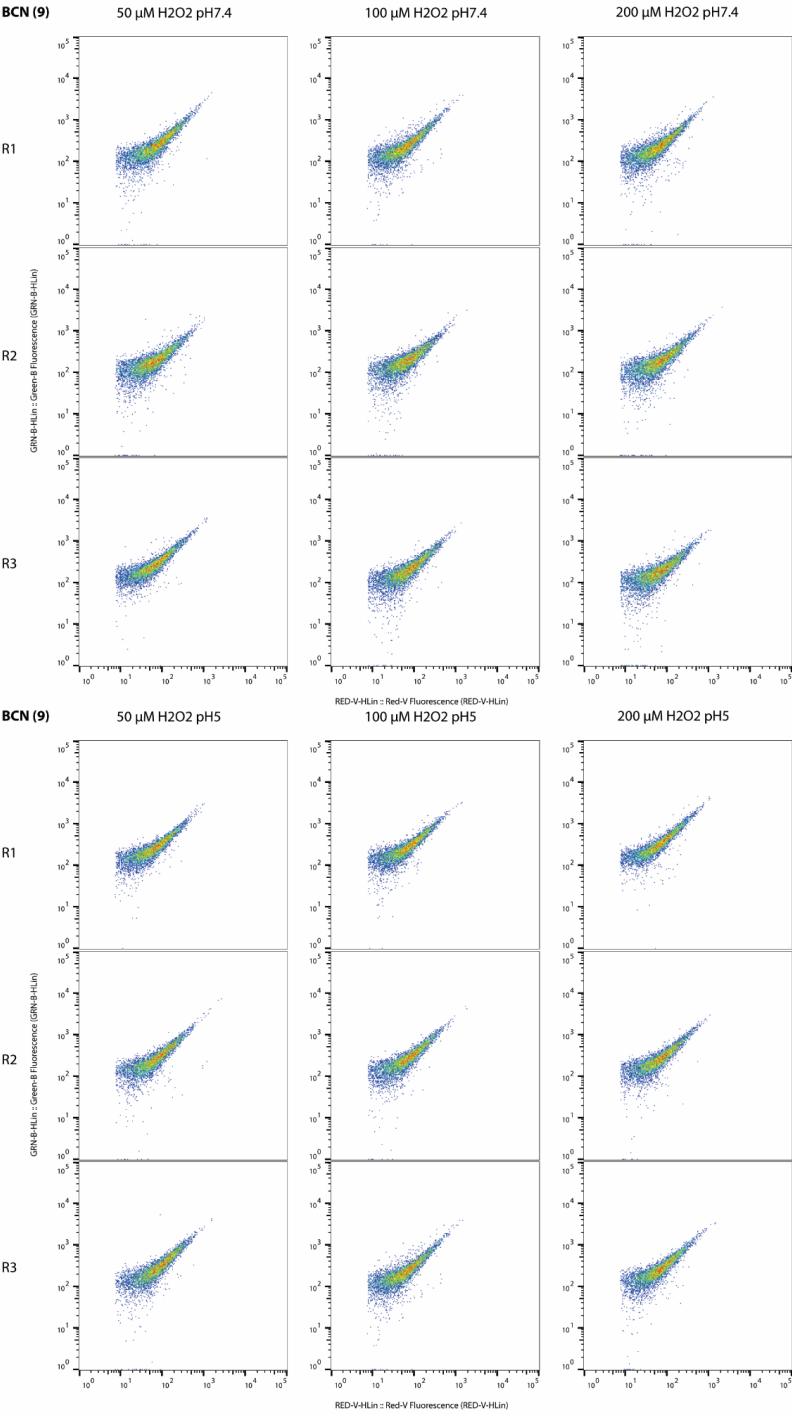




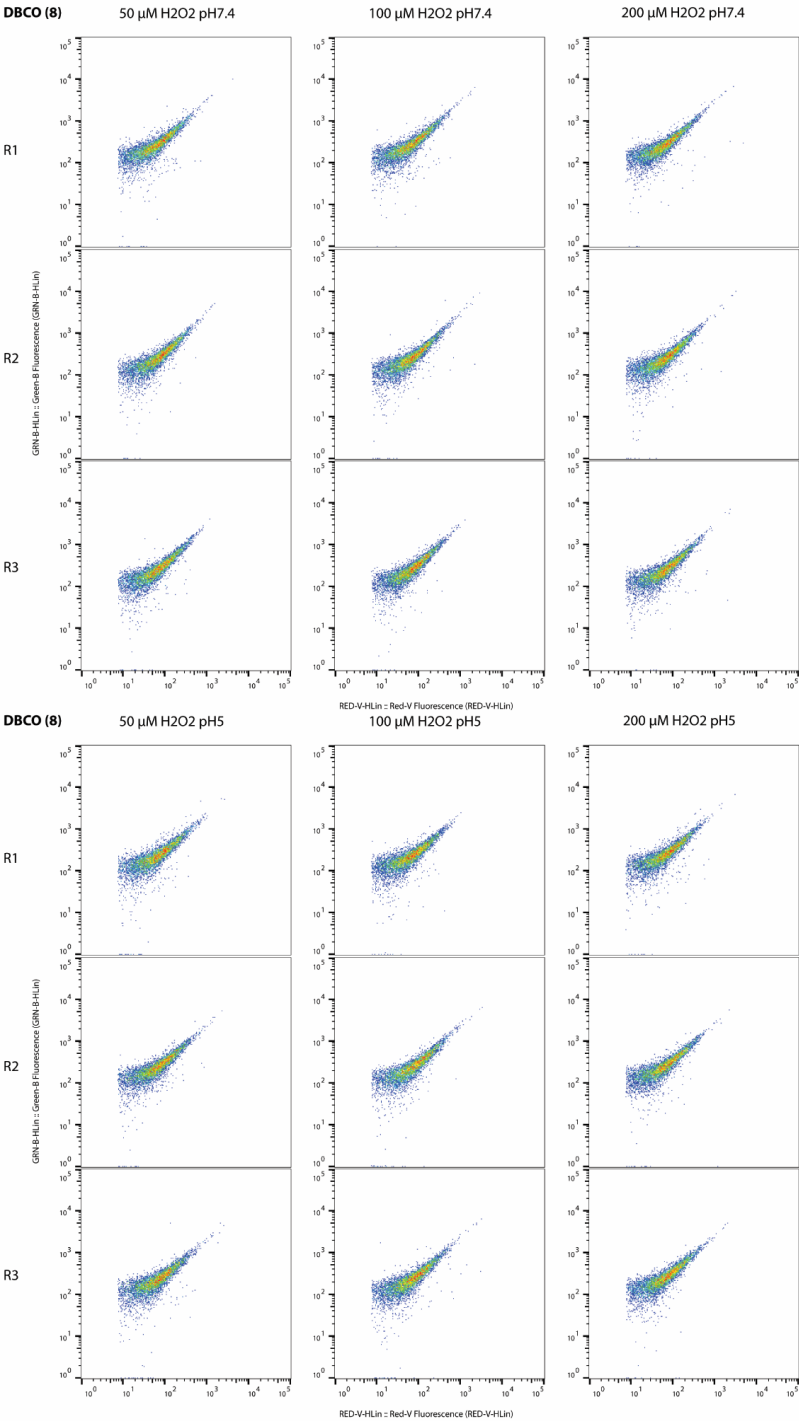


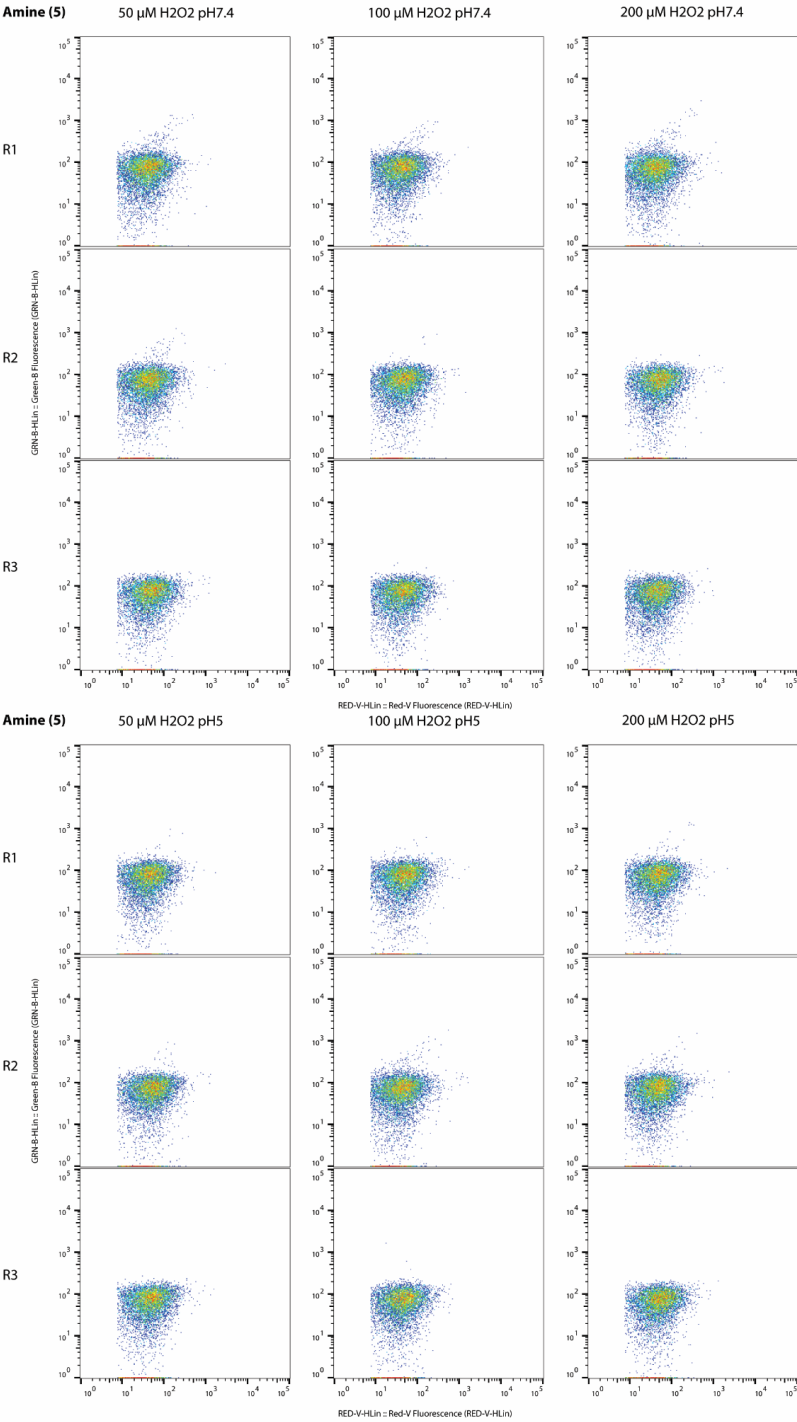
**Figure S11.** Stability assessment of bioorthogonal groups in RAW264.7 phagocytic cells stimulated with zymosan and PMA. Cells were pre-stimulated with zymosan and PMA 24 hours before adding the bioorthogonal FluoSpheres as in Figure S9. N=3 shown for all experiments (R1-3).



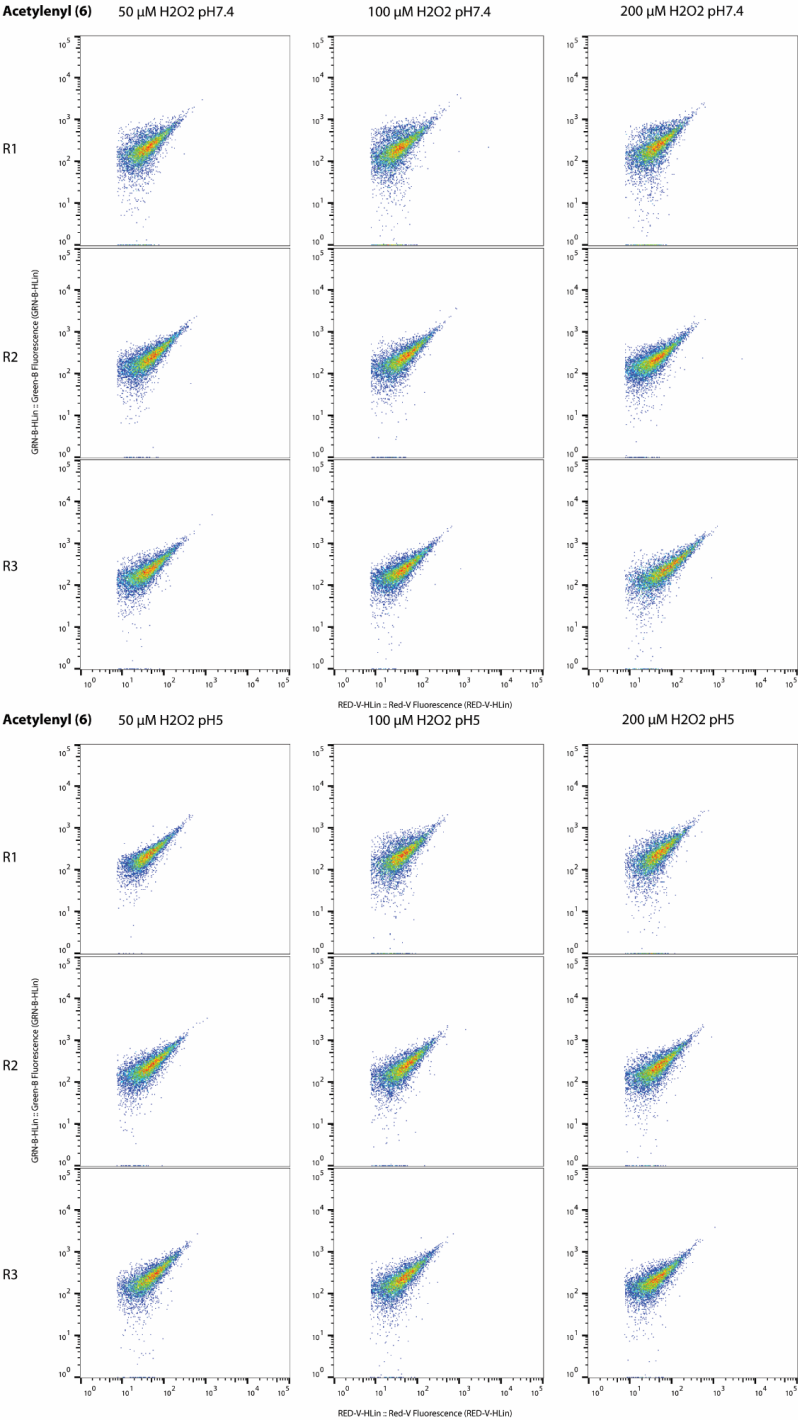


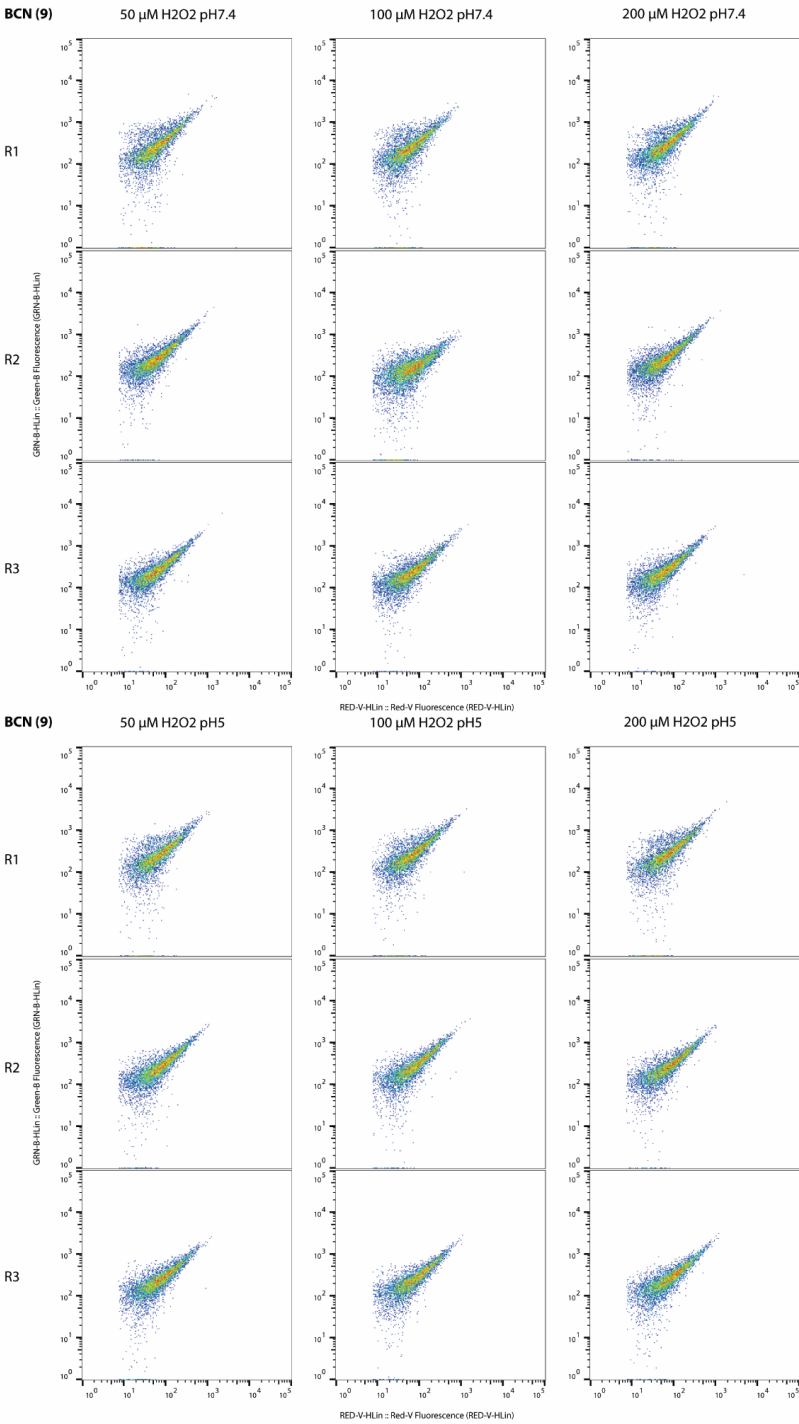


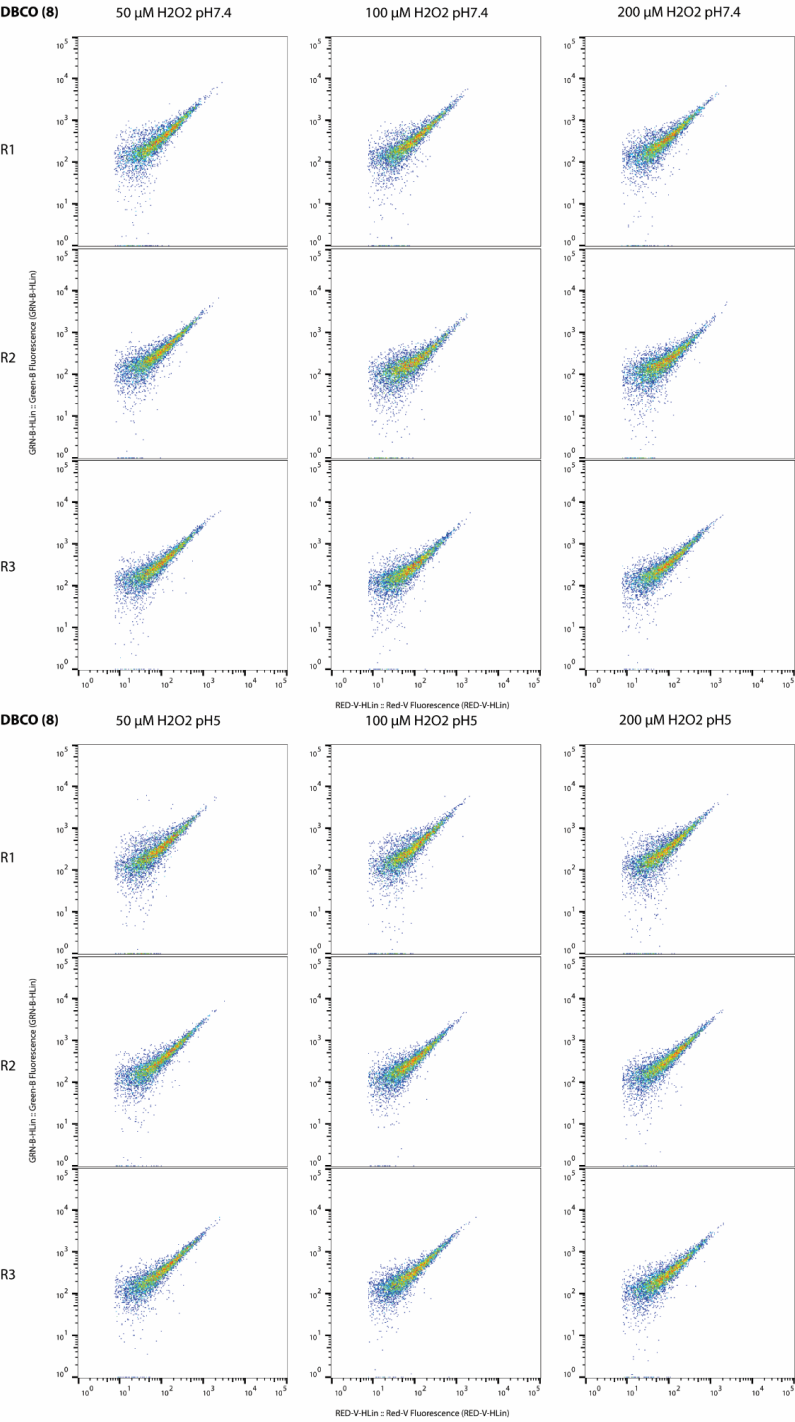


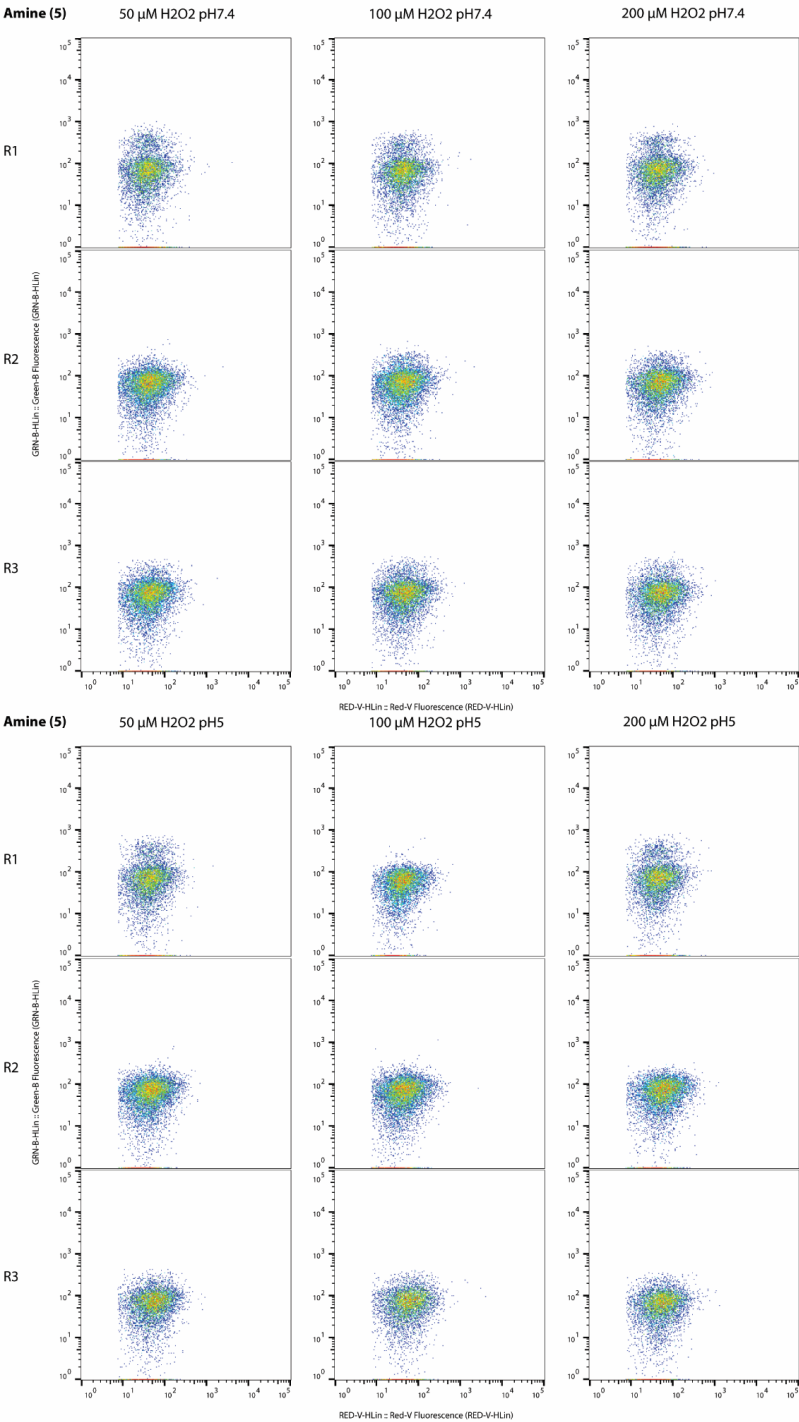


**Figure S12.** Stability assessment of bioorthogonal groups incubated with hydrogen peroxide concentrations of 50, 100 or 200  $\mu\text{M}$  at pH 7.4 or pH 5.0. Samples were incubated in the dark at RT for 30 minutes. N =3 shown for all experiments (R1-3).



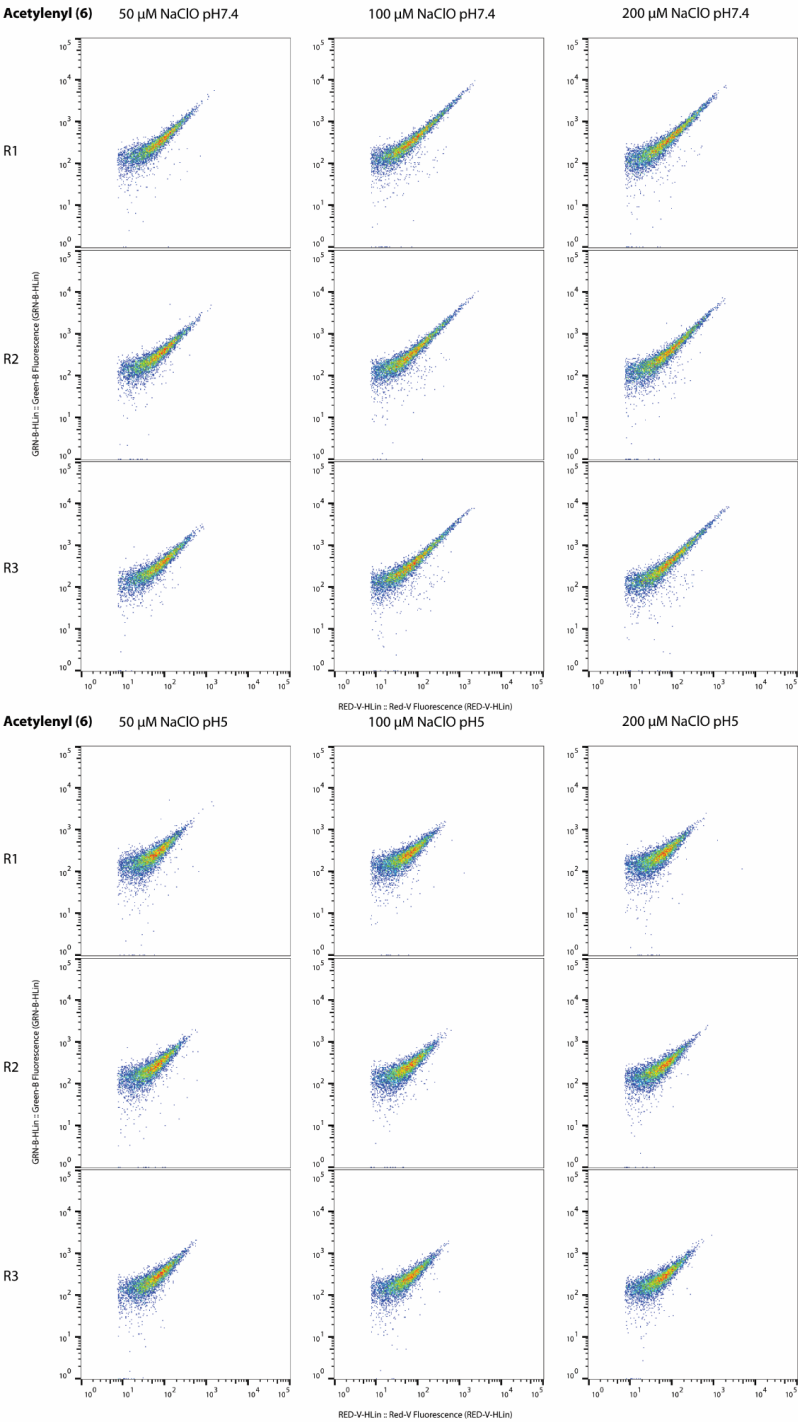


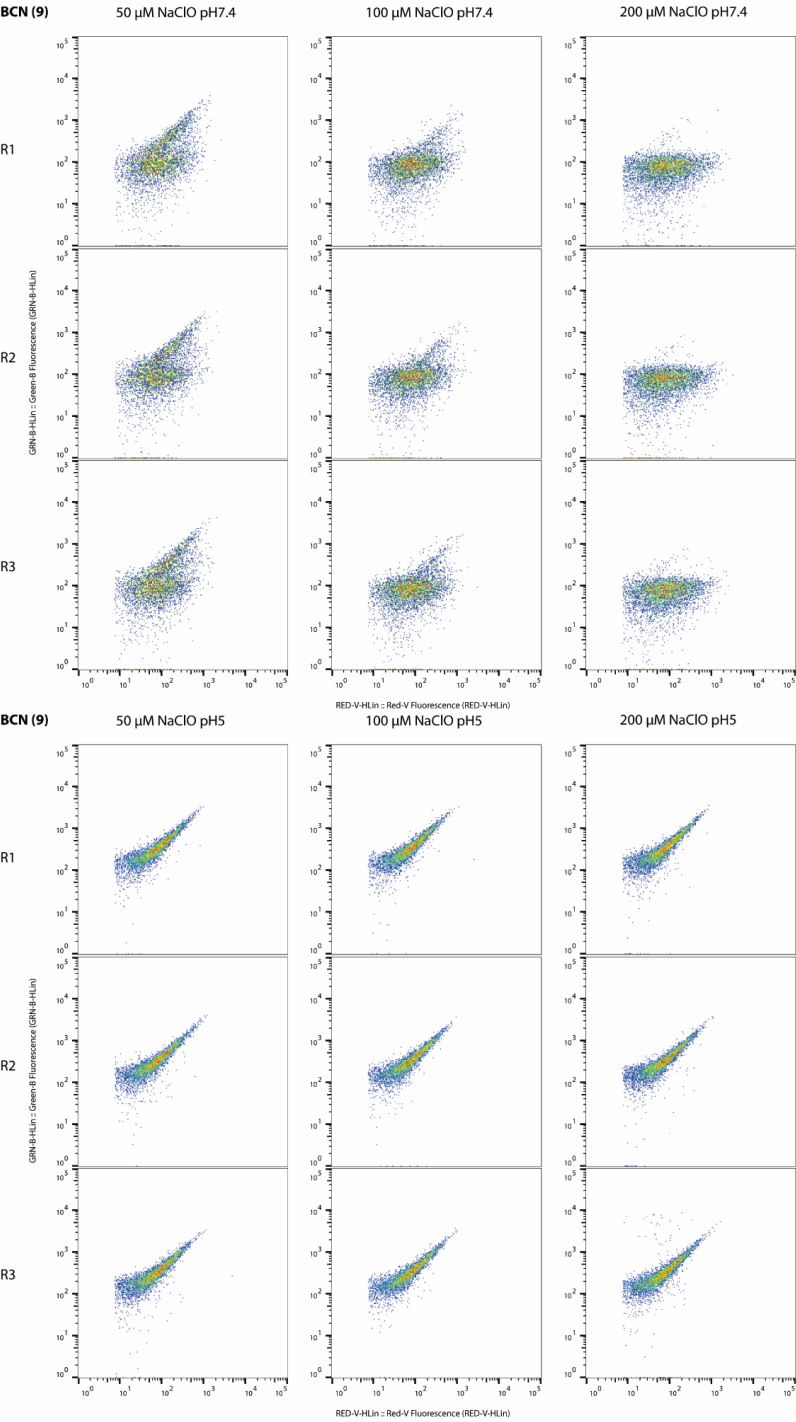


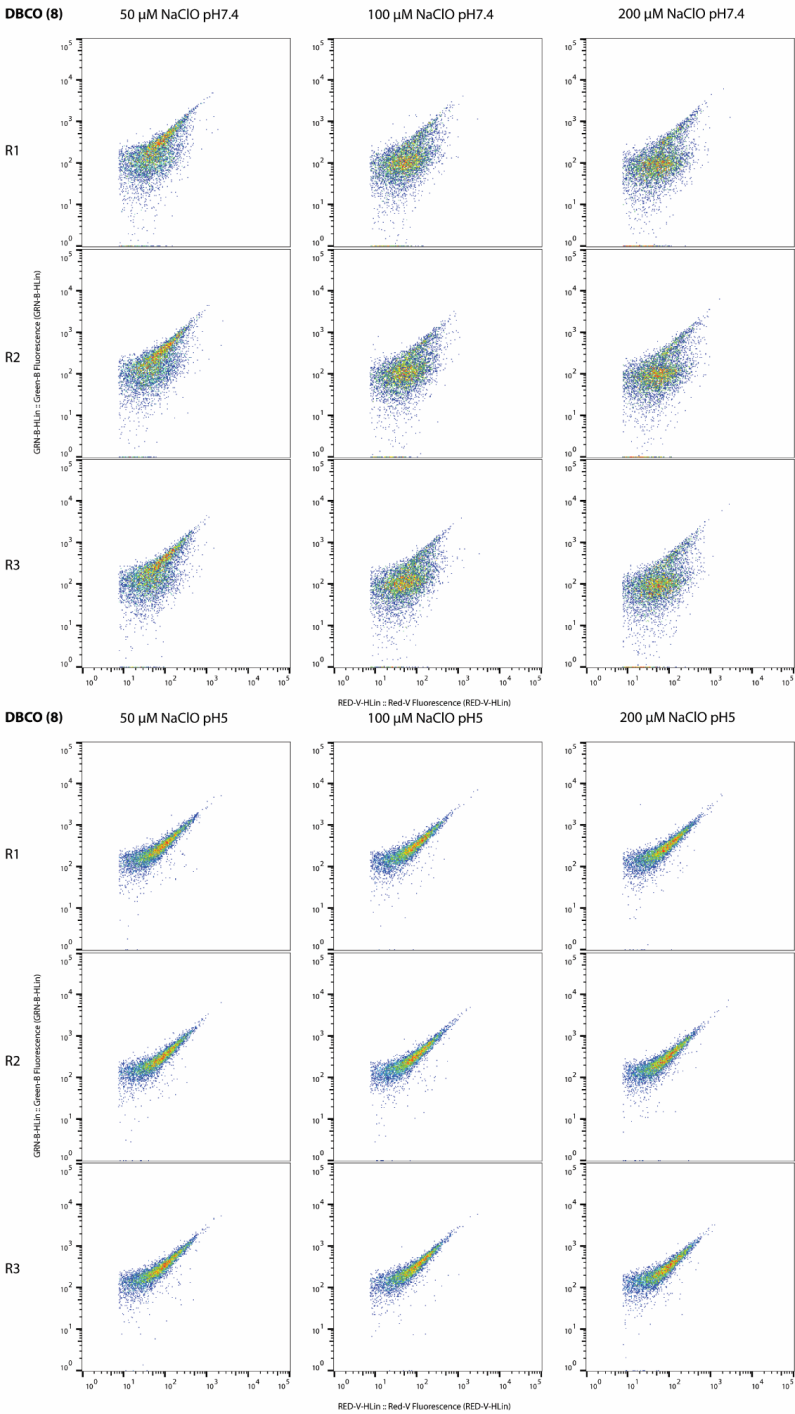


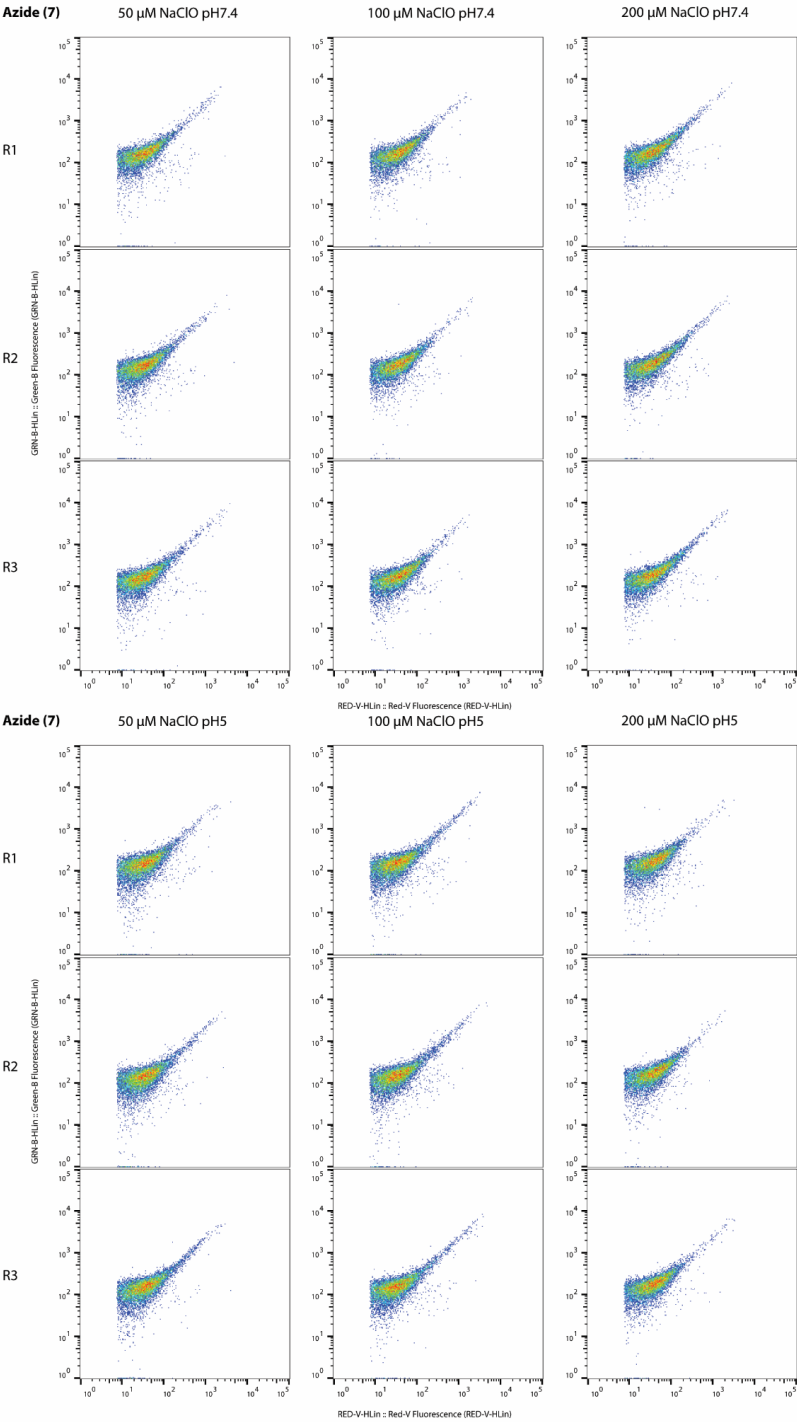
**Figure S13.** Stability assessment of bioorthogonal groups incubated with hydrogen peroxide concentrations of 50, 100 or 200  $\mu\text{M}$  at pH 7.4 or pH 5.0. Samples were exposed to UV-irradiation (280-320 nm, 145  $\mu\text{W}/\text{cm}^2$ ) for 5 minutes, followed by incubation for 30 minutes in total. Due to reduction of both bead- and bioorthogonal fluorescence signal, azide **7** was excluded from analysis in this experiment. N=3 shown for all experiments (R1-3).

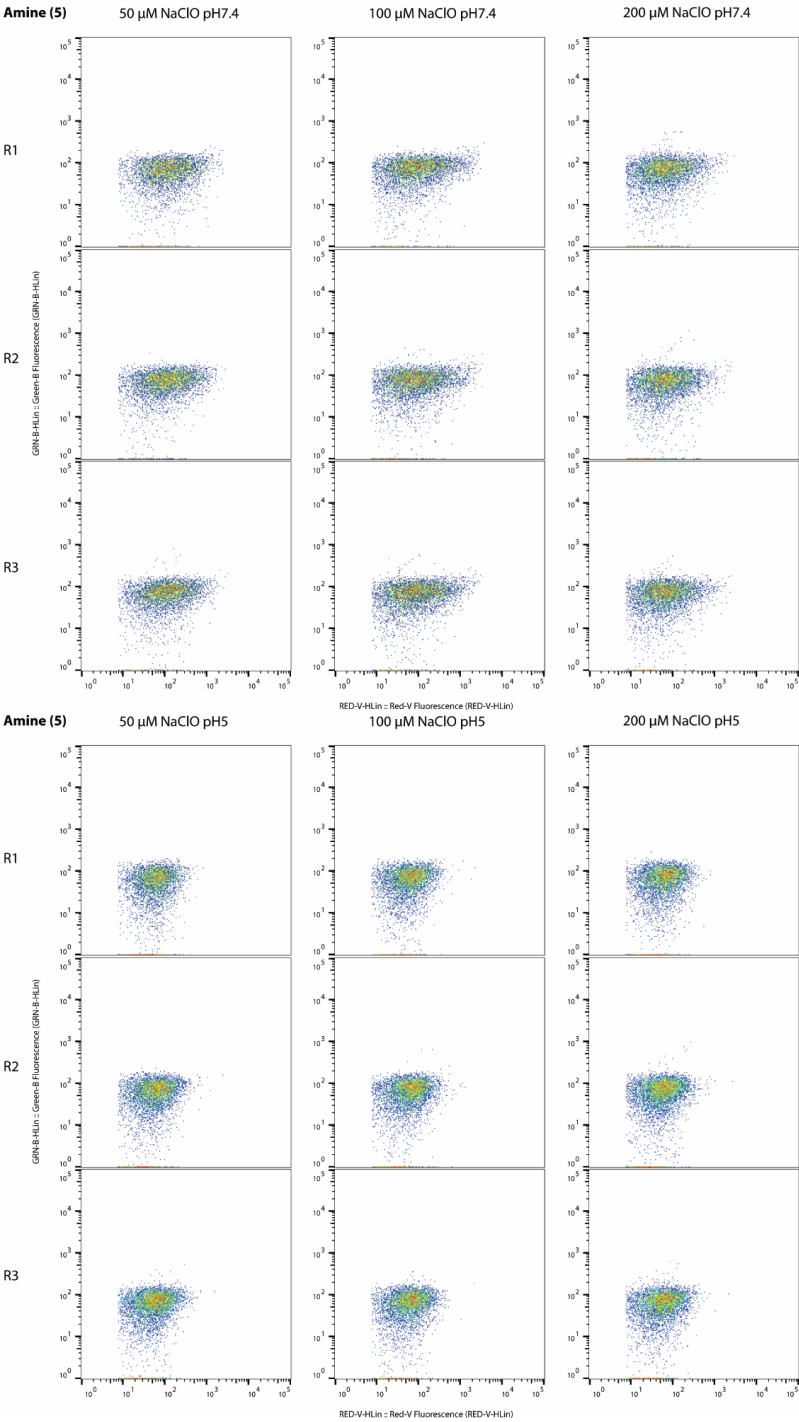




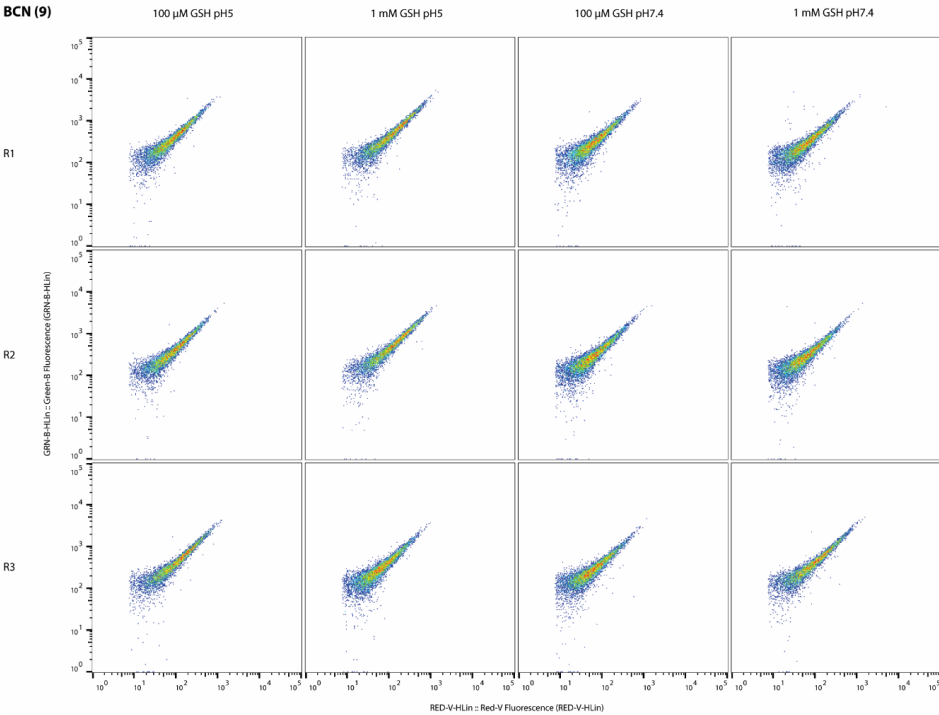
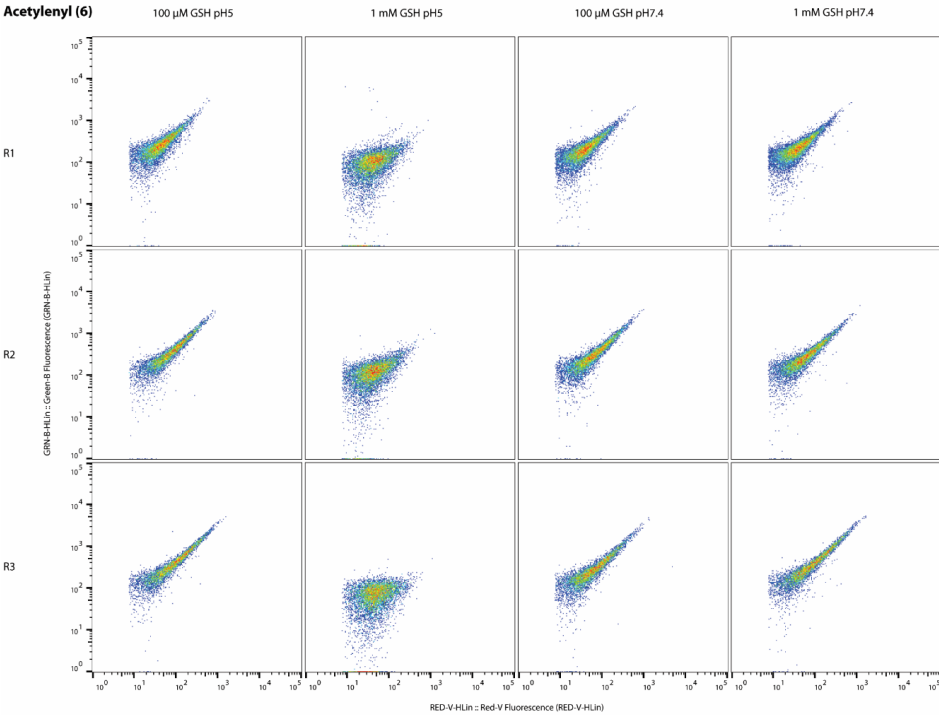


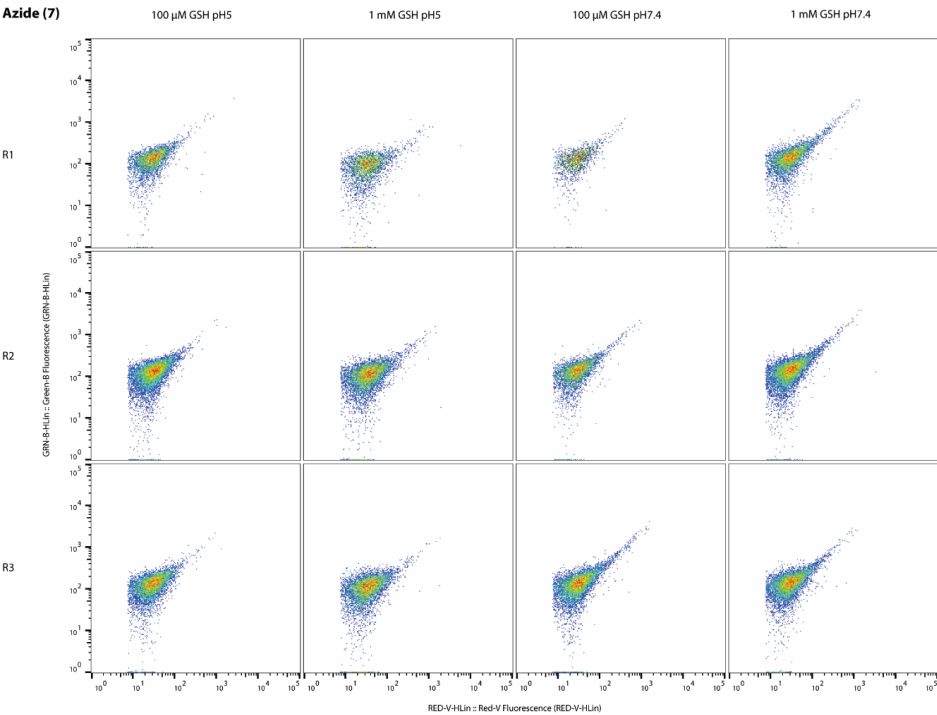
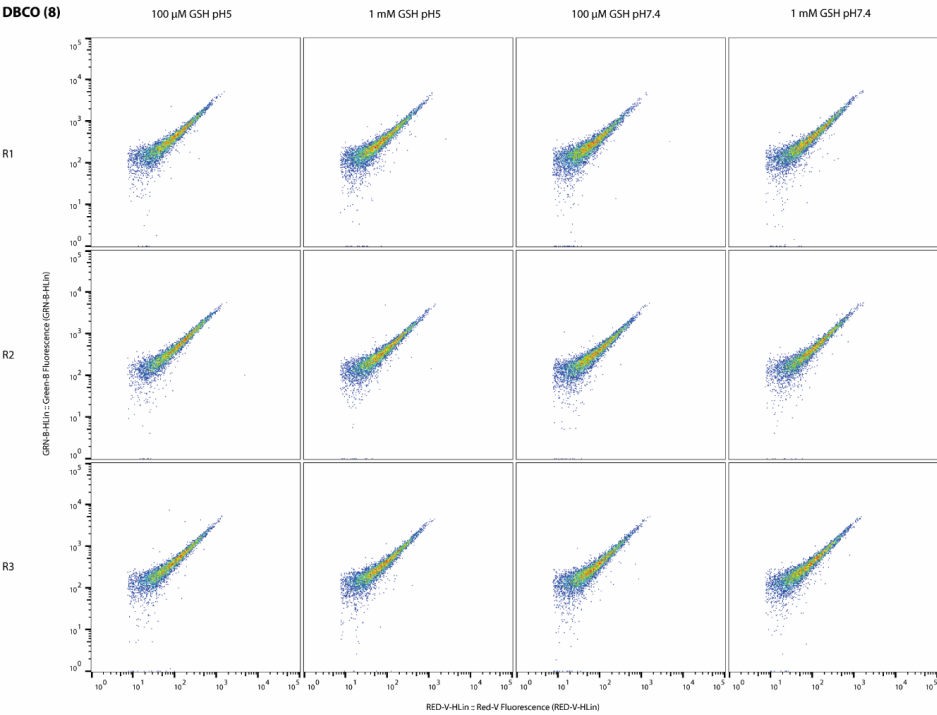






**Figure S14.** Stability assessment of bioorthogonal groups incubated with sodium hypochlorite concentrations of 50, 100 or 200  $\mu$ M at pH 7.4 or 5.0. Samples were incubated at RT for 30 minutes. N=3 for all experiments shown (R1-3).







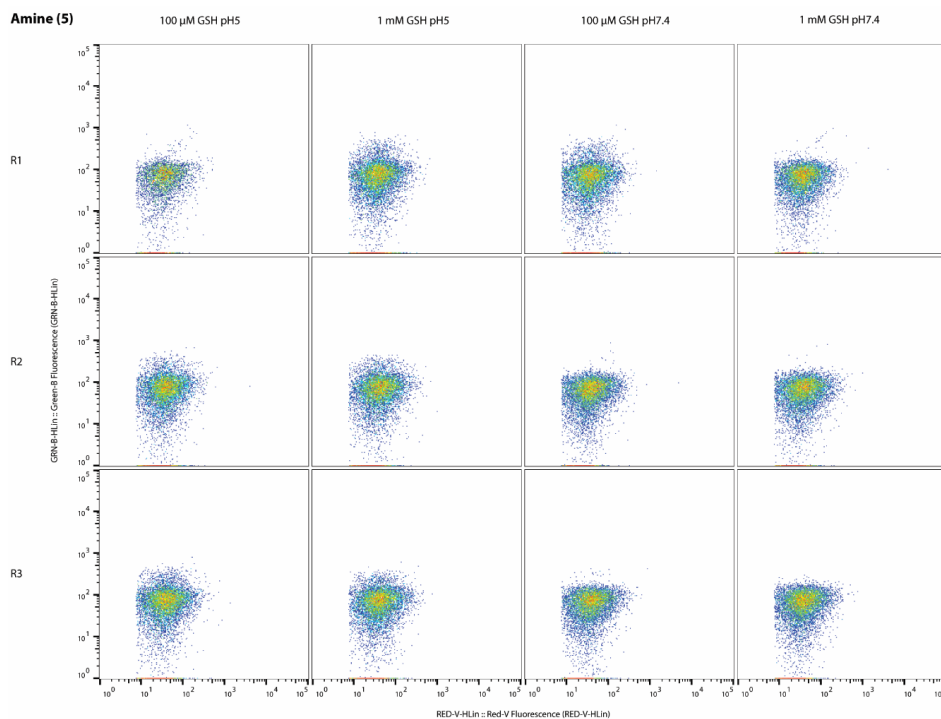


**Figure S15.** Stability assessment of bioorthogonal groups incubated with concentrations of 100  $\mu$ M or 1 mM GSH and 10% light-activated radical initiator at pH 7.4 or pH 5.0. Samples were exposed to UV-irradiation (280-320 nm, 145  $\mu$ W/cm<sup>2</sup>) for 5 minutes, followed by incubation totaling 30 minutes. N=3 shown for all experiments (R1-3).

### 3.6 References

- (1) Sletten, E. M.; Bertozzi, C. R. Bioorthogonal Chemistry: Fishing for Selectivity in a Sea of Functionality. *Angew. Chemie - Int. Ed.* **2009**, *48* (38), 6974–6998.
- (2) McKay, C. S.; Finn, M. G. Click Chemistry in Complex Mixtures: Bioorthogonal Bioconjugation. *Chem. Biol.* **2014**, *21* (9), 1075–1101.
- (3) Saxon, E.; Bertozzi, C. R. Cell Surface Engineering by a Modified Staudinger Reaction. *Science* **2000**, *287* (5460), 2007–2010.
- (4) Yarema, K. J.; Mahal, L. K.; Bruehl, R. E.; Rodriguez, E. C.; Bertozzi, C. R. Metabolic Delivery of Ketone Groups to Sialic Acid Residues. Application to Cell Surface Glycoform Engineering. *J. Biol. Chem.* **1998**, *273* (47), 31168–31179.
- (5) Laughlin, S. T.; Baskin, J. M.; Amacher, S. L.; Bertozzi, C. R. In Vivo Imaging of Membrane-Associated Glycans in Developing Zebrafish. *Science* (80-. ). **2008**, *320* (5876), 664–667.
- (6) Hang, H. C.; Wilson, J. P.; Charron, G. Bioorthogonal Chemical Reporters for Analyzing Protein Lipidation and Lipid Trafficking. *Acc. Chem. Res.* **2011**, *44* (9), 699–708.
- (7) Jao, C. Y.; Salic, A. Exploring RNA Transcription and Turnover in Vivo by Using Click Chemistry. *Proc. Natl. Acad. Sci. U. S. A.* **2008**, *105* (41), 15779–15784.
- (8) Salic, A.; Mitchison, T. J. A Chemical Method for Fast and Sensitive Detection of DNA Synthesis in Vivo. *Proc. Natl. Acad. Sci.* **2008**, *105* (7), 2415–2420.
- (9) Van Hest, J. C. M.; Klück, K. L.; Tirrell, D. A. Efficient Incorporation of Unsaturated Methionine Analogues into Proteins in Vivo. *J. Am. Chem. Soc.* **2000**, *122* (7), 1282–1288.
- (10) Dieterich, D. C.; Link, A. J.; Graumann, J.; Tirrell, D. A.; Schuman, E. M. Selective Identification of Newly Synthesized Proteins in Mammalian Cells Using Bioorthogonal Noncanonical Amino Acid Tagging (BONCAT). *Proc. Natl. Acad. Sci.* **2006**, *103* (25), 9482–9487.
- (11) Siegrist, M. S.; Whiteside, S.; Jewett, J. C.; Aditham, A.; Cava, F.; Bertozzi, C. R. D-Amino Acid Chemical Reporters Reveal Peptidoglycan Dynamics of an Intracellular Pathogen. *ACS Chem. Biol.* **2013**, *8* (3), 500–505.
- (12) Siegrist, S. M.; Aditham, A. K.; Espaillet, A.; Cameron, T. A.; Whiteside, S. A.; Cava, F.; Portnoy, D. A.; Bertozzi, C. R. Host Actin Polymerization Tunes the Cell Division Cycle of an Intracellular Pathogen. *Cell Rep.* **2015**, *11* (4), 499–507.
- (13) van Elsland, D. M.; Bos, E.; de Boer, W.; Overkleeft, H. S.; Koster, A. J.; van Kasteren, S. I. Detection of Bioorthogonal Groups by Correlative Light and Electron Microscopy Allows Imaging of Degraded Bacteria in Phagocytes. *Chem. Sci.* **2016**, *7* (1), 752–758.
- (14) van Elsland, D. M.; van Kasteren, S. I. Imaging Bioorthogonal Groups in Their Ultrastructural Context with Electron Microscopy. *Angew. Chemie - Int. Ed.* **2016**, *55* (33), 9472–9473.
- (15) Pawlak, J. B.; Hos, B. J.; Van De Graaff, M. J.; Megantari, O. A.; Meeuwenoord, N.; Overkleeft, H. S.; Filippov, D. V.; Ossendorp, F.; Van Kasteren, S. I. The Optimization of Bioorthogonal Epitope Ligation within MHC-I Complexes. *ACS Chem. Biol.* **2016**, *11*, 3172–3178.
- (16) Pawlak, J. B.; Gential, G. P. P.; Ruckwardt, T. J.; Bremmers, J. S.; Meeuwenoord, N. J.; Ossendorp, F. A.; Overkleeft, H. S.; Filippov, D. V.; Van Kasteren, S. I. Bioorthogonal Deprotection on the Dendritic Cell Surface for Chemical Control of Antigen Cross-Presentation. *Angew. Chemie - Int. Ed.* **2015**, *54* (19), 5628–5631.
- (17) Flannagan, R. S.; Cosío, G.; Grinstein, S. Antimicrobial Mechanisms of Phagocytes and Bacterial Evasion Strategies. *Nat. Rev. Microbiol.* **2009**, *7* (5), 355–366.
- (18) Fang, F. C. Antimicrobial Actions of Reactive Oxygen Species. *MBio* **2011**, *2* (5), 1–6.
- (19) Winterbourn, C. C.; Hampton, M. B.; Livesey, J. H.; Kettle, A. J. Modeling the Reactions

- of Superoxide and Myeloperoxidase in the Neutrophil Phagosome: Implications for Microbial Killing. *J. Biol. Chem.* **2006**, *281* (52), 39860–39869.
- (20) Xiong, Q.; Tezuka, Y.; Kaneko, T.; Li, H.; Tran, L. Q.; Hase, K.; Namba, T.; Kadota, S. Inhibition of Nitric Oxide by Phenylethanoids in Activated Macrophages. *Eur. J. Pharmacol.* **2000**, *400* (1), 137–144.
- (21) Slauch, J. M. How Does the Oxidative Burst of Macrophages Kill Bacteria? Still an Open Question. *Mol. Microbiol.* **2011**, *80* (3), 580–583.
- (22) Furtmüller, P. G.; Obinger, C.; Hsuanyu, Y.; Dunford, H. B. Mechanism of Reaction of Myeloperoxidase with Hydrogen Peroxide and Chloride Ion. *Eur. J. Biochem.* **2000**, *267* (19), 5858–5864.
- (23) Klebanoff, S. J.; Kettle, A. J.; Rosen, H.; Winterbourn, C. C.; Nauseef, W. M. Myeloperoxidase: A Front-Line Defender against Phagocytosed Microorganisms. *J. Leukoc. Biol.* **2013**, *93* (2), 185–198.
- (24) Ohkuma, S.; Poole, B. Fluorescence Probe Measurement of the Intralysosomal PH in Living Cells and the Perturbation of PH by Various Agents. *Proc. Natl. Acad. Sci.* **1978**, *75* (7), 3327–3331.
- (25) Arunachalam, B.; Phan, U. T.; Geuze, H. J.; Cresswell, P. Enzymatic Reduction of Disulfide Bonds in Lysosomes: Characterization of a Gamma-Interferon-Inducible Lysosomal Thiol Reductase (GILT). *Proc. Natl. Acad. Sci. U. S. A.* **2000**, *97* (2), 745–750.
- (26) Stoka, V.; Turk, V.; Turk, B. Lysosomal Cathepsins and Their Regulation in Aging and Neurodegeneration. *Ageing Res. Rev.* **2016**, *32*, 22–37.
- (27) Turk, V.; Stoka, V.; Vasiljeva, O.; Renko, M.; Sun, T.; Turk, B.; Turk, D. Cysteine Cathepsins: From Structure, Function and Regulation to New Frontiers. *Biochim. Biophys. Acta - Proteins Proteomics* **2012**, *1824* (1), 68–88.
- (28) Balce, D. R.; Yates, R. M. Redox-Sensitive Probes for the Measurement of Redox Chemistries within Phagosomes of Macrophages and Dendritic Cells. *Redox Biol.* **2013**, *1* (1), 467–474.
- (29) Zhang, X. X.; Wang, Z.; Yue, X.; Ma, Y.; Kiesewetter, D. O.; Chen, X. PH-Sensitive Fluorescent Dyes: Are They Really Ph-Sensitive in Cells? *Mol. Pharm.* **2013**, *10* (5), 1910–1917.
- (30) Shieh, P.; Siegrist, M. S.; Cullen, A. J.; Bertozzi, C. R. Imaging Bacterial Peptidoglycan with Near-Infrared Fluorogenic Azide Probes. *Proc. Natl. Acad. Sci.* **2014**, *111* (15), 5456–5461.
- (31) Liechti, G. W.; Kuru, E.; Hall, E.; Kalinda, A.; Brun, Y. V.; Vannieuwenhze, M.; Maurelli, A. T. A New Metabolic Cell-Wall Labelling Method Reveals Peptidoglycan in Chlamydia Trachomatis. *Nature* **2014**, *506* (7489), 507–510.
- (32) Lo Conte, M.; Staderini, S.; Marra, A.; Sanchez-Navarro, M.; Davis, B. G.; Dondoni, A. Multi-Molecule Reaction of Serum Albumin Can Occur through Thiol-Yne Coupling. *Chem. Commun.* **2011**, *47* (39), 11086.
- (33) Ekkebus, R.; Van Kasteren, S. I.; Kulathu, Y.; Scholten, A.; Berlin, I.; Geurink, P. P.; De Jong, A.; Goerdayal, S.; Neefjes, J.; Heck, A. J. R.; Komander, D.; Ovaa, H. On Terminal Alkynes That Can React with Active-Site Cysteine Nucleophiles in Proteases. *J. Am. Chem. Soc.* **2013**, *135* (8), 2867–2870.
- (34) Sommer, S.; Weikart, N. D.; Linne, U.; Mootz, H. D. Covalent Inhibition of SUMO and Ubiquitin-Specific Cysteine Proteases by an in Situ Thiol-Alkyne Addition. *Bioorganic Med. Chem.* **2013**, *21* (9), 2511–2517.
- (35) Tian, H.; Sakmar, T. P.; Huber, T. A Simple Method for Enhancing the Bioorthogonality of Cyclooctyne Reagent. *Chem. Commun.* **2016**, *52* (31), 5451–5454.
- (36) Jiang, X.; Yu, Y.; Chen, J.; Zhao, M.; Chen, H.; Song, X.; Matzuk, A. J.; Carroll, S. L.; Tan, X.; Sizovs, A.; Cheng, N.; Wang, M. C.; Wang, J. Quantitative Imaging of Glutathione in Live Cells Using a Reversible Reaction-Based Ratiometric Fluorescent Probe. *ACS Chem.*

- Biol.* **2015**, *10* (3), 864–874.
- (37) Murrey, H. E.; Judkins, J. C.; Am Ende, C. W.; Ballard, T. E.; Fang, Y.; Riccardi, K.; Di, L.; Guilmette, E. R.; Schwartz, J. W.; Fox, J. M.; Johnson, D. S. Systematic Evaluation of Bioorthogonal Reactions in Live Cells with Clickable HaloTag Ligands: Implications for Intracellular Imaging. *J. Am. Chem. Soc.* **2015**, *137* (35), 11461–11475.
- (38) Beatty, K. E.; Fisk, J. D.; Smart, B. P.; Lu, Y. Y.; Szychowski, J.; Hangauer, M. J.; Baskin, J. M.; Bertozzi, C. R.; Tirrell, D. A. Live-Cell Imaging of Cellular Proteins by a Strain-Promoted Azide-Alkyne Cycloaddition. *ChemBioChem* **2010**, *11* (15), 2092–2095.
- (39) Hume, D. A. Macrophages as APC and the Dendritic Cell Myth. *J. Immunol.* **2008**, *181* (9), 5829–5835.
- (40) Vono, M.; Lin, A.; Norrby-Teglund, A.; Koup, R. A.; Liang, F.; Loré, K. Neutrophils Acquire the Capacity for Antigen Presentation to Memory CD41 T Cells in Vitro and Ex Vivo. *Blood* **2017**, *129* (14), 1991–2001.
- (41) Oh, N.; Park, J. H. Endocytosis and Exocytosis of Nanoparticles in Mammalian Cells. *Int. J. Nanomedicine* **2014**, *9* (SUPPL.1), 51–63.
- (42) Helft, J.; Böttcher, J.; Chakravarty, P.; Zelenay, S.; Huotari, J.; Schraml, B. U.; Goubau, D.; Reis e Sousa, C. GM-CSF Mouse Bone Marrow Cultures Comprise a Heterogeneous Population of CD11c+MHCII+ Macrophages and Dendritic Cells. *Immunity* **2015**, *42* (6), 1197–1211.
- (43) Steinkamp, J.; Wilson, J.; Saunders, G.; Stewart, C. Phagocytosis: Flow Cytometric Quantitation with Fluorescent Microspheres. *Science* (80-. ). **1982**, *215* (4528), 64–66.
- (44) Borrmann, A.; Milles, S.; Plass, T.; Dommerholt, J.; Verkade, J. M. M.; Wießler, M.; Schultz, C.; van Hest, J. C. M.; van Delft, F. L.; Lemke, E. A. Genetic Encoding of a Bicyclo[6.1.0]Nonyne-Charged Amino Acid Enables Fast Cellular Protein Imaging by Metal-Free Ligation. *ChemBioChem* **2012**, *13* (14), 2094–2099.
- (45) Meldal, M.; Tomøe, C. W. Cu-Catalyzed Azide - Alkyne Cycloaddition. *Chem. Rev.* **2008**, *108* (8), 2952–3015.
- (46) Agard, N. J.; Prescher, J. A.; Bertozzi, C. R. A Strain-Promoted [3 + 2] Azide-Alkyne Cycloaddition for Covalent Modification of Biomolecules in Living Systems. *J. Am. Chem. Soc.* **2004**, *126* (46), 15046–15047.
- (47) Dommerholt, J.; Rutjes, F. P. J. T.; van Delft, F. L. Strain-Promoted 1,3-Dipolar Cycloaddition of Cycloalkynes and Organic Azides. *Top. Curr. Chem.* **2016**, *374* (2), 1–20.
- (48) Lang, K.; Davis, L.; Wallace, S.; Mahesh, M.; Cox, D. J.; Blackman, M. L.; Fox, J. M.; Chin, J. W. Genetic Encoding of Bicyclononynes and Trans-Cyclooctenes for Site-Specific Protein Labeling in Vitro and in Live Mammalian Cells via Rapid Fluorogenic Diels-Alder Reactions. *J. Am. Chem. Soc.* **2012**, *134* (25), 10317–10320.
- (49) van den Bosch, S. M.; Rossin, R.; Renart Verkerk, P.; ten Hoeve, W.; Janssen, H. M.; Lub, J.; Robillard, M. S. Evaluation of Strained Alkynes for Cu-Free Click Reaction in Live Mice. *Nucl. Med. Biol.* **2013**, *40* (3), 415–423.
- (50) Bernardin, A.; Cazet, A.; Guyon, L.; Delannoy, P.; Vinet, F.; Bonnafe, D.; Texier, I. Copper-Free Click Chemistry for Highly Luminescent Quantum Dot Conjugates: Application to in Vivo Metabolic Imaging. *Bioconjug. Chem.* **2010**, *21* (4), 583–588.
- (51) Ngo, J. T.; Adams, S. R.; Deerinck, T. J.; Boassa, D.; Rodriguez-Rivera, F.; Palida, S. F.; Bertozzi, C. R.; Ellisman, M. H.; Tsien, R. Y. Click-EM for Imaging Metabolically Tagged Nonprotein Biomolecules. *Nat. Chem. Biol.* **2016**, *12* (6), 459–465.
- (52) Patterson, D. M.; Prescher, J. A. Orthogonal Bioorthogonal Chemistries. *Curr. Opin. Chem. Biol.* **2015**, *28*, 141–149.
- (53) Hong, V.; Steinmetz, N. F.; Manchester, M.; Finn, M. G. Labeling Live Cells by Copper-Catalyzed Alkyne - Azide Click Chemistry. *Bioconjugate chem.* **2010**, *21* (10), 1912–1916.

- (54) Udenfriend, S.; Stein, S.; Böhlen, P.; Dairman, W.; Leimgruber, W.; Weigele, M. Fluorescamine: A Reagent for Assay of Amino Acids, Peptides, Proteins, and Primary Amines in the Picomole Range. *Science* (80-. ). **1972**, *178* (4063), 871–872.
- (55) van Geel, R.; Pruijn, G. J. M.; van Delft, F. L.; Boelens, W. C. Preventing Thiol-Yne Addition Improves the Specificity of Strain-Promoted Azide–Alkyne Cycloaddition. *Bioconjug. Chem.* **2012**, *23* (3), 392–398.
- (56) Lockhart, J.; Blitz, M.; Heard, D.; Seakins, P.; Shannon, R. Kinetic Study of the OH + Glyoxal Reaction: Experimental Evidence and Quantification of Direct OH Recycling. *J. Phys. Chem. A* **2013**, *117* (43), 11027–11037.
- (57) Senosiain, J. P.; Klippenstein, S. J.; Miller, J. A. The Reaction of Acetylene with Hydroxyl Radicals. *J. Phys. Chem. A* **2005**, *109* (27), 6045–6055.
- (58) Shen, Z.; Reznikoff, G.; Dranoff, G.; Rock, K. L. Cloned Dendritic Cells Can Present Exogenous Antigens on Both MHC Class I and Class II Molecules. *J. Immunol.* **1997**, *158* (6), 2723–2730.
- (59) Ralph, P.; Nakoinz, I. Antibody-Dependent Killing of Erythrocyte and Tumor Targets by Macrophage-Related Cell Lines: Enhancement by PPD and LPS. *J. Immunol.* **1977**, *119* (3), 950–954.
- (60) Raschke, W.; Baird, S.; Ralph, P.; Nakoinz, I. Functional Macrophage Cell Lines Transformed by Abelson Leukaemia Virus. *Cell* **1978**, *15* (September), 261–267.
- (61) Ferenbach, D.; Hughes, J. Macrophages and Dendritic Cells: What Is the Difference? *Kidney Int.* **2008**, *74* (1), 5–7.
- (62) Rybicka, J. M.; Balce, D. R.; Chaudhuri, S.; Allan, E. R. O.; Yates, R. M. Phagosomal Proteolysis in Dendritic Cells Is Modulated by NADPH Oxidase in a PH-Independent Manner. *EMBO J.* **2012**, *31* (4), 932–944.
- (63) Savina, A.; Peres, A.; Cebrian, I.; Carmo, N.; Moita, C.; Hacohen, N.; Moita, L. F.; Amigorena, S. The Small GTPase Rac2 Controls Phagosomal Alkalinization and Antigen Crosspresentation Selectively in CD8+ Dendritic Cells. *Immunity* **2009**, *30* (4), 544–555.
- (64) Savina, A.; Jancic, C.; Hugues, S.; Guernonprez, P.; Vargas, P.; Moura, I. C.; Lennon-Duménil, A. M.; Seabra, M. C.; Raposo, G.; Amigorena, S. NOX2 Controls Phagosomal PH to Regulate Antigen Processing during Crosspresentation by Dendritic Cells. *Cell* **2006**, *126* (1), 205–218.
- (65) Kapellos, T. S.; Taylor, L.; Lee, H.; Cowley, S. A.; James, W. S.; Iqbal, A. J.; Greaves, D. R. A Novel Real Time Imaging Platform to Quantify Macrophage Phagocytosis. *Biochem. Pharmacol.* **2016**, *116*, 107–119.
- (66) Rybicka, J. M.; Balce, D. R.; Khan, M. F.; Krohn, R. M.; Yates, R. M. NADPH Oxidase Activity Controls Phagosomal Proteolysis in Macrophages through Modulation of the Lumenal Redox Environment of Phagosomes. *Proc. Natl. Acad. Sci. U. S. A.* **2010**, *107* (23), 10496–10501.
- (67) Adachi, Y.; Kindzelskii, A. L.; Petty, A. R.; Huang, J.-B.; Maeda, N.; Yotsumoto, S.; Aratani, Y.; Ohno, N.; Petty, H. R. IFN- $\gamma$  Primes RAW264 Macrophages and Human Monocytes for Enhanced Oxidant Production in Response to CpG DNA via Metabolic Signaling: Roles of TLR9 and Myeloperoxidase Trafficking. *J. Immunol.* **2006**, *176* (8), 5033–5040.
- (68) Vandervén, B. C.; Yates, R. M.; Russell, D. G. Intraphagosomal Measurement of the Magnitude and Duration of the Oxidative Burst. *Traffic* **2009**, *10* (4), 372–378.
- (69) van Kasteren, S. I.; Overkleeft, H. S. Endo-Lysosomal Proteases in Antigen Presentation. *Curr. Opin. Chem. Biol.* **2014**, *23*, 8–15.
- (70) Van Kasteren, S. I.; Berlin, I.; Colbert, J. D.; Keane, D.; Ova, H.; Watts, C. A Multifunctional Protease Inhibitor to Regulate Endolysosomal Function. *ACS Chem. Biol.* **2011**, *6* (11), 1198–1204.
- (71) Mantegazza, A. R.; Savina, A.; Vermeulen, M.; Pérez, L.; Geffner, J.; Hermine, O.;

- Rosenzweig, S. D.; Faure, F.; Amigorena, S. NADPH Oxidase Controls Phagosomal PH and Antigen Cross-Presentation in Human Dendritic Cells. *Blood* **2008**, *112* (12), 4712–4722.
- (72) Song, J. S.; Kim, Y. J.; Han, K. U.; Yoon, B. D.; Kim, J. W. Zymosan and PMA Activate the Immune Responses of Mutz3-Derived Dendritic Cells Synergistically. *Immunol. Lett.* **2015**, *167* (1), 41–46.
- (73) Kelly, E. K.; Wang, L.; Ivashkiv, L. B. Calcium-Activated Pathways and Oxidative Burst Mediate Zymosan-Induced Signaling and IL-10 Production in Human Macrophages. *J. Immunol.* **2010**, *184* (10), 5545–5552.
- (74) Winterbourn, C. C.; Kettle, A. J. Redox Reactions and Microbial Killing in the Neutrophil Phagosome. *Antioxidants Redox Signal.* **2013**, *18* (6), 642–660.
- (75) Klebanoff, S. J. Myeloperoxidase: Friend and Foe. *J. Leukoc. Biol.* **2005**, *77* (5), 598–625.
- (76) Scholz, W.; Platzer, B.; Schumich, A.; Höcher, B.; Fritsch, G.; Knapp, W.; Strobl, H. Initial Human Myeloid/Dendritic Cell Progenitors Identified by Absence of Myeloperoxidase Protein Expression. *Exp. Hematol.* **2004**, *32* (3), 270–276.
- (77) Pickl, W. F.; Majdic, O.; Kohl, P.; Stöckl, J.; Riedl, E.; Scheinecker, C.; Bello-Fernandez, C.; Knapp, W. Molecular and Functional Characteristics of Dendritic Cells Generated from Highly Purified CD14+ Peripheral Blood Monocytes. *J. Immunol.* **1996**, *157* (9), 3850–3859.
- (78) Nunes, P.; Demaurex, N.; Dinauer, M. C. Regulation of the NADPH Oxidase and Associated Ion Fluxes During Phagocytosis. *Traffic* **2013**, *14* (11), 1118–1131.
- (79) Segal, A. W.; Geisow, M.; Garcia, R.; Harper, A.; Miller, R. The Respiratory Burst of Phagocytic Cells Is Associated with a Rise in Vacuolar PH. *Nature* **1981**, *290* (5805), 406–409.
- (80) Yuan, K.; Liu, Y.; Chen, H. N.; Zhang, L.; Lan, J.; Gao, W.; Dou, Q.; Nice, E. C.; Huang, C. Thiol-Based Redox Proteomics in Cancer Research. *Proteomics* **2015**, *15* (2–3), 287–299.
- (81) Zeida, A.; Guardia, C. M.; Lichtig, P.; Perissinotti, L. L.; Defelipe, L. A.; Turjanski, A.; Radi, R.; Trujillo, M.; Estrin, D. A. Thiol Redox Biochemistry: Insights from Computer Simulations. *Biophys. Rev.* **2014**, *6* (1), 27–46.
- (82) Poole, T. H.; Reisz, J. A.; Zhao, W.; Poole, L. B.; Furdui, C. M.; King, S. B. Strained Cycloalkynes as New Protein Sulfenic Acid Traps. *J. Am. Chem. Soc.* **2014**, *136* (17), 6167–6170.
- (83) Lang, K.; Chin, J. W. Bioorthogonal Reactions for Labeling Proteins. *ACS Chem. Biol.* **2014**, *9* (1), 16–20.
- (84) Blackman, M. L.; Royzen, M.; Fox, J. M. Tetrazine Ligation: Fast Bioconjugation Based on Inverse-Electron-Demand Diels-Alder Reactivity. *J. Am. Chem. Soc.* **2008**, *130* (41), 13518–13519.
- (85) Oliveira, B. L.; Guo, Z.; Bernardes, G. J. L. Inverse Electron Demand Diels–Alder Reactions in Chemical Biology. *Chem. Soc. Rev.* **2017**, *46* (16), 4895–4950.
- (86) Song, W.; Wang, Y.; Qu, J.; Lin, Q. Selective Functionalization of a Genetically Encoded Alkene-Containing Protein via “Photoclick Chemistry” in Bacterial Cells. *J. Am. Chem. Soc.* **2008**, *130* (30), 9654–9655.
- (87) Andersen, K. A.; Aronoff, M. R.; McGrath, N. A.; Raines, R. T. Diazo Groups Endure Metabolism and Enable Chemoselectivity in Cellulo. *J. Am. Chem. Soc.* **2015**, *137* (7), 2412–2415.



# Chapter 4

## Ultrastructural Imaging of *Salmonella*-Host Interactions Using Super-Resolution Correlative Light-Electron Microscopy of Bioorthogonal Pathogens

Published part of this chapter as part of:

- 1) Daphne M. van Elsland\*, Sílvia Pujals\*, Thomas Bakkum\*, Erik Bos, Nikolaos Oikonomou-Koppas, Ilana Berlin, Jacques Neefjes, Annemarie H. Meijer, Abraham J. Koster, Lorenzo Albertazzi and Sander I. van Kasteren. *ChemBioChem*, **2018**; 19(16): 1766-1770 (\*Authors contributed equally).
- 2) Teodora Andriana\*, Thomas Bakkum\*, Daphne M. van Elsland, Erik Bos, Abraham J. Koster, Lorenzo Albertazzi, Sander I. van Kasteren and Sílvia Pujals. *Methods in Cell Biology: Correlative Light and Electron Microscopy IV*, **2021**; Volume 162, Chapter 13: 303-33 (\*Authors contributed equally).





## **Abstract**

The imaging of intracellular pathogens inside host cells is complicated by the low resolution and sensitivity of fluorescence microscopy and by the lack of ultrastructural information to visualize the pathogens. This chapter describes a new method to visualize these pathogens during infection that circumvents these problems. Using a metabolic labeling approach to bioorthogonally label the intracellular pathogen *Salmonella typhimurium*, in combination with fluorophores that are compatible with Stochastic Optical Reconstruction Microscopy (STORM), and placing this in a Correlative Light-Electron Microscopy (CLEM) workflow, the pathogen can be imaged within its host cell context with a resolution of 20 nm. This STORM-CLEM approach thus presents a new approach to understand these pathogens during infection.

## 4.1 Introduction

The rise of antibiotic resistance is one of the major threats to global health. One class of pathogens proving particularly troublesome in this regard is that of the intracellular bacteria. These thwart immune detection by residing and replicating inside host-cell phagosomes.<sup>1</sup> Through secretion of factors that manipulate phagosomal maturation, they ensure their intracellular survival, despite an extensive arsenal of defense mechanisms deployed by the mammalian host.<sup>2</sup> It is, therefore, of utmost importance to understand bacterium-host interactions at the cellular and molecular levels. Bioorthogonal chemistry has proven to be a major breakthrough technique to study such host-pathogen interactions. Through hijacking the biosynthetic machinery of the cell wall with bioorthogonal analogues of D-alanine<sup>3–5</sup> or trehalose<sup>6–8</sup>, intracellular pathogens have been visualized selectively within host-cell phagosomes. Bioorthogonal Non-Canonical Amino acid Tagging (BONCAT<sup>9</sup>) – the incorporation of bioorthogonal amino acids into a target cell proteome – has also proven valuable in this context, for example, to image bacterial protein synthesis or retrieve pathogenic proteins secreted into the host cytosol by *Yersinia enterocolitica*<sup>10</sup>, *Salmonella enterica*<sup>11–13</sup>, *Escherichia coli*<sup>14</sup>, and *Mycobacterium smegmatis*.<sup>15</sup> However, these labeling approaches either require the mutant tRNA/tRNA synthetase pair specific for the bioorthogonal analogue of methionine, phenylalanine, or norleucine analogues to be introduced into the pathogen to achieve incorporation of the desired groups or suffer from low sensitivity.<sup>16</sup> This has limited their use to bacterial strains for which these techniques are available.

In an effort to image the subcellular location of bacteria in host phagocytes, an approach was recently developed that allowed visualization of bacteria within the ultrastructural context of the host cells, by using Correlative Light-Electron Microscopy (CLEM).<sup>17–19</sup> After sectioning frozen cell samples down to a thickness of 75 nm followed by an on-section copper-catalyzed Huisgen cycloaddition (ccHc) reaction<sup>20,21</sup>, intracellular BONCAT-labeled *E. coli* were visualized by confocal microscopy. Subsequent Transmission Electron Microscopy (TEM) of the same section allowed the placement of the fluorescent signal within the ultrastructural context of the phagocytic immune cell (phagocyte). If this approach could be extended to pathogenic species, it would provide a powerful tool to study the interaction of host phagocytes with intracellular pathogens. However, for the approach to be of use for unmodified strains, two major constraints relating to both BONCAT and CLEM have to be overcome. The first is the reliance on mutant tRNA/tRNA synthetases for the incorporation of the bioorthogonal amino acids,

compounded by the low overall signal in BONCAT-CLEM (stemming from the thinness of the samples). It was hypothesized that metabolic hijacking approaches reported for *E. coli* auxotrophic strains<sup>22</sup> would need to be extended and optimized to allow sufficient label incorporation with non-auxotrophic bacterial species, thus ensuring their detection by CLEM. The second limitation is related to the CLEM imaging itself: whereas the resolution of the electron micrograph is of the order of 1 nm, that of fluorescence microscopy is limited by the Abbe diffraction limit of half the photon wavelength ( $\lambda \approx 250$  nm)<sup>23</sup>, resulting in a resolution gap between the two techniques.

Over the last few years, super-resolution imaging techniques have flourished<sup>24</sup>, breaking Abbe's law of limiting resolution<sup>25</sup> and allowing for resolution on the nanoscale. Recently, the combination of fluorescent protein super-resolution imaging was combined with CLEM, and this allowed a tenfold improvement in the fluorescence resolution of fluorescent proteins.<sup>26,27</sup> By lowering OsO<sub>4</sub> concentrations during post-fixing and optimizing resin embedding, fluorophore quenching could be partially prevented. This sample preparation technique was reported with both Photoactivated Localization Microscopy (PALM)<sup>26,28,29</sup> and Stimulated Emission Depletion (STED) microscopy in combination with TEM<sup>30–32</sup> and Scanning Electron Microscopy (SEM).<sup>27,33,34</sup> Of the various super-resolution imaging techniques, stochastic optical resolution microscopy (STORM) offers higher spatial resolution and sensitivity<sup>35–38</sup> at the cost of longer acquisition times. Although this is a drawback for *in vivo* imaging, it presents no problem upon imaging fixed sections. The other limitation of STORM is the need to observe close to the glass surface owing to total internal reflection fluorescence illumination. The thinness of the cryo-sections (75 nm) makes the two approaches very compatible. The two-step nature of bioorthogonal ligations also simplifies the STORM-CLEM workflow, because the fluorophore is introduced after the biological time course and sample preparation. The choice of fluorophore can therefore be made independently of the requirements of the biological experiment. The limited availability of dyes for STORM is thus circumvented.<sup>39</sup> The combination of BONCAT-CLEM methodology with super-resolution microscopy could aid in overcoming some of the hurdles related to pathogen BONCAT-CLEM: the sensitivity and suboptimal resolution of confocal fluorescence microscopy. STORM brings the resolution of the fluorescent signals in closer alignment with TEM and improves sensitivity of detection, allowing imaging of genetically unmodified pathogenic bacteria by BONCAT-STORM-CLEM.

One pathogen that would benefit from lifecycle studies using STORM-CLEM is *Salmonella enterica* serovar Typhimurium (*Stm*). This is a Gram-negative facultative intracellular pathogen that ensures its intracellular survival by secreting various effector proteins after uptake.<sup>40</sup> These modulate the maturation of the phagosome in which the bacterium resides to yield a parasitic vacuole suitable for its survival and replication.<sup>41–44</sup> Van Elsland<sup>45</sup> previously reported the successful application of STORM-CLEM for the imaging of *Stm* (**Figure 1**). However, further optimization and validation of bioorthogonal amino acid incorporation is needed to improve the technique and facilitate its translation to other pathogens.

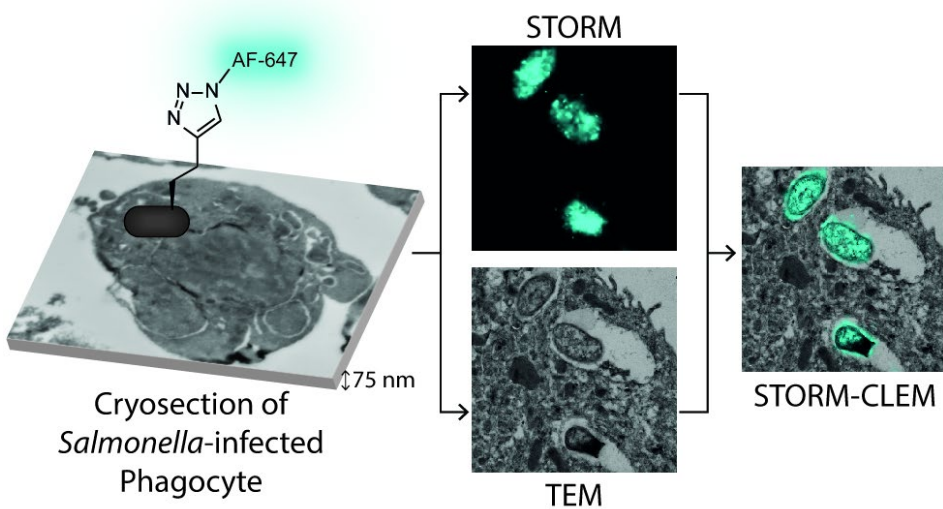


**Figure 1.** Graphical summary of the BONCAT-STORM-CLEM technique for studying intracellular pathogenic bacteria such as *Salmonella enterica*.

## 4.2 Results and Discussion

### 4.2.1 Optimization of bioorthogonal label incorporation in *Stm*

Incorporation of bioorthogonal amino acid analogues was first assessed to allow for optimal cHc detection of the bacterial proteome while minimizing the effect on bacterial viability and infectivity. Azidohomoalanine (Aha; an azide-analogue of methionine (Met)) was previously used to bioorthogonally label Met-auxotrophic *E. coli* and visualize these bacteria inside bone marrow-derived dendritic cells (BMDCs<sup>46</sup>) using CLEM.<sup>18</sup> In order to find out if non-auxotrophic *Stm* would incorporate Aha into its proteome in detectable amounts, an in-gel fluorescence assay was used (**Figure S1**), using the previously described experimental conditions<sup>18</sup> in which a fluorophore (Alexa Fluor 647; AF647) is attached to the bioorthogonal group through cHc. Detectable incorporation was observed after a 30 min pulse with Aha (0.04-4 mM) and increases with longer incubation times (60-120 min). These observations were confirmed by flow cytometry, which provides a more accurate representation of the total label incorporation per bacterium. In order to remove any bacteria-unrelated particles from the flow cytometric measurements, the bacteria were gated on size (**Figure S2A**) and shape (**Figure S2B**), and completely non-fluorescent were removed with a cleanup gate (**Figure S2C**). Aha incorporation follows a clear trend, increasing with higher concentrations and longer incubation times (**Figure 2A, Figure S3A**) but decreasing again after 30 min at 4 mM or 60 min at lower concentrations. Even after 30 min, close to 100% of bacteria contained sufficient Aha to be detected, no matter which concentration was used (**Figure 2C**). Aha labeling of a DsRed-expressing strain of *Stm*<sup>47</sup> revealed that DsRed fluorescence is slightly reduced with increasing concentrations of Aha (**Figure 2B, Figure S3B**). This implies that incorporation of this non-canonical amino acid has a negligible effect on protein function but should simultaneously serve as a warning against excessive label concentrations. *Stm* growth rates remain virtually unaffected up to 30 min incubation with Aha for all of the conditions tested (**Figure S3C**), implying minimal interference with bacterial viability.

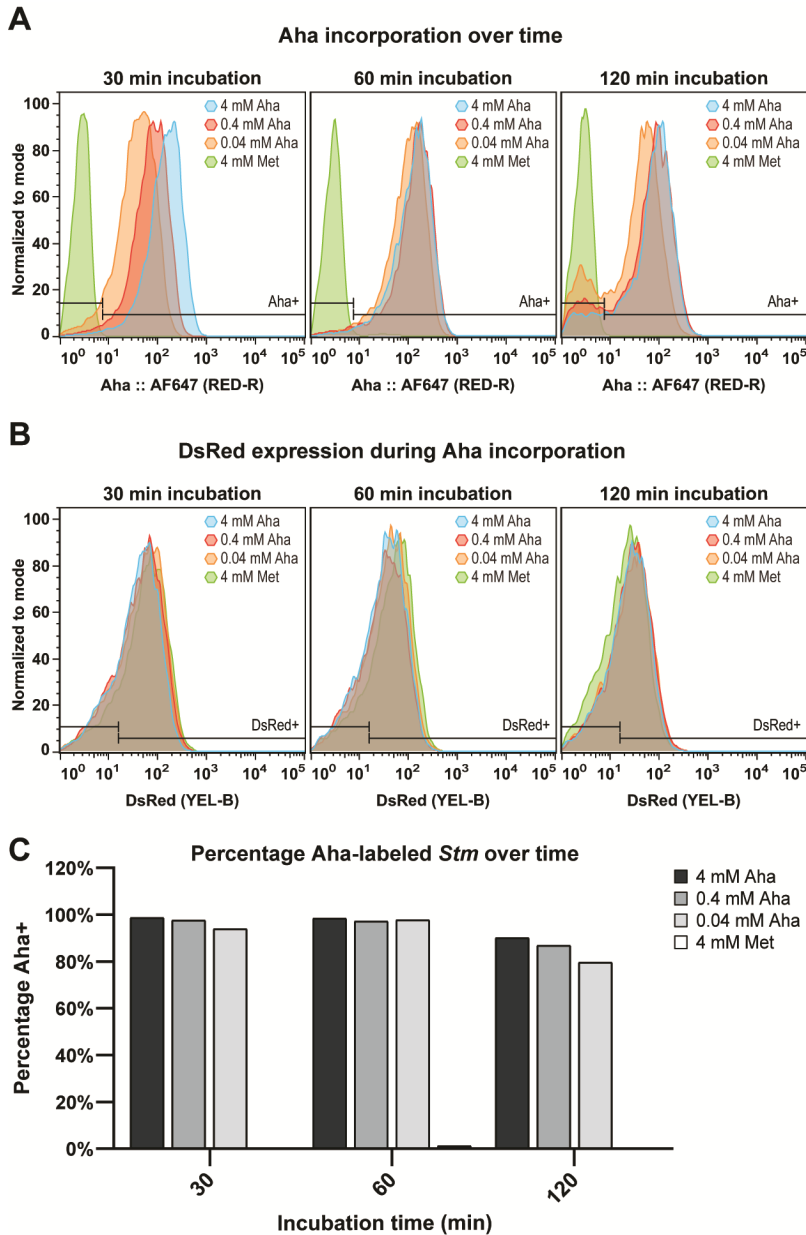


**Figure 2.** Optimization of Aha incorporation in *Stm* by flow cytometric analysis. DsRed-expressing *Stm* were incubated with increasing concentrations of Aha or 4 mM Met (control) in SelenoMet medium for up to 120 min, then cChc-reacted with AF647-alkyne for detection by flow cytometry. **(A)** Aha incorporation over time is shown as the flow cytometric distributions of the conjugated AF647. **(B)** The effect of Aha incorporation on the DsRed fluorescent protein is shown as the flow cytometric distributions of DsRed. **(C)** The percentage Aha-labeled *Stm* (Aha+) over time is shown, based on the fluorescence intensity of the reacted AF647 and the threshold set for unlabeled *Stm* (4 mM Met).

Since previous studies revealed that an azide-containing label results in a suboptimal fluorescent signal – due to non-specific reactions of the alkyne-containing fluorophore<sup>48</sup> – the inverse approach was attempted as well. Therefore, incorporation of homopropargylglycine (Hpg; an alkyne analogue of Met) into the proteome was assessed as well using the in-gel fluorescence assay (**Figure S4**). Detectable incorporation was again observed after a 30 min pulse with Hpg (0.04–4 mM) and increases with longer incubation times (1–2 hours). Flow cytometry confirmed a similar trend for Hpg incorporation, increasing with higher concentration and longer incubation times (**Figure 3A**, **Figure S5A**) but plateauing after 30 min at 4 mM or around 60 min at lower concentrations. After 30 min incubation with 4 or 0.4 mM Hpg, nearly all bacteria contained sufficient Hpg to be detected (**Figure 3C**). DsRed fluorescence was virtually unaffected by incorporation of Hpg up to a concentration of 0.4 mM (**Figure 3B**, **Figure S5B**). *Stm* growth rates remain virtually unaffected up to 30 min of incubation with Hpg for all of the conditions tested (**Figure S5C**). Notably, even after a 120 min pulse with Hpg, the growth rates of these Hpg-labeled *Stm* in fresh LB medium recovered to >85% after 120 min for all Hpg concentrations (**Figure S7C**), implying that the observed (minor) growth-inhibiting effect is reversible. Label retention of Hpg-*Stm* during bacterial division ('outgrowth') was also followed by in-gel fluorescence (**Figure S6**) and flow cytometry (**Figure 4A**, **Figure S7A**), following a 120 min pulse with Hpg and a subsequent medium exchange with fresh LB. Nearly all bacteria retained sufficient Hpg to be detected after 120 min of outgrowth ( $\approx 2$ –6 divisions<sup>49</sup>) for all Hpg concentrations (**Figure 4C**). On the basis of these observations, balancing the signal intensity, percentage of Hpg-labeled *Stm* and the impact on growth and DsRed fluorescence, the optimal conditions were chosen as a 30 min pulse with 0.4 mM Hpg.

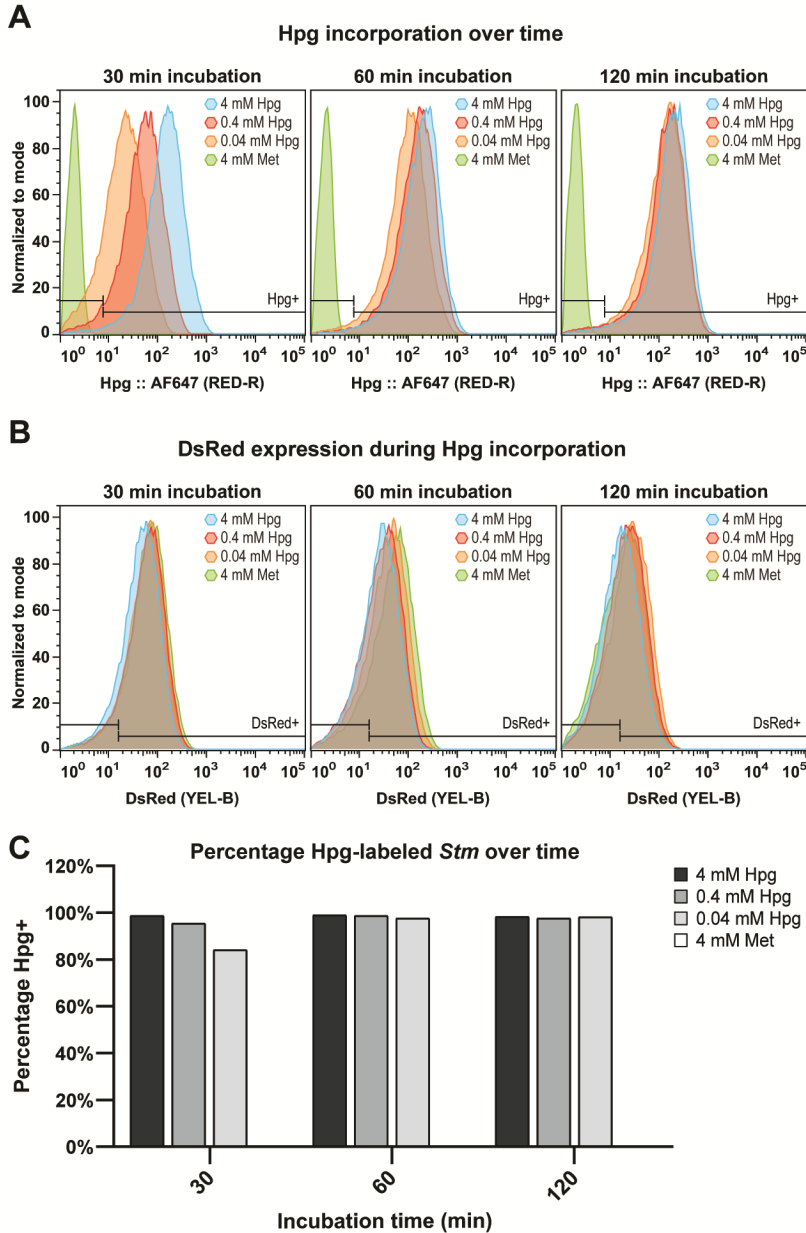


**Figure 3.** Optimization of Hpg incorporation in *Stm* by flow cytometric analysis. DsRed-expressing *Stm* were incubated with increasing concentrations of Hpg or 4 mM Met (control) in SelenoMet medium for up to 120 min, then ccHc-reacted with AF647-azide for detection by flow cytometry. **(A)** Hpg incorporation over time is shown as the flow cytometric distributions of the conjugated AF647. **(B)** The effect of Hpg incorporation on the DsRed fluorescent protein is shown as the flow cytometric distributions of DsRed. **(C)** The percentage Hpg-labeled *Stm* (Hpg+) over time is shown, based on the fluorescence intensity of the reacted AF647 and the threshold set for unlabeled *Stm* (4 mM Met).



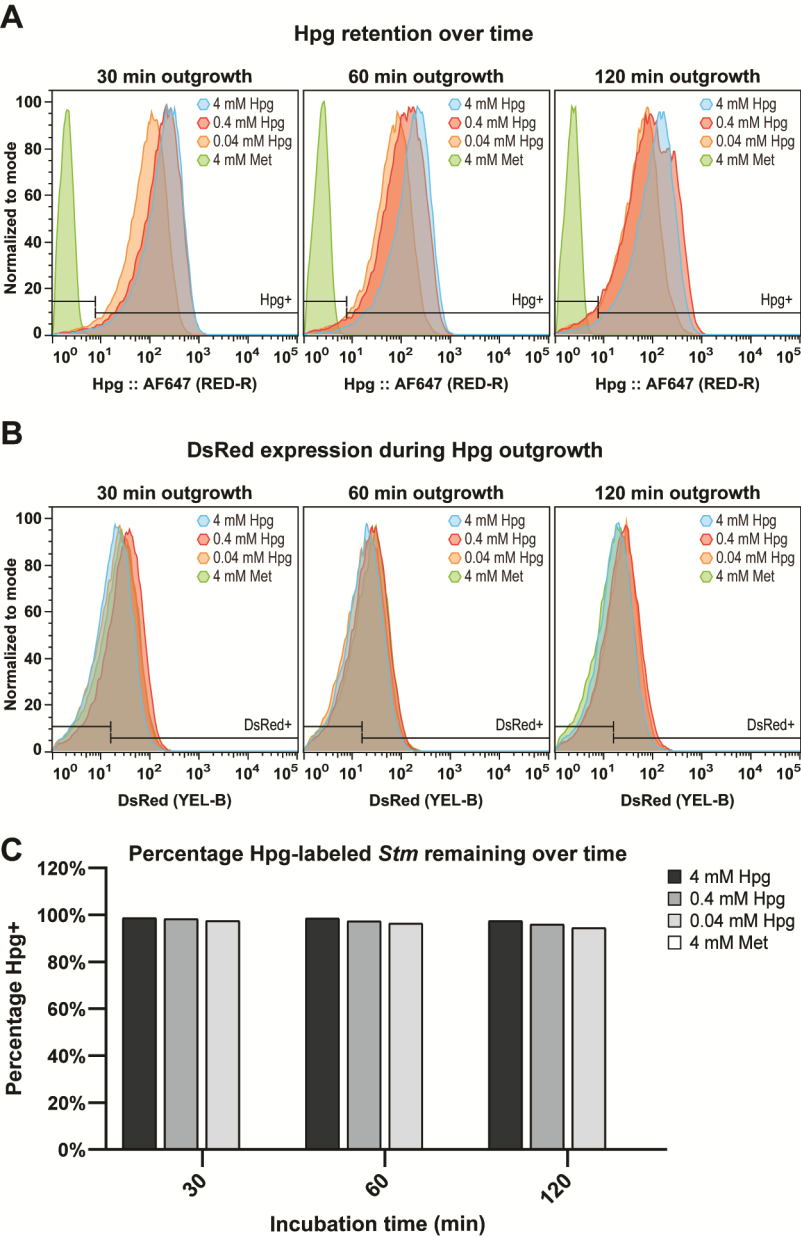


**Figure 4.** Label retention and growth recovery of Hpg-labeled *Stm* by flow cytometric analysis. DsRed-expressing *Stm* were incubated with increasing concentrations of Hpg or 4 mM Met (control) in SelenoMet medium for 120 min, washed with PBS and resuspended in fresh LB medium and incubated again for up to 120 min, then cHc-reacted with AF647-azide for detection by flow cytometry. **(A)** Hpg retention over time (outgrowth) is shown as the flow cytometric distributions of the conjugated AF647. **(B)** The effect of Hpg outgrowth on the DsRed fluorescent protein is shown as the flow cytometric distributions of DsRed. **(C)** The percentage Hpg-labeled *Stm* (Hpg+) remaining over time is shown, based on the fluorescence intensity of the reacted AF647 and the threshold set for unlabeled *Stm* (4 mM Met).

Alternatively, D-propargylglycine (alkDala; an alkyne-analogue of D-alanine) could be used to metabolically label the cell wall of *Stm*. If successful, this could additionally allow simultaneous labeling of the cell wall with alkDala and the proteome with Aha. To achieve this, two sequential cHc reactions with compatible fluorophores (e.g., AF647-azide and AF488-alkyne) are required with intermediate washing steps to remove all excess of the first fluorophore before adding the second. Indeed, incubating *Stm* with 5 mM alkDala for 30 min or longer resulted in a detectable fluorescent signal, measured by flow cytometry (**Figure 5A**, **Figure S8/S9**). Incubating *Stm* with 5 mM alkDala and 4 mM Aha simultaneously for 30 min or longer resulted in successful dual labeling (**Figure 5C**, **Figure S8/S9**). However, since incubation with alkDala for up to 120 min resulted in less than 60% labeled bacteria (**Figure S8A**), Hpg was used for all subsequent experiments.

To determine whether infectivity was affected for the Hpg-labelled *Stm*, dendritic cells (DC2.4 cell line) were infected for 45 min with the aforementioned DsRed-expressing *Stm*, incubated with either Hpg or Met as a control. Uptake of the bacteria and their subsequent intracellular division were assessed with flow cytometry, measuring the entire *Stm*-containing DCs at different time points. DCs were gated on size, shape and DsRed to select for *Stm*-containing cells (**Figure S10**). By quantifying both the DsRed and bioorthogonal signals over time, bacterial cell divisions and label loss could be calculated simultaneously. Hpg modification did not affect the infectivity of *Stm*, judged by the mean fluorescence intensity (MFI) of DsRed per DC as a proxy of the average number of intracellular *Stm* (**Figure 6A**, **Figure S11A**). Furthermore, the change in DsRed expression over time was the same for both Met- and Hpg-grown *Stm*, indicating no detectable impact of Hpg on intracellular survival and proliferation. Fluorophore ligation of the Hpg-*Stm* within DCs showed only negligible reduction in fluorescent signal per cell over time (**Figure 6B**, **Figure S11B**), confirming previous findings that terminal alkynes are stable to the phagolysosomal pathway.<sup>48</sup> Corresponding *in vitro* controls show a steady dilution of Hpg over time, when the bacteria are able to proliferate freely in label-free medium (**Figure 6C**).

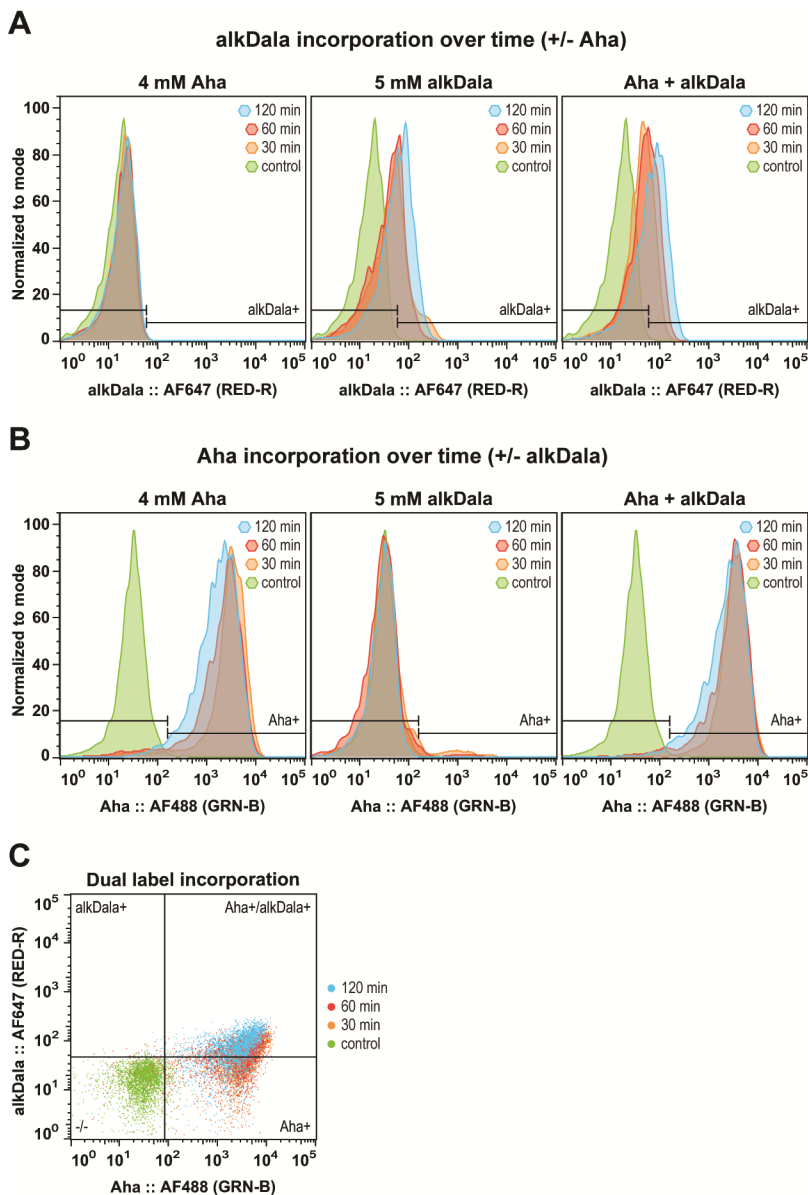


**Figure 5.** Optimization of alkDala labeling and Aha/alkDala dual labeling of *Stm* by flow cytometric analysis. *Stm* were incubated with 4 mM Aha, 4 mM Met + 5 mM alkDala or 4 mM Aha + 5 mM alkDala in SelenoMet medium for up to 120 min, then cChc-reacted with AF647-azide (alkDala) and AF488-alkyne (Aha) for detection by flow cytometry. **(A)** alkDala incorporation over time is shown as the flow cytometric distributions of the conjugated AF647. **(B)** Aha incorporation over time is shown as the flow cytometric distributions of the conjugated AF488. **(C)** Dual label incorporation over time is shown as 2-dimensional dot plots of the conjugated AF647 (alkDala) vs. the conjugated AF488 (Aha).

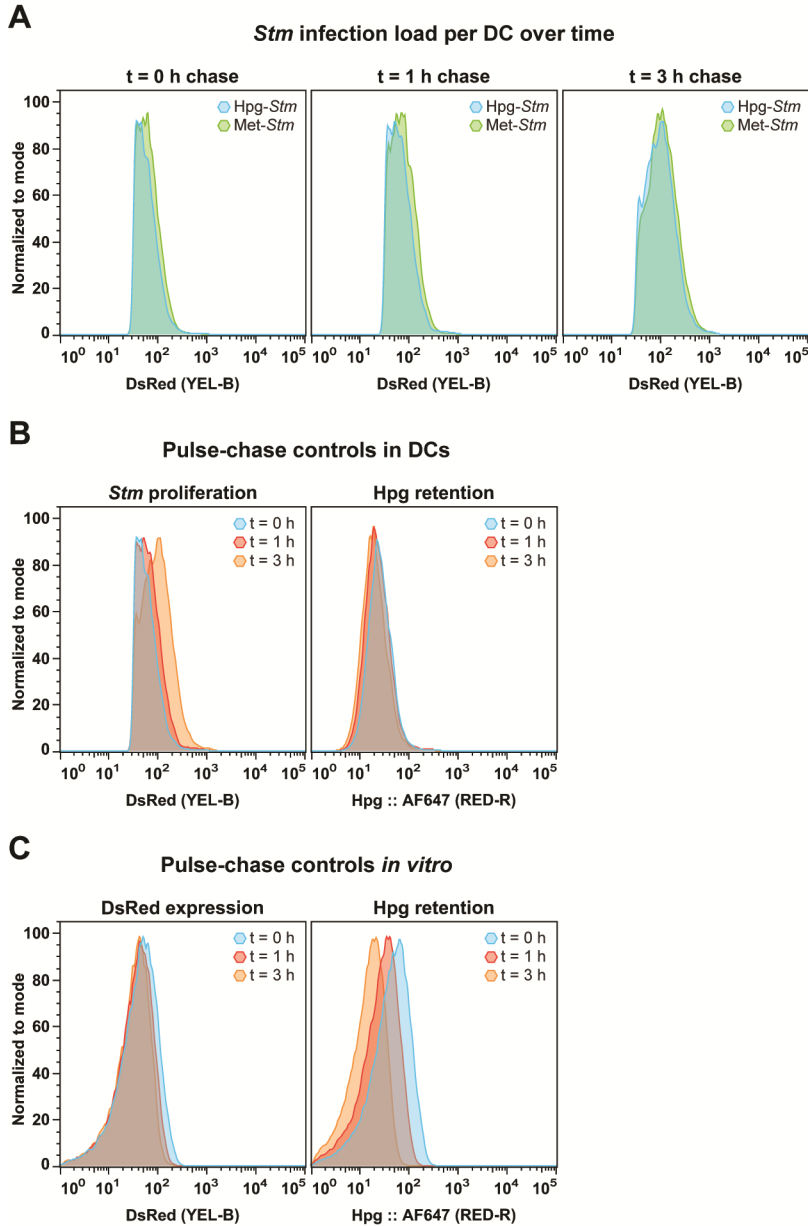


**Figure 6.** Infection controls, bioorthogonal label retention and *Stm* proliferation in DC2.4 cells. DsRed-expressing *Stm* were first incubated with 0.4 mM Hpg (Hpg-*Stm*) or 4 mM Met (Met-*Stm*) for 30 min in SelenoMet, then washed to remove excess Hpg and added to DCs at an MOI of 50 for 45 min (pulse). *Stm*-infected BDMCs were then washed to remove non-internalized *Stm* and incubated for an additional 0, 1 or 3 hours (chase), followed by ccHc-reaction with AF647-azide for detection by flow cytometry. **(A)** The *Stm* infection load was compared between Hpg-*Stm* and Met-*Stm* over time, based on the DsRed intensity per DC. **(B)** Intracellular *Stm* proliferation and Hpg retention were followed over time in DCs. **(C)** Corresponding *in vitro* DsRed expression and Hpg retention of *Stm* were simultaneously followed over time as controls.

### 4.2.2 The application of STORM-CLEM to visualize intracellular *Stm* in BMDCs

In order to validate the use of STORM for visualizing Hpg-labeled *Stm* in thin sections that can be used for CLEM, a mixture of labeled and unlabeled *Stm* is required to detect single bacteria without the signals overflowing. To achieve this, Hpg- and Met-grown *Stm* were mixed in various ratios and subsequently fixed for analysis. Flow cytometric analysis revealed that Hpg-labeled bacteria could still be detected at a labeled:unlabeled ratio of 1:25 (**Figure S12**). The detection limit of STORM was then assessed by imaging thin sections of *Stm* grown in the presence of decreasing concentrations of Hpg. Samples were cryo-sectioned, ccHc-ligated with AF647-azide, and imaged by using standard catalase, glucose and glucose oxidase-containing buffer (GLOX) or other oxygen-consuming buffers, such as the OxEA buffer<sup>50</sup> supplemented with 30% glycerol to decrease drift during STORM image acquisition. The acquired STORM images of *Stm* sections labeled with 0.4 or 4 mM Hpg revealed clear bacteria-sized regions (230-400 nm × 180-280 nm, **Figure 7A/B**). *Stm* grown in the presence of 0.04 mM Hpg could be detected, but the signal was too low to allow full reconstruction of the bacteria (**Figure 7C**).

To achieve STORM-CLEM imaging of intracellular *Stm* in BMDCs, Hpg-labeled *Stm* (0.4 mM Hpg for 30 min) were added to a culture of freshly isolated BMDCs at an MOI of 50 and co-incubated for 45 min. After washing away the non-internalized bacteria, the infected cells were processed for cryo-sectioning according to the Tokuyasu method.<sup>18</sup> In short, cells were fixed for 24h in freshly prepared 2% PFA in 0.1M phosphate buffer, embedded in 12% gelatin, cut in cubes of approx. 0.5 mm<sup>3</sup> and sucrose-infiltrated O/N at 4°C. Ultrathin cryo-sections were prepared using a cryo-ultramicrotome and a cryo-immuno diamond knife, transferred to Formvar/carbon-coated titanium TEM grids and thawed in a closed environment to protect from water condensation (suspected to be a major cause of sample deformation and folding). The thawed sections were first incubated on 2% gelatin, then washed with PBS containing 15 mM glycine (to quench any remaining aldehyde residues) and subjected to ccHc-reaction with AF647-azide. Finally, the sections were washed again and the nuclei were counter-stained with DAPI to provide markers for correlation (matching the fluorescence image to the electron micrograph). The fluorescently labeled sections were first imaged with low-resolution confocal fluorescence microscopy (FM) to locate areas of interest and to record the position of the nuclei. Next, the fluorescently labeled *Stm* were imaged by STORM to obtain the corresponding super-resolution fluorescence images. Finally, the sections were post-stained with uranyl acetate (to provide contrast) and imaged by TEM. The resulting images were stepwise correlated to obtain the final

STORM-CLEM image (a projection of the multi-modal dataset). The entire STORM-CLEM protocol is summarized in **Figure 8** and the corresponding workflow and timeline are shown in **Figure 9**.

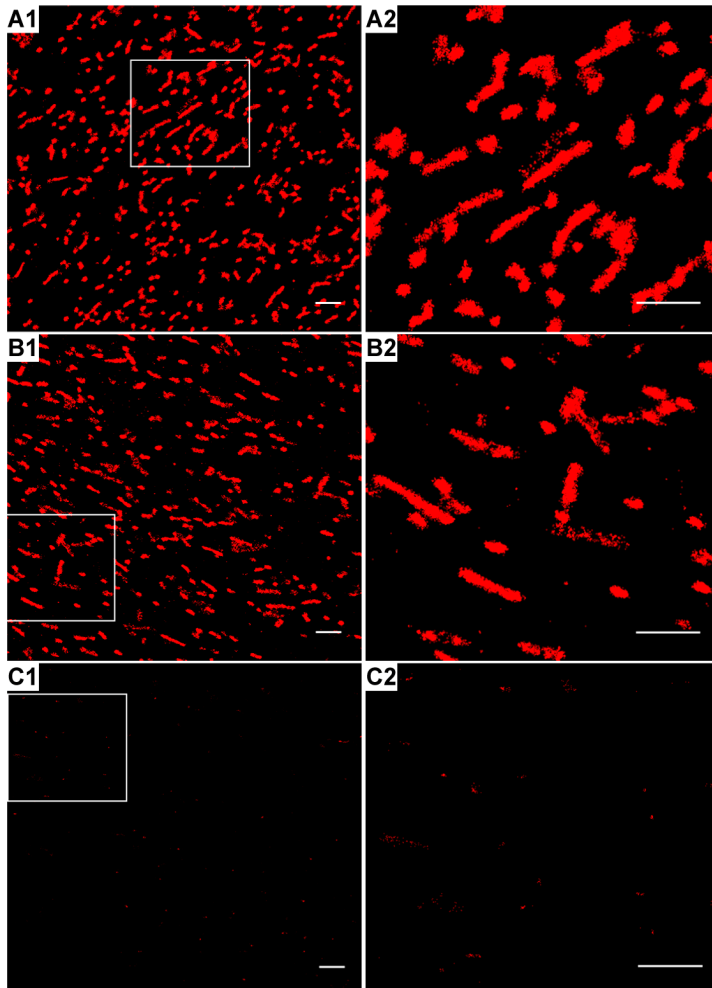


**Figure 7.** CLEM-compatible ultrathin (75 nm) sections of Hpg-labeled *Stm*, grown in presence of decreasing concentrations of Hpg, mixed in a ratio of 1:25 with unlabeled *Stm*, grown in presence of 4 mM Met. *Stm* were grown in the presence of (A) 4 mM Hpg, (B) 0.4 mM Hpg or (C) 0.04 mM Hpg. The second column (A2-C2) shows zoom-ins of the first column (A1-C1). All scale bars represent 2 μm.

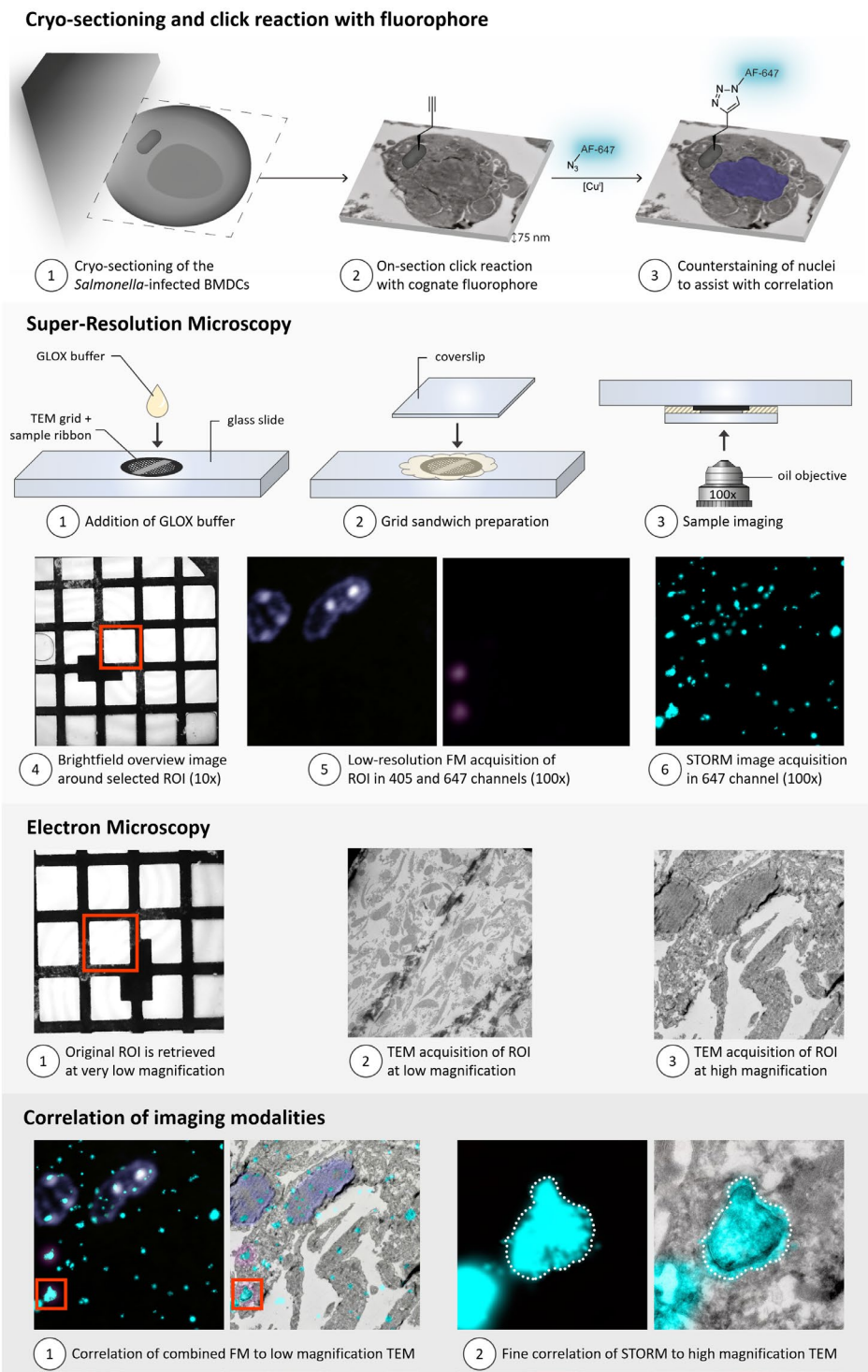


**Figure 8.** Graphical summary of the bioorthogonal STORM-CLEM protocol.

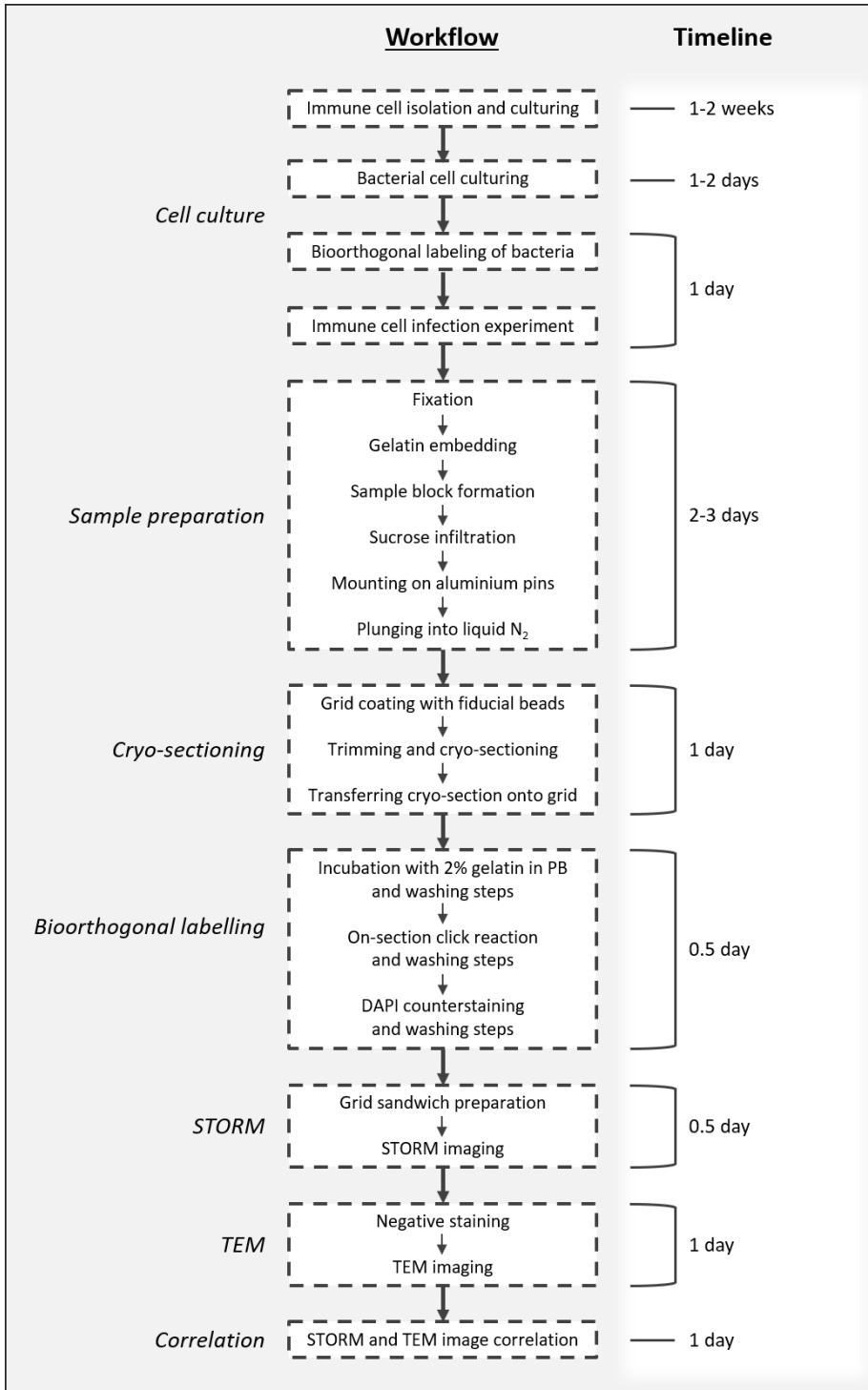


**Figure 9.** Workflow and timeline of the bioorthogonal STORM-CLEM protocol.



STORM was able to reconstruct the intracellular *Stm* to a high degree, which could then be fitted cleanly onto the bacterial ultrastructure of the TEM image. The sensitivity of STORM allows for the detection of bacterial components that are below the detection limit of low-resolution FM. The observed spatial resolution of STORM is at least tenfold better than the optimal resolution that could be obtained with confocal microscopy (20 nm vs. ~250 nm). Whereas STORM is able to detect single fluorophores (attached to a biomolecule of interest), the label density of the here-observed *Stm* is too high to observe distinct molecules. However, separate puncta can be observed outside the bacterial perimeter, which may indicate single molecules or small clusters. As these puncta appear to be located outside the bacterial cell wall, they may represent either secreted proteins or bacterial degradation products, containing one or more Hpg moieties. However, no conclusions can be drawn about these puncta, due to the current level of non-specific fluorophore labeling (fluorescent spots that are not associated with any observable bacterial structure in the electron micrograph). Further optimization of the fluorophore attachment by ccHc could provide more information about the origin of these extra-bacterial fluorescent puncta. Alternatively, a BONCAT-proteomics approach could be used to identify potential Hpg-labeled proteins secreted by intracellular *Stm*.

### 4.3 Conclusion

BONCAT-STORM-CLEM allowed for the detection of wild type *Stm* within the ultrastructural context of the host phagocyte, with high sensitivity and high resolution. Although further optimization of the technique is needed to reduce non-specific fluorophore labeling, it represents a promising new approach to study intracellular bacterial pathogens with higher accuracy and sensitivity than any previous method.<sup>18,51–53</sup> This opens up the possibility of imaging pathogens for which previous BONCAT approaches were not efficient. The combination of STORM-CLEM with BONCAT, tRNA/tRNA synthetase mutants, or bio-orthogonal cell-wall labeling will be valuable in studying the *in vivo* lifecycle of these pathogens.<sup>11–13</sup> Application of this technique to other areas in which bioorthogonal chemistry has been transformative would also add an extra dimension of ultrastructure to these fields.<sup>54,55</sup>

## 4.4 Experimental

### Safety statement

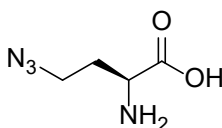
All biological experiments with *S. enterica* serovar Typhimurium described in this study were performed under strict Bio Safety Level 2 conditions. Following fixation and disinfection of the tubes, further sample preparation for CLEM was performed under normal laboratory conditions. No unexpected or unusually high safety hazards were encountered.

### Reagents

Lysogeny broth (LB) medium, methionine (Met), Dulbecco's modified Eagle medium (DMEM), Iscove's Modified Dulbecco's Medium (IMDM), GlutaMAX, pyruvate, 4-(2-hydroxyethyl)-1-piperazineethanesulfonic acid (HEPES), glycine, gelatin type A bloom 300 (gelatin), paraformaldehyde (PFA), bovine serum albumin (BSA), Copper(II) sulfate pentahydrate, (+)-sodium L-ascorbate, tris(3-hydroxypropyl)triazolymethylamine (THPTA), aminoguanidine hydrochloride, and IGEPAL CA-630 were purchased from Sigma-Aldrich, Zwijndrecht, The Netherlands. Non-essential amino acids (NEAA), 2-mercaptoethanol, L-glutamine, Hoechst 33342, 4',6-Diamidino-2-Phenylindole (DAPI) and azide-/alkyne-modified Alexa Fluor dyes (AF488 and AF647) were purchased from Thermo Fisher Scientific, Bleiswijk, The Netherlands. SelenoMet minimal medium was purchased from Molecular Dimensions, Sheffield, UK. D-propargylglycine (alkDala) was purchased from Combi-Blocks, San Diego, USA. EM-grade 8% paraformaldehyde and EM-grade 8% glutaraldehyde were purchased from Electron Microscopy Sciences, Hatfield, USA. Fetal calf serum (FCS) was purchased from VWR International, Amsterdam, The Netherlands. Penicillin G sodium and streptomycin sulphate were purchased from Duchefa, Haarlem, The Netherlands. Granulocyte-Macrophage Colony-Stimulating Factor (GM-CSF) was purchased from ImmunoTools, Friesoythe, Germany.

### Organic synthesis

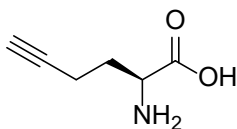
Synthesis of (S)-2-amino-4-azidobutanoic acid (L-azidohomoalanine; Aha)



Aha was synthesized according to a previously described procedure by Zhang et al., 2010<sup>56</sup>.

$^1\text{H}$ -NMR ( $\text{D}_2\text{O}$ ), 400 MHz:  $\delta$  [ppm] = 4.05 (t, 1H,  $\alpha$ -CH), 3.55 (t, 2H,  $\gamma$ - $\text{CH}_2$ ), 2.15 (m, 2H,  $\beta$ - $\text{CH}_2$ ).

Synthesis of (S)-2-Aminohex-5-ynoic acid (L-homopropargylglycine; Hpg)



Hpg was synthesized according to previously described procedure by Li et al.<sup>57</sup>, adjusted to obtain the enantiomerically pure L-Hpg variant based on Chenault et al.<sup>58</sup>, Biagini et al.<sup>59</sup> and Dong et al.<sup>60</sup>

#### Chiral deprotection of *N*-acetyl-DL-homopropargylglycine (2-acetamidohex-5-ynoic acid)

A solution of 303 mg (1.13 mmol, 1 eq.) *N*-acetyl-DL-homopropargylglycine in 20 mL  $\text{H}_2\text{O}$  and adjusted to pH 7.5 using 1M  $\text{NH}_4\text{OH}$ . 1 mg kidney acylase I ( $\geq 2000$  units/mg) was added and the mixture was stirred for 16 h at  $37^\circ\text{C}$ . The enzyme was recovered by centrifugation dialysis, using a 10kDa membrane at 4000 rpm for 35 min at  $10^\circ\text{C}$ . Next, the solution was acidified to pH 3 with 2M HCl and extracted with 3 x 20 mL diethyl ether. The organic layers were concentrated to retrieve the *N*-acetyl-D-homopropargylglycine. The aqueous layer was loaded on a pre-washed and regenerated Dowex 50WX8 cation exchange resin (60 mL). The column was washed with 5 x bed volume of water, maintaining a pH of 5.5 at the exit and eluted with 200 mL 1.5M  $\text{NH}_4\text{OH}$ . Product was detected by TLC and the eluate was concentrated and lyophilized to yield chirally pure L-Hpg (68 mg, 0.535 mmol, 95%) as a white powder.

$^1\text{H}$  NMR (400MHz,  $\text{D}_2\text{O}$ ):  $\delta$  [ppm] = 4.11 (t,  $J$  = 6.4 Hz, 1H), 2.42 – 2.36 (m, 2H), 2.36 (s, 1H), 2.19 – 2.10 (m, 1H), 2.07 – 1.98 (m, 1H);  $^{13}\text{C}$  NMR (101MHz,  $\text{D}_2\text{O}$ ):  $\delta$  82.28, 71.16, 52.05, 28.44, 14.16; HRMS (ESI):  $\text{C}_6\text{H}_9\text{NO}_2$   $[\text{M}+\text{H}]^+$  128.06, found 128.07;  $[\alpha]_{20}^{\text{D}}$ : +32.4 ( $c$  = 1, 1 M HCl); Ref <sup>60</sup>: +28 ( $c$  = 1, 1 M HCl).

#### Bacterial culture, metabolic labeling and viability assessment based on growth rate

*Stm* SL1344 expressing DsRed<sup>61</sup> were grown overnight at  $37^\circ\text{C}$  in LB medium. The following day cultures were diluted 1:33 and grown at  $37^\circ\text{C}$  to an  $\text{OD}_{600}$  between 0.3-0.5. Subsequently bacteria were collected and resuspended in SelenoMet medium and supplemented with either 0.04, 0.4 or 4 mM Aha, 0.04, 0.4 or 4 mM

Hpg, 5 mM alkDala + 4 mM Met, 5 mM alkDala + 4 mM Aha (dual) or 4 mM Met (control). After 30, 60 and 120 minutes OD<sub>600</sub> were measured and bacteria were collected by centrifugation for SDS-PAGE, flow cytometry analysis and DC infection experiments. For outgrowth experiments after 120 minutes of label incorporation, bacteria were collected by centrifugation and resuspended in LB medium and incubated for another 120 minutes with intermittent sampling. Throughout culturing, the medium was supplemented with 100 µg/ml ampicillin.

### **Mammalian cell culture and infection with *Stm***

DC2.4 cells were cultured in IMDM, supplemented with 10% heat-inactivated FCS, 2 mM GlutaMAX, 10 mM HEPES pH 7.3, 1 mM pyruvate, penicillin 100 I.U./mL and streptomycin 50 µg/mL, 50 µM 2-Mercaptoethanol and 1X non-essential amino acids.

Mouse bone marrow-derived dendritic cells (BMDCs) were generated from B57BL/6 mice bone marrow essentially as described<sup>62</sup> with some modifications. Briefly, bone marrow was flushed from femurs and tibia and cells were cultured in IMDM supplemented with 8% heat-inactivated FCS, 2 mM L-glutamine, 20 µM 2-Mercaptoethanol, penicillin 100 I.U./mL and streptomycin 50 µg/mL in the presence of 20 ng/mL GM-CSF. Medium was replaced on day 3 and 7 of culture and the cells were used between days 10 and 13.

*Stm* expressing DsRed and cultured in the presence of 0.4 mM Hpg for 30 minutes were added to the DC2.4 cells or BMDCs in the above medium without antibiotics as suspensions in PBS at an MOI of 50. After 45 minutes of incubation unbound/non-internalized *Stm* were washed off (2x PBS) and medium was replaced for immediate analysis (t = 0) or further incubation for 1 or 3 hours. Subsequently cells were subjected to flow cytometry, confocal microscopy or Tokuyasu sample preparation for CLEM. Label persistence was determined by incubating bacteria in cell medium at 37°C, collecting samples simultaneously with the cells to obtain identical time points, which were then subjected to flow cytometry sample preparation.

### **Analysis of label incorporation by in-gel fluorescence**

At the indicated time points *Stm* were collected lysed with lysis buffer (50 mM HEPES pH 7.3, 150 mM NaCl and 1% IGEPAL) and incubated at 4°C for 18 h. Subsequently protein concentrations were determined with a Qubit 2.0 fluorimeter (Life Technologies) after which 20 µg of the protein was incubated for 1 h with ccHc-cocktail (0.1 M HEPES pH 7.3, 1 mM CuSO<sub>4</sub>, 10 mM sodium ascorbate, 1 mM THPTA

ligand, 10 mM amino-guanidine, 5  $\mu$ M AF647-azide. Samples were then resuspended in 4x SDS Sample buffer (250 mM Tris HCl pH 6.8, 8% w/v SDS, 40% glycerol, 0.04% w/v bromophenol blue, 5% 2-mercaptoethanol) and incubated at 100°C for 5 minutes before subjecting to SDS-PAGE. Gels were then directly imaged with a Bio-Rad Universal Hood III for in-gel visualization of the fluorescent labelling. As a loading control gels were stained with Coomassie Brilliant Blue. PageRuler Plus Prestained Protein Ladder (Thermo Scientific) was used as a protein standard.

### **Analysis of label incorporation by flow cytometry**

Hpg-labeled *Stm* were collected by centrifugation (3000 rcf) at the indicated time points. DC2.4 cells infected with Hpg-*Stm* were harvested with 0.25% trypsin supplemented with 0.5 mM EDTA and collected by centrifugation (300 rcf) at the indicated time points. Both *Stm* and DC2.4 cells were subjected to the same treatment, with the exception of a differential centrifugation speed and a 1:20 predilution made for the bacteria after fixation: Cells were washed with PBS and fixed in suspension in 4% PFA for 18 h at 4°C, then washed again with PBS and incubated for 20 minutes in staining buffer (100 mM HEPES pH 7.3, 150 mM NaCl, 3% BSA, 0.1% IGEPAL CA-630 and 1  $\mu$ g/mL Hoechst 33342), then washed again with PBS and incubated for 1 h with click cocktail (0.1 M HEPES pH 7.3, 1 mM CuSO<sub>4</sub>, 10 mM sodium ascorbate, 1 mM THPTA ligand, 10 mM amino-guanidine, 5  $\mu$ M AF647-azide), then washed repeatedly (3x5 minutes each) with FACS buffer (PBS pH 7.4, 1% FCS, 1% BSA, 0.1% NaN<sub>3</sub> and 2 mM EDTA) and resuspended in FACS buffer for measurements. All measurements were performed with a Guava easyCyte 12HT Benchtop Flow Cytometer and analyzed with FlowJo V10 (FlowJo software).

### **Preparation of *Stm*-infected BMDC samples for CLEM**

Samples were prepared for cryo-sectioning as described elsewhere.<sup>63,64</sup> Briefly, BMDCs infected with *Stm* were fixed for 24 h in freshly prepared 2% PFA in 0.1 M phosphate buffer. Fixed cells were embedded in 12% gelatin and cut with a razor blade into approx. 1 mm<sup>3</sup> cubes. The sample blocks were infiltrated in phosphate buffer containing 2.3 M sucrose for 3 h. Sucrose-infiltrated sample blocks were mounted on aluminum pins and plunged in liquid nitrogen. The frozen samples were stored under liquid nitrogen.

Ultrathin cell sections were obtained as described elsewhere.<sup>63,64</sup> Briefly, the frozen sample was mounted in a cryo-ultramicrotome (Leica). The sample was trimmed to yield a squared block with a front face of about 300 x 250  $\mu$ m (Diatome trimming tool). Using a diamond knife (Diatome) and antistatic devise (Leica) a ribbon of 150 nm thick sections was produced that was retrieved from the cryo-chamber with a

droplet of 1.15 M sucrose containing 1% methylcellulose. Obtained sections were transferred to a Formvar/carbon-coated titanium TEM grid, additionally coated with blue 0.2  $\mu\text{m}$  FluoSpheres (Thermo Fisher) as fiducial markers.

Sections were labelled as follows; thawed cryo-sections on an EM grid were left for 30 minutes on the surface of 2% gelatin in phosphate buffer at 37°C. Subsequently grids were incubated on drops of PBS/Glycine and PBS/Glycine containing 1% BSA. Grids were then incubated on top of the ccHc-cocktail (0.1 M HEPES pH 7.3, 1 mM  $\text{CuSO}_4$ , 10 mM sodium ascorbate, 1 mM THPTA ligand, 10 mM amino-guanidine, 5  $\mu\text{M}$  AF647-azide) for 1 h and washed 6 times with PBS. In case of confocal microscopy the grids were blocked again with PBS containing 1% BSA. After washing with PBS the sections were then labelled with DAPI (2  $\mu\text{g}/\text{ml}$ ), and additionally washed with PBS and water.

### Microscopy and correlation

The CLEM approach used was adapted from Vicidomini et al.<sup>65</sup> Grids containing the sample sections were washed with 50% glycerol and placed on glass slides (pre-cleaned with 100% ethanol). Grids were then covered with a small drop of 50% glycerol after which a coverslip was mounted over the grid. Coverslips were fixed using Scotch Pressure Sensitive Tape. Samples were imaged with a Leica TCS SP8 confocal microscope (63x oil lens, N.A.=1.4). Confocal microscopy was used as it allowed to make image stacks from the sections at different focus planes, this was convenient as the sections were found to be in different focus planes whilst placed between the glass slides and coverslip.

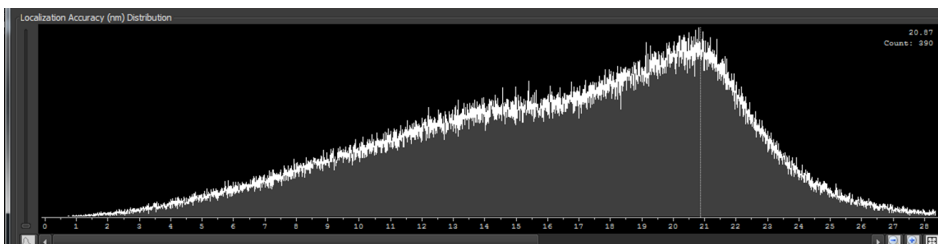
In case of STORM imaging grids containing the sample sections were washed with GLOX buffer (100  $\mu\text{l}$  PBS, 20  $\mu\text{l}$  50% glucose, 20  $\mu\text{l}$  MEA 1M (ethanolamine) and 2  $\mu\text{l}$  GLOX (0.7 mg/ml GLOX, 5 mg/ml catalase in PBS) supplemented with 30% glycerol (60  $\mu\text{L}$ ) and placed on glass slides. Grids were then covered with a small drop of GLOX buffer after which a coverslip was mounted over the grid. STORM images were acquired using a Nikon N-STORM system configured for total internal reflection fluorescence (TIRF) imaging. Excitation inclination was tuned to adjust focus and to maximize the signal-to-noise ratio. AF647 was excited illuminating the sample with the 647 nm (160 mW, 1.9  $\text{kW cm}^{-2}$ ) laser line built into the microscope. Fluorescence was collected by means of a Nikon 100x, 1.4NA oil immersion objective and passed through a quad-band-pass dichroic filter (97335 Nikon). 20,000 frames at 50 Hz were acquired for the 647 channel. Images were recorded onto a 256  $\times$  256 pixel region (pixel size 160 nm) of a CMOS camera. STORM images were analyzed with the STORM module of the NIS element Nikon software.<sup>66</sup>

After fluorescence or STORM microscopy the EM grid with the sections was removed from the glass slide, rinsed in distilled water and incubated for 5 minutes on droplets of uranyl acetate (0.4%)/methylcellulose (1.8%). Excess of uranyl acetate/methylcellulose was blotted away and grids were air-dried. EM imaging was performed with an Tecnai 12 BioTwin transmission electron microscope (FEI) at 120 kV acceleration voltage.<sup>67</sup>

Correlation of confocal and EM images was performed in Adobe Photoshop CS6. In Adobe Photoshop, the LM image was copied as a layer into the EM image and made 50% transparent. Transformation of the LM image was necessary to match it to the larger scale of the EM image. This was performed via isotropic scaling and rotation. Interpolation settings; bicubic smoother. Alignment at low magnification was carried out with the aid of nuclear DAPI staining in combination with the shape of the cells, at high magnification alignment was performed using the fiducial beads.<sup>68</sup>

### STORM analysis

Resolution Calculations STORM module in the Nikon NIS-software is able to automatically calculate the localization precision distribution for each image. As it can be seen below, the maximum of the distribution is 20 nm, with most of the localizations below 20 and decreasing sharply from 20 to 25 nm.



These numbers are well in agreement with the theoretical localization precision. The localization precision is defined as:

$$\sigma^2 = \frac{s^2 + a^2/12}{N} + \frac{8\pi^2 s^4 b^2}{a^2 N^2}$$

Where,

s: width of the PFS

N: number of detected photons

a: size of pixels on the camera

b: background intensity

Which can be simplified<sup>69</sup> to:

$$\sigma_x \geq \frac{s}{\sqrt{N}}$$

The average  $s$  for one of the images was calculated to be  $338 \pm 44$  nm (for 538948 localizations). Also, the average for the number of photons for the same image is 1253, with a significant population above that value. Therefore, as the average  $s = 338$  nm and the average  $N=1253$  photons,  $\sigma_x \geq 9.54$  nm, resulting in the claimed 20 nm resolution. Single molecule localization and fitting was performed using the STORM module of NIS Elements by performing a Gaussian fitting based on the following parameters:

*Minimum and maximum height:* The darkest bright point was selected to be identified as a molecule and its brightness minus the background intensity was the minimum height. In our case it was set to 150. The maximum height for the used system with a sCMOS camera is 65000 and the baseline was set to 100.

For the PSF, the initial fit width was set to 300, with a minimum width of 200 and a maximum width of 400. The average for an image was calculated to be  $338 \pm 44$  nm (based on 538948 localizations).

This parameter was tested on different frames and optimized using all frames selected. The first 500 frames were discarded, due to incomplete photo-switching. This analysis yielded a molecule list in binary format from which multiple emitters are automatically discarded prior to analysis.

STORM NIS-software renders a molecule list in binary format whose coordinates are translated into an image. STORM images are shown in cross or Gaussian display mode in Nikon software. Cross takes into account directly the localizations while Gaussian, the one used in our case, is a Gaussian rendering of the localizations considering lateral localization accuracy (with an average of  $17.9 \pm 4.6$ ) for each localization.



4.5 Supplemental Figures

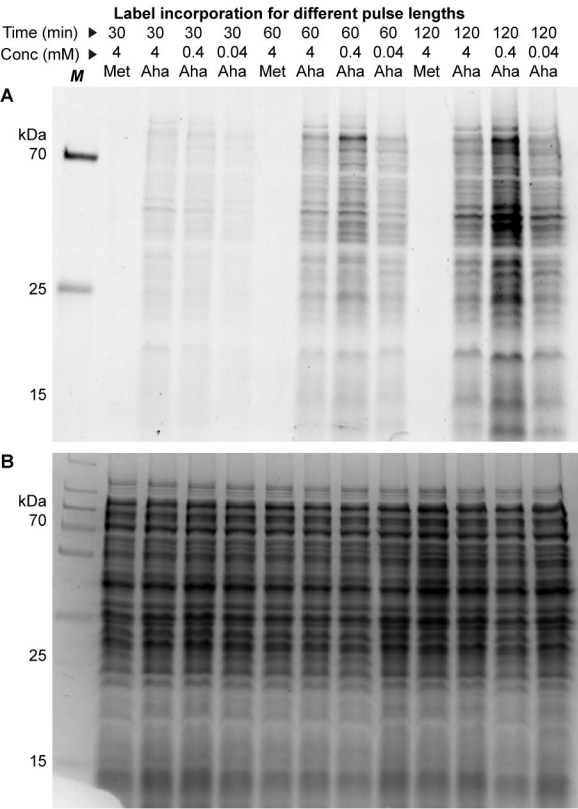


**Figure S1.** Optimization of Aha incorporation in *Stm* by SDS-PAGE. *Stm* were incubated with increasing concentrations of Aha or 4 mM Met (control) in SelenoMet medium for up to 120 min, then lysed, ccHc-reacted with AF647-alkyne and separated by SDS-PAGE for in-gel fluorescence analysis (**A**). Coomassie Brilliant Blue staining was used to show comparable protein loading for each lane (**B**).

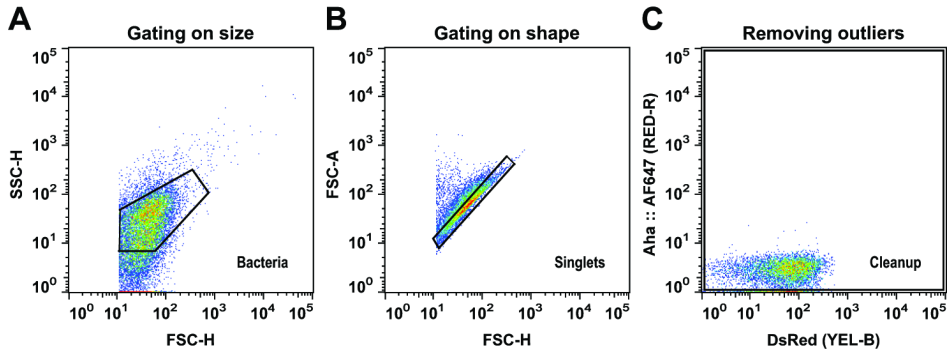


**Figure S2.** Gating strategy for measurement of *Stm* by flow cytometry. The bacteria were gated on size (A) and shape (B), and completely non-fluorescent were removed with a cleanup gate (C) to exclude any bacteria-unrelated particles from analysis.

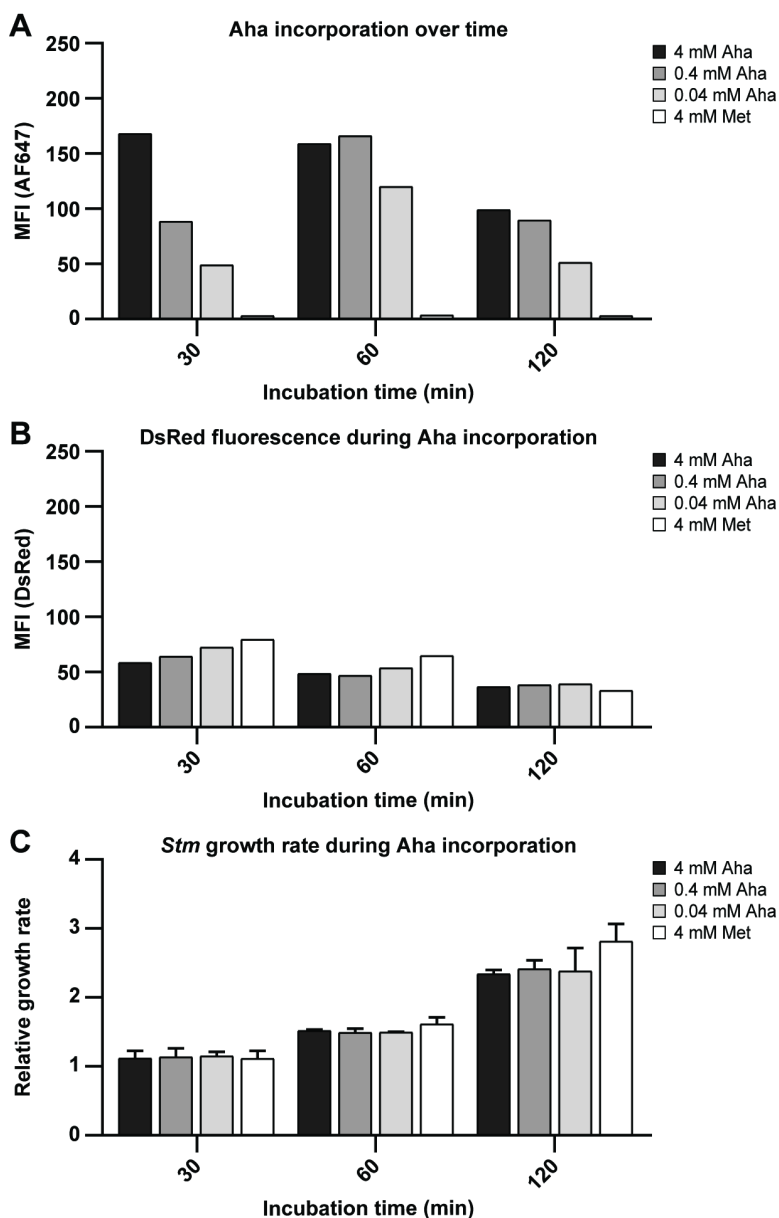


**Figure S3.** Optimization of Aha incorporation in *Stm* by flow cytometric analysis, part 2. DsRed-expressing *Stm* were incubated with increasing concentrations of Aha or 4 mM Met (control) in SelenoMet medium for up to 120 min, then ccHc-reacted with AF647-alkyne for detection by flow cytometry. **(A)** Aha incorporation over time is shown as the Mean Fluorescence Intensity (MFI) of the reacted AF647 (Figure 2A). **(B)** The effect of Aha incorporation on the DsRed fluorescent protein is shown as the MFI of DsRed (Figure 2B). **(C)** The effect of Aha incorporation on the viability of *Stm* is shown as the relative growth rate, determined by OD<sub>600</sub> measurements, normalized to the initial OD value at t = 0. Error bars represent the standard deviation from the mean (n = 2).

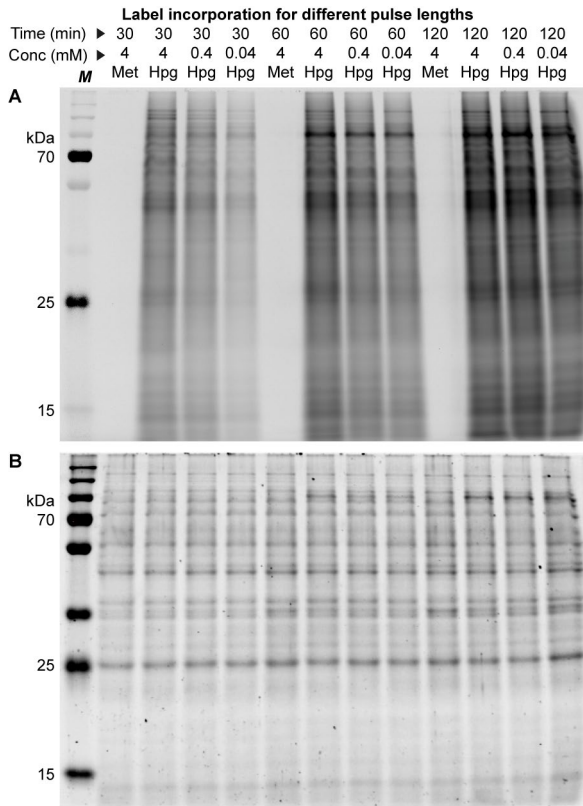


**Figure S4.** Optimization of Hpg incorporation in *Stm* by SDS-PAGE. *Stm* were incubated with increasing concentrations of Hpg or 4 mM Met (control) in SelenoMet medium for up to 120 min, then lysed, ccHc-reacted with AF647-azide and separated by SDS-PAGE for in-gel fluorescence analysis (**A**). Coomassie Brilliant Blue staining was used to show comparable protein loading for each lane (**B**).

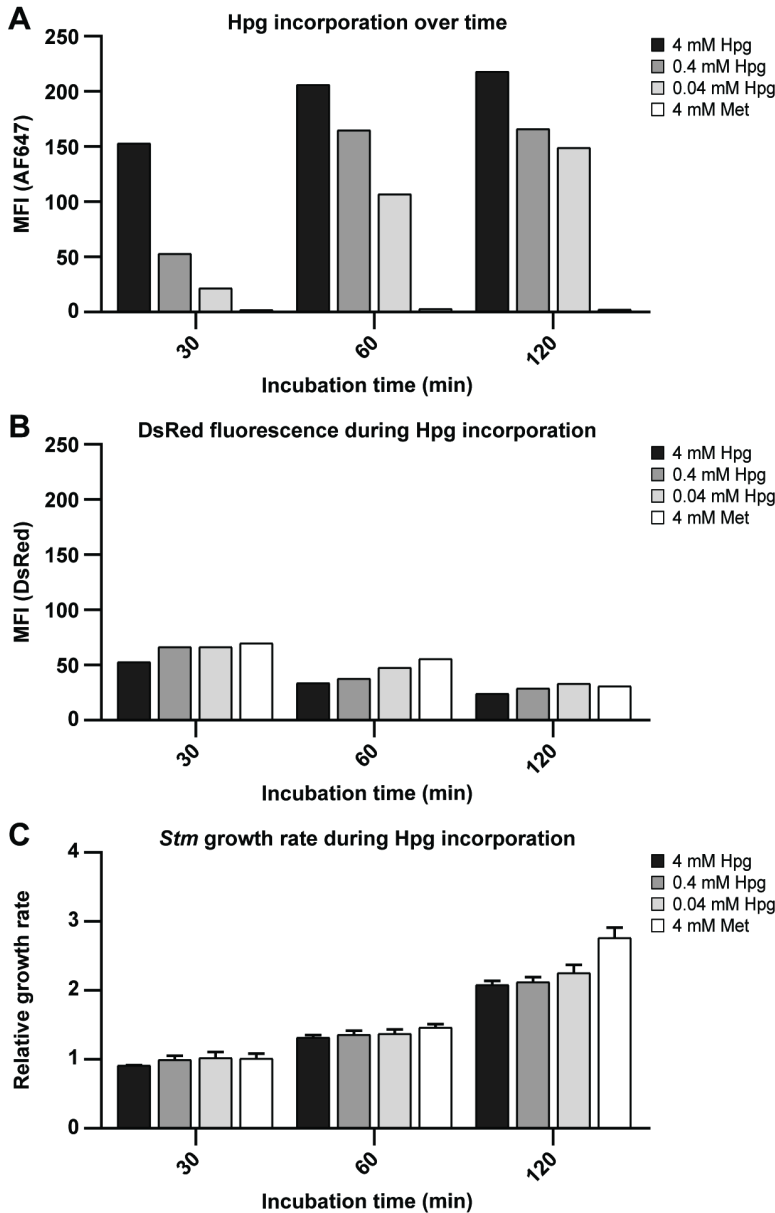


**Figure S5.** Optimization of Hpg incorporation in *Stm* by flow cytometric analysis, part 2. DsRed-expressing *Stm* were incubated with increasing concentrations of Hpg or 4 mM Met (control) in SelenoMet medium for up to 120 min, then ccHc-reacted with AF647-azide for detection by flow cytometry. **(A)** Hpg incorporation over time is shown as the Mean Fluorescence Intensity (MFI) of the reacted AF647 (Figure 3A). **(B)** The effect of Hpg incorporation on the DsRed fluorescent protein is shown as the MFI of DsRed (Figure 3B). **(C)** The effect of Hpg incorporation on the viability of *Stm* is shown as the relative growth rate, determined by OD<sub>600</sub> measurements, normalized to the initial OD value at t = 0. Error bars represent the standard deviation from the mean (n = 2).

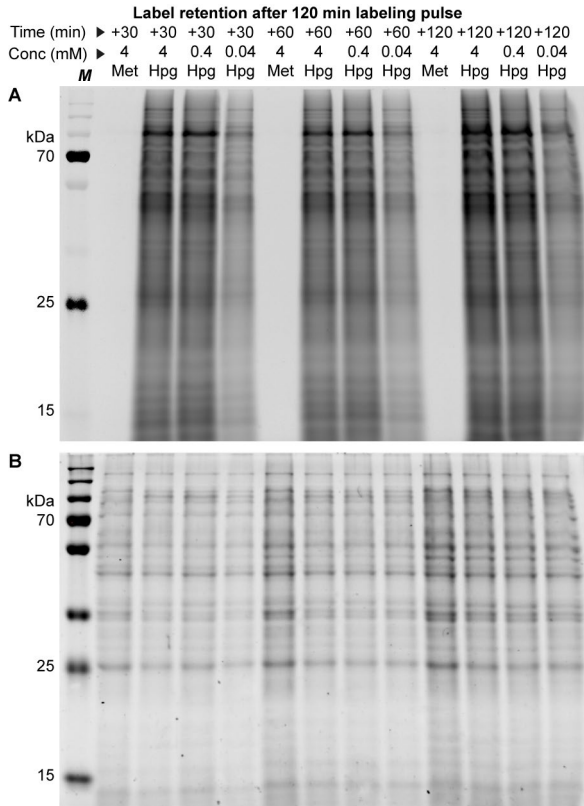


**Figure S6.** Hpg retention during outgrowth of *Stm* by SDS-PAGE. *Stm* were incubated with increasing concentrations of Hpg or 4 mM Met (control) in SelenoMet medium for up to 120 min, then washed and resuspended in fresh LB medium and additionally incubated for up to 120 min. *Stm* were then lysed, ccHc-reacted with AF647-azide and separated by SDS-PAGE for in-gel fluorescence analysis (**A**). Coomassie Brilliant Blue staining was used to show comparable protein loading for each lane (**B**).

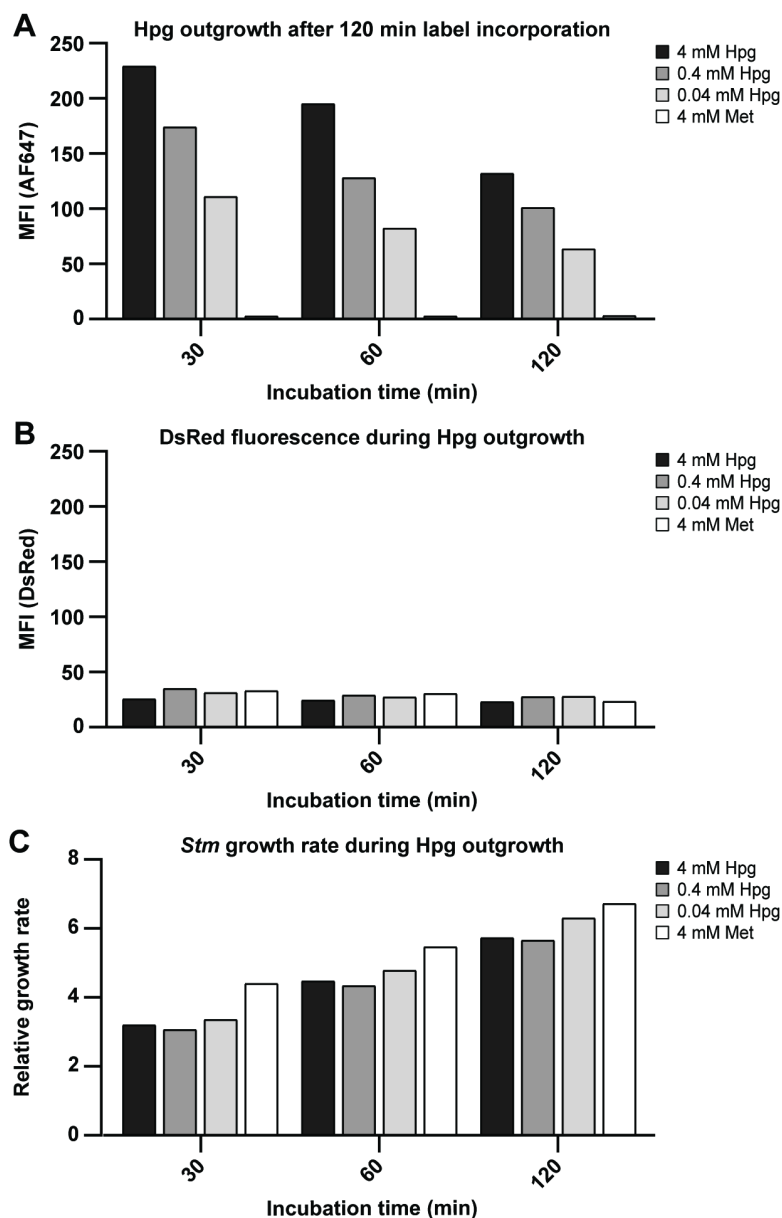


**Figure S7.** Label retention and growth recovery of Hpg-labeled *Stm* by flow cytometric analysis, part 2. DsRed-expressing *Stm* were incubated with increasing concentrations of Hpg or 4 mM Met (control) in SelenoMet medium for 120 min, washed with PBS and resuspended in fresh LB medium and incubated again for up to 120 min, then cHc-reacted with AF647-azide for detection by flow cytometry. **(A)** Hpg retention over time (outgrowth) is shown as the Mean Fluorescence Intensity (MFI) of the reacted AF647 (Figure 4A). **(B)** The effect of Hpg outgrowth on the DsRed fluorescent protein is shown as the MFI of DsRed (Figure 4B). **(C)** The effect of Hpg incorporation on the growth recovery of *Stm* is shown as the relative growth rate, determined by OD<sub>600</sub> measurements, normalized to the initial OD value at t = 0 before label incorporation (n = 1).

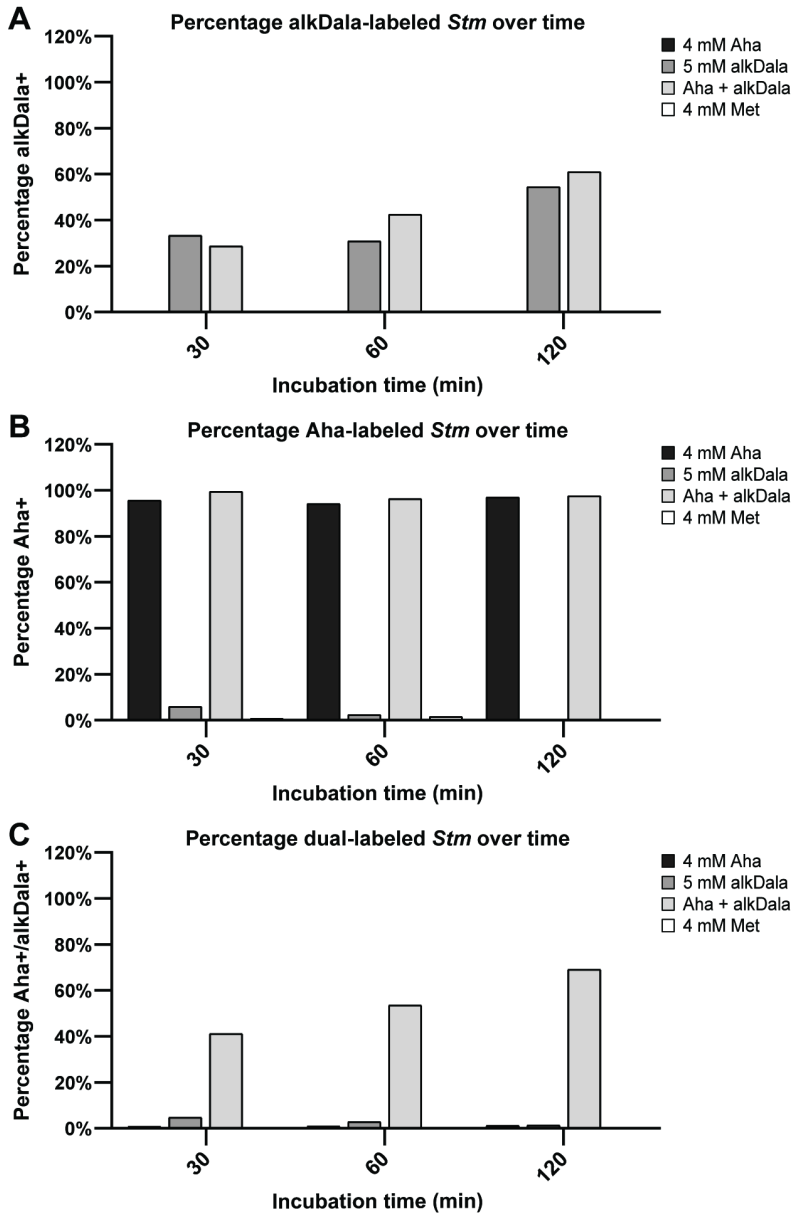


**Figure S8.** Optimization of alkDala labeling and Aha/alkDala dual labeling of *Stm* by flow cytometric analysis, part 2. *Stm* were incubated with 4 mM Aha, 4 mM Met + 5 mM alkDala, 4 mM Aha + 5 mM alkDala or 4 mM Met (control) in SelenoMet medium for up to 120 min, then ccHc-reacted with AF647-azide (alkDala) and AF488-alkyne (Aha) for detection by flow cytometry. (A) The percentage alkDala-labeled *Stm* (alkDala+) over time is shown, based on the fluorescence intensity of the reacted AF647 (Figure 5A). (B) The percentage Aha-labeled *Stm* (Aha+) over time is shown, based on the fluorescence intensity of the reacted AF488 (Figure 5B). (C) The percentage dual-labeled *Stm* (Aha+/alkDala+) over time is shown, based on the fluorescence intensity of the reacted AF647 and AF488 (Figure 5C).



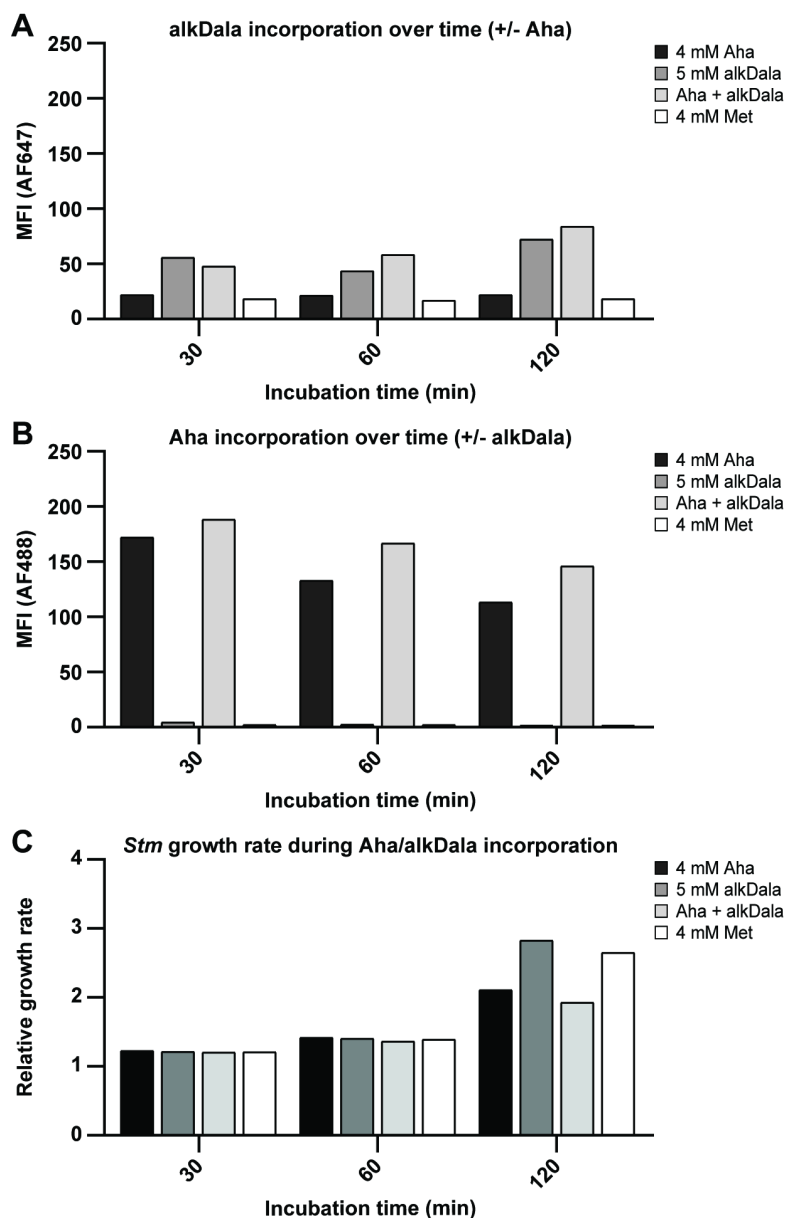


**Figure S9.** Optimization of alkDala labeling and Aha/alkDala dual labeling of *Stm* by flow cytometric analysis, part 3. *Stm* were incubated with 4 mM Aha, 4 mM Met + 5 mM alkDala, 4 mM Aha + 5 mM alkDala or 4 mM Met (control) in SelenoMet medium for up to 120 min, then ccHc-reacted with AF647-azide (alkDala) and AF488-alkyne (Aha) for detection by flow cytometry. **(A)** alkDala incorporation over time is shown as the Mean Fluorescence Intensity (MFI) of the reacted AF647 (Figure 5A). **(B)** Aha incorporation over time is shown as the MFI of the reacted AF488 (Figure 5B). **(C)** The effect of alkDala and/or Aha incorporation on the viability of *Stm* is shown as the relative growth rate, determined by OD<sub>600</sub> measurements, normalized to the initial OD value at t = 0 (n = 1).

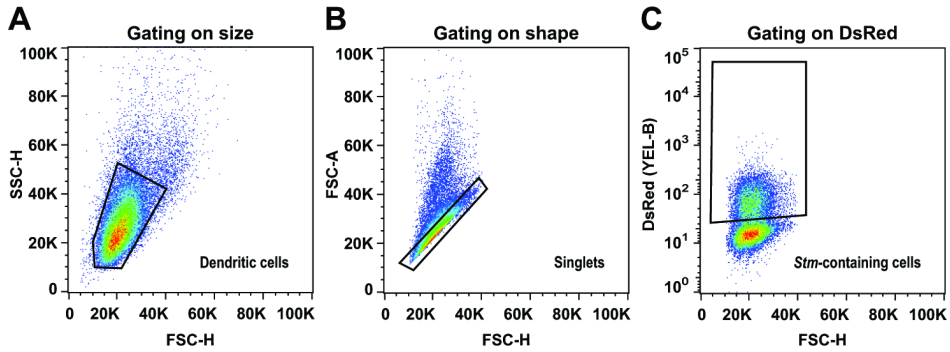


**Figure S10.** Gating strategy for measurement of *Stm*-containing DC2.4 cells by flow cytometry. DCs were gated on size (A) and shape (B) and *Stm*-containing cells were selected based on DsRed (C), which is only expressed by *Stm*.

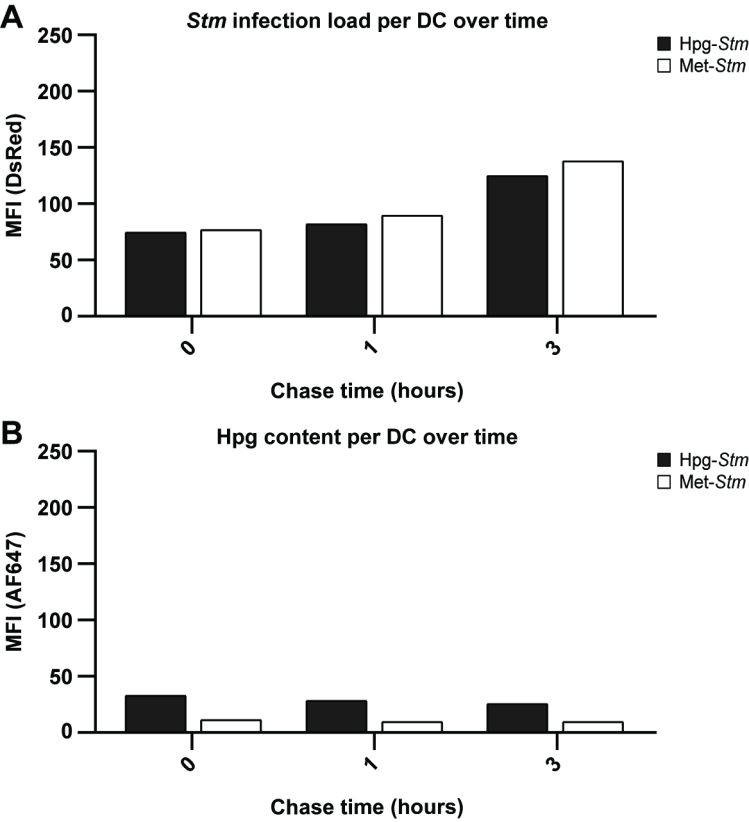


**Figure S11.** Infection controls, bioorthogonal label retention and *Stm* proliferation in DC2.4 cells, part 2. DsRed-expressing *Stm* were first incubated with 0.4 mM Hpg (Hpg-*Stm*) or 4 mM Met (Met-*Stm*) for 30 min in SelenoMet, then washed to remove excess Hpg and added to DCs at an MOI of 50 for 45 min (pulse). *Stm*-infected BDMCs were then washed to remove non-internalized *Stm* and incubated for an additional 0, 1 or 3 hours (chase), followed by ccHc-reaction with AF647-azide for detection by flow cytometry. **(A)** The *Stm* infection load was compared between Hpg-*Stm* and Met-*Stm* over time, based on the DsRed intensity per DC, shown as MFI. **(B)** The intracellular Hpg retention of *Stm* was followed over time in DCs, shown as MFI of the reacted AF647.

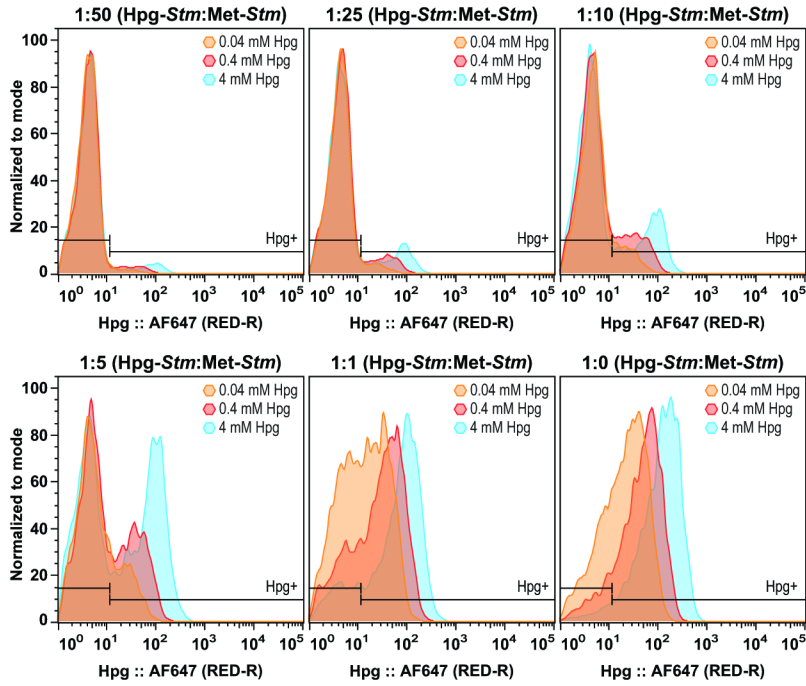


**Figure S12.** Hpg-labeled and unlabeled *Stm* mixed in various ratios for the optimization of STORM. *Stm* were grown in presence of increasing concentrations of Hpg (0.04–4 mM) and mixed in various ratios with unlabeled *Stm*, grown in presence of 4 mM Met.

## 4.6 References

- (1) Mitchell, G.; Isberg, R. R. Innate Immunity to Intracellular Pathogens: Balancing Microbial Elimination and Inflammation. *Cell Host and Microbe*. Cell Press August 9, **2017**, pp 166–175.
- (2) Pandey, S.; Kawai, T.; Akira, S. Microbial Sensing by Toll-like Receptors and Intracellular Nucleic Acid Sensors. *Cold Spring Harb. Perspect. Biol.* **2015**, *7* (1), a016246.
- (3) Siegrist, M. S.; Whiteside, S.; Jewett, J. C.; Aditham, A.; Cava, F.; Bertozzi, C. R. D-Amino Acid Chemical Reporters Reveal Peptidoglycan Dynamics of an Intracellular Pathogen. *ACS Chem. Biol.* **2013**, *8* (3), 500–505.
- (4) Shieh, P.; Siegrist, M. S.; Cullen, A. J.; Bertozzi, C. R. Imaging Bacterial Peptidoglycan with Near-Infrared Fluorogenic Azide Probes. *Proc. Natl. Acad. Sci.* **2014**, *111* (15), 5456–5461.
- (5) Liechti, G. W.; Kuru, E.; Hall, E.; Kalinda, A.; Brun, Y. V.; Vannieuwenhze, M.; Maurelli, A. T. A New Metabolic Cell-Wall Labelling Method Reveals Peptidoglycan in Chlamydia Trachomatis. *Nature* **2014**, *506* (7489), 507–510.
- (6) Swarts, B. M.; Holsclaw, C. M.; Jewett, J. C.; Alber, M.; Fox, D. M.; Siegrist, M. S.; Leary, J. A.; Kalscheuer, R.; Bertozzi, C. R. Probing the Mycobacterial Trehalome with Bioorthogonal Chemistry. *J. Am. Chem. Soc.* **2012**, *134* (39), 16123–16126.
- (7) Backus, K. M.; Boshoff, H. I.; Barry, C. E. C. S.; Boutureira, O.; Patel, M. K.; D'Hooge, F.; Lee, S. S.; Via, L. E.; Tahlan, K.; Barry, C. E. C. S.; Davis, B. G. Uptake of Unnatural Trehalose Analogs as a Reporter for Mycobacterium Tuberculosis. *Nat. Chem. Biol.* **2011**, *7* (4), 228–235.
- (8) Rodriguez-Rivera, F. P.; Zhou, X.; Theriot, J. A.; Bertozzi, C. R. Visualization of Mycobacterial Membrane Dynamics in Live Cells. *J. Am. Chem. Soc.* **2017**, *139* (9), 3488–3495.
- (9) Dieterich, D. C.; Link, A. J.; Graumann, J.; Tirrell, D. A.; Schuman, E. M. Selective Identification of Newly Synthesized Proteins in Mammalian Cells Using Bioorthogonal Noncanonical Amino Acid Tagging (BONCAT). *Proc. Natl. Acad. Sci.* **2006**, *103* (25), 9482–9487.
- (10) Mahdavi, A.; Szychowski, J.; Ngo, J. T.; Sweredoski, M. J.; Graham, R. L. J.; Hess, S.; Schneewind, O.; Mazmanian, S. K.; Tirrell, D. A. Identification of Secreted Bacterial Proteins by Noncanonical Amino Acid Tagging. *Proc. Natl. Acad. Sci.* **2014**, *111* (1), 433–438.
- (11) Grammel, M.; Dossa, P. D.; Taylor-Salmon, E.; Hang, H. C. Cell-Selective Labeling of Bacterial Proteomes with an Orthogonal Phenylalanine Amino Acid Reporter. *Chem. Commun.* **2012**, *48* (10), 1473–1474.
- (12) Grammel, M.; Zhang, M. M.; Hang, H. C. Orthogonal Alkynyl Amino Acid Reporter for Selective Labeling of Bacterial Proteomes during Infection. *Angew. Chemie - Int. Ed.* **2010**, *49* (34), 5970–5974.
- (13) Lin, S.; Zhang, Z.; Xu, H.; Li, L.; Chen, S.; Li, J.; Hao, Z.; Chen, P. R. Site-Specific Incorporation of Photo-Cross-Linker and Bioorthogonal Amino Acids into Enteric Bacterial Pathogens. *J. Am. Chem. Soc.* **2011**, *133* (50), 20581–20587.
- (14) Ngo, J. T.; Champion, J. A.; Mahdavi, A.; Tanrikulu, I. C.; Beatty, K. E.; Connor, R. E.; Yoo, T. H.; Dieterich, D. C.; Schuman, E. M.; Tirrell, D. A. Cell-Selective Metabolic Labeling of Proteins. *Nat. Chem. Biol.* **2009**, *5* (10), 715–717.
- (15) Chande, A. G.; Siddiqui, Z.; Midha, M. K.; Sirohi, V.; Ravichandran, S.; Rao, K. V. S. Selective Enrichment of Mycobacterial Proteins from Infected Host Macrophages. *Sci. Rep.* **2015**, *5* (13430), 1–15.
- (16) Hatzenpichler, R.; Connon, S. A.; Goudeau, D.; Malmstrom, R. R.; Woyke, T.; Orphan, V. J. Visualizing in Situ Translational Activity for Identifying and Sorting Slow-Growing

- Archaeal - Bacterial Consortia. *Proc. Natl. Acad. Sci. U. S. A.* **2016**, *113* (28), E4069–E4078.
- (17) van Elsland, D. M.; Bos, E.; Overkleeft, H. S.; Koster, A. J.; van Kasteren, S. I. The Potential of Bioorthogonal Chemistry for Correlative Light and Electron Microscopy: A Call to Arms. *J. Chem. Biol.* **2015**, *8* (4), 153–157.
  - (18) van Elsland, D. M.; Bos, E.; de Boer, W.; Overkleeft, H. S.; Koster, A. J.; van Kasteren, S. I. Detection of Bioorthogonal Groups by Correlative Light and Electron Microscopy Allows Imaging of Degraded Bacteria in Phagocytes. *Chem. Sci.* **2016**, *7* (1), 752–758.
  - (19) van Elsland, D. M.; Bos, E.; Pawlak, J. B.; Overkleeft, H. S.; Koster, A. J.; van Kasteren, S. I. Correlative Light and Electron Microscopy Reveals Discrepancy between Gold and Fluorescence Labelling. *J. Microsc.* **2017**, *267* (3), 309–317.
  - (20) Tornøe, C. W.; Christensen, C.; Meldal, M. Peptidotriazoles on Solid Phase: [1,2,3]-Triazoles by Regiospecific Copper(I)-Catalyzed 1,3-Dipolar Cycloadditions of Terminal Alkynes to Azides. *J. Org. Chem.* **2002**, *67* (9), 3057–3064.
  - (21) Rostovtsev, V. V.; Green, L. G.; Fokin, V. V.; Sharpless, K. B. A Stepwise Huisgen Cycloaddition Process: Copper(I)-Catalyzed Regioselective “Ligation” of Azides and Terminal Alkynes. *Angew. Chemie - Int. Ed.* **2002**, *41* (14), 2596–2599.
  - (22) Klück, K. L.; Tirrell, D. A. Protein Engineering by in Vivo Incorporation of Non-Natural Amino Acids: Control of Incorporation of Methionine Analogues by Methionyl-TRNA Synthetase. *Tetrahedron* **2000**, *56* (48), 9487–9493.
  - (23) Abbe, E. Beiträge Zur Theorie Des Mikroskops Und Der Mikroskopischen Wahrnehmung: I. Die Construction von Mikroskopen Auf Grund Der Theorie. *Arch. für mikroskopische Anat.* **1873**, *9* (1), 413–418.
  - (24) Sahl, S. J.; Hell, S. W.; Jakobs, S. Fluorescence Nanoscopy in Cell Biology. *Nat. Rev. Mol. Cell Biol.* **2017**, *18* (11), 685–701.
  - (25) Beyond the Diffraction Limit. *Nature Photonics*. Nature Publishing Group July **2009**, p 361.
  - (26) Betzig, E.; Patterson, G. H.; Sougrat, R.; Lindwasser, O. W.; Olenych, S.; Bonifacino, J. S.; Davidson, M. W.; Lippincott-Schwartz, J.; Hess, H. F. Imaging Intracellular Fluorescent Proteins at Nanometer Resolution. *Science (80- )*. **2006**, *313* (5793), 1642–1645.
  - (27) Kopeck, B. G.; Paez-Segala, M. G.; Shtengel, G.; Sochacki, K. A.; Sun, M. G.; Wang, Y.; Xu, C. S.; Van Engelenburg, S. B.; Taraska, J. W.; Looger, L. L.; Hess, H. F. Diverse Protocols for Correlative Super-Resolution Fluorescence Imaging and Electron Microscopy of Chemically Fixed Samples. *Nat. Protoc.* **2017**, *12* (5), 916–946.
  - (28) De Souza, N. Super-Resolution CLEM: Correlated Light and Electron Microscopy (CLEM) Is Particularly Powerful When Applied in Super-Resolution. *Nat. Methods* **2014**, *12* (1), 37.
  - (29) Suleiman, H.; Zhang, L.; Roth, R.; Heuser, J. E.; Miner, J. H.; Shaw, A. S.; Dani, A. Nanoscale Protein Architecture of the Kidney Glomerular Basement Membrane. *Elife* **2013**, *2013* (2).
  - (30) Watanabe, S.; Punge, A.; Hollopeter, G.; Willig, K. I.; Hobson, R. J.; Davis, M. W.; Hell, S. W.; Jorgensen, E. M. Protein Localization in Electron Micrographs Using Fluorescence Nanoscopy. *Nat. Methods* **2011**, *8* (1), 80–84.
  - (31) Sochacki, K. A.; Shtengel, G.; van Engelenburg, S. B.; Hess, H. F.; Taraska, J. W. Correlative Super-Resolution Fluorescence and Metal-Replica Transmission Electron Microscopy. *Nat. Methods* **2014**, *11* (3), 305–308.
  - (32) Watanabe, S.; Richards, J.; Hollopeter, G.; Hobson, R. J.; Davis, W. M.; Jorgensen, E. M. Nano-FEM: Protein Localization Using Photo-Activated Localization Microscopy and Electron Microscopy. *J. Vis. Exp.* **2012**, No. 69, 3995.
  - (33) Kopeck, B. G.; Shtengel, G.; Xu, C. S.; Clayton, D. A.; Hess, H. F. Correlative 3D Superresolution Fluorescence and Electron Microscopy Reveal the Relationship of

- Mitochondrial Nucleoids to Membranes. *Proc. Natl. Acad. Sci. U. S. A.* **2012**, *109* (16), 6136–6141.
- (34) Kopek, B. G.; Shtengel, G.; Grimm, J. B.; Clayton, D. A.; Hess, H. F. Correlative Photoactivated Localization and Scanning Electron Microscopy. *PLoS One* **2013**, *8* (10), e77209.
  - (35) Tam, J.; Merino, D. Stochastic Optical Reconstruction Microscopy (STORM) in Comparison with Stimulated Emission Depletion (STED) and Other Imaging Methods. *J. Neurochem.* **2015**, *135* (4), 643–658.
  - (36) Godin, A. G.; Lounis, B.; Cognet, L. Super-Resolution Microscopy Approaches for Live Cell Imaging. *Biophys. J.* **2014**, *107* (8), 1777–1784.
  - (37) MacDonald, L.; Baldini, G.; Storrie, B. Does Super Resolution Fluorescence Microscopy Obsolete Previous Microscopic Approaches to Protein Co-Localization? *Methods Mol. Biol.* **2015**, *1270*, 255–275.
  - (38) Oddone, A.; Vilanova, I. V.; Tam, J.; Lakadamyali, M. Super-Resolution Imaging with Stochastic Single-Molecule Localization: Concepts, Technical Developments, and Biological Applications. *Microsc. Res. Tech.* **2014**, *77* (7), 502–509.
  - (39) Dempsey, G. T.; Vaughan, J. C.; Chen, K. H.; Bates, M.; Zhuang, X. Evaluation of Fluorophores for Optimal Performance in Localization-Based Super-Resolution Imaging. *Nat. Methods* **2011**, *8* (12), 1027–1040.
  - (40) Alpuche-Aranda, C. M.; Racoosin, E. L.; Swanson, J. A.; Miller, S. I. Salmonella Stimulate Macrophage Macropinocytosis and Persist within Spacious Phagosomes. *J. Exp. Med.* **1994**, *179* (2), 601–608.
  - (41) Haraga, A.; Ohlson, M. B.; Miller, S. I. Salmonellae Interplay with Host Cells. *Nature Reviews Microbiology*. Nature Publishing Group January **2008**, pp 53–66.
  - (42) Forest, C. G.; Ferraro, E.; Sabbagh, S. C.; Daigle, F. Intracellular Survival of Salmonella Enterica Serovar Typhi in Human Macrophages Is Independent of Salmonella Pathogenicity Island (SPI)-2. *Microbiology* **2010**, *156* (12), 3689–3698.
  - (43) Krieger, V.; Liebl, D.; Zhang, Y.; Rajashekar, R.; Chlanda, P.; Giesker, K.; Chikaballi, D.; Hensel, M. Reorganization of the Endosomal System in Salmonella-Infected Cells: The Ultrastructure of Salmonella-Induced Tubular Compartments. *PLoS Pathog.* **2014**, *10* (9), e1004374.
  - (44) Scanu, T.; Spaapen, R. M.; Bakker, J. M.; Pratap, C. B.; Wu, L. en; Hofland, I.; Broeks, A.; Shukla, V. K.; Kumar, M.; Janssen, H.; Song, J. Y.; Neefjes-Borst, E. A.; te Riele, H.; Holden, D. W.; Nath, G.; Neefjes, J. Salmonella Manipulation of Host Signaling Pathways Provokes Cellular Transformation Associated with Gallbladder Carcinoma. *Cell Host Microbe* **2015**, *17* (6), 763–774.
  - (45) van Elsland, D. M. A Bioorthogonal Chemistry Approach to the Study of Biomolecules in Their Ultrastructural Cellular Context, **2018**.
  - (46) West, M. A.; Wallin, R. P. A.; Matthews, S. P.; Svensson, H. G.; Zaru, R.; Ljunggren, H. G.; Prescott, A. R.; Watts, C. Enhanced Dendritic Cell Antigen Capture via Toll-like Receptor-Induced Actin Remodeling. *Science (80-. ).* **2004**, *305* (5687), 1153–1157.
  - (47) Méresse, S.; Steele-Mortimer, O.; Finlay, B. B.; Gorvel, J. P. The Rab7 GTPase Controls the Maturation of Salmonella Typhimurium-Containing Vacuoles in HeLa Cells. *EMBO J.* **1999**, *18* (16), 4394–4403.
  - (48) Bakkum, T.; van Leeuwen, T.; Sarris, A. J. C.; van Elsland, D. M.; Poulcharidis, D.; Overkleeft, H. S.; van Kasteren, S. I. Quantification of Bioorthogonal Stability in Immune Phagocytes Using Flow Cytometry Reveals Rapid Degradation of Strained Alkynes. *ACS Chem. Biol.* **2018**, *13* (5), 1173–1179.
  - (49) Lowrie, D. B.; Aber, V. R.; Carrol, M. E. Division and Death Rates of Salmonella Typhimurium inside Macrophages: Use of Penicillin as a Probe. *J. Gen. Microbiol.* **1979**, *110* (2), 409–419.

- (50) Nahidiazar, L.; Agronskaia, A. V.; Broertjes, J.; van den Broek, B.; Jalink, K. Optimizing Imaging Conditions for Demanding Multi-Color Super Resolution Localization Microscopy. *PLoS One* **2016**, *11* (7), e0158884.
- (51) Ngo, J. T.; Adams, S. R.; Deerinck, T. J.; Boassa, D.; Rodriguez-Rivera, F.; Palida, S. F.; Bertozzi, C. R.; Ellisman, M. H.; Tsien, R. Y. Click-EM for Imaging Metabolically Tagged Nonprotein Biomolecules. *Nat. Chem. Biol.* **2016**, *12* (6), 459–465.
- (52) Scotuzzi, M.; Kuipers, J.; Wensveen, D. I.; De Boer, P.; Hagen, K. C. W.; Hoogenboom, J. P.; Giepmans, B. N. G. Multi-Color Electron Microscopy by Element-Guided Identification of Cells, Organelles and Molecules. *Sci. Rep.* **2017**, *7* (March), 1–8.
- (53) Adams, S. R.; Mackey, M. R.; Ramachandra, R.; Palida Lemieux, S. F.; Steinbach, P.; Bushong, E. A.; Butko, M. T.; Giepmans, B. N. G.; Ellisman, M. H.; Tsien, R. Y. Multicolor Electron Microscopy for Simultaneous Visualization of Multiple Molecular Species. *Cell Chem. Biol.* **2016**, *23* (11), 1417–1427.
- (54) Mateos-Gil, P.; Letschert, S.; Doose, S.; Sauer, M. Super-Resolution Imaging of Plasma Membrane Proteins with Click Chemistry. *Front. Cell Dev. Biol.* **2016**, *4* (SEP), 1–16.
- (55) Erdmann, R. S.; Takakura, H.; Thompson, A. D.; Rivera-Molina, F.; Allgeyer, E. S.; Bewersdorf, J.; Toomre, D.; Schepartz, A. Super-Resolution Imaging of the Golgi in Live Cells with a Bioorthogonal Ceramide Probe. *Angew. Chemie - Int. Ed.* **2014**, *53* (38), 10242–10246.
- (56) Zhang, M. M.; Tsou, L. K.; Charron, G.; Raghavan, A. S.; Hang, H. C. Tandem Fluorescence Imaging of Dynamic S-Acylation and Protein Turnover. *Proc. Natl. Acad. Sci. U. S. A.* **2010**, *107* (19), 8627–8632.
- (57) Li, N.; Lim, R. K. V.; Edwardraja, S.; Lin, Q. Copper-Free Sonogashira Cross-Coupling for Functionalization of Alkyne-Encoded Proteins in Aqueous Medium and in Bacterial Cells. *J. Am. Chem. Soc.* **2011**, *133* (39), 15316–15319.
- (58) Chenault, H. K.; Dahmer, J.; Whitesides, G. M. Kinetic Resolution of Unnatural and Rarely Occurring Amino Acids: Enantioselective Hydrolysis of N-Acyl Amino Acids Catalyzed by Acylase I. *J. Am. Chem. Soc.* **1989**, *111* (16), 6354–6364.
- (59) Biagini, S. C. G.; Gibson, S. E.; Keen, S. P. Cross-Metathesis of Unsaturated Alpha-Amino Acid Derivatives. *J. Chem. Soc. Perkin Trans. 1* **1998**, *1*, 2485–2500.
- (60) Dong, S.; Merkel, L.; Moroder, L.; Budisa, N. Convenient Syntheses of Homopropargylglycine. *J. Pept. Sci.* **2008**, *14* (10), 1148–1150.
- (61) Albers, H. M. H. G.; Kuijl, C.; Bakker, J.; Hendrickx, L.; Wekker, S.; Farhou, N.; Liu, N.; Blasco-Moreno, B.; Scanu, T.; Den Hertog, J.; Celie, P.; Ova, H.; Neefjes, J. Integrating Chemical and Genetic Silencing Strategies to Identify Host Kinase-Phosphatase Inhibitor Networks That Control Bacterial Infection. *ACS Chem. Biol.* **2014**, *9* (2), 414–422.
- (62) Lutz, M. B.; Kukutsch, N.; Ogilvie, A. L. ; Rößner, S.; Koch, F.; Romani, N.; Schuler, G. An Advanced Culture Method for Generating Large Quantities of Highly Pure Dendritic Cells from Mouse Bone Marrow. *J. Immunol. Methods* **1999**, *223* (1), 77–92.
- (63) Peters, P. J. Cryo-Immunogold Electron Microscopy. *Curr. Protoc. Cell Biol.* **1999**, *2* (1), 4.7.1-4.7.12.
- (64) Peters, P. J.; Bos, E.; Griekspoor, A. Cryo-Immunogold Electron Microscopy. *Curr. Protoc. Cell Biol.* **2006**, *30* (1), 4.7.1-4.7.19.
- (65) Vicidomini, G.; Gagliani, M. C.; Cortese, K.; Krieger, J.; Buescher, P.; Bianchini, P.; Boccacci, P.; Tacchetti, C.; Diaspro, A. A Novel Approach for Correlative Light Electron Microscopy Analysis. *Microsc. Res. Tech.* **2010**, *73* (3), 215–224.
- (66) Van Der Zwaag, D.; Vanparijs, N.; Wijnands, S.; De Rycke, R.; De Geest, B. G.; Albertazzi, L. Super Resolution Imaging of Nanoparticles Cellular Uptake and Trafficking. *ACS Appl. Mater. Interfaces* **2016**, *8* (10), 6391–6399.
- (67) Kremer, J. R.; Mastronarde, D. N.; McIntosh, J. R. Computer Visualization of Three-



- Dimensional Image Data Using IMOD. *J. Struct. Biol.* **1996**, *116* (1), 71–76.
- (68) Kukulski, W.; Schorb, M.; Welsch, S.; Picco, A.; Kaksonen, M.; Briggs, J. A. G. Correlated Fluorescence and 3D Electron Microscopy with High Sensitivity and Spatial Precision. *J. Cell Biol.* **2011**, *192* (1), 111–119.
- (69) Deschout, H.; Zanicchi, F. C.; Mlodzianoski, M.; Diaspro, A.; Bewersdorf, J.; Hess, S. T.; Braeckmans, K. Precisely and Accurately Localizing Single Emitters in Fluorescence Microscopy. *Nat. Methods* **2014**, *11* (3), 253–266.

# Chapter 5

## **Bioorthogonal Correlative Light-Electron Microscopy of *Mycobacterium tuberculosis* in Macrophages Reveals the Effect of Anti-Tuberculosis Drugs on Subcellular Bacterial Distribution**

Published as:

Thomas Bakkum, Matthias T. Heemskerk, Erik Bos, Mirjam Groenewold, Nikolaos Oikonomas-Koppas, Kimberley V. Walburg, Suzanne van Veen, Martijn J.C. van der Lienden, Tyrza van Leeuwen, Marielle C. Haks, Tom H.M. Ottenhoff, Abraham J. Koster, Sander I. van Kasteren. *ACS Central Science*, **2020**; 6(11): 1997-2007



**Abstract**

Bioorthogonal Correlative Light-Electron Microscopy (B-CLEM) can give a detailed overview of multicomponent biological systems. It can provide information on the ultrastructural context of bioorthogonal handles and other fluorescent signals, as well as information about subcellular organization. In this chapter, B-CLEM is applied to the study of the intracellular pathogen *Mycobacterium tuberculosis* (*Mtb*) by generating a triply labeled *Mtb* through combined metabolic labeling of the cell wall and the proteome of a DsRed-expressing *Mtb* strain. Study of this pathogen in a B-CLEM setting was used to provide information about the intracellular distribution of the pathogen, as well as its in situ response to various clinical antibiotics, supported by flow cytometric analysis of the bacteria, after recovery from the host cell (*ex cellula*). The RNA polymerase-targeting drug rifampicin displayed the most prominent effect on subcellular distribution, suggesting the most direct effect on pathogenicity and/or viability, while the cell wall synthesis-targeting drugs isoniazid and ethambutol effectively rescued bacterial division-induced loss of metabolic labels. The three drugs combined did not give a more pronounced effect but rather an intermediate response, whereas gentamicin displayed a surprisingly strong additive effect on subcellular distribution.

## 5.1 Introduction

*Mycobacterium tuberculosis* (*Mtb*), the causative agent of tuberculosis (TB), is currently the deadliest pathogen in the world. It is responsible for approximately 10 million cases and 1.6 million deaths every year.<sup>1</sup> Moreover, a quarter of the world's population is estimated to be carrying the latent form of the disease.<sup>1</sup> All this has become even more urgent over the last few decades with multi-drug resistant (MDR-) and extensive drug resistant (XDR-) variants becoming increasingly prevalent.<sup>1</sup> Vaccine and drug development for *Mtb* has proven slow and challenging, in part due to the highly complex pathogen-host interactions, and lack of suitable antigens.<sup>2,3</sup>

The intracellular lifecycle of *Mtb* further affects this problem. Upon infection of host cell macrophages, its behavior is highly heterogeneous. Both fast, and slow growing forms of the bacteria exist<sup>4,5</sup>; the latter displaying tolerance to most of the available drugs.<sup>6–12</sup> This has resulted in the requirement for long treatment periods with cocktails of antibiotics, with the current standard of care being a six to nine-month course of rifampicin, isoniazid, ethambutol and/or pyrazinamide.<sup>13</sup> Treatment of MDR-TB requires more extensive antibiotic treatment, lasting up to 2 years, with poor side-effect profiles.<sup>14</sup> Recently, a new therapy for MDR-TB and XDR-TB was approved consisting of pretomanid in combination with bedaquiline and linezolid, and several others are currently under clinical development.<sup>13</sup>

*Mtb* is a facultative intracellular pathogen that primarily colonizes the lungs of patients by entering the upper and lower airways, through aerosol-transfer.<sup>15</sup> At these sites, *Mtb* is phagocytosed by alveolar macrophages, which – rather than clearing the pathogen – serve as their host cells.<sup>16</sup> The longstanding co-evolution of *Mtb* with humans has resulted in the emergence of many mechanisms by which *Mtb* can interfere with the cellular and organismal immune responses.<sup>17</sup> It can, for example inhibit phagosome acidification, block the recruitment of EEA1 and interfere with the Rab5-to-Rab7 conversion<sup>18</sup>, resulting in the formation of a nutrient-rich compartment that favors survival and replication of the pathogen.<sup>18,19</sup> *Mtb* is also able to inhibit autophagy and apoptosis, effectively blocking all of the backup mechanisms for microbial killing.<sup>20,21</sup> Even if maturation of the phagosome does occur, *Mtb* is known to be strongly resistant to both acidic conditions (down to pH 4.5) and the reactive oxygen and nitrogen species (ROS/RNS) normally employed to kill phagosomal pathogens, by virtue of its thick cell wall<sup>21</sup>, the production of antioxidative mycothiol (MSH)<sup>21</sup>, and several neutralizing enzymes.<sup>20,21</sup>

It has recently been shown that the localization of *Mtb* within the cell is also a complex and highly dynamic process: some phagosomes are arrested in an early state, while the majority of phagosomes will follow the conventional maturation pathway, or a Rab20-dependent pathway to form a spacious phagosome.<sup>22</sup> Damaging of the phagosome allows the bacterium to avoid degradation or even escape to the cytosol, followed by rapid replication and host cell necrosis.<sup>23</sup> Recapture of the cytosolic bacteria may occur through ubiquitin-mediated autophagy, which again may lead to either autophagosome maturation or arrest.<sup>24–26</sup> The precise contribution of these stages to overall *Mtb* survival is not yet known, nor is the change in these processes during drug treatment, but it implicates a dynamic host-pathogen ‘arms race’. Even if a successful immune response – usually supported by T-cell help – is mounted against *Mtb*, generally a subpopulation of so-called ‘persister cells’ remain in a dormant state. These bacteria have downregulated metabolic activity, upregulated stress-related genes, and as a result can establish a drug-tolerant, latent infection.<sup>7</sup>

This complex intracellular life cycle has made the study of *Mtb* difficult. Development of imaging techniques that allow the identification and study of the various stages of intracellular survival or killing of *Mtb* has long been sought after. Fluorescent protein-modified *Mtb* has allowed its imaging by confocal microscopy, but the reliability of fluorescent proteins varies and the fluorescence is lost upon degradation of the protein by the host.<sup>27</sup> Metabolic labeling of the mycobacterial cell wall, using fluorescent or bioorthogonal analogues of D-alanine<sup>28,29</sup> or trehalose<sup>30–32</sup>, or using fluorescent antibiotic analogues has allowed the study of growing and dividing *Mtb*.<sup>33–35</sup> This has, for example, allowed the discrimination of live from dead *Mtb* in sputum samples.<sup>32</sup> Finally, a dual-targeting Activity-Based Probe (ABP) was recently reported, combining the activity of two *Mtb*-specific enzymes to obtain extremely high specificity for *Mtb* over other mycobacteria.<sup>36</sup> These approaches are, however, all based on fluorescent techniques. They – in view of the complex life cycle of *Mtb* in the host – therefore do not provide information on, for example, host compartments and other ultrastructural features during infection.

Electron microscopy (EM) provides ultrastructural information but has limited options for labeling specific components of the bacterium and host, compared to fluorescent labeling techniques. For the study of *Mtb*, EM has proven useful to delineate parts of its life cycle, such as phagosome maturation, perturbation and repair, as well as cytosolic entry and reuptake by autophagy.<sup>22,25,37–39</sup> Correlative techniques, in which light and electron microscopy are combined have proven to

be powerful by providing both structural and functional information in one multimodal dataset, that can be visualized in a single image. The combination of fluorescence microscopy and Transmission Electron Microscopy (TEM) is known as Correlative Light-Electron Microscopy (CLEM).<sup>40</sup> For the study of *Mtb*, CLEM has been used to show *Mtb* replication within necrotic macrophages<sup>41</sup>, to discover a previously unknown niche for *Mtb* replication in the lymph nodes of TB patients<sup>42</sup>, and to visualize the subcellular distribution of bedaquiline in *Mtb*-infected macrophages.<sup>43</sup>

In order to combine the information that metabolic labeling studies can provide on the intracellular life cycle of *Mtb* with the information on bacterial structure and host cell biology that CLEM can provide, these approaches were integrated (**Figure 1**). Previous studies have shown that an intracellular proteome labeled with alkyne or azide-containing amino acids can be selectively visualized by CLEM within a mammalian host cell (including degradation products stemming from the phagocytosed bacteria).<sup>44,45</sup> However, this only provided one parameter to study and in order to provide a useful imaging approach for intracellular *Mtb*, multiple parameters relating to the intracellular lifecycle of the bacterium had to be visualized in parallel.

To this end, two bioorthogonal labels are here used in parallel – one for labeling the proteome and one for labeling the peptidoglycan layer – as well as the expression of a fluorescent protein. These three parameters, in combination with ultrastructural information, can yield information on where the bacteria are localized intracellularly, whether the bacteria are dividing, and to what extent antibiotics exert their anti-microbial effects. The resulting pathogen, labeled with L-azidohomoalanine (Aha; incorporated into proteome), D-propargylglycine (alkDala; incorporated into peptidoglycan), and DsRed fluorescent protein (anabolic activity) is used to study its fate inside a macrophage cell line (**Figure 1**). Using a dual copper-catalyzed Huisgen cycloaddition (ccHc) ‘click’ reaction on thin sections, these three parameters could be studied in their ultrastructural context. The two handles could be consecutively reacted without apparent cross-reactivity between handles (no loss of signal or altered patterns were observed compared to single labels). This bioorthogonal-CLEM (B-CLEM) approach makes it possible to study the intracellular distribution of *Mtb* and link this information to the retention of the metabolic labels over time. Comparing these parameters between untreated cells and cells treated with rifampicin, isoniazid, ethambutol or a combination of the three, provided valuable insights into the subcellular effect of these clinical antibiotics. These observations were then further substantiated using a flow

cytometry-based assay that allowed a more thorough quantification of the label retention under these conditions. An overview of the chemical structures and mechanisms of action of the antibiotics used in this chapter can be found in **Figure S1**.

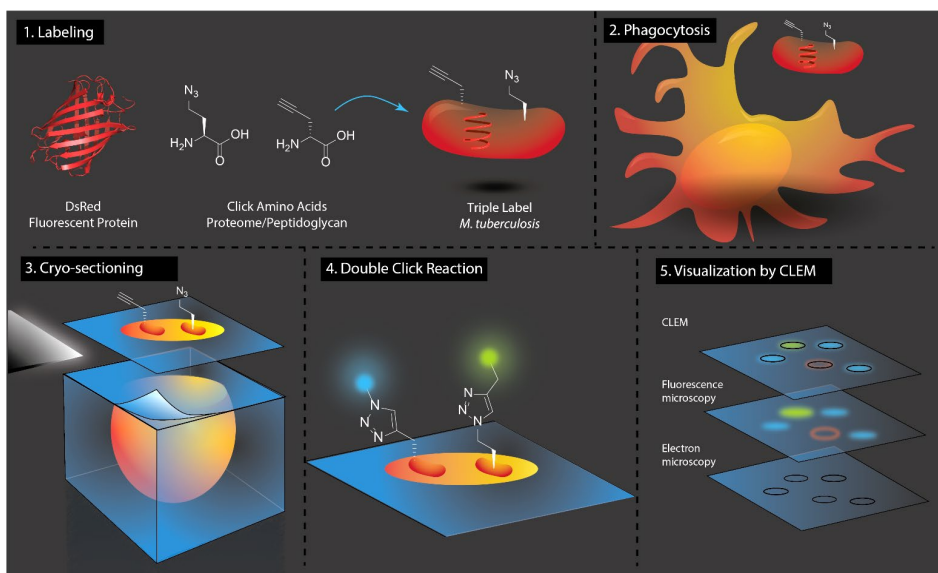


**Figure 1.** Bioorthogonal Correlative Light-Electron Microscopy (B-CLEM) strategy for *in situ* imaging of *Mtb*. Triple labeling of *Mtb* (1) is combined with two sequential on-section click reactions (4) and visualized with correlated fluorescence and electron microscopy (5) to provide information on the in-cell life cycle of *Mtb*.

## 5.2 Results and Discussion

### 5.2.1 Production and validation of triple-label *Mtb*.

The incorporation of bioorthogonal amino acids in *E. coli* and *S. enterica* serovar Typhimurium was previously optimized, based on the BONCAT-protocol developed by the Tirrell-lab.<sup>46–49</sup> Using in-gel fluorescence after cChc of bacterial lysates, label incorporation into the bacterial proteome could be quantified on the population level. Flow cytometry of fixed bacteria allowed for the quantification of the label on a per-bacterium level.<sup>44,45</sup> These studies have yielded optimal labeling conditions consisting of a pulse with the bioorthogonal amino acid (4 mM) for approx. 1-2 doubling times (30 min in case of the above species), with increased incubation leading to reduced growth and viability.<sup>44,45</sup>

In order to optimize bioorthogonal amino acid-incorporation into the *Mtb*-proteome, the lysis conditions for *Mtb* were optimized first, to maximize protein recovery (and killing of the pathogen to allow handling outside the BSL-III facility). This was achieved with a combination of 1% SDS and heat treatment, as detergents alone were found to be insufficient for both killing and protein recovery (**Table 1**).

**Table 1.** Optimization of lysis conditions for analysis of label incorporation by in-gel fluorescence. The condition shown in bold was chosen as the optimal lysis method.

Lysis conditions	Fluorescence	Protein recovery
1% IGEPAL* <sup>1</sup>	+/-	- <sup>2</sup>
1% SDS <sup>1</sup>	+/-	- <sup>2</sup>
5% SDS <sup>1</sup>	+/-	- <sup>2</sup>
Lysozyme <sup>3</sup> ; 1% IGEPAL* <sup>1</sup>	+	+/- <sup>2</sup>
Lysozyme <sup>3</sup> ; 10% IGEPAL* <sup>1</sup>	-	- <sup>2</sup>
Lysozyme <sup>3</sup> ; 1% IGEPAL* + 1% SDS <sup>1</sup>	+	++/-
Lysozyme <sup>3</sup> ; heat <sup>4</sup>	-	-
Lysozyme <sup>3</sup> ; 4% IGEPAL* + heat <sup>4</sup>	-	-
Lysozyme <sup>3</sup> ; 4% SDS + heat <sup>4</sup>	+	+/-
Lysozyme <sup>3</sup> ; 4% CHAPS + heat <sup>4</sup>	-	-
Lysozyme <sup>3</sup> ; 6M urea + heat <sup>4</sup>	+/-	-
Lysozyme <sup>3</sup> ; 1M NaCl + heat <sup>4</sup>	-	-
Lysozyme <sup>3</sup> ; 4% CHAPS + 6M urea + 1M NaCl + heat <sup>4</sup>	+/-	-
Lysozyme <sup>3</sup> ; 4% CHAPS + 4% IGEPAL* + 4% SDS + heat <sup>4</sup>	+/-	+/-
ddH <sub>2</sub> O + heat <sup>4</sup>	+/-	-
<b>1% SDS + heat<sup>4</sup></b>	<b>+</b>	<b>++</b>
1% SDS 30 min at 4°C; heat <sup>4</sup>	+/-	++
1% SDS 18 hours at -30°C; heat <sup>4</sup>	+/-	++
1% SDS added to growth culture + heat <sup>4</sup>	+/-	+++ <sup>5</sup>

\* = IGEPAL CA-630; <sup>1</sup> = in 150 mM NaCl, 50 mM HEPES pH 8, O/N at 4°C; <sup>2</sup> = after 0.2 µm filtration to remove live/intact bacteria, due to insufficient killing of *Mtb* (!); <sup>3</sup> = 2 mg/mL lysozyme for 1 hour at 37°C; <sup>4</sup> = 30 min at 80°C, to guarantee sufficient killing of *Mtb* (!); <sup>5</sup> = may include potentially unwanted proteins from growth culture.



These lysis conditions were used to assess bioorthogonal amino acid incorporation by in-gel fluorescence, following SDS-PAGE. As the generation time of *Mtb* is approximately 24h, various conditions were explored, starting from 4 mM L-azidohomoalanine (Aha) or L-homopropargylglycine (Hpg) for 48h. Label incorporation plateaued around 48h, but labeling times >48h reduced cell growth; particularly for Hpg-treated cells (**Figure 2A**). Hpg was therefore excluded from further analysis.

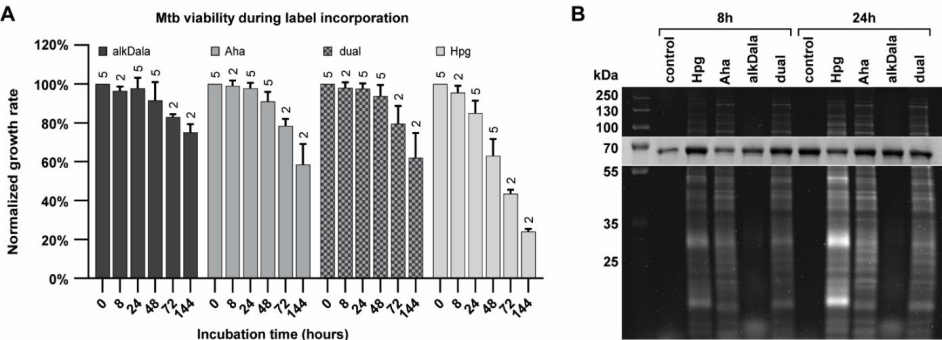


**Figure 2.** Production and validation of triple label *Mtb*. DsRed-expressing *Mtb* H37Rv were incubated with 4 mM Hpg, 4 mM Aha, 5 mM alkDala or a combination of 4 mM Aha and 5 mM alkDala (dual), for the indicated time in Middlebrook 7H9 broth. **A:** Bacterial viability during label incorporation was assessed by normalizing the growth rate (OD<sub>600</sub> measurements) to control bacteria, grown in the absence of metabolic labels. The number of biological replicates for each OD<sub>600</sub> measurement is indicated above the bar, error bars indicate standard deviation from the mean. **B:** Label incorporation throughout the proteome was analyzed by in-gel fluorescence, following bacterial lysis, cHc reaction with AF647-azide (alkDala/Hpg) or AF647-alkyne (Aha/dual) and SDS-PAGE. Coomassie Brilliant Blue staining was used as a loading control; shown as an insert around the most prominent 60 kDa band, resulting from the DsRed-expression plasmid containing the Hsp60 promoter.<sup>50</sup>

Cell wall labeling conditions with D-propargylglycine (alkDala), a ccHc-reactive precursor in the cell wall synthesis, were inspired by Siegrist et al.<sup>28</sup> Single labeling experiments with Aha or alkDala showed that no detrimental effects on viability were observed up to 48h for either label in terms of viability (**Figure 2A**). Even extensively labeled *Mtb* (144h) seemed to recover their growth rate after medium exchange (**Figure S2**). It was next determined whether this was also the case for dual labeling with Aha and alkDala (**Figure 2A, Figure S2**). Co-incubation of *Mtb* with both labels did not enhance toxicity up to the 48h timepoint and revealed homogeneous proteome labeling (**Figure 2B**). The gel-based assay revealed that treatment of *Mtb* for 48h with both labels provided the highest label incorporation (combined with the most facile protocol).

To determine whether all cells incorporated the label to an equal extent, a flow cytometry-based assay was used. Again, previous protocols for bacterial fixation and permeabilization for flow cytometry were found to be incompatible with ccHc-reaction in *Mtb*. This was likely due to the thick (40-100 nm) and highly complex mycobacterial cell wall.<sup>51</sup> The mycobacterial cell wall contains multiple layers of (peptido)glycans and lipids, including the ultra-lipophilic mycolic acids that can be up to 90 carbons in length.<sup>52</sup> In practice, this results in hydrophobic aggregation of bacteria (especially after fixation) and an impermeability to the ccHc-reactive fluorophores. It is likely that this thick and impermeable cell wall reduces the yields of the two ccHc-reactions. A wide range of permeabilization conditions was explored, varying detergents, permeabilization and fixation conditions (**Table 2**). After this extensive optimization, it was found that the most effective conditions for permeabilizing the bacteria for flow cytometric analysis – that balanced the permeability with the structural integrity required to remain intact during ccHc reaction – are pre-treatment with 1% SDS for 15 minutes, followed by overnight fixation with 4% paraformaldehyde at room temperature (**Table 2**). Addition of BSA as an anti-clumping additive during staining steps (**Table 3**) was required to avoid hydrophobic aggregation of the fixed bacteria.

**Table 2.** Optimization of fixation & permeabilization conditions for analysis of label incorporation by flow cytometry. The condition shown in bold was chosen as the optimal fixation/permeabilization method.

Fixation conditions	Permeabilization conditions	Aha-click positive
2% PFA <sup>1</sup>	Lysozyme <sup>2</sup> ; 0.1% IGEPAL <sup>*3</sup>	7% <sup>4</sup>
2% PFA <sup>1</sup>	Lysozyme <sup>2</sup> ; 1% SDS <sup>3</sup>	18% <sup>4</sup>
2% PFA <sup>1</sup>	Lysozyme <sup>2</sup> ; 0.1% IGEPAL <sup>*</sup> + 1% SDS <sup>3</sup>	12% <sup>4</sup>
2% PFA <sup>1</sup>	Lysozyme <sup>2</sup> ; 1% IGEPAL <sup>*</sup> + 1% SDS <sup>3</sup>	9% <sup>4</sup>
2% PFA <sup>1</sup>	Lysozyme <sup>2</sup> ; 1% SDS <sup>3</sup>	14% <sup>4</sup>
2% PFA <sup>1</sup>	Lysozyme <sup>2</sup> ; 2% SDS <sup>3</sup>	22% <sup>4</sup>
2% PFA <sup>1</sup>	Lysozyme <sup>2</sup> ; 4% SDS <sup>3</sup>	21% <sup>4</sup>
2% PFA <sup>1</sup>	Lysozyme <sup>2</sup> ; 1% SDS + 5 mM EDTA <sup>3</sup>	19% <sup>4</sup>
2% PFA <sup>1</sup>	Lysozyme <sup>2</sup> ; 2% SDS + 5 mM EDTA <sup>3</sup>	26% <sup>4</sup>
2% PFA <sup>1</sup>	Lysozyme <sup>2</sup> ; 1% SDS + 1% EtOH <sup>3</sup>	16% <sup>4</sup>
2% PFA <sup>1</sup>	Lysozyme <sup>2</sup> ; 2% SDS + 1% EtOH <sup>3</sup>	18% <sup>4</sup>
2% PFA/0.1% SDS <sup>1</sup>	Lysozyme <sup>2</sup> ; 2% SDS + 5 mM EDTA <sup>3</sup>	18% <sup>4</sup>
2% PFA/0.1% SDS <sup>1</sup>	Lysozyme <sup>2</sup> ; 2% SDS + 10 mM EDTA <sup>3</sup>	20% <sup>4</sup>
2% PFA/0.1% SDS <sup>1</sup>	Lysozyme <sup>2</sup> ; 2% SDS + 100 mM EDTA <sup>3</sup>	29% <sup>4</sup>
2% PFA/0.1% SDS <sup>1</sup>	Lysozyme <sup>2</sup> ; 2% SDS + 200 mM EDTA <sup>3</sup>	29% <sup>4</sup>
4% PFA <sup>1</sup>	None	17% <sup>4</sup>
8% PFA <sup>1</sup>	None	33% <sup>4</sup>
4% PFA/0.1% SDS <sup>1</sup>	None	53% <sup>4</sup>
1% SDS; 4% PFA/0.1% SDS <sup>1</sup>	None	70% <sup>4</sup>
1% SDS; 4% PFA/0.1% SDS <sup>1</sup>	0.1% SDS <sup>5</sup>	61% <sup>5</sup>
1% SDS; 4% PFA/0.1% SDS <sup>1</sup>	Lysozyme <sup>2</sup> ; 2% SDS + 10 mM EDTA <sup>3</sup>	57% <sup>5</sup>
1% SDS; 4% PFA/0.1% SDS <sup>1</sup>	0.1% Tween <sup>#6</sup>	22% <sup>6</sup>
1% SDS; 4% PFA/0.1% SDS <sup>1</sup>	Lysozyme <sup>2</sup> ; 0.1% Triton <sup>‡</sup> + 0.1% Tween <sup>#3</sup>	19% <sup>6</sup>
1% SDS; 4% PFA <sup>1</sup>	None	63% <sup>7</sup>
<b>1% SDS; 4% PFA<sup>1</sup> at RT</b>	<b>None</b>	<b>76%<sup>7,8</sup></b>
4% PFA <sup>1</sup> at RT	None	4% <sup>7</sup>
4% PFA <sup>1</sup> at RT	Lysozyme <sup>2</sup> for 30 min at 37°C	39% <sup>7</sup>
4% PFA <sup>1</sup> at RT	Lysozyme <sup>2</sup> for 60 min at 37°C	51% <sup>7</sup>
4% PFA <sup>1</sup> at RT	Lysozyme <sup>2</sup> for 90 min at 37°C	59% <sup>7</sup>
4% PFA <sup>1</sup> at RT	Lysozyme <sup>2</sup> for 90 min at 37°C; 0.1% Triton <sup>‡</sup>	70% <sup>7</sup>
4% PFA <sup>1</sup> at RT	Lysozyme <sup>2</sup> for 90 min at 37°C; 0.5% Triton <sup>‡</sup>	69% <sup>7</sup>
4% PFA <sup>1</sup> at RT	Lysozyme <sup>2</sup> for 90 min at 37°C; 0.1% SDS	64% <sup>7</sup>

\* = IGEPAL CA-630; # = Tween-80; ‡ = Triton-X100; <sup>1</sup> = in PBS for ≥18h at 4°C, unless otherwise specified; <sup>2</sup> = 2 mg/mL lysozyme for 60 min at 37°C, unless otherwise specified; <sup>3</sup> = in PBS; <sup>4</sup> = no anti-clumping agent used, resulting in a very low yield after staining; <sup>5</sup> = 0.1% SDS used as anti-clumping agent during all washing steps; <sup>6</sup> = 0.1% Tween-80 used as anti-clumping agent during all washing steps; <sup>7</sup> = 0.1% BSA used as anti-clumping agent during all washing steps; <sup>8</sup> = higher signal observed for alkDala, compared to other conditions

**Table 3.** Anti-clumping additives to reduce hydrophobic aggregation of fixed *Mtb* during washing steps, during sample preparation for flow cytometry. The condition shown in bold was considered optimal.

Anti-clumping additive	Effect on aggregation	Effect on yield
0.1% Tween <sup>#</sup> in PBS	++	+/- <sup>1</sup>
0.1% SDS in PBS	+	- <sup>2</sup>
0.1% gelatin <sup>†</sup> in PBS	+	+/-
<b>0.1% BSA in PBS</b>	<b>+</b>	<b>+</b>

<sup>#</sup> = Tween-80; <sup>†</sup> = gelatin from cold water fish skin; <sup>1</sup> = loss of alkDala signal due to apparent over-permeabilization (dismissed); <sup>2</sup> = loss of Aha due to apparent over-permeabilization.

Despite this extensive set of optimization experiments, a subpopulation of DsRed positive events (~25%) remained unlabeled by both click reactions, perhaps due to them being permeabilization resistant, metabolically inactive or even dead prior to labeling.<sup>7,53</sup> These unlabeled bacteria were excluded from quantification by gating for the double positive (Aha+/alkDala+) quadrant (**Figure 3A**, **Figure S3**). To confirm that the observed label incorporation was indeed selective and related to metabolic activity, it was shown that pre-incubation with Rifampicin for 1h and 24h respectively reduced or abolished Aha-incorporation at 0.1, 1.0 and 10 µg/mL (**Figure S4**). The cell wall inhibitor D-cycloserine achieved the same for alkDala incorporation (**Figure S5**). Heat killing (**Figure S6B**) or paraformaldehyde fixation (**Figure S6C**) abolished the incorporation of both labels. With these restrictions applied, label incorporation for Aha and alkDala seemed to follow a similar trend as observed for the SDS-PAGE assay. Incorporation of both labels plateaued at 48 hours incubation, in high signal-to-background ratios (**Figure 3A-viii**).

### 5.2.2 Bioorthogonal CLEM as a multi-parameter analysis method to study intracellular *Mtb*.

After successfully constructing triple label *Mtb*, their compatibility with B-CLEM was assessed (**Figure 3B**, **Figure 4**). To this end, DsRed-expressing *Mtb* were incubated with Aha (4 mM) and alkDala (5 mM) simultaneously for 48 hours for maximum label incorporation. The bacteria were prepared for cryo-sectioning, according to the Tokuyasu method.<sup>54–56</sup> Briefly, samples were fixed with paraformaldehyde and glutaraldehyde (2% w/v and 0.2% w/v respectively for 2 hours), after which the bacterial pellet was rinsed with PBS and embedded in 12% gelatin. Millimeter-sized cubes were prepared manually, followed by sucrose infiltration and plunge-freezing on sample pins. Ultrathin cryo-sections (75 nm) were prepared and transferred to a Formvar/carbon-coated titanium TEM-grid. Thawed cryo-sections were subjected to on section click-reaction with AF647-azide or AF647-alkyne for equal comparison between Aha and alkDala incorporation. Using these

experiments, the label incorporations could be confirmed (with the sectioning being used in lieu of permeabilization). Both alkDala and Aha were minimally detectable after 1 hour with the signal increasing upon longer incubation (**Figure 3B**). Optimal label incorporation is observed after 48 hours without any noticeable effect on DsRed fluorescence. No detectable background fluorescence was observed for the unlabeled control samples (**Figure S7**).

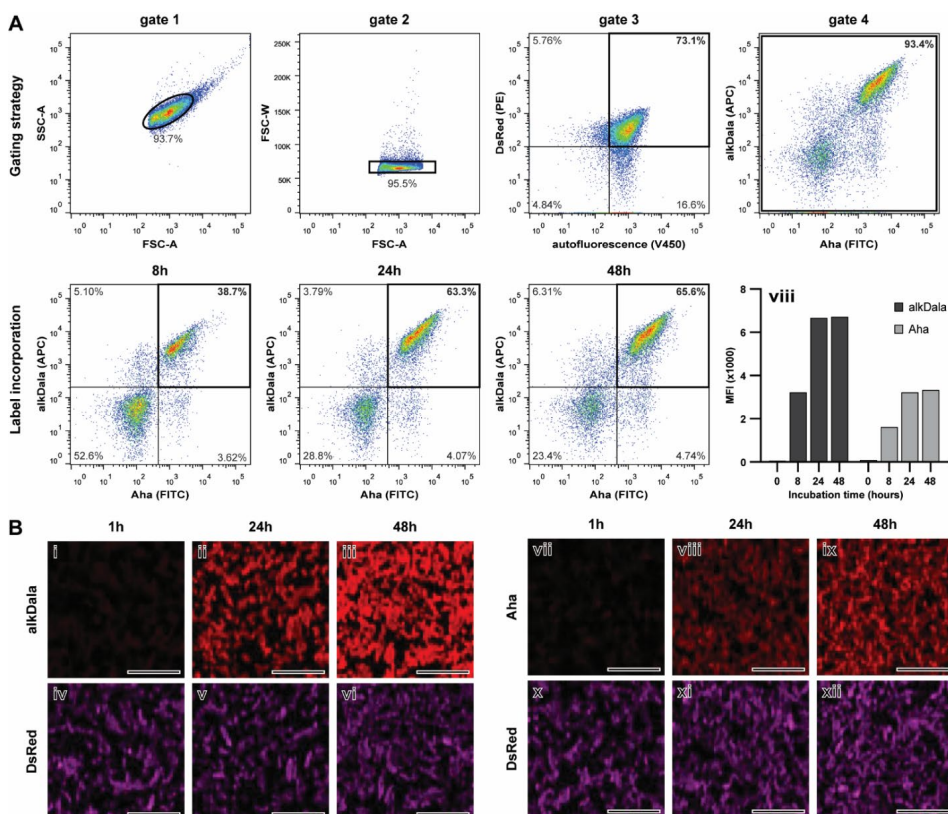


**Figure 3.** Optimization of label incorporation. DsRed-expressing *Mtb* H37Rv were incubated with 4 mM Aha, 5 mM alkDala or a combination of 4 mM Aha and 5 mM alkDala (dual), for the indicated time in Middlebrook 7H9 broth. **A:** Label incorporation per bacterium was quantified by flow cytometry after sequential cHc reaction with AF647-azide (alkDala) and AF488-alkyne (Aha) on fixed and permeabilized bacteria. Bacteria were selected based on size (gate 1), shape (gate 2), fluorescence (gate 3) and exclusion of extreme outliers (gate 4). Quantification of the label incorporation was achieved by selecting the median fluorescence intensity (MFI) of the major [Aha+/alkDala+] population for dually-labeled *Mtb* or the major [Aha-/alkDala-] population for unlabeled *Mtb*. Controls and normalized MFI values are shown in Figure S2. **B:** Triple label *Mtb* were processed for cryo-sectioning, followed by cHc reaction with AF647-azide (alkDala) or AF647-alkyne (Aha), to confirm the increase in label incorporation over time on ultrathin sections that can be directly used for CLEM. All scale bars represent 5  $\mu$ m.

Next, these single bacteria were subjected to B-CLEM as follows. Fresh sections were prepared and subjected to double on-section click-reaction with AF647-azide and AF488-alkyne, with washing in between. The labeled sections were first imaged by confocal microscopy, then stained with uranyl acetate and finally imaged by TEM. The resulting images were then correlated using Photoshop to obtain the final CLEM images (**Figure 4, Figure S8**). These CLEM images show that >80% (n=200) of bacteria were positive for alkDala, Aha and/or DsRed, suggesting sub-optimal permeabilization was responsible for the incomplete labeling observed by flow cytometry above. The proteome label Aha colocalized largely with the fluorescent protein DsRed.

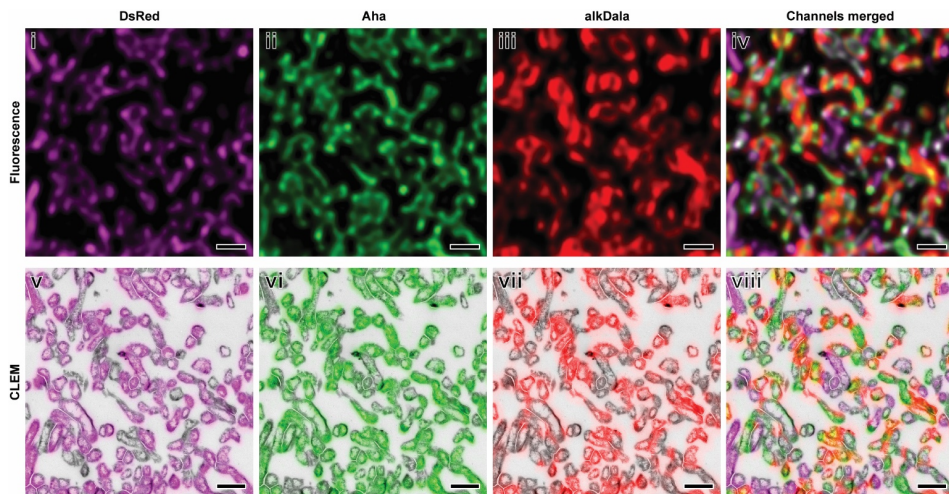


**Figure 4.** Bioorthogonal CLEM of triple label *Mtb* in vitro. Triple label *Mtb* were processed for cryo-sectioning, followed by sequential ccHc reaction with AF647-azide and AF488-alkyne. The fluorescently-labeled sections were imaged by confocal microscopy, followed by TEM and the images were correlated to obtain the CLEM image. The lower panel shows details from the large field of view CLEM image presented in Figure S4. The top panel shows the corresponding fluorescence channels separately for clarity. All scale bars represent 1 μm.

To explore the possibility of studying intracellular *Mtb* localization and processing, a murine (LPS-stimulated) macrophage cell line (RAW 264.7)<sup>57,58</sup> was infected with the double labeled DsRed-positive *Mtb* (MOI 25). The goal was to study whether signs of viability could be extrapolated from the information-dense CLEM images, containing both the ultrastructural information of EM and the functional information of the multi-label fluorescence microscopy. After Tokuyasu sample preparation, large field of view CLEM images containing over 100 cell-profiles per image could be obtained at 11,000x magnification by applying an in-house developed EM-stitching algorithm.<sup>59</sup> This approach provides a large dataset for qualitative and quantitative analysis of EM structures, guided by the fluorescence (illustrated in **Figure S9**). As observed in previous EM studies<sup>19,60</sup>, the mycobacterial cell wall shows a typical electron translucent layer, representing the mycomembrane (MM), enclosed by an electron-dense outer layer (OL) and the peptidoglycan layer (PGL) (**Figure 5i**). The bacterial cell wall is delineated by the signal distribution of alkDala (**Figure 5iv**). *Mtb* was found to be spread over different compartments, such as small or tight vacuoles (**Figure 5v**, **Figure S10B**), large or spacious vacuoles (**Figure 5ix**, **Figure S10C**), or what appeared to be non-membrane-bound compartments (which could be due an insufficient membrane preservation on EM) (**Figure 5i**, **Figure S10A**). The presence of *Mtb* in these apparently non-membrane-bound compartments suggests escape from the parasitic vacuole to the cytosol, as reported in multiple studies.<sup>19,23,61–64</sup> In some cases, a double membrane was observed in proximity of an apparently cytosolic bacterium (**Figure S9D**, **Figure S10A-iv**), which is a hallmark of autophagy<sup>65</sup>, implying that this process may occur.

At 24 hours post-infection, 23% of bacteria were found in small vacuoles, 72% in large vacuoles and 5% with no detectable membrane ( $n > 500$  bacteria counted). Additionally, a small percentage of bacteria ( $< 5\%$  of total) was found extracellularly, surrounded by cell debris (illustrated in **Figure S11A/B**). Many large vacuoles contained both bacteria and cell debris, suggesting the bacteria could have escaped from the previous host cell<sup>23,66</sup>, before reuptake by another macrophage (**Figure S11B**). If host cell necrosis occurs, the plasma membrane integrity is lost, causing the cell to fall apart, which allows the bacteria to escape. However, if the host cell initiates apoptosis, the entire cell including bacteria can be taken up by a neighboring macrophage in a process called efferocytosis.<sup>67</sup> Distributions of bacteria indicative for either secondary phagocytosis of *Mtb*, following necrosis of the host cell (**Figure S11C-i**) or efferocytosis, when the entire apoptotic cell is internalized (**Figure S11C-ii**), were observed.



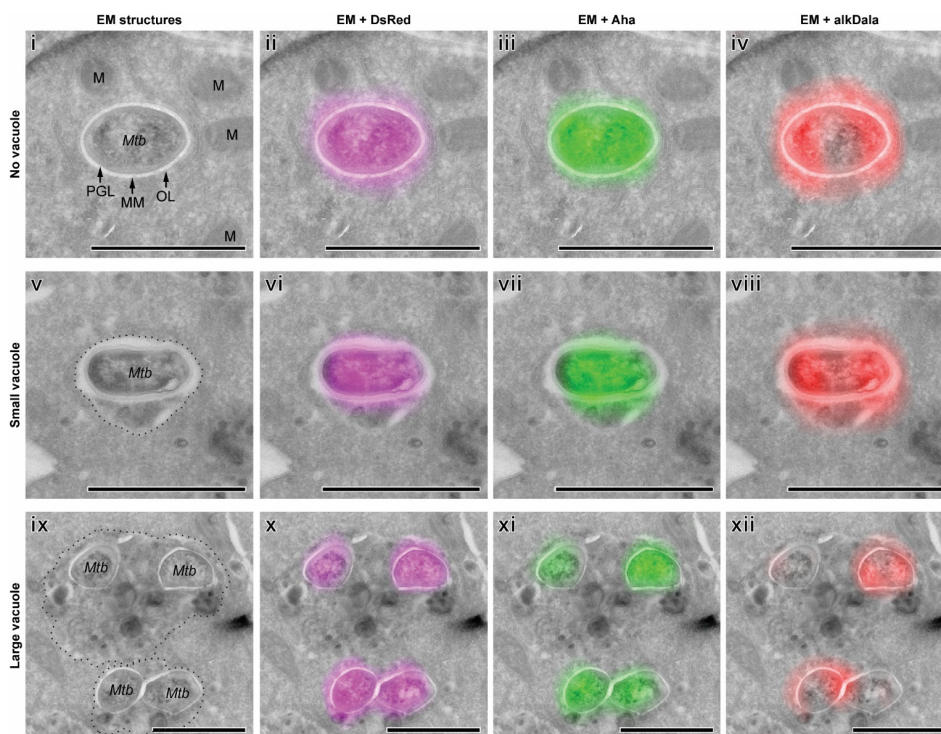


**Figure 5.** Bioorthogonal CLEM of triple label *Mtb* in RAW 264.7 macrophages. Triple label *Mtb* were processed for cryo-sectioning, followed by sequential ccHc reaction with AF647-azide and AF488-alkyne, and counterstaining with DAPI. Fluorescently-labeled sections were imaged by confocal microscopy, followed by TEM and the images were correlated to obtain the CLEM image. The fuzziness of the fluorescent signal is a result of the difference in resolution between the techniques as governed by the Abbe-limit of diffraction. Representative examples of intracellular triple label *Mtb* are shown, not within a vacuole (i-iv), in a small/tight vacuole (v-viii), or in a large/spacious vacuole (ix-xii). Small field of view CLEM images with separated fluorescence channels are shown for clarity. Corresponding large field of view image is presented in Figure S5. N = nucleus, M = mitochondria, PGL = peptidoglycan layer, MM = mycomembrane, OL = outer layer. A dotted line indicates the apparent vacuole where relevant. All scale bars represent 1  $\mu$ m.

### 5.2.3 Bioorthogonal CLEM of *Mtb*-infected macrophages reveals the effect of antibiotics on the bacterial integrity and intracellular processing.

To determine how the intracellular distribution and fluorescent signals of triple label *Mtb* would be affected by the commonly-used antibiotics used in the treatment of tuberculosis, the experiment was repeated in the presence of rifampicin, isoniazid, ethambutol or a combination of the three for 24 hours. All drugs except ethambutol alone induced a significant alteration in the intracellular distribution of the bacteria (**Figure 6A**), with the triple-antibiotic cocktail showing the most pronounced effect, with 15% of bacteria residing in small vacuoles, 84%



in large vacuoles and only 1% did not appear to be within a vacuole ( $n > 500$ ). Interestingly, when cells were incubated with heat-killed bacteria, 95% of all bacteria were found in large vacuoles, with  $< 0.5\%$  present in structures without a detectable membrane. The individual drugs had less pronounced effects on distribution (**Figure 6A**). Rifampicin caused the largest shift in sub-cellular localization, with 12% of bacteria residing in small vacuoles, 85% in large vacuoles and 3% not within a vacuole ( $n > 500$ ). Isoniazid had a less pronounced effect, with 20% of bacteria in small vacuoles, 78% in large vacuoles and 3% not within a vacuole ( $n > 500$ ). Ethambutol did not show a significant difference compared to the control.

A large percentage of bacteria were found to be extracellular upon treatment with isoniazid (41% of total,  $n > 500$ ) or ethambutol (12% of total,  $n > 500$ ; Figure S12A), suggesting different drug mechanisms of action are involved. In addition, isoniazid treatment appeared to increase the occurrence of apparent host cell death (37%,  $n > 500$ ), while ethambutol appeared to decrease host cell death (2%,  $n > 500$ ; Figure S12B). These findings imply a need to reconsider the standard infection protocol, in which the infected cells are co-incubated with a low concentration of gentamicin (5  $\mu\text{g/mL}$ ) to kill off extracellular bacteria. During the 24 hours of incubation, many bacteria may escape from the host cell, which would then be exposed to the extracellular gentamicin before being taken up by another macrophage. This could result in an artificially high number of dead bacteria, thereby skewing the relative intracellular sub-populations. To confirm this hypothesis, *Mtb*-infected cells were incubated with or without the triple-antibiotic cocktail, in the presence or absence of gentamicin, for 24 hours and processed for CLEM. Indeed, a significant effect on the intracellular distribution was observed for both the triple-antibiotic cocktail and the untreated cells, when comparing the presence or absence of gentamicin (Figure 6B). Interestingly, a similar effect can be observed when comparing the triple-antibiotic cocktail to the control, either with gentamicin or without. This implies an additive drug effect for gentamicin, on top of the other antibiotics. Indeed, *Mtb*-infected cells in the complete absence of antibiotics showed only 50% of the bacteria residing in large vacuoles versus 31% in small vacuoles and 19% without an apparent vacuole ( $n > 500$ ). Gentamicin was therefore excluded from all further experiments.

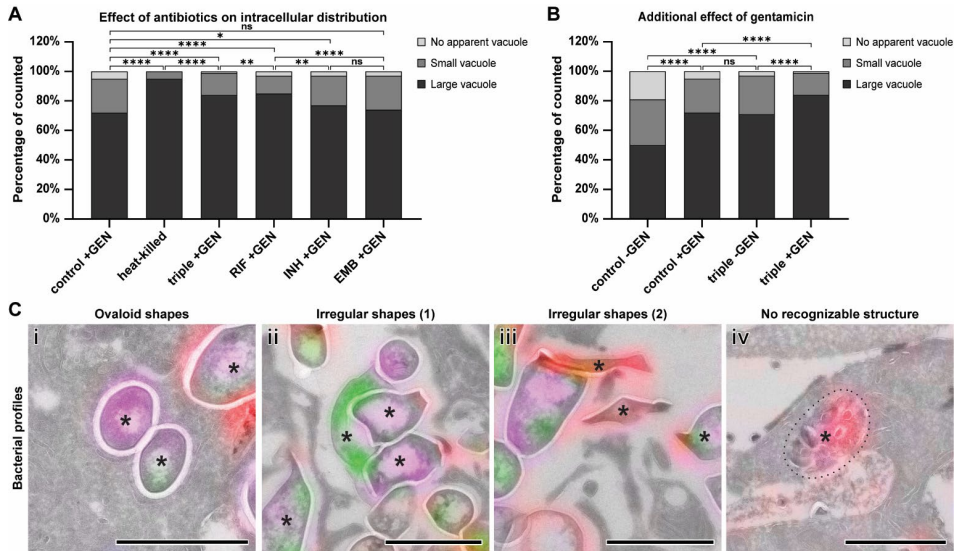


**Figure 6.** The effect of different antibiotics on the intracellular distribution and shape of triple label *Mtb* in RAW 264.7 macrophages. **A:** Intracellular distribution of *Mtb* was manually classified as not within a vacuole (none), small/tight vacuole (small) or large/spacious vacuole (large), after 24 hours of incubation with rifampicin (RIF), isoniazid (INH), ethambutol (EMB), triple antibiotics cocktail (triple), or without antibiotics (control). Shown as percentage relative to total number of intracellular *Mtb* counted in the analyzed region;  $n > 500$  for all. **B:** The additional effect of gentamicin (GEN) on the intracellular distribution of *Mtb* was assessed after 24 hours of incubation with triple antibiotic cocktail (triple +/-GEN) or without antibiotics (control +/-GEN). Raw distributions were pairwise compared using the chi-square test and corrected for multiple testing using the Benjamini-Hochberg procedure, with a false discovery rate (FDR) of 0.1 (\*\*\*\*:  $p < 0.0001$ , \*\*:  $p < 0.01$ , \*:  $p < 0.05$ , ns: not significant). **C:** Zoom-in CLEM examples of the most common shapes, observed for bacterial profiles, classified as ovaloid (i), irregular (ii/iii) or no recognizable structure (iv; enhanced contrast of fluorescence for visual purposes). Relevant structures are indicated with an asterisk (\*). A dotted line indicates the apparent vacuole where relevant. All scale bars represent 1  $\mu\text{m}$ .

In addition to the intracellular distribution of *Mtb*, the shape of the bacterial profile appeared to be affected by the antibiotics as well. After (cryo-)sectioning of the rod-shaped *Mtb*, the expected bacterial profile is somewhere between circular and elongated, but always ovaloid in shape (**Figure 6C-i**). Indeed, the bacterial profiles after 24h intracellular incubation without antibiotics were primarily ovaloid in shape (69%,  $n > 500$ ; **Figure S14D**). The remaining bacterial profiles display an irregular ‘pointy’ shape (**Figure 6C-ii/iii**, **Figure S14B**), perhaps suggesting a loss of bacterial integrity prior to fixation. Triple antibiotics treatment appeared to increase the number of irregular profiles (57%,  $n > 500$ ; **Figure S14D**), which may indicate an increase in *Mtb* killing. Some vacuoles were even found to contain distinct fluorescence while entirely lacking any recognizable bacterial structure

(**Figure 6C-iv**, **Figure S14C**), potentially carrying degradation products of the labeled *Mtb*. Interestingly, heat-killed bacteria were predominantly observed as irregular shapes (95%,  $n > 500$ ; **Figure S14D**) but with a well-preserved cell wall.

The early intracellular population of *Mtb*, immediately after infection, was highly concentrated in large vacuoles ( $>80\%$ ,  $n > 200$ ). At this time point (0h post-infection), no significant effect of antibiotic pre-treatment (24 hours triple-antibiotic cocktail in vitro, before infection) on the subcellular distribution (**Figure S13A**) nor on the bacterial profiles of *Mtb* (**Figure S14F**) was observed, suggesting that more time is required for processing of the bacteria by the host cell. The untreated bacteria do appear to reside more in large clusters of smaller vacuoles, while the pre-treated bacteria were mostly found in large and spacious vacuoles (See **Figure S13B** for examples). However, this classification criterion was too subtle for unbiased manual quantification and was therefore excluded from further analysis.

#### 5.2.4 CLEM and flow cytometry-based quantification of label retention upon antibiotic treatment.

The average fluorescence intensity, resulting from the metabolic labels Aha and alkDala, can be used as a measure for bacterial division, as the label content per bacterium will ‘dilute’ upon division. By combining existing Photoshop tools with a custom-build JavaScript, as well as a custom-build ImageJ macro, it was possible to quantify the average fluorescence intensity per bacterium-profile from the CLEM images (i.e. multimodal datasets). Using this method, the bacteria were segmented out of the finely correlated CLEM image, and the mean fluorescence intensity (MFI) was analyzed for each of the three fluorescence channels ( $n > 200$  bacteria analyzed). These results show that intracellular *Mtb*, treated with the triple-antibiotic cocktail, retain more Aha and lose DsRed compared to the untreated control (**Figure 7A**, **Figure S15**). No significant difference in alkDala retention was observed (**Figure 7B**), although analysis artifacts cannot be excluded, due to the smudging of alkDala fluorescence beyond the selected bacterial outline (**Figure S15**) or variations in section thickness that may affect the fluorescence intensity.

Since quantification of CLEM is intrinsically limited by its laborious correlation procedure, a higher-throughput technique was required for unambiguous quantification of the effect of antibiotics on bacterial proliferation, to support the observations done in CLEM. To achieve this, a custom flow cytometry-based method was developed to analyze the bacteria after recovery from the infected host cells (*ex cellula*). This was achieved by selective host cell lysis (adapted from Liu et al.<sup>68</sup>), followed by fixation and click labeling of the recovered bacteria, using

the method described above, to obtain optimal signal-to-noise and optimal recovery of bacteria. The cytometry results show a clear loss of Aha and alkDala retention per bacterium over time (24h vs 0h control), in the absence of antibiotics (**Figure 7B, Figure S16**). This loss was largely avoided by isoniazid and ethambutol. Heat-killed bacteria showed no loss of label over time (**Figure S17J**). Rifampicin does not show an effect on label retention, suggesting a different mechanism of action (**Figure 7B, Figure S16, Figure S17**). The triple-antibiotic cocktail showed an intermediate effect on label retention, suggesting a combinatorial but non-additive effect on label retention. No significant effect on DsRed was observed for any of the antibiotics, through this quantification approach. However, isoniazid and ethambutol show a distinct reduction in the typical *Mtb* autofluorescence<sup>69</sup>, similar but to a smaller degree as heat-killed *Mtb* (**Figure S17F**). This reduction in autofluorescence has previously been suggested as an indication for mycobacterial viability.<sup>70</sup>

Taken together, these results indicate that – within the context of an LPS-stimulated murine macrophage infection system – rifampicin mostly affects *Mtb* pathogenicity, while isoniazid and ethambutol seem to affect *Mtb* division more directly; although the complexity and heterogeneity of the life cycle of *Mtb* in host cells remains profound.

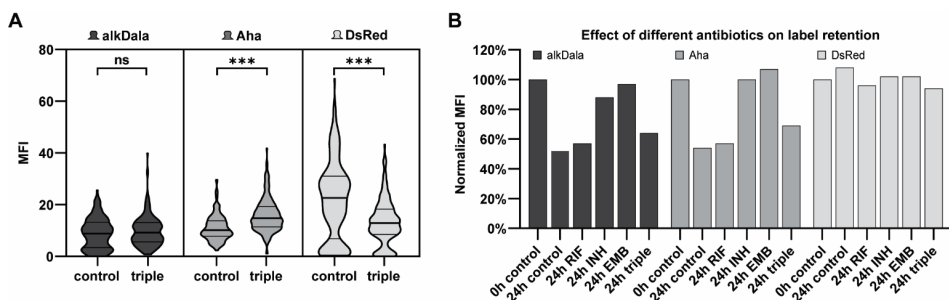


**Figure 7.** Quantification of label retention after intracellular incubation of triple label *Mtb* in RAW 264.7 macrophages with antibiotics. **A:** CLEM-based semi-automatic quantification of label retention after 24 hours intracellular incubation with triple antibiotics cocktail (triple) or without antibiotics (control). Distribution of the mean fluorescence intensity per bacterial profile (n=200). Thick horizontal line represents population mean, thin horizontal lines represent standard deviation (\*\*\*: p<0.001, ns: not significant, Mann-Whitney U test). **B:** Flow cytometry-based quantification of label retention ex cellula, after 24 hours intracellular incubation with rifampicin (RIF), isoniazid (INH), ethambutol (EMB), triple antibiotic treatment (triple) or without antibiotics (24h control), normalized on bacteria recovered immediately after infection (0h control). Corresponding dot plots and MFI values, before normalization, are shown in Figure S12.

### 5.3 Conclusion

The here-described combinatorial method allows for the study of intracellular localization of pathogenic bacteria *in situ*, as well as the effect of clinical or experimental drugs on the entire host-pathogen system. By combining fluorescent protein expression, proteome and cell wall labeling with high-content CLEM and flow cytometry, new information about the complex intracellular behavior of *Mtb* in macrophages was obtained. CLEM allows for simple fluorescence-guided detection of bacterial structures, and inversely, EM-guided analysis of fluorescent labels. The ultrastructural information of EM provides a subcellular description of both the bacterial behavior and that of the host cell. In addition, flow cytometry provides a quantification method for bacterial label retention under varying conditions. Using a triple labeling strategy, different components of the bacterium could be visualized, providing multi-parameter information about the metabolic state of the pathogen, although the sought-after *in vivo* unambiguous identification of live, dormant and dead bacteria remains elusive. Using multiple labels also significantly reduces the chance of missing events due to absence of a fluorescent label, and at the minimum, provides an internal standard for equivalent labels (Aha and alkDala). Alternatively, using a single bioorthogonal label could bypass the arduous task of genetically labeling a complicated level-3 pathogen, like *Mtb*.

Large differences were observed between intracellular distribution of *Mtb* under normal conditions versus treatment with various clinical antibiotics. Rifampicin displayed the clearest effect on distribution, while isoniazid and ethambutol only had a mild effect. These observations suggest a more direct effect of rifampicin on bacterial pathogenicity and/or viability, which is in agreement with its proposed mechanism of action.<sup>71</sup> Surprisingly, a routine low dose of gentamicin displayed a strong effect on distribution, which was additive to both untreated cells or cells treated with all three antibiotics simultaneously. This effect of gentamicin was probably due to bacteria escaping from the host cell, undergoing gentamicin-induced extracellular killing, followed by re-internalization by surrounding macrophages. Although the additive effect of gentamicin is unlikely to interfere with routine assays, it should still be considered as a potential bias on drug efficacy.

Besides broadly occurring phenomena, such as the subcellular distribution of *Mtb*, many less common events were observed such as apparent phagosome-lysosome fusion, possible autophagy of cytosolic *Mtb*, partially degraded *Mtb* fragments, leakage and vesicular transport of fluorescently labeled *Mtb* components, bacterial lipid inclusions and exocytosis of mycolic acids. Although these observations could

not yet be supported by sufficient evidence, they present an interesting starting point for follow-up studies, highlighting the exploratory power of CLEM.

Flow cytometry-based quantification of label retention showed a clear loss of label retention over time, that was almost completely rescued by isoniazid or ethambutol treatment, but to a far lesser extent by rifampicin or the triple antibiotics combination. Label dilution over time is expected due to bacterial division without additional metabolic labels present in the medium. Label retention over time is therefore a result of inhibition of bacterial division, which is in accordance with the proposed mechanism of action for these antibiotics.<sup>71</sup> Perhaps most surprising is the apparently intermediate efficacy of the triple antibiotic combination in terms of label retention. However, since the triple antibiotic combination showed the most pronounced effect on intracellular distribution, the overall therapeutic effect is likely a combination of bacteriostatic and bactericidal effects, as can be expected from these antibiotics. If future research provides a way to unequivocally distinguish dead from live *Mtb*, this would greatly benefit the interpretation of these results and assist in the discovery of novel antibiotics.

## 5.4 Experimental

### Safety statement

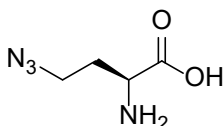
All biological experiments with *M. tuberculosis* described in this study were performed under strict Bio Safety Level 3 conditions. Following fixation and disinfection of the tubes, further sample preparation for CLEM was performed under normal laboratory conditions. No unexpected or unusually high safety hazards were encountered.

### Reagents

Difco Middlebrook 7H9 broth and ADC growth supplement were purchased from Becton Dickinson, Breda, The Netherlands. Hygromycin B, gentamicin and azide- or alkyne-modified Alexa Fluor dyes (AF488 and AF647) were purchased from Thermo Fisher Scientific, Bleiswijk, The Netherlands. Dulbecco's modified Eagle medium (DMEM), GlutaMAX, Copper(II) sulfate pentahydrate, (+)-sodium L-ascorbate, tris(3-hydroxypropyltriazolylmethyl)amine (THPTA), aminoguanidine hydrochloride, paraformaldehyde, glycine, gelatin type A bloom 300 (gelatin), cold water fish skin gelatin, Lysozyme from hen egg white, bovine serum albumin (BSA), IGEPAL CA-630, Triton-X100 and Tween-80 were purchased from Sigma-Aldrich, Zwijndrecht, The Netherlands. D-propargylglycine (alkDala) was purchased from Combi-Blocks, San Diego, USA. EM-grade 8% paraformaldehyde and EM-grade 8% glutaraldehyde were purchased from Aurion, Wageningen, The Netherlands. Fetal calf serum (FCS) was purchased from VWR International, Amsterdam, The Netherlands. Penicillin G sodium and streptomycin sulphate were purchased from Duchefa, Haarlem, The Netherlands.

### Organic synthesis

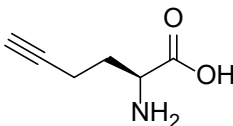
Synthesis of (S)-2-amino-4-azidobutanoic acid (L-azidohomoalanine; Aha)



Aha was synthesized according to a previously described procedure by Zhang et al., 2010<sup>72</sup>.

<sup>1</sup>H-NMR (D<sub>2</sub>O), 400 MHz:  $\delta$  [ppm] = 4.05 (t, 1H,  $\alpha$ -CH), 3.55 (t, 2H,  $\gamma$ -CH<sub>2</sub>), 2.15 (m, 2H,  $\beta$ -CH<sub>2</sub>).

### Synthesis of (S)-2-Aminohex-5-ynoic acid (L-homopropargylglycine; Hpg)



Hpg was synthesized according to previously described procedure by Li et al.<sup>73</sup>, adjusted to obtain the enantiomerically pure L-Hpg variant based on Chenault et al.<sup>74</sup>, Biagini et al.<sup>75</sup> and Dong et al.<sup>76</sup>

### Chiral deprotection of *N*-acetyl-DL-homopropargylglycine (2-acetamidohex-5-ynoic acid)

A solution of 303 mg (1.13 mmol, 1 eq.) *N*-acetyl-DL-homopropargylglycine in 20 mL H<sub>2</sub>O and adjusted to pH 7.5 using 1M NH<sub>4</sub>OH. 1 mg kidney acylase I (≥2000 units/mg) was added and the mixture was stirred for 16 h at 37 °C. The enzyme was recovered by centrifugation dialysis, using a 10kDa membrane at 4000 rpm for 35 min at 10 °C. Next, the solution was acidified to pH 3 with 2M HCl and extracted with 3 x 20 mL diethyl ether. The organic layers were concentrated to retrieve the *N*-acetyl-D-homopropargylglycine. The aqueous layer was loaded on a pre-washed and regenerated Dowex 50WX8 cation exchange resin (60 mL). The column was washed with 5 x bed volume of water, maintaining a pH of 5.5 at the exit and eluted with 200 mL 1.5M NH<sub>4</sub>OH. Product was detected by TLC and the eluate was concentrated and lyophilized to yield chirally pure L-Hpg (68 mg, 0.535 mmol, 95%) as a white powder.

<sup>1</sup>H NMR (400MHz, D<sub>2</sub>O): δ [ppm] = 4.11 (t, J = 6.4 Hz, 1H), 2.42 – 2.36 (m, 2H), 2.36 (s, 1H), 2.19 – 2.10 (m, 1H), 2.07 – 1.98 (m, 1H); <sup>13</sup>C NMR (101MHz, D<sub>2</sub>O): δ 82.28, 71.16, 52.05, 28.44, 14.16; HRMS (ESI): C<sub>6</sub>H<sub>9</sub>NO<sub>2</sub> [M+H]<sup>+</sup> 128.06, found 128.07; [α]<sub>20</sub><sup>D</sup>: +32.4 (c = 1, 1 M HCl); Ref <sup>76</sup>: +28 (c = 1, 1 M HCl).

### Bacterial culture, metabolic labeling and viability assessment based on growth rate

*Mycobacterium tuberculosis* (*Mtb*) strain H37Rv, expressing DsRed from a pSMT3[Phsp60/DsRed] plasmid<sup>50</sup>, was cultured in Difco Middlebrook 7H9 broth with 10% ADC, 0.05% Tween-80, 0.2% glycerol and 50 µg/mL hygromycin B (Thermo Fisher Scientific) shaking at 37°C. Fresh cultures were inoculated from glycerol stocks every 2 months due to loss of DsRed expression over time. For metabolic labeling of *Mtb*, cultures were supplemented with 4 mM Hpg, 4 mM Aha, 5 mM alkDala or a combination of 4 mM Aha and 5 mM alkDala ('dual') and incubated



under normal culturing conditions. After 0h, 8h, 24h, 48h, 72h and 144h, bacterial growth was assessed by OD<sub>600</sub> measurement and normalized on the first time point to determine the growth rate in the presence or absence of metabolic labels. These growth rates were plotted as percentages of the unlabeled *Mtb* control culture. After the last time point, the bacteria were collected by centrifugation (15 min at 3200 rcf) and resuspended in fresh 7H9 to assess the bacterial growth recovery after label incorporation, over another incubation period of 144h.

### **Mammalian cell culture and infection experiments**

RAW 264.7 cells (ATCC TIB-71), a mouse monocyte/macrophage cell line, were cultured in DMEM (Sigma-Aldrich) supplemented with 10% FCS, GlutaMAX, penicillin 100 I.U./mL and streptomycin 50 µg/mL and incubated at 37°C, 5% CO<sub>2</sub>. For infection experiments, 10 million cells were seeded on a 10 cm dish for each condition in minimal medium (DMEM, 10% FCS, GlutaMAX), allowed to attach for 8 hours and pre-stimulated with 25 ng/mL LPS-B4 (Sigma-Aldrich) for an additional 18 hours. Cells were infected with triple label *Mtb* at an MOI of 25 for 1 hour, washed three times with minimal medium containing 30 µg/mL gentamicin and incubated for 24 hours, in the presence or absence of 5 µg/mL gentamicin. For intracellular treatment with antibiotics, 1 µg/mL (1.2 µM) rifampicin, 2 µg/mL (14.6 µM) isoniazid, 5 µg/mL (18.0 µM) ethambutol or a combination of the three ('triple-antibiotics cocktail'), was added to the medium during the 24-hour incubation post-infection. For *in vitro* *Mtb* treatment with antibiotics, triple label *Mtb* were incubated for 24 hours in minimal cell medium containing the triple-antibiotics cocktail, washed once with fresh minimal cell medium and subsequently added to the cells for 1 hour to allow phagocytosis (infection).

### **Analysis of label incorporation by in-gel fluorescence**

*Mtb* expressing DsRed were metabolically labeled as described above and samples of OD<sub>600</sub> ≈ 0.5 were collected after 8h, 24h and 48h to analyze the label incorporation levels into the bacterial proteome, by in-gel fluorescence. Bacterial samples were pelleted by centrifugation (10 min at 9000 rcf), washed once with PBS and resuspended in 100 µL lysis buffer. Lysis buffer and conditions were varied (**Table 1**) to allow for optimal killing and recovery of bacterial proteins, while maintaining compatibility with subsequent copper(I)-catalyzed Huisgen cycloaddition (ccHc or 'click') reaction. Optimal lysis and protein recovery was achieved with 1% SDS and immediate heat treatment (30 min at 80°C). Protein concentration of the lysates was determined using Qubit Protein Assay (Thermo Fisher Scientific) and 10 µg protein was diluted to 20 µL total volume. Lysates were

reacted with AF647-azide (Hpg/alkDala) or alkyne (Aha/dual) by ccHc, through direct addition of 10  $\mu$ L 3X concentrated 'click cocktail' (3 mM copper sulfate, 30 mM sodium ascorbate, 3 mM THPTA ligand, 30 mM aminoguanidine, 100 mM HEPES pH 8 and 15  $\mu$ M fluorophore; mixed in this exact order) and incubated for 1 hour at room temperature. The reaction was quenched by adding 10  $\mu$ L 4X concentrated Laemmli sample buffer and boiling for 5-10 min at 95°C, followed by brief cooling on ice. 10  $\mu$ L of the fluorophore-labeled lysates was loaded on a 15-slot 12.5% gel and separated by SDS-PAGE. In-gel fluorescence was measured on a Bio-Rad Chemidoc MP Imaging System (Bio-Rad Laboratories), followed by Coomassie Brilliant Blue staining and imaging as a protein loading control. Gel images were analyzed with Bio-Rad Image Lab Software (Bio-Rad Laboratories).

### **Analysis of label incorporation by flow cytometry**

*Mtb* expressing DsRed were metabolically labeled as described above and samples of OD<sub>600</sub>  $\approx$  0.5 were collected after 8h, 24h and 48h to analyze the label incorporation levels per bacterium, by flow cytometry. Bacterial samples were pelleted by centrifugation (10 min at 9000 rcf), washed once with PBS and resuspended in 100  $\mu$ L fixative. Fixation and permeabilization conditions were varied (**Table 2**) to allow for optimal penetration of click fluorophores into the fixed bacteria, to reach the targeted bioorthogonal labels. Washing conditions were varied (**Table 3**) to allow for optimal resuspension and recovery of fixed bacteria, using an anti-clumping additive. Optimal fluorophore penetration and recovery of fixed bacteria were achieved by pre-permeabilizing the bacteria with 1% SDS in PBS for 15 min at room temperature, followed by fixation with 4% paraformaldehyde in PBS for 24 hours at room temperature, after collecting the bacteria by centrifugation (10 min at 9000 rcf). Fixed bacteria were collected by low-speed centrifugation (10 min at 2000 rcf) and stored in 0.5% paraformaldehyde in PBS at 4°C until all time points were collected. Low-speed centrifugation was used to collect the fixed bacteria in between all further steps, to avoid damage due to excessive G-forces. Bacteria were washed once with PBS to remove residual paraformaldehyde and once with FACS buffer (0.1% BSA, 20 mM glycine in PBS) to quench free aldehydes. The first ccHc reaction, with AF647-azide, was performed, by resuspending the bacteria in 'click cocktail' (1 mM copper sulfate, 10 mM sodium ascorbate, 1 mM THPTA ligand, 10 mM aminoguanidine, 100 mM HEPES pH 8 and 5  $\mu$ M fluorophore; mixed in this exact order), and incubating for 1 hour at room temperature. After a single wash with FACS buffer, the second ccHc reaction, with AF488-alkyne, was performed in the same manner. After another wash with FACS buffer, the bacteria were resuspended in blocking buffer (1% BSA, 10 mM EDTA in

PBS) and incubated for 30 min at room temperature, to assist the removal of non-specifically bound fluorophores. After a final wash with FACS buffer, the bacteria were resuspended in FACS buffer and measured on a BD FACSLytic Flow Cytometer (BD Biosciences). The UV-autofluorescence of *Mtb* was detected in the V450 channel, Aha-AF488 was detected in the FITC channel, DsRed was detected in the PE channel and alkDala-AF647 was detected in the APC channel. Automatic compensation was provided by the integrated BD FACSuite software (BD Biosciences) and all subsequent analysis was performed with FlowJo V10 (FlowJo software). The measured events were gated on size, shape and fluorescence to accurately select single bacteria (Fig. 2A). Quantification of label incorporation was achieved by selecting the median fluorescence intensity (MFI) of the major [Aha+/alkDala+] population for dually-labeled *Mtb* or the major [Aha-/alkDala-] population for unlabeled *Mtb* (Fig. 2A, Fig. S2).

### **Preparation of single-bacteria samples for CLEM**

*Mtb* expressing DsRed were metabolically labeled as described above and samples of 50 mL were collected after 1h, 24h and 48h to analyze the label incorporation levels into the bacterial proteome and cell wall, by on-section ccHc reaction. Unlabeled control bacteria were included as a control for background fluorescence of on-section ccHc reaction. Bacteria were collected by centrifugation (15 min 3000 rcf), washed once with PBS and resuspended in a fixation solution optimized for Transmission Electron Microscopy (TEM) (2% EM-grade paraformaldehyde, 0.2% EM-grade glutaraldehyde in 0.1M phosphate buffer pH 7.2) and rotated for 2 hours at room temperature. The fixed bacteria were collected by centrifugation and stored in storage buffer (0.5% EM-grade paraformaldehyde in 0.1M phosphate buffer pH 7.2) at 4°C until all time points were collected. The fixed bacteria were washed with PBS and aldehyde residues were quenched with 20 mM glycine in PBS. Next, the bacteria were collected by centrifugation, resuspended in warm 1% gelatin in PBS, transferred to a 1.5 mL Eppendorf tube, resuspended in warm 12% gelatin in PBS and pelleted by centrifugation (3 min at 5000 rcf). After jellification on ice, the sample pellet was cut off from the tube and cut in half with a razor knife. Sample cubes of approx. 1 mm<sup>2</sup> were prepared and rotated in a 2.3 M sucrose solution for 18 hours to allow for sucrose infiltration, as a cryo-protectant, followed by plunge-freezing the cubes on metal support pins.

### **Preparation of *Mtb*-infected macrophage samples for CLEM**

Following infection and post-infection incubation of triple labeled *Mtb* in RAW 264.7 cells, in the presence or absence of antibiotics, the cells were washed three

times with minimal cell medium containing 30 µg/mL gentamicin and once with PBS. The cells were fixed with TEM-optimized fixation solution (2% EM-grade paraformaldehyde, 0.2% EM-grade glutaraldehyde in 0.1M phosphate buffer pH 7.2) for 2 hours at room temperature, rinsed with PBS and stored in storage buffer (0.5% EM-grade paraformaldehyde in 0.1M phosphate buffer pH 7.2) at 4°C until all time points were collected. Fixed cells were rinsed with PBS, harvested in warm 1% gelatin in PBS with cell scrapers and transferred to a 15 mL Falcon tube. The cells were collected by centrifugation, resuspended in warm 1% gelatin in PBS, transferred to a 1.5 mL Eppendorf tube, resuspended in warm 12% gelatin in PBS and pelleted by centrifugation (3 min at 800 rcf). Samples were further processed for plunge-freezing as described for the bacteria-only samples above.

### **Cryo-sectioning and on-section ccHc reaction**

Ultrathin (75 nm) cryo-sections were prepared according to the Tokuyasu technique<sup>54,55</sup>, using a cryo-ultramicrotome (Leica) and diamond knife (Diatome). Sections were thawed on a droplet of pickup fluid (1.15 M sucrose, 1% methylcellulose) and transferred to a Formvar/carbon-coated TEM grid (titanium, 100 square mesh, 3.05 mm, center-marked; Agar Scientific), pre-coated with blue 0.2 µm FluoSpheres (Thermo Fisher) as fiducial markers. Thawed cryo-sections attached to the TEM grid were incubated on 2% gelatin in PBS for 30 min at 37°C, followed by washing on 20 mM glycine in PBS (5x 2 min). Next, the sections were subjected to ccHc reaction with AF647-azide (or AF647-alkyne for analysis of label incorporation) on a droplet of 'click cocktail' (1 mM copper sulfate, 10 mM sodium ascorbate, 1 mM THPTA ligand, 10 mM aminoguanidine, 100 mM HEPES pH 8 and 5 µM fluorophore; mixed in this exact order), for 1 hour at room temperature. After several washes with PBS, the second ccHc reaction with AF488-alkyne was performed, followed by several washes with PBS. The sections were then incubated on droplets of 1% BSA in PBS for 3 x 10 min at room temperature, to assist the removal of non-specifically bound fluorophores. Nuclear staining of the host cells was achieved by incubating the sections on a droplet of 0.2 µg/mL DAPI in PBS for 5 min.

### **Confocal microscopy**

After several washes with PBS, the fluorescently-labeled sections attached to TEM grids were mounted in water containing 30% glycerol between a microscopy slide and a coverslip, and sealed with silver Scotch tape. The samples were imaged on an Andor Dragonfly 505 Spinning Disk Confocal (Oxford Instruments), containing an 8-line integrated laser engine, on a Leica DMI8 inverted microscope equipped with a

100X/1.47 HC PL APO TIRF-corrected oil objective. FluoSpheres were excited with the 405 line and collected with the 450/50 BP emission filter, AF488 was excited with the 488 line and collected with the 525/50 BP emission filter, DsRed was excited with the 561 line and collected with the 620/60 BP emission filter and AF647 was excited with the 637 line and collected with the 700/75 BP emission filter. Images were acquired with the Zyla 2048x2048 sCMOS camera and 2x2 camera binning controlled with the integrated Fusion software. Z-series optical sections were collected with a system-optimized step-size of 0.13 microns and deconvolved using the integrated ClearView-GPU™ deconvolution software. Z-series are displayed as maximum z-projections, and gamma, brightness and contrast were carefully adjusted (identically for compared image sets) using FIJI.<sup>77</sup> Maximum intensity projections were made, in order to compensate for non-flat sections.

### **TEM imaging and correlation**

After acquiring the fluorescence microscopy (FM) images, the TEM grids containing the sections were recovered from the microscopy slides, rinsed in distilled water and incubated for 5 min on droplets of uranyl acetate/methylcellulose. The negatively-stained sections were then imaged on a FEI Tecnai 12 BioTwin TEM System (FEI Technologies) at 120 kV acceleration voltage. Correlation of FM and TEM images was performed in Adobe Photoshop CC 2020 (Adobe Systems). The separate fluorescence channels were imported as layers, set to overlay mode 'Lighten', then grouped and set to overlay mode 'Color', placed on top of the TEM image. Transformation of the FM image to match the TEM image was achieved by isotropic scaling with interpolation setting 'bicubic smoother', translation and rotation. Alignment at low magnification was guided by the grid bars and sample shape for single bacteria or nuclei for *Mtb*-infected cells. Alignment at high magnification was guided by the fiducial beads and the position of the bacteria. Minor manual corrections for chromatic aberration were applied where required, guided by the obvious bacterial shapes, showing a clear internal [DsRed+/Aha+] part and a ring-like [alkDala+] cell wall.

### **Quantification of intracellular *Mtb* localization and shape *in situ* by CLEM-based data analysis**

The intracellular localization and shape of triple label *Mtb*, in the presence or absence of antibiotics, was quantified by manual counting of bacteria in the large CLEM image, using Adobe Photoshop CC 2020 (Adobe Systems). Fluorescence was used to guide the detection of bacteria, and the geometrical shapes tool ('rectangle', 'rounded rectangle', 'ellipse', 'polygon' and 'custom shape') was used

to classify bacteria and host cells based on their appearance and localization, which allowed for facile automatic counting for each of the categories (geometric shapes) by Photoshop. The complete large field of view CLEM image was used for quantification, which allowed for a large data set of over 500 bacteria per condition. The distribution of intracellular bacteria was classified as either 'no vacuole', 'small/tight vacuole' or 'large/spacious vacuole' to allow unbiased counting, and plotted as percentage relative to the total number of intracellular bacteria counted. Extracellular bacteria were counted separately and plotted as percentage relative to the total number of intracellular and extracellular bacteria counted. The appearance (bacterial profile) of intracellular bacteria was classified as either 'regular shape' or 'irregular shape' to allow unbiased counting, and plotted as percentage relative to the total number of bacteria counted. Host cell death was quantified by counting disintegrated cell profiles, still containing a DAPI-positive compartment to allow unbiased counting, and plotted as percentage relative to the total number of nucleus-containing cell profiles counted. Each of the conditions was tested at least twice but the quantified data were obtained from a single experiment in which all conditions were tested simultaneously in parallel, to avoid technical variations.

### **Quantification of intracellular *Mtb* size and label retention *in situ* by CLEM-based data analysis**

Label retention of intracellular triple label *Mtb*, in the presence or absence of antibiotics, was quantified by semi-automatic analysis of the fluorescence (DsRed, Aha-AF488, alkDala-AF647). To this end, a JavaScript was created using the Adobe Photoshop CC Script Listener Plug-in for Windows (2020 version, downloaded from <https://helpx.adobe.com/photoshop/kb/downloadable-plugins-and-content.html>), in combination with some manual modifications, and is freely available upon request. The resulting script only requires manual selection of the outline of a bacterium using the 'lasso tool', and allows for automatic cropping of the selected bacterium, followed by removal of the external area surrounding the outline. The bacterial fluorescence profiles for each channel (as well as the TEM image) are exported separately and saved as TIF files in a '[channel]\_bacterium\_[number]' format that allows automatic pairing and counting. A secondary ImageJ (IJ1) Macro-style script was created to automatically analyze all exported bacterial fluorescence profiles, based on average fluorescence intensity, and is freely available upon request. The resulting data points were plotted individually in violin plots using GraphPad Prism 8 (GraphPad Software). Each of the conditions was tested at least twice but the

quantified data were obtained from a single experiment in which all conditions were tested simultaneously in parallel, to avoid technical variations.

### **Quantification of *Mtb* label retention by flow cytometry after recovery from host cell (*ex cellula*)**

Following infection and post-infection incubation of triple labeled *Mtb* in RAW 264.7 cells, in the presence or absence of antibiotics (identical to CLEM experiment), the cells were washed three times with minimal cell medium containing 30 µg/mL gentamicin and once with PBS. Cells were lysed with lysis buffer (0.1% Triton-X100, 150 mM NaCl, 20 mM Tris-HCl) for 15 min at room temperature and the cell debris was separated from the bacteria by centrifugation (5 min at 600 rcf) and pellet discarded. The bacteria were collected by centrifugation (15 min at 3000 rcf), pre-permeabilized with 1% SDS in PBS and fixed with 4% paraformaldehyde in PBS for 24 hours at room temperature. Fixed bacteria were collected by low-speed centrifugation (10 min at 2000 rcf) and stored in 0.5% paraformaldehyde in PBS at 4°C until all time points were collected. The isolated bacteria were further processed and measured by flow cytometry, as described for the freshly labeled *Mtb* above. The measured events were gated on size, shape and fluorescence to accurately select single bacteria (Fig. 2A). Quantification of label retention was achieved by selecting the MFI of the major [Aha+/alkDala+] population and corresponding [autofluorescence+/DsRed+] population (Fig. 6B, Fig. S12). Each of the conditions was tested at least twice but the quantified data were obtained from a single experiment in which all conditions were tested simultaneously in parallel, to avoid technical variations.

### **Statistics**

The unpaired two-tailed Mann-Whitney U test and Chi-Square ( $\chi^2$ ) test were performed using GraphPad Prism 8 (GraphPad Software). The Benjamini-Hochberg procedure for multiple testing was performed in Microsoft Excel 2016 (Microsoft), with a False Discovery Rate (FDR) of 0.1.

## 5.5 Supplemental Figures

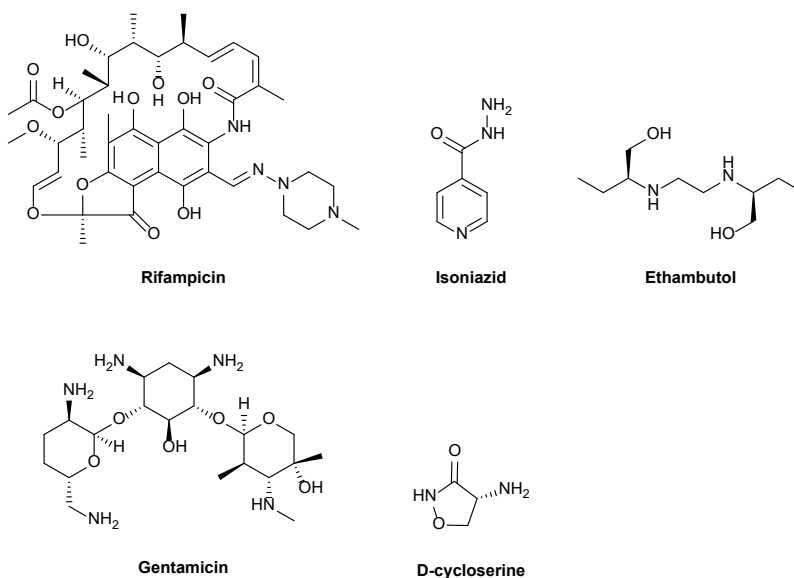


**Figure S1.** Overview of antibiotics used in this study. Rifampicin is a polyketide antibiotic that inhibits bacterial RNA synthesis by binding to the RNA polymerase  $\beta$  subunit.<sup>78</sup> Isoniazid is a prodrug that is activated by KatG to form a nicotinoyl-NAD adduct, which in turn inhibits mycolic acid synthesis, thereby interfering with the mycobacterial cell wall synthesis.<sup>79</sup> Ethambutol is a small molecule antibiotic that inhibits arabinogalactan synthesis, thereby interfering with the bacterial cell wall synthesis.<sup>80</sup> The bacteriostatic and/or bactericidal effect of these antibiotics are concentration-, time- and growth phase dependent, and may differ when used in combination.<sup>81,82</sup> Gentamicin is a bactericidal aminoglycoside antibiotic that inhibits bacterial protein synthesis by binding to the bacterial ribosome.<sup>83</sup> Gentamicin is not cell permeable but is actively taken up by Gram-negative bacteria in an oxygen-dependent manner.<sup>84</sup> D-cycloserine is a cyclic D-alanine analogue that blocks peptidoglycan synthesis, thereby interfering with the bacterial cell wall synthesis.<sup>85</sup> D-cycloserine can be bacteriostatic or bactericidal depending on the concentration and the susceptibility of the bacterial species.<sup>86</sup>



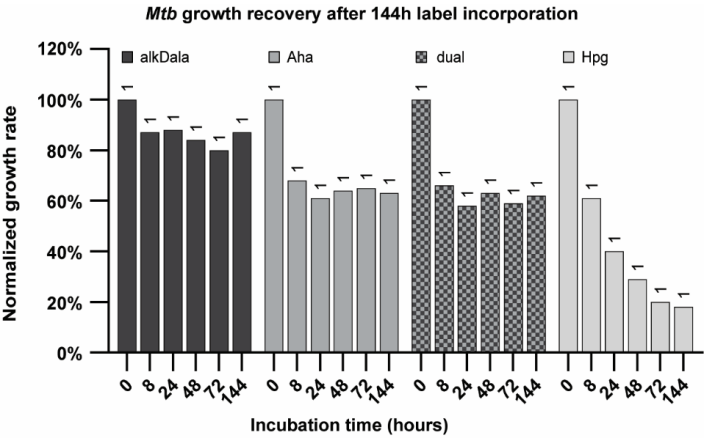


**Figure S2.** Growth recovery of *Mtb* after 144h label incorporation relative to control. DsRed-expressing *Mtb* H37Rv were first incubated with 4 mM Hpg, 4 mM Aha, 5 mM alkDala or a combination of 4 mM Aha and 5 mM alkDala (dual), for 144h in Middlebrook 7H9 broth (shown in Fig. 1A). The medium was then replaced by fresh 7H9 broth without metabolic labels and the bacterial growth recovery after labeling was assessed for another 144h by OD<sub>600</sub> measurements, normalized on the first time point. The number of biological replicates for each OD<sub>600</sub> measurement is indicated above the bar.

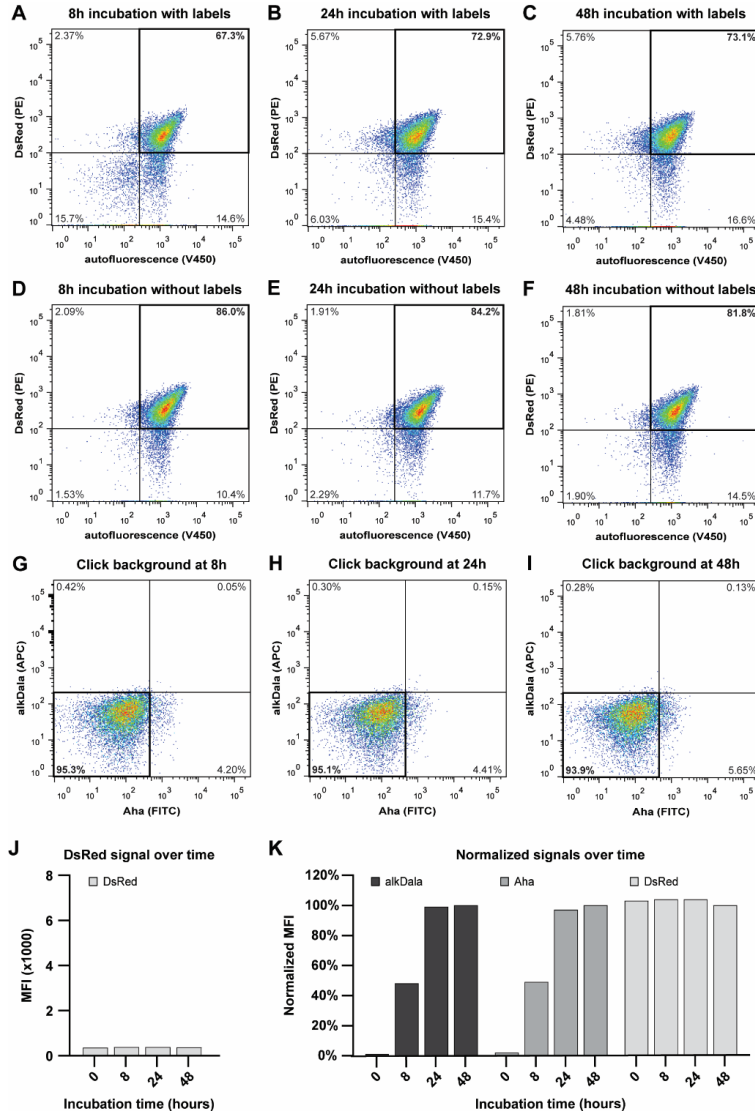


**Figure S3.** Controls of label incorporation over time by flow cytometry. DsRed-expressing *Mtb* H37Rv were incubated with a combination of 4 mM Aha and 5 mM alkDala or without labels, for the indicated time in Middlebrook 7H9 broth. Bacterial samples of 0.5 OD were collected, pre-permeabilized with 1% SDS and fixed in 4% paraformaldehyde. Fixed and permeabilized bacteria were reacted with AF647-azide (alkDala) and AF488-alkyne (Aha) by two sequential cChc reactions. The effect of label incorporation on DsRed fluorescence was assessed after 8 h (A), 24 h (B) and 48 h (C) incubation and compared to incubation without metabolic labels after 8 h (D), 24 h (E) and 48 h (F). The background fluorescence of the cChc (click) reaction was analyzed after incubation without metabolic labels for 8 h (G), 24 h (H) and 48 h (I). J: The effect of label incorporation on DsRed fluorescence over time is shown as the median fluorescence intensity (MFI), on the same scale as used in Fig. 2A for comparison. K: The relative change in label incorporation over time and the resulting effect on DsRed fluorescence are shown as normalized MFI values, corresponding to the MFI values presented in Fig. 2A and panel J of this figure.

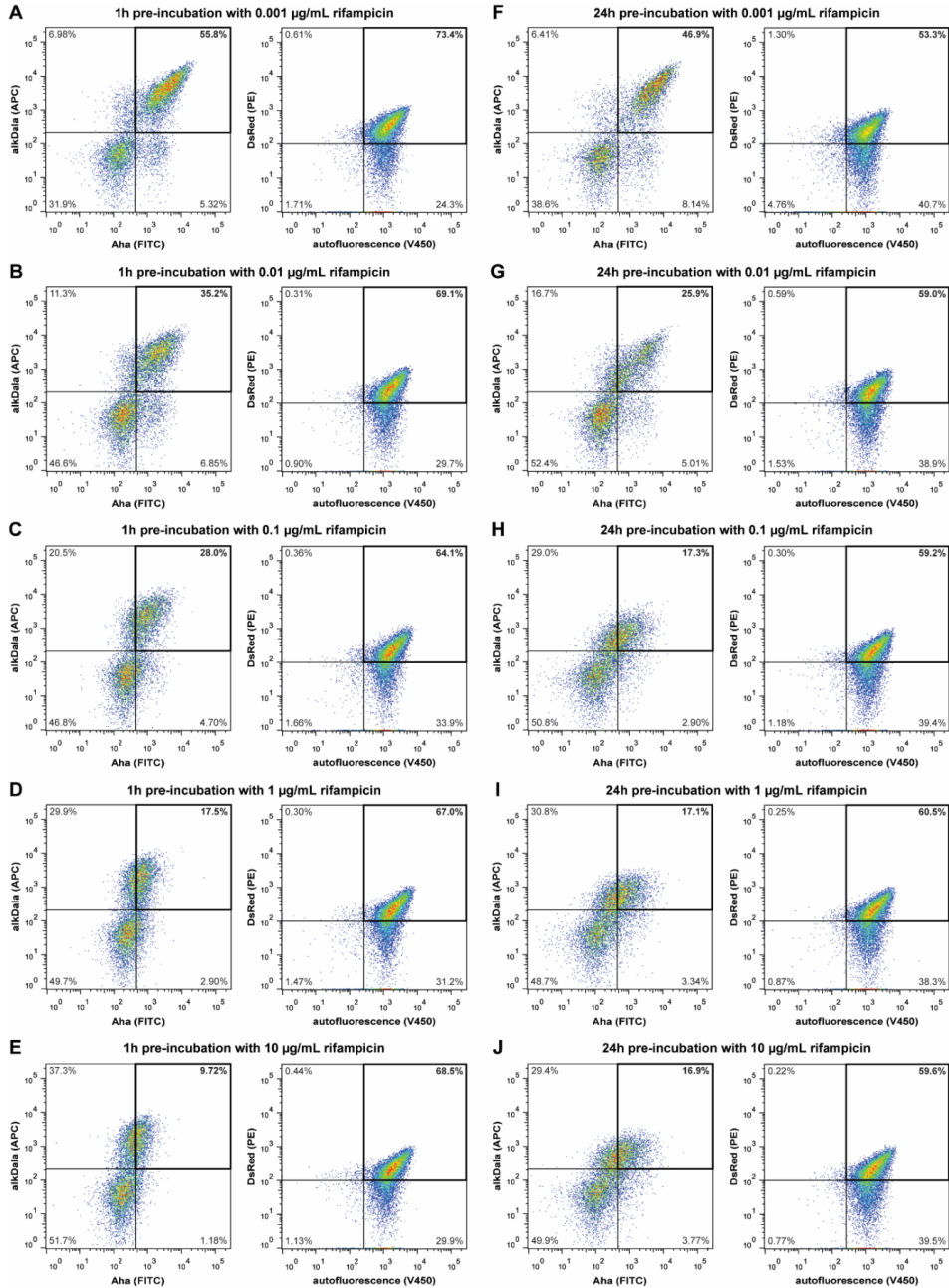


**Figure S4.** Controls of label incorporation over time by flow cytometry in presence of increasing concentrations of Rifampicin. DsRed-expressing *Mtb* H37Rv were cultured and analyzed as for Figure S2 after pretreatment with for either 1h (A-E) or 24h (F-J) with rifampicin in increasing concentrations.

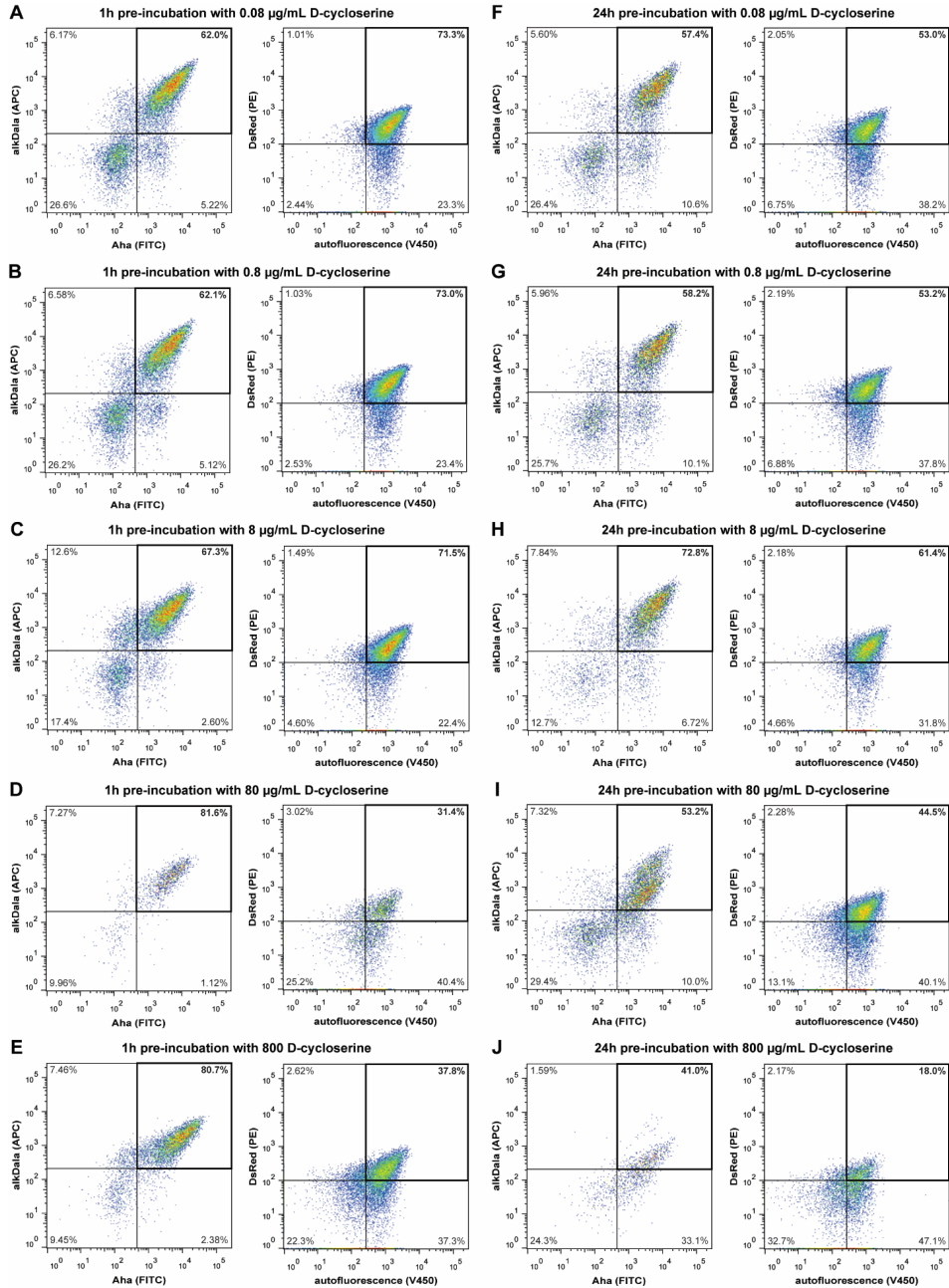


**Figure S5.** Controls of label incorporation over time by flow cytometry in presence of increasing concentrations of D-cycloserine. DsRed-expressing *Mtb* H37Rv were cultured and analyzed as for Figure S2 after pretreatment with for either 1h (A-E) or 24h (F-J) with D-cycloserine in increasing concentrations.

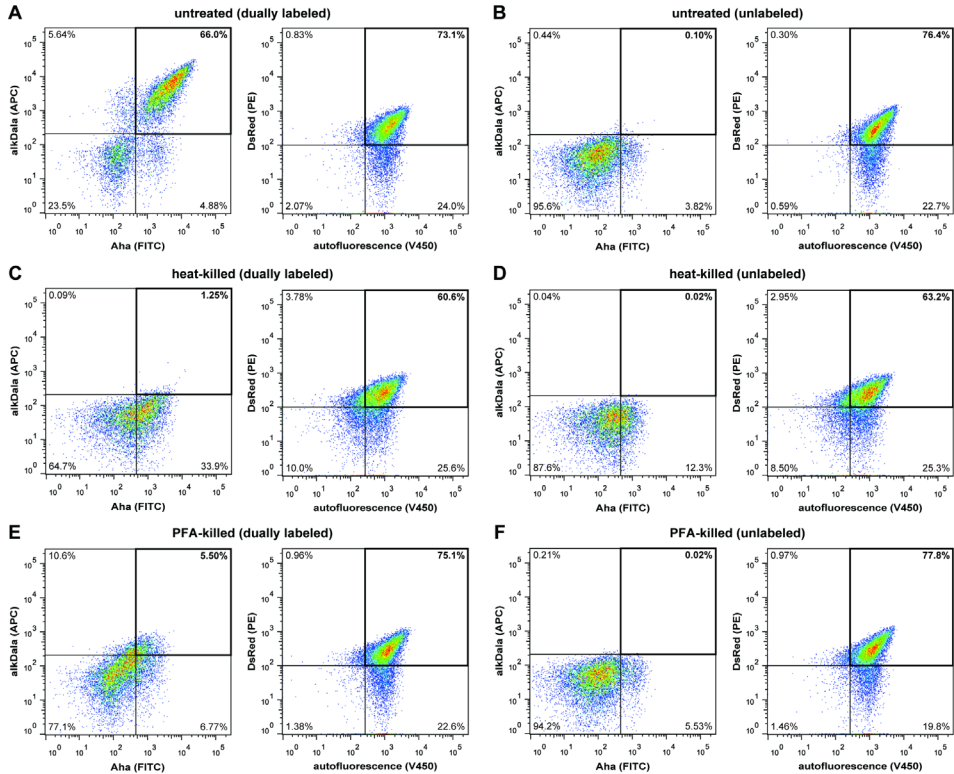


**Figure S6.** Controls of label incorporation by flow cytometry after heat-killing or PFA-fixation. **A/B:** Untreated control bacteria with or without metabolic labels. **C/D:** Heat-killed bacteria (30 min at 80 °C) with or without metabolic labels. **E/F:** PFA-killed bacteria (30 min in 4% PFA) with or without metabolic labels.



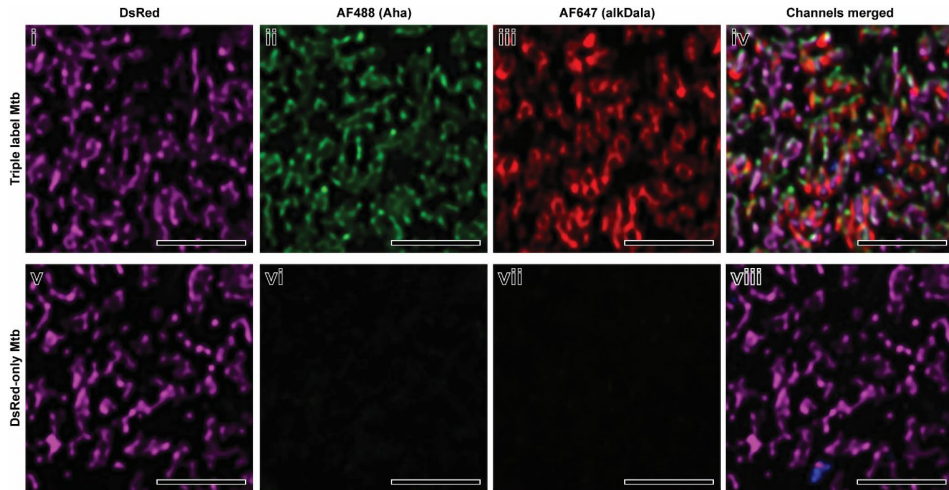


**Figure S7.** Signal and background fluorescence of on-section click reactions. Triple label *Mtb* and DsRed-only *Mtb* were prepared, followed by cryo-sectioning and dual on-section ccHc reaction with AF647-azide (alkDala) and AF488-alkyne (Aha), sequentially. The resulting confocal microscopy images are shown as separated fluorescence channels for clarity. All scale bars represent 5  $\mu$ m.

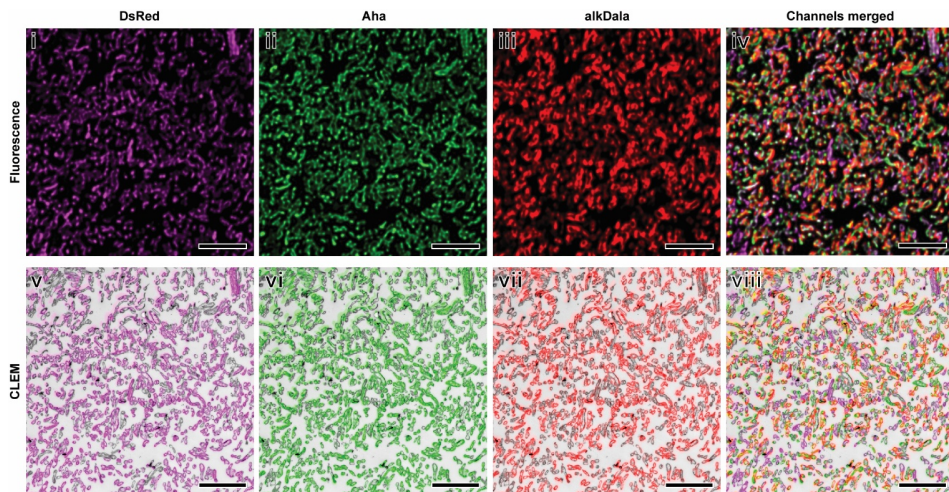


**Figure S8.** Large area CLEM image of *Mtb in vitro*, corresponding to the details presented in Fig. 3. Triple label *Mtb* and DsRed-only *Mtb* were prepared and subsequently prepared for cryo-sectioning, followed by cryo-sectioning and dual on-section ccHc reaction with AF647-azide (alkDala) and AF488-alkyne (Aha), sequentially. The sections were imaged by confocal microscopy, then stained with uranyl acetate and imaged by TEM. The resulting fluorescence and TEM images were correlated in Photoshop to obtain the CLEM image, shown in the bottom panel. The top panel shows the corresponding fluorescence channels separately for clarity. All scale bars represent 5  $\mu$ m.

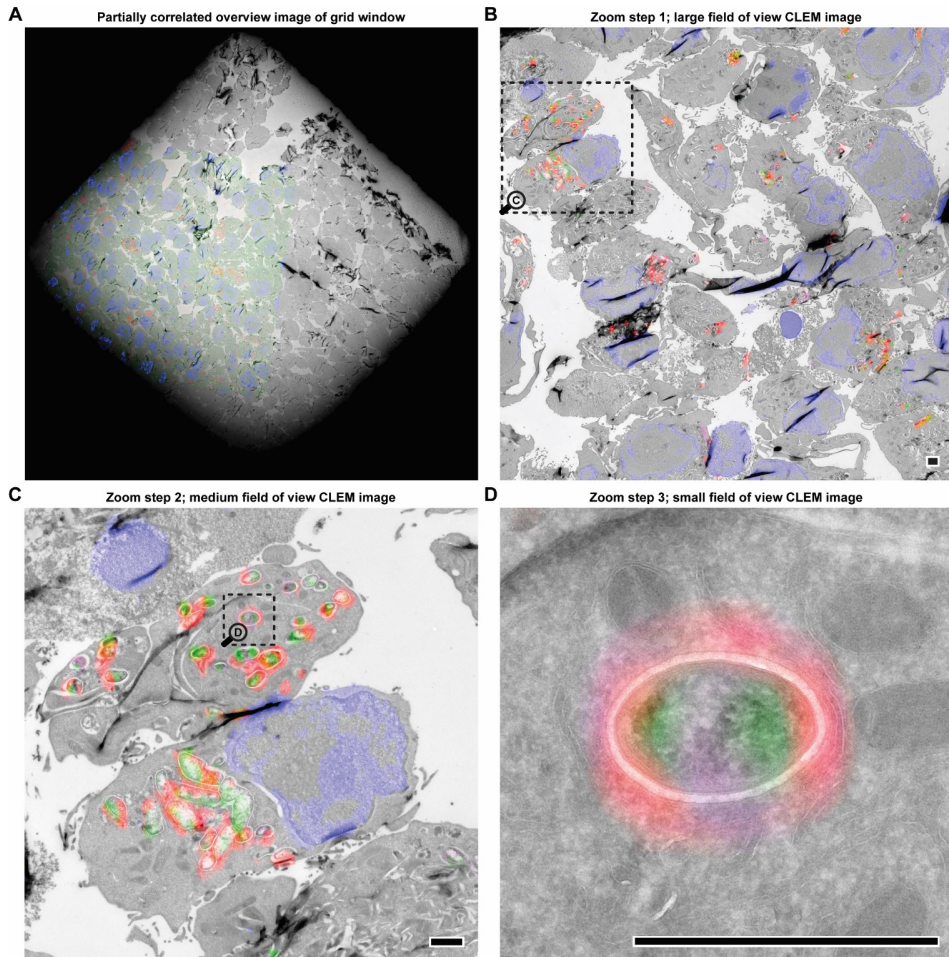


**Figure S9.** Stepwise zooming in from an ultra large field of view CLEM image, corresponding to the details presented in Fig. 4. RAW 264.7 macrophages were infected with triple label *Mtb*, incubated for 24 hours without antibiotics, and subsequently prepared for cryo-sectioning, followed by dual on-section ccHc reaction with AF647-azide and AF488-alkyne. The resulting confocal fluorescence image was correlated onto the corresponding large field of view (stitched) TEM image, using Photoshop. An entire window in the TEM grid could be partially correlated with the available fluorescence image, depending on the orientation of the grid during acquisition (**A**). Photoshop allows zooming to an area of interest to provide the required details, while keeping the channels separated (i.e. multimodal dataset). The boxed area in the large field of view CLEM image (**B**) corresponds to the medium field of view image (**C**), in which the boxed area corresponds to the small field of view image (**D**; separated channels shown in Fig. 4i-iv). All scale bars represent 1  $\mu\text{m}$ .



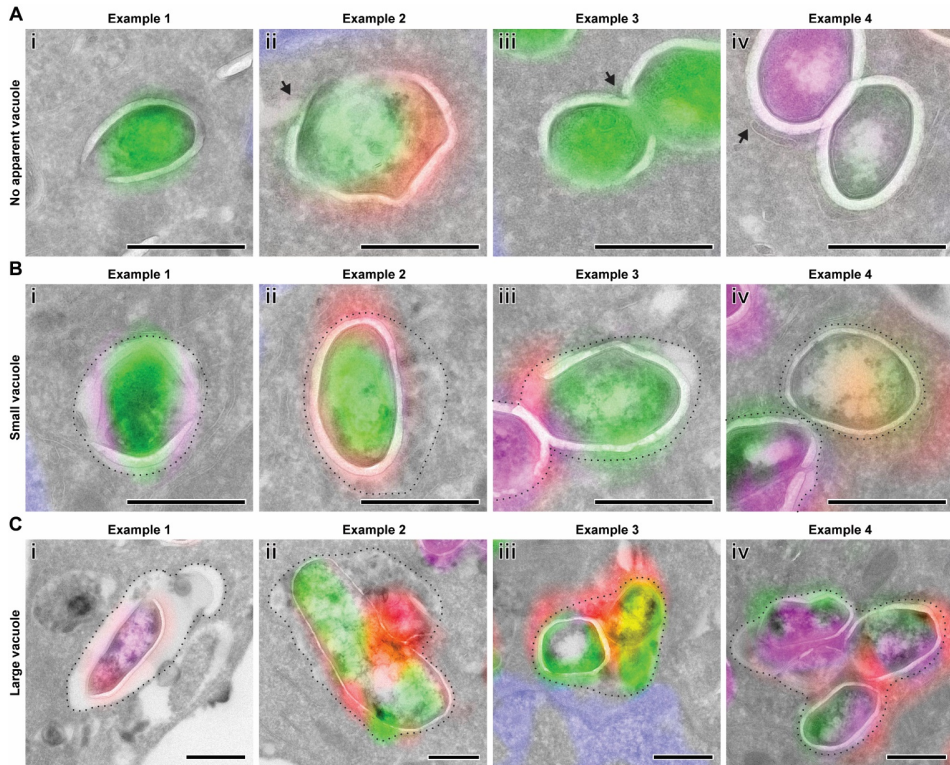


**Figure S10.** *Mtb* displays a heterogeneous intracellular distribution in host cells. RAW 264.7 macrophages were infected with triple label *Mtb* and incubated with or without antibiotics, and subsequently prepared for cryo-sectioning, followed by dual on-section ccHc reaction with AF647-azide and AF488-alkyne. The resulting confocal fluorescence image was correlated onto the corresponding large field of view (stitched) TEM image, using Photoshop. A small percentage of bacteria appears to have escaped into the cytosol, as no vacuole can be observed (A). These bacteria may fuse again with a vacuole (ii), divide cytosolically (iii) or potentially be re-compartmentalized into a double membrane autophagosome (iv). An intermediate percentage of bacteria resides in a small vacuole (B), that can appear empty (i) or filled with smaller vacuoles/granules (ii). Bacteria may divide within small vacuoles (iii) and the vacuole may wrap tightly around the bacterium (iv). A large percentage of bacteria resides in large vacuoles (C) that may appear spacious (i) or filled with smaller vesicles/granules (ii). Vacuoles containing a cluster of bacteria were classified as large, regardless of being smaller (iii) or larger (iv). A dotted line indicates the apparent vacuole where relevant. All scale bars represent 500 nm.



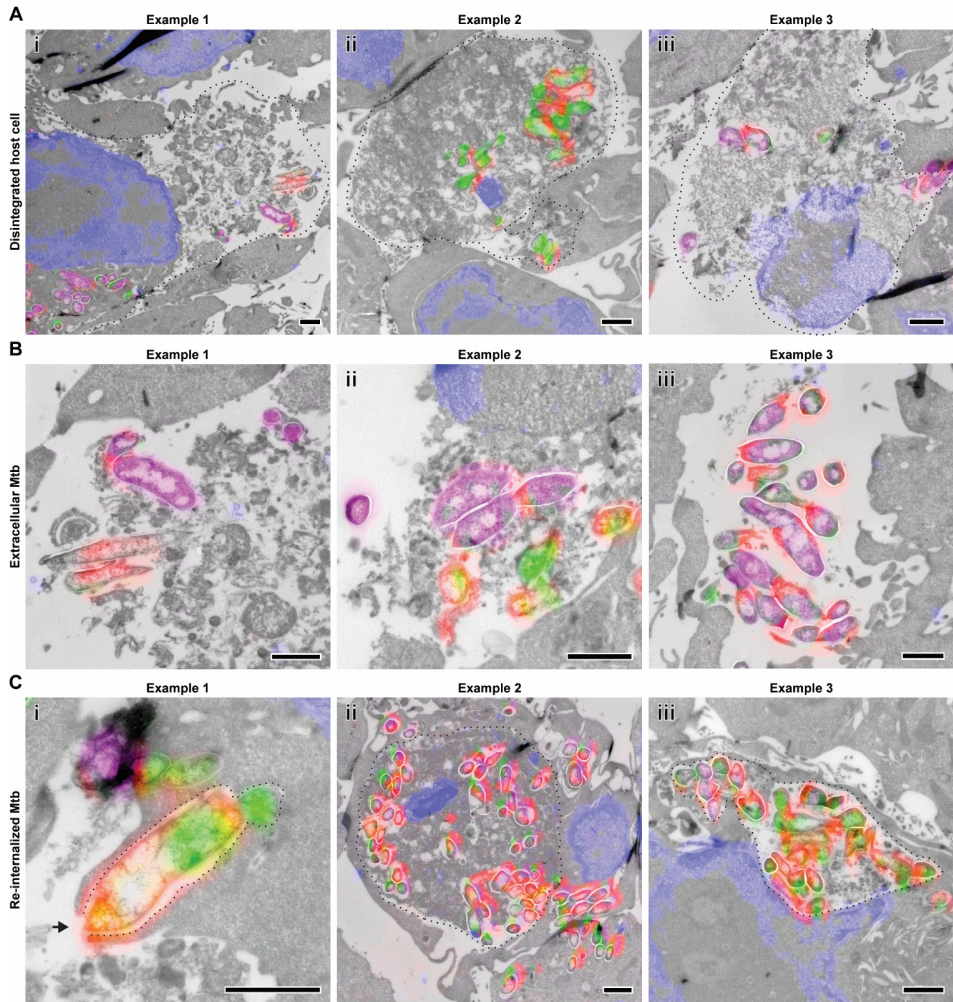


**Figure S11.** *Mtb* is released from host cell and subsequently re-internalized by surrounding macrophages. RAW 264.7 macrophages were infected with triple label *Mtb* and incubated with or without antibiotics. The resulting confocal fluorescence image was correlated onto the corresponding large field of view (stitched) TEM image, using Photoshop. Some *Mtb*-containing macrophages are disintegrated (**A**), probably as a result of the *Mtb* infection. The escaped bacteria reside extracellularly (**B**), surrounded by cell debris. Extracellular bacteria appear to be re-internalized by neighboring cells (**C**), through phagocytosis of separate bacteria (i) or internalization of the entire necrotic cell (ii), which can result in large vacuoles that contain both bacteria and cell debris (iii). A dotted line indicates the apparent cell outline or vacuole where relevant. All scale bars represent 1  $\mu\text{m}$ .

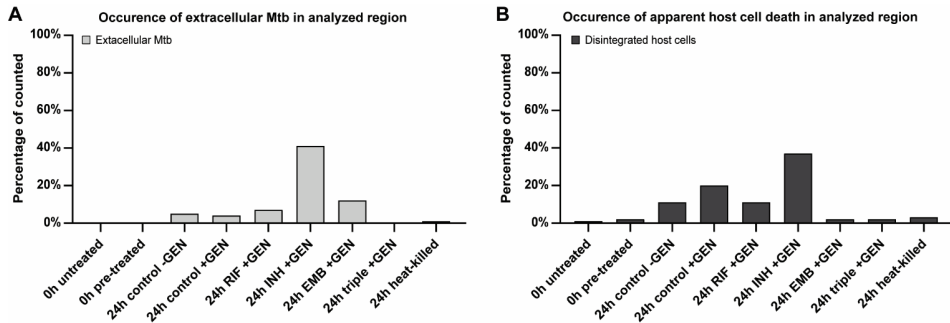


**Figure S12.** The occurrence of extracellular *Mtb* and apparent host cell death changes upon treatment with antibiotics. RAW 264.7 macrophages were infected with triple label *Mtb* for 1 hour and immediately analyzed (0h untreated) or further incubated for 24 hours with rifampicin (RIF), isoniazid (INH), ethambutol (EMB), a combination of the three (triple) or no antibiotics (24h control) and compared to *Mtb* pre-treated with triple antibiotics before infection (0h pre-treated). An additional control with heat-killed *Mtb* (prior to infection) was included as a negative control for pathogenicity. **A:** *Mtb* in the absence of host cell or inside a disintegrating host cell were classified as extracellular *Mtb*. Shown as percentage relative to total number of *Mtb* counted in the analyzed region;  $n > 500$  bacteria counted. **B:** Disintegrating and/or entirely phagocytosed macrophages were classified as host cell death. Shown as percentage relative to total number of macrophages counted in the analyzed region;  $n > 80$  cells counted.

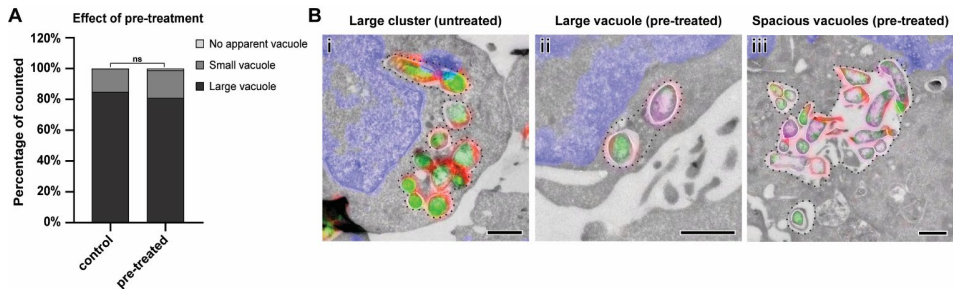


**Figure S13.** *Mtb* resides primarily in large vacuoles directly after infection. RAW 264.7 macrophages were infected with triple label *Mtb* for 1 hour with viable *Mtb* (0h control) or *Mtb* pre-treated with rifampicin, isoniazid and ethambutol (0h pre-treated), and analyzed immediately after infection. The resulting confocal fluorescence image was correlated onto the corresponding large field of view (stitched) TEM image, using Photoshop. **A:** Intracellular distribution of *Mtb* was manually classified as no vacuole/cytosolic (none), small/tight vacuole (small) or large/spacious vacuole (large). Shown as percentage relative to total number of intracellular *Mtb* counted in the analyzed region;  $n > 200$  bacteria counted. **B:** Most untreated bacteria reside in large clusters of smaller vacuoles (i), that were considered large vacuoles for unbiased counting, while most of the pre-treated bacteria reside in large (ii) and spacious (iii) vacuoles. This distinction was not considered in the quantification in order to avoid interpretation bias. A dotted line indicates the apparent vacuole where relevant. All scale bars represent 1  $\mu\text{m}$ .

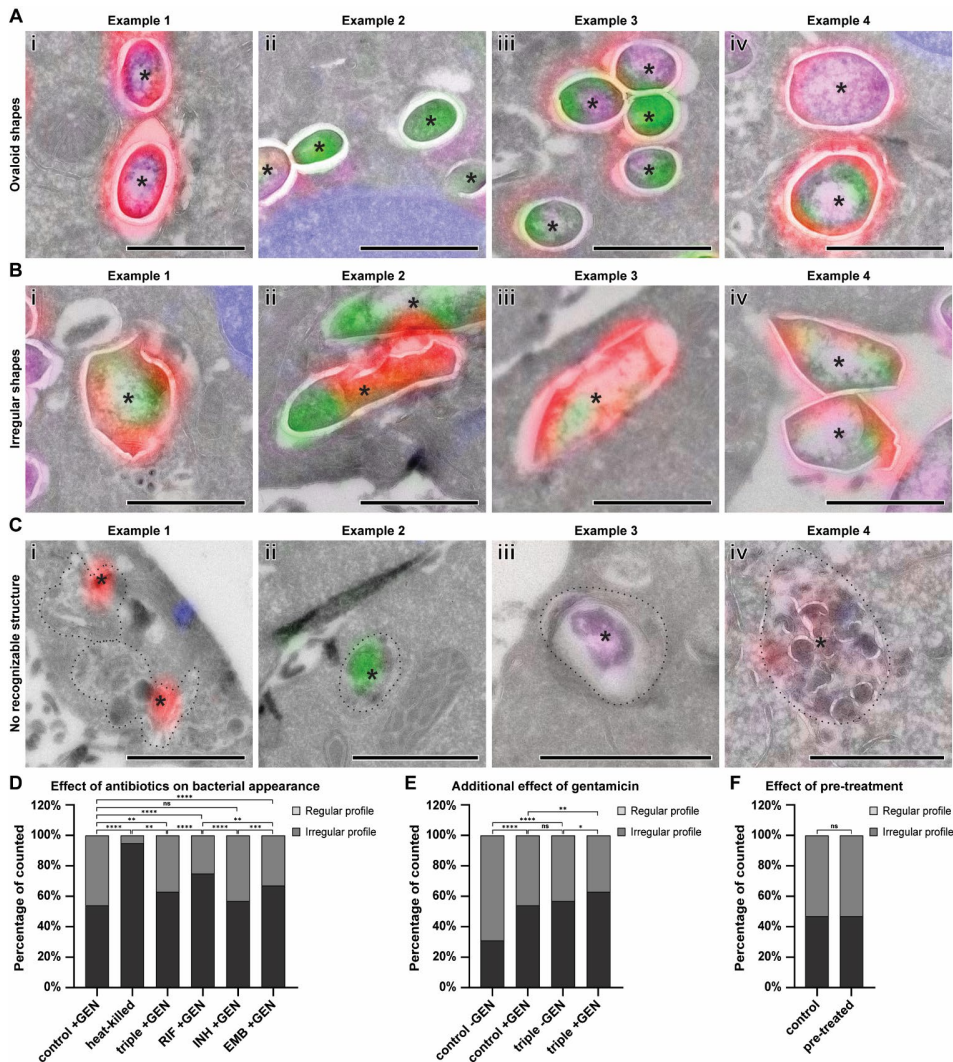


**Figure S14.** Intracellular *Mtb* displays bacterial profiles in various shapes. RAW 264.7 macrophages were infected with triple label *Mtb* for 1 hour (0h untreated) and incubated for 24 hours without antibiotics (24h control) or with rifampicin, isoniazid and ethambutol (24h triple antibiotics) and compared to *Mtb* pre-treated with triple antibiotics before infection (0h pre-treated). The variety of shapes, observed for the bacterial profiles, were classified into ovaloid (A) or irregular (B). In some cases, clear fluorescence was observed without any recognizable bacterial structure (C), containing either alkDala (i), Aha (ii), DsRed (iii) or all three combined (iv). Relevant structures are indicated with an asterisk (\*). A dotted line indicates the apparent vacuole where relevant. All scale bars represent 1  $\mu$ m. **D:** The intracellular appearance of *Mtb* was manually classified as ovaloid or irregular, shown as percentage relative to the total number of *Mtb* counted in the analyzed region; n>500 bacteria counted. **E:** The additional effect of gentamicin (GEN) on the intracellular appearance of *Mtb* was assessed after 24 hours of incubation with triple antibiotic cocktail (triple +/-GEN) or without antibiotics (control +/-GEN); n>500 bacteria counted. **F:** The early intracellular appearance of *Mtb* was assessed directly after infection with *Mtb* pre-treated with triple antibiotics cocktail or with untreated



control bacteria; n>200 bacteria counted. Raw distributions were pairwise compared using the chi-square test and corrected for multiple testing using the Benjamini-Hochberg procedure, with a false discovery rate (FDR) of 0.1 (\*\*\*\*: p<0.0001, \*\*\*: p<0.001, \*\*: p<0.01, \*: p<0.05, ns: not significant).

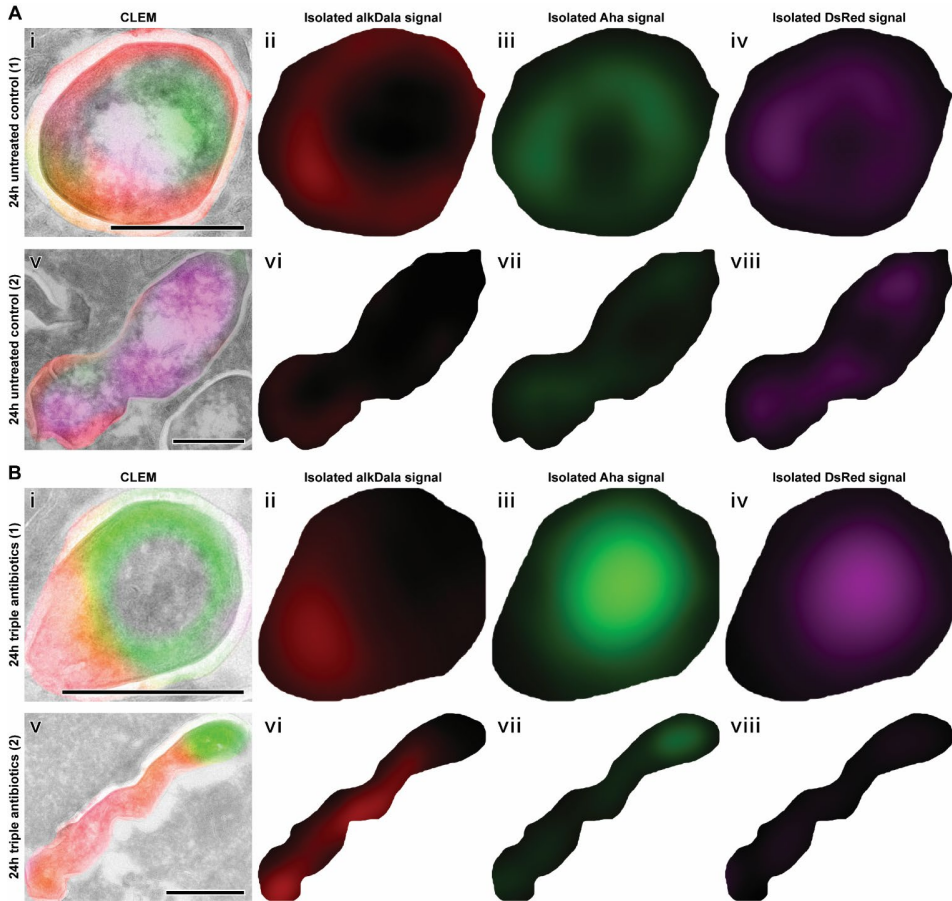


**Figure S15.** Semi-automatic CLEM-based quantification of label retention in intracellular *Mtb*. RAW 264.7 macrophages were infected with triple label *Mtb* for 1 hour and incubated for 24 hours with rifampicin, isoniazid and ethambutol (24h triple antibiotics) or no antibiotics (24h untreated control). The resulting confocal fluorescence image was correlated onto the corresponding large field of view (stitched) TEM image, using Photoshop. Bacterial outline was drawn manually in Photoshop, using the 'lasso tool', followed by automatic cropping and separation of channels, using a JavaScript. Raw fluorescence images (brightness/contrast unchanged) were subsequently analyzed based on the average fluorescence intensity of the non-white area (masked), using an ImageJ macro. **A:** Two examples of untreated control bacteria, incubated for 24 hours intracellularly without antibiotics, showing the color-merged CLEM image (i,v), isolated alkDala signal (ii,vi), isolated Aha signal (iii,vii) and isolated DsRed signal (iv,viii). **B:** Two examples of triple antibiotics treated bacteria, incubated for 24 hours intracellularly with rifampicin, isoniazid and ethambutol, showing the color-merged CLEM image (i,v), isolated alkDala signal (ii,vi), isolated Aha signal (iii,vii) and isolated DsRed signal (iv,viii). All scale bars represent 500 nm.

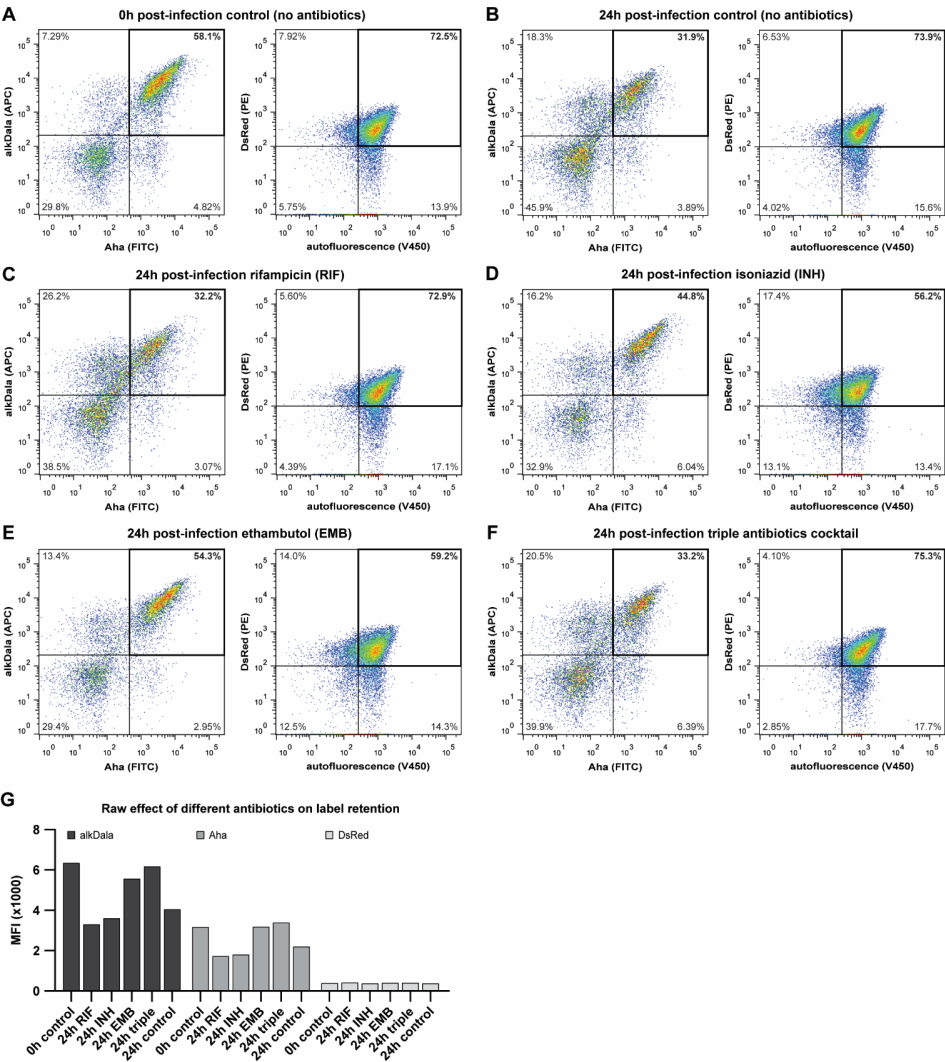


**Figure S16.** Quantification of label retention by flow cytometry. RAW 264.7 macrophages were infected with triple label *Mtb* for 1 hour (0h control; **A**) and further incubated for 24 hours without antibiotics (24h control; **B**) or with rifampicin (RIF; **C**), isoniazid (INH; **D**), ethambutol (EMB; **E**) or a combination of the three (triple; **F**). Bacteria were recovered by selective lysis of the host cell, fixed and processed for flow cytometry. The average label retention was quantified by selecting the Aha+/alkDala+ quadrant or the autofluorescence+/DsRed+ quadrant. **G**: The median fluorescence intensity (MFI) was used for the quantification of all signals, as it reflects the average signal intensity for a local population most accurately. Corresponding normalized MFI values are presented in Fig. 6B.

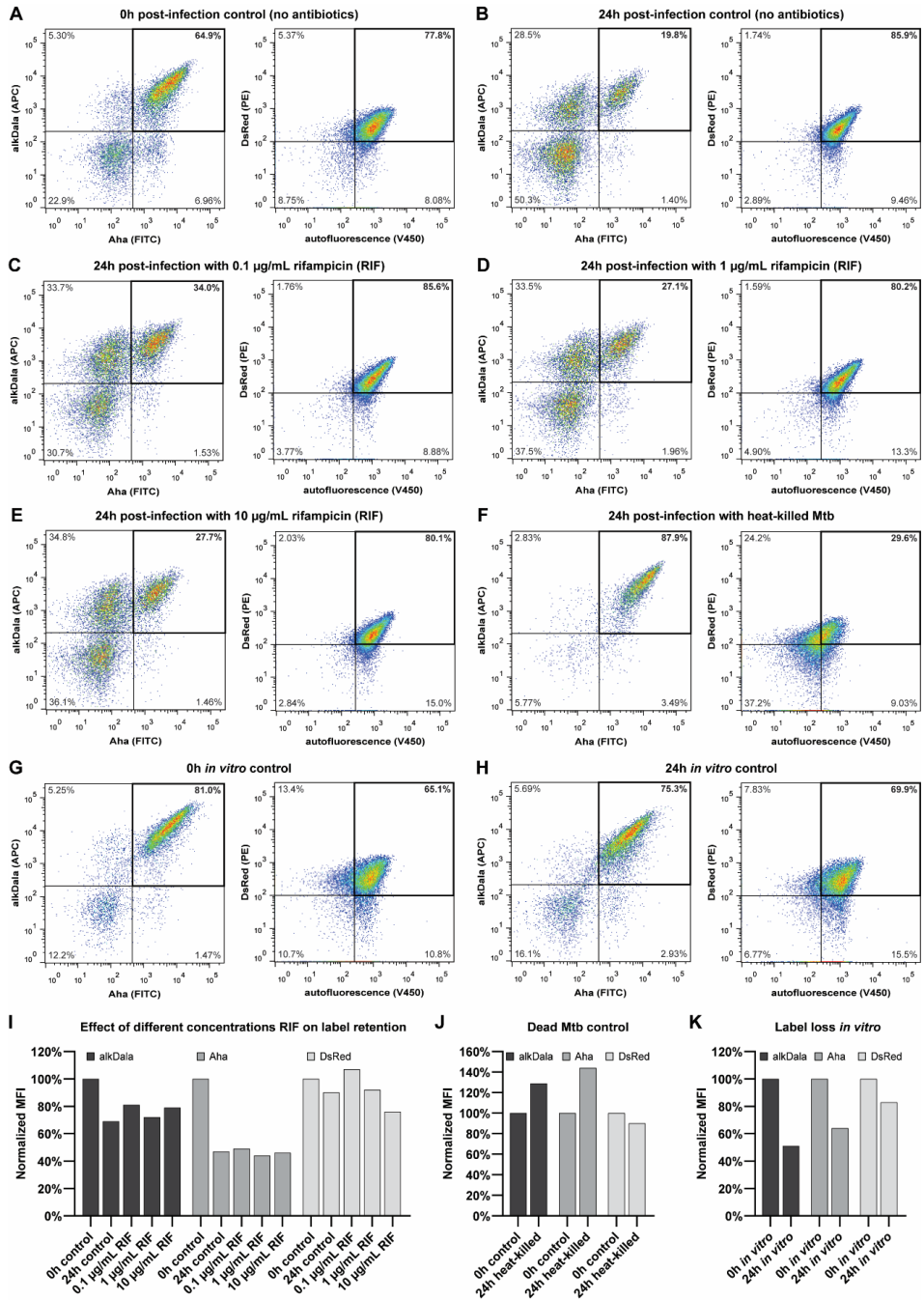


**Figure S17.** Additional controls for bacterial recovery from host cells. RAW 264.7 macrophages were infected with triple label *Mtb* for 1 hour (0h control; **A**) and further incubated for 24 hours without antibiotics (24h control; **B**) or with increasing concentrations of rifampicin (RIF; **C**, **D**, **E**) or heat-killed (30 min at 80°C) *Mtb*

(F). Bacteria were recovered by selective lysis of the host cell, fixed and processed for flow cytometry. Additional in vitro controls were included, in which the *Mtb* were incubated in cell medium for 0h (G) or 24h (H). The average label retention was quantified by selecting the Aha+/alkDala+ quadrant or the autofluorescence+/DsRed+ quadrant. I/J/K: MFI was used for the quantification of all signals and subsequently normalized to the 0h time point.

## 5.6 References

- (1) World Health Organization. *Global Tuberculosis Report 2018*; **2018**.
- (2) Fletcher, H. A.; Voss, G.; Casimiro, D.; Neyrolles, O.; Williams, A.; Kaufmann, S. H. E.; McShane, H.; Hatherill, M. Progress and Challenges in TB Vaccine Development. *F1000Research* **2018**, 7 (Mvi), 1–14.
- (3) Schluger, N. W. Host-Pathogen Interactions in Tuberculosis: The Evolving Story. *J. Infect. Dis.* **2016**, 214 (8), 1137–1138.
- (4) Bald, D.; Villellas, C.; Lu, P.; Koul, A. Targeting Energy Metabolism in Mycobacterium Tuberculosis, a New Paradigm in Antimycobacterial Drug Discovery. *MBio* **2017**, 8 (2), 1–11.
- (5) Jnawali, H. N.; Ryoo, S. First – and Second – Line Drugs and Drug Resistance. In *Tuberculosis - Current Issues in Diagnosis and Management*; Mahboub, B. H., Vats, M. G., Eds.; InTech, **2013**; pp 163–180.
- (6) Deb, C.; Lee, C.-M. M.; Dubey, V. S.; Daniel, J.; Abomoelak, B.; Sirakova, T. D.; Pawar, S.; Rogers, L.; Kolattukudy, P. E. A Novel in Vitro Multiple-Stress Dormancy Model for Mycobacterium Tuberculosis Generates a Lipid-Loaded, Drug-Tolerant, Dormant Pathogen. *PLoS One* **2009**, 4 (6), e6077.
- (7) Dutta, N. K.; Karakousis, P. C. Latent Tuberculosis Infection: Myths, Models, and Molecular Mechanisms. *Microbiol. Mol. Biol. Rev.* **2014**, 78 (3), 343–371.
- (8) Baker, J. J.; Abramovitch, R. B. Genetic and Metabolic Regulation of Mycobacterium Tuberculosis Acid Growth Arrest. *Sci. Rep.* **2018**, 8 (1), 4168.
- (9) Daniel, J.; Maamar, H.; Deb, C.; Sirakova, T. D.; Kolattukudy, P. E. Mycobacterium Tuberculosis Uses Host Triacylglycerol to Accumulate Lipid Droplets and Acquires a Dormancy-like Phenotype in Lipid-Loaded Macrophages. *PLoS Pathog.* **2011**, 7 (6), e1002093.
- (10) Pullan, S. T.; Allnutt, J. C.; Devine, R.; Hatch, K. A.; Jeeves, R. E.; Hendon-Dunn, C. L.; Marsh, P. D.; Bacon, J. The Effect of Growth Rate on Pyrazinamide Activity in Mycobacterium Tuberculosis - Insights for Early Bactericidal Activity? *BMC Infect. Dis.* **2016**, 16 (205), 1–11.
- (11) Evangelopoulos, D.; Fonseca, J. D. da; Waddell, S. J. Understanding Anti-Tuberculosis Drug Efficacy: Rethinking Bacterial Populations and How We Model Them. *Int. J. Infect. Dis.* **2015**, 32, 76–80.
- (12) Sarathy, J. P.; Via, L. E.; Weiner, D.; Blanc, L.; Boshoff, H.; Eugenin, E. A.; Barry, C. E.; Dartois, V. A. Extreme Drug Tolerance of Mycobacterium Tuberculosis in Caseum. *Antimicrob. Agents Chemother.* **2018**, 62 (2), 1–11.
- (13) Hoagland, D. T.; Liu, J.; Lee, R. B.; Lee, R. E. New Agents for the Treatment of Drug-Resistant Mycobacterium Tuberculosis. *Adv. Drug Deliv. Rev.* **2016**, 102, 55–72.
- (14) Sarkar, S.; Ganguly, A. Current Overview of Anti-Tuberculosis Drugs: Metabolism and Toxicities. *Mycobact. Dis.* **2016**, 6 (2), 1–6.
- (15) Philips, J. a.; Ernst, J. D. Tuberculosis Pathogenesis and Immunity. *Annu. Rev. Pathol. Mech. Dis.* **2012**, 7 (1), 353–384.
- (16) North, R. J.; Jung, Y.-J. Immunity to Tuberculosis. *Annu. Rev. Immunol.* **2004**, 22 (1), 599–623.
- (17) Wilburn, K. M.; Fieweger, R. A.; VanderVen, B. C. Cholesterol and Fatty Acids Grease the Wheels of Mycobacterium Tuberculosis Pathogenesis. *Pathog. Dis.* **2018**, 76 (2), 1–14.
- (18) Omotade, T. O.; Roy, C. R. Manipulation of Host Cell Organelles by Intracellular Pathogens. *Microbiol. Spectr.* **2019**, 7 (2), 1–18.
- (19) van der Wel, N.; Hava, D.; Houben, D.; Fluitsma, D.; van Zon, M.; Pierson, J.; Brenner, M.; Peters, P. J. M. Tuberculosis and M. Leprae Translocate from the Phagolysosome to



- the Cytosol in Myeloid Cells. *Cell* **2007**, *129* (7), 1287–1298.
- (20) Zhai, W.; Wu, F.; Zhang, Y.; Fu, Y.; Liu, Z. The Immune Escape Mechanisms of Mycobacterium Tuberculosis. *Int. J. Mol. Sci.* **2019**, *20* (2).
  - (21) Ehrh, S.; Schnappinger, D. Mycobacterial Survival Strategies in the Phagosome: Defense against Host Stresses. *Cell Microbiol.* **2009**, *11* (8), 1170–1178.
  - (22) Schnettger, L.; Rodgers, A.; Repnik, U.; Lai, R. P.; Pei, G.; Verdoes, M.; Wilkinson, R. J.; Young, D. B.; Gutierrez, M. G. A Rab20-Dependent Membrane Trafficking Pathway Controls M. Tuberculosis Replication by Regulating Phagosome Spaciousness and Integrity. *Cell Host Microbe* **2017**, *21* (5), 619–628.e5.
  - (23) Simeone, R.; Bobard, A.; Lippmann, J.; Bitter, W.; Majlessi, L.; Brosch, R.; Enninga, J. Phagosomal Rupture by Mycobacterium Tuberculosis Results in Toxicity and Host Cell Death. *PLoS Pathog.* **2012**, *8* (2).
  - (24) Romagnoli, A.; Etna, M. P.; Giacomini, E.; Pardini, M.; Remoli, M. E.; Corazzari, M.; Falasca, L.; Goletti, D.; Gafa, V.; Simeone, R.; Delogu, G.; Piacentini, M.; Brosch, R.; Fimia, G. M.; Coccia, E. M. ESX-1 Dependent Impairment of Autophagic Flux by Mycobacterium Tuberculosis in Human Dendritic Cells. *Autophagy* **2012**, *8* (9), 1357–1370.
  - (25) Lerner, T. R.; Carvalho-Wodarz, C. D. S.; Repnik, U.; Russell, M. R. G.; Borel, S.; Diedrich, C. R.; Rohde, M.; Wainwright, H.; Collinson, L. M.; Wilkinson, R. J.; Griffiths, G.; Gutierrez, M. G. Lymphatic Endothelial Cells Are a Replicative Niche for Mycobacterium Tuberculosis. *J. Clin. Invest.* **2016**, *126* (3), 1093–1108.
  - (26) Kimmey, J. M.; Stallings, C. L. Bacterial Pathogens versus Autophagy: Implications for Therapeutic Interventions. *Trends Mol. Med.* **2016**, *22* (12), 1060–1076.
  - (27) MacGilvary, N. J.; Tan, S. Fluorescent Mycobacterium Tuberculosis Reporters: Illuminating Host-Pathogen Interactions. *Pathog. Dis.* **2018**, *76* (3), 1–12.
  - (28) Siegrist, M. S.; Whiteside, S.; Jewett, J. C.; Aditham, A.; Cava, F.; Bertozzi, C. R. D-Amino Acid Chemical Reporters Reveal Peptidoglycan Dynamics of an Intracellular Pathogen. *ACS Chem. Biol.* **2013**, *8* (3), 500–505.
  - (29) Botella, H.; Yang, G.; Ouerfelli, O.; Ehrh, S.; Nathan, C. F.; Vaubourgeix, J. Distinct Spatiotemporal Dynamics of Peptidoglycan Synthesis between Mycobacterium Smegmatis and Mycobacterium Tuberculosis. *MBio* **2017**, *8* (5), 12–14.
  - (30) Backus, K. M.; Boshoff, H. I.; Barry, C. E. C. S.; Boutureira, O.; Patel, M. K.; D’Hooge, F.; Lee, S. S.; Via, L. E.; Tahlan, K.; Barry, C. E. C. S.; Davis, B. G. Uptake of Unnatural Trehalose Analogs as a Reporter for Mycobacterium Tuberculosis. *Nat. Chem. Biol.* **2011**, *7* (4), 228–235.
  - (31) Hodges, H. L.; Brown, R. A.; Crooks, J. A.; Weibel, D. B.; Kiessling, L. L. Imaging Mycobacterial Growth and Division with a Fluorogenic Probe. *Proc. Natl. Acad. Sci. U. S. A.* **2018**, *115* (20), 5271–5276.
  - (32) Kamariza, M.; Shieh, P.; Ealand, C. S.; Peters, J. S.; Chu, B.; Rodriguez-Rivera, F. P.; Babu Sait, M. R.; Treuren, W. V.; Martinson, N.; Kalscheuer, R.; Kana, B. D.; Bertozzi, C. R. Rapid Detection of Mycobacterium Tuberculosis in Sputum with a Solvatochromic Trehalose Probe. *Sci. Transl. Med.* **2018**, *10* (430), eaam6310.
  - (33) Yang, D.; Ding, F.; Mitachi, K.; Kurosu, M.; Lee, R. E.; Kong, Y. A Fluorescent Probe for Detecting Mycobacterium Tuberculosis and Identifying Genes Critical for Cell Entry. *Front. Microbiol.* **2016**, *7* (DEC), 1–13.
  - (34) Cheng, Y.; Xie, H.; Sule, P.; Hassounah, H.; Graviss, E. A.; Kong, Y.; Cirillo, J. D.; Rao, J. Fluorogenic Probes with Substitutions at the 2 and 7 Positions of Cephalosporin Are Highly BlaC-Specific for Rapid Mycobacterium Tuberculosis Detection. *Angew. Chemie - Int. Ed.* **2014**, *53* (35), 9360–9364.
  - (35) Stone, M. R. L.; Butler, M. S.; Phetsang, W.; Cooper, M. A.; Blaskovich, M. A. T. Fluorescent Antibiotics: New Research Tools to Fight Antibiotic Resistance. *Trends*

- Biotechnol.* **2018**, *36* (5), 523–536.
- (36) Cheng, Y.; Xie, J.; Lee, K.-H.; Gaur, R. L.; Song, A.; Dai, T.; Ren, H.; Wu, J.; Sun, Z.; Banaei, N.; Akin, D.; Rao, J. Rapid and Specific Labeling of Single Live *Mycobacterium Tuberculosis* with a Dual-Targeting Fluorogenic Probe. *Sci. Transl. Med.* **2018**, *10* (454), eaar4470.
  - (37) Armstrong, J. A.; D'Arcy Hart, P. Response of Cultured Macrophages to Mycobacterium Tuberculosis, with Observations on Fusion of Lysosomes with Phagosomes. *J Exp Med* **1971**, *134* (3), 713–740.
  - (38) Leake, E. S.; Myrvik, Q. N.; Wright, M. J. Phagosomal Membranes of Mycobacterium Bovis BCG-Immune Alveolar Macrophages Are Resistant to Disruption by Mycobacterium Tuberculosis H37Rv. *Infect. Immun.* **1984**, *45* (2), 443–446.
  - (39) McDonough, K. A.; Kress, Y.; Bloom, B. R. The Interaction of Mycobacterium Tuberculosis with Macrophages: A Study of Phagolysosome Fusion. *Infect. Agents Dis.* **1993**, *2* (4), 232–235.
  - (40) de Boer, P.; Hoogenboom, J. P.; Giepmans, B. N. G. Correlated Light and Electron Microscopy: Ultrastructure Lights Up! *Nat. Methods* **2015**, *12* (6), 503–513.
  - (41) Lerner, T. R.; Borel, S.; Greenwood, D. J.; Repnik, U.; Russell, M. R. G.; Herbst, S.; Jones, M. L.; Collinson, L. M.; Griffiths, G.; Gutierrez, M. G. Mycobacterium Tuberculosis Replicates within Necrotic Human Macrophages. *J. Cell Biol.* **2017**, *216* (3), 583–594.
  - (42) Russell, M. R. G.; Lerner, T. R.; Burden, J. J.; Nkwe, D. O.; Pelchen-Matthews, A.; Domart, M. C.; Durgan, J.; Weston, A.; Jones, M. L.; Peddie, C. J.; Carzaniga, R.; Florey, O.; Marsh, M.; Gutierrez, M. G.; Collinson, L. M. 3D Correlative Light and Electron Microscopy of Cultured Cells Using Serial Blockface Scanning Electron Microscopy. *J. Cell Sci.* **2017**, *130* (1), 278–291.
  - (43) Greenwood, D. J.; Dos Santos, M. S.; Huang, S.; Russell, M. R. G.; Collinson, L. M.; MacRae, J. I.; West, A.; Jiang, H.; Gutierrez, M. G. Subcellular Antibiotic Visualization Reveals a Dynamic Drug Reservoir in Infected Macrophages. *Science* **2019**, *364* (6447), 1279–1282.
  - (44) van Elsland, D. M.; Bos, E.; de Boer, W.; Overkleeft, H. S.; Koster, A. J.; van Kasteren, S. I. Detection of Bioorthogonal Groups by Correlative Light and Electron Microscopy Allows Imaging of Degraded Bacteria in Phagocytes. *Chem. Sci.* **2016**, *7* (1), 752–758.
  - (45) van Elsland, D. M.; Pujals, S.; Bakkum, T.; Bos, E.; Oikonomas-Koppas, N.; Berlin, I.; Neefjes, J.; Meijer, A. H.; Koster, A. J.; Albertazzi, L.; van Kasteren, S. I. Ultrastructural Imaging of Salmonella–Host Interactions Using Super-Resolution Correlative Light-Electron Microscopy of Bioorthogonal Pathogens. *ChemBioChem* **2018**, *19* (16), 1766–1770.
  - (46) Van Hest, J. C. M.; Kiick, K. L.; Tirrell, D. A. Efficient Incorporation of Unsaturated Methionine Analogues into Proteins in Vivo. *J. Am. Chem. Soc.* **2000**, *122* (7), 1282–1288.
  - (47) Kiick, K. L.; Saxon, E.; Tirrell, D. A.; Bertozzi, C. R. Incorporation of Azides into Recombinant Proteins for Chemoselective Modification by the Staudinger Ligation. *Proc. Natl. Acad. Sci. U. S. A.* **2002**, *99* (1), 19–24.
  - (48) Dieterich, D. C.; Link, A. J.; Graumann, J.; Tirrell, D. A.; Schuman, E. M. Selective Identification of Newly Synthesized Proteins in Mammalian Cells Using Bioorthogonal Noncanonical Amino Acid Tagging (BONCAT). *Proc. Natl. Acad. Sci.* **2006**, *103* (25), 9482–9487.
  - (49) Hatzenpichler, R.; Scheller, S.; Tavormina, P. L.; Babin, B. M.; Tirrell, D. A.; Orphan, V. J. In Situ Visualization of Newly Synthesized Proteins in Environmental Microbes Using Amino Acid Tagging and Click Chemistry. *Environ. Microbiol.* **2014**, *16* (8), 2568–2590.
  - (50) Korbee, C. J.; Heemskerk, M. T.; Kocev, D.; Van Strijen, E.; Rabiee, O.; Franken, K. L. M. C.; Wilson, L.; Savage, N. D. L.; Džeroski, S.; Haks, M. C.; Ottenhoff, T. H. M. Combined

- Chemical Genetics and Data-Driven Bioinformatics Approach Identifies Receptor Tyrosine Kinase Inhibitors as Host-Directed Antimicrobials. *Nat. Commun.* **2018**, *9* (1).
- (51) Vincent, A. T.; Nyongesa, S.; Morneau, I.; Reed, M. B.; Tocheva, E. I.; Veyrier, F. J. The Mycobacterial Cell Envelope: A Relict from the Past or the Result of Recent Evolution? *Front. Microbiol.* **2018**, *9* (OCT), 1–9.
- (52) Daffé, M.; Quémar, A.; Marrakchi, H. Mycolic Acids: From Chemistry to Biology. In *Biogenesis of Fatty Acids, Lipids and Membranes*; 2017; pp 1–36.
- (53) Gengenbacher, M.; Kaufmann, S. H. E. Mycobacterium Tuberculosis: Success through Dormancy. *FEMS Microbiol. Rev.* **2012**, *36* (3), 514–532.
- (54) Tokuyasu, K. T. A Technique for Ultracryotomy of Cell Suspensions and Tissues. *J. Cell Biol.* **1973**, *57* (2), 551–565.
- (55) Peters, P. J.; Bos, E.; Griekspoor, A. Cryo-Immunogold Electron Microscopy. *Curr. Protoc. Cell Biol.* **2006**, *30* (1), 4.7.1-4.7.19.
- (56) Möbius, W.; Posthuma, G. Sugar and Ice: Immunoelectron Microscopy Using Cryosections According to the Tokuyasu Method. *Tissue Cell* **2018**, No. July, 1–13.
- (57) Gupta, A.; Bhakta, S. An Integrated Surrogate Model for Screening of Drugs against Mycobacterium Tuberculosis. *J. Antimicrob. Chemother.* **2012**, *67* (6), 1380–1391.
- (58) Wang, X.; Grace, P. M.; Pham, M. N.; Cheng, K.; Strand, K. A.; Smith, C.; Li, J.; Watkins, L. R.; Yin, H. Rifampin Inhibits Toll-like Receptor 4 Signaling by Targeting Myeloid Differentiation Protein 2 and Attenuates Neuropathic Pain. *FASEB J.* **2013**, *27* (7), 2713–2722.
- (59) Faas, F. G. A.; Cristina Avramut, M.; van den Berg, B. M.; Mieke Mommaas, A.; Koster, A. J.; Ravelli, R. B. G. Virtual Nanoscopy: Generation of Ultra-Large High Resolution Electron Microscopy Maps. *J. Cell Biol.* **2012**, *198* (3), 457–469.
- (60) Vijay, S.; Hai, H. T.; Thu, D. D. A.; Johnson, E.; Pielach, A.; Phu, N. H.; Thwaites, G. E.; Thuong, N. T. T. Ultrastructural Analysis of Cell Envelope and Accumulation of Lipid Inclusions in Clinical Mycobacterium Tuberculosis Isolates from Sputum, Oxidative Stress, and Iron Deficiency. *Front. Microbiol.* **2018**, *8* (JAN), 1–12.
- (61) Acosta, Y.; Zhang, Q.; Rahaman, A.; Ouellet, H.; Xiao, C.; Sun, J.; Li, C. Imaging Cytosolic Translocation of Mycobacteria with Two-Photon Fluorescence Resonance Energy Transfer Microscopy. *Biomed. Opt. Express* **2014**, *5* (11), 3990.
- (62) Houben, D.; Demangel, C.; van Ingen, J.; Perez, J.; Baldeón, L.; Abdallah, A. M.; Caleechurn, L.; Bottai, D.; van Zon, M.; de Punder, K.; van der Laan, T.; Kant, A.; Bossers-de Vries, R.; Willemsen, P.; Bitter, W.; van Soolingen, D.; Brosch, R.; van der Wel, N.; Peters, P. J. ESX-1-Mediated Translocation to the Cytosol Controls Virulence of Mycobacteria. *Cell. Microbiol.* **2012**, *14* (8), 1287–1298.
- (63) Simeone, R.; Sayes, F.; Song, O.; Gröschel, M. I.; Brodin, P.; Brosch, R.; Majlessi, L. Cytosolic Access of Mycobacterium Tuberculosis: Critical Impact of Phagosomal Acidification Control and Demonstration of Occurrence In Vivo. *PLoS Pathog.* **2015**, *11* (2), 1–24.
- (64) Jamwal, S. V.; Mehrotra, P.; Singh, A.; Siddiqui, Z.; Basu, A.; Rao, K. V. S. Mycobacterial Escape from Macrophage Phagosomes to the Cytoplasm Represents an Alternate Adaptation Mechanism. *Sci. Rep.* **2016**, *6* (February), 1–9.
- (65) Chandra, P.; Ghanwat, S.; Matta, S. K.; Yadav, S. S.; Mehta, M.; Siddiqui, Z.; Singh, A.; Kumar, D. Mycobacterium Tuberculosis Inhibits RAB7 Recruitment to Selectively Modulate Autophagy Flux in Macrophages. *Sci. Rep.* **2015**, *5* (October), 1–10.
- (66) Abdallah, A. M.; Bestebroer, J.; Savage, N. D. L.; de Punder, K.; van Zon, M.; Wilson, L.; Korbee, C. J.; van der Sar, A. M.; Ottenhoff, T. H. M.; van der Wel, N. N.; Bitter, W.; Peters, P. J. Mycobacterial Secretion Systems ESX-1 and ESX-5 Play Distinct Roles in Host Cell Death and Inflammasome Activation. *J. Immunol.* **2011**, *187* (9), 4744–4753.
- (67) Martin, C. J.; Booty, M. G.; Rosebrock, T. R.; Nunes-Alves, C.; Desjardins, D. M.; Keren,

- I.; Fortune, S. M.; Remold, H. G.; Behar, S. M. Efferocytosis Is an Innate Antibacterial Mechanism. *Cell Host Microbe* **2012**, *12* (3), 289–300.
- (68) Liu, Y.; Zhang, Q.; Hu, M.; Yu, K.; Fu, J.; Zhou, F.; Liu, X. Proteomic Analyses of Intracellular *Salmonella* Enterica Serovar Typhimurium Reveal Extensive Bacterial Adaptations to Infected Host Epithelial Cells. *Infect. Immun.* **2015**, *83* (7), 2897–2906.
- (69) Patiño, S.; Alamo, L.; Cimino, M.; Casart, Y.; Bartoli, F.; García, M. J.; Salazar, L. Autofluorescence of *Mycobacteria* as a Tool for Detection of *Mycobacterium Tuberculosis*. *J. Clin. Microbiol.* **2008**, *46* (10), 3296–3302.
- (70) Wong, C.; Ha, N. P.; Pawlowski, M. E.; Graviss, E. A.; Tkaczyk, T. S. Differentiating between Live and Dead *Mycobacterium Smegmatis* Using Autofluorescence. *Tuberculosis* **2016**, *101*, S119–S123.
- (71) Shetty, A.; Dick, T. *Mycobacterial* Cell Wall Synthesis Inhibitors Cause Lethal ATP Burst. *Front. Microbiol.* **2018**, *9* (AUG), 1–9.
- (72) Zhang, M. M.; Tsou, L. K.; Charron, G.; Raghavan, A. S.; Hang, H. C. Tandem Fluorescence Imaging of Dynamic S-Acylation and Protein Turnover. *Proc. Natl. Acad. Sci. U. S. A.* **2010**, *107* (19), 8627–8632.
- (73) Li, N.; Lim, R. K. V.; Edwardraja, S.; Lin, Q. Copper-Free Sonogashira Cross-Coupling for Functionalization of Alkyne-Encoded Proteins in Aqueous Medium and in Bacterial Cells. *J. Am. Chem. Soc.* **2011**, *133* (39), 15316–15319.
- (74) Chenault, H. K.; Dahmer, J.; Whitesides, G. M. Kinetic Resolution of Unnatural and Rarely Occurring Amino Acids: Enantioselective Hydrolysis of N-Acyl Amino Acids Catalyzed by Acylase I. *J. Am. Chem. Soc.* **1989**, *111* (16), 6354–6364.
- (75) Biagini, S. C. G.; Gibson, S. E.; Keen, S. P. Cross-Metathesis of Unsaturated Alpha-Amino Acid Derivatives. *J. Chem. Soc. Perkin Trans. 1* **1998**, *1*, 2485–2500.
- (76) Dong, S.; Merkel, L.; Moroder, L.; Budisa, N. Convenient Syntheses of Homopropargylglycine. *J. Pept. Sci.* **2008**, *14* (10), 1148–1150.
- (77) Schindelin, J.; Arganda-Carreras, I.; Frise, E.; Kaynig, V.; Longair, M.; Pietzsch, T.; Preibisch, S.; Rueden, C.; Saalfeld, S.; Schmid, B.; Tinevez, J. Y.; White, D. J.; Hartenstein, V.; Eliceiri, K.; Tomancak, P.; Cardona, A. Fiji: An Open-Source Platform for Biological-Image Analysis. *Nat. Methods* **2012**, *9* (7), 676–682.
- (78) Wehrli, W. Rifampin: Mechanisms of Action and Resistance. *Rev. Infect. Dis.* **1983**, *5*, S407–S411.
- (79) Timmins, G. S.; Deretic, V. Mechanisms of Action of Isoniazid. *Mol. Microbiol.* **2006**, *62* (5), 1220–1227.
- (80) Goude, R.; Amin, A. G.; Chatterjee, D.; Parish, T. The Arabinosyltransferase EmbC Is Inhibited by Ethambutol in *Mycobacterium Tuberculosis*. *Antimicrob. Agents Chemother.* **2009**, *53* (10), 4138–4146.
- (81) Yamori, S.; Ichiyama, S.; Shimokata, K.; Tsukamura, M. Bacteriostatic and Bactericidal Activity of Antituberculosis Drugs against *Mycobacterium Tuberculosis*, *Mycobacterium Avium-Mycobacterium Intracellulare* Complex and *Mycobacterium Kansasii* in Different Growth Phases. *Microbiol. Immunol.* **1992**, *36* (4), 361–368.
- (82) Bakker-Woudenberg, I. A. J. M.; Van Vianen, W.; Van Soolingen, D.; Verbrugh, H. A.; Van Agtmael, M. A. Antimycobacterial Agents Differ with Respect to Their Bacteriostatic versus Bactericidal Activities in Relation to Time of Exposure, *Mycobacterial* Growth Phase, and Their Use in Combination. *Antimicrob. Agents Chemother.* **2005**, *49* (6), 2387–2398.
- (83) Prokhorova, I.; Altman, R. B.; Djumagulov, M.; Shrestha, J. P.; Urzhumtsev, A.; Ferguson, A.; Chang, C. W. T.; Yusupov, M.; Blanchard, S. C.; Yusupova, G.; Puglisi, J. D. Aminoglycoside Interactions and Impacts on the Eukaryotic Ribosome. *Proc. Natl. Acad. Sci. U. S. A.* **2017**, *114* (51), E10899–E10908.
- (84) McCollister, B. D.; Hoffman, M.; Husain, M.; Vázquez-Torres, A. Nitric Oxide Protects

- Bacteria from Aminoglycosides by Blocking the Energy-Dependent Phases of Drug Uptake. *Antimicrob. Agents Chemother.* **2011**, 55 (5), 2189–2196.
- (85) Batson, S.; De Chiara, C.; Majce, V.; Lloyd, A. J.; Gobec, S.; Rea, D.; Fülöp, V.; Thoroughgood, C. W.; Simmons, K. J.; Dowson, C. G.; Fishwick, C. W. G.; De Carvalho, L. P. S.; Roper, D. I. Inhibition of D-Ala:D-Ala Ligase through a Phosphorylated Form of the Antibiotic D-Cycloserine. *Nat. Commun.* **2017**, 8 (1), 1–7.
- (86) Durrant, A. R.; Heresco-Levy, U. D-Cycloserine. In *Encyclopedia of Psychopharmacology*; Springer Berlin Heidelberg: Berlin, Heidelberg, **2013**; pp 1–5.

# Chapter 6

## Summary and Future Prospects

Part of this chapter was published as part of:

Floris J. van Dalen, Thomas Bakkum, Tyrza van Leeuwen, Mirjam Groenewold, Edgar Deu, Abraham Koster, Sander I. Van Kasteren, Martijn Verdoes. *Frontiers in Chemistry*, **2021**; 8(628433): 1-13.



## **Abstract**

This chapter provides a summary of the work presented, as well as several future prospects that could be pursued, based on the techniques developed in this thesis. In the first example, both highly selective and broad-spectrum Activity Based-Probes (ABPs) are combined with Bioorthogonal Correlative Light-Electron Microscopy (B-CLEM) to study the intracellular localization of active cathepsin populations with regard to bacterial antigens, within the ultrastructure of the cell. In the second example, the localization of cathepsins is studied in combination with pathogenic and non-pathogenic bacteria, and compared to a co-infection system. In the third example, the possibility of multiple orthogonal bioorthogonal reactions is explored, for simultaneous labeling of multiple biomolecules in a single sample. Finally, the remaining challenges and limitations of the current technique are discussed, and potential improvements and alternative approaches are suggested.

## 6.1 Summary

In this thesis, bioorthogonal (click) chemistry is combined with in-gel fluorescence, flow cytometry, fluorescence (confocal) microscopy, super-resolution Stochastic Optical Reconstruction Microscopy (STORM), Correlative Light-Electron Microscopy (CLEM) and STORM-CLEM. Bioorthogonal chemistry as developed and applied in this thesis comprises a two-step labeling approach, in which first a bioorthogonal group or 'click handle' is incorporated into a biological system of interest by exploiting the organism's natural metabolism (also known as metabolic labeling), followed by a biocompatible ligation reaction or 'click reaction' to attach a fluorophore for detection. In this way, the initial label exerts minimal interference on the biochemistry and biology of the targeted organism, while it can be detected by exploiting its intrinsic capability to selectively attach a fluorophore at the desired time. For many purposes, the fluorophore can be attached at the end of a biological time course, following chemical fixation to preserve the (sub)cellular distribution of biological components like proteins, carbohydrates and fatty acids. Combining this convenient labeling strategy with the appropriate analysis technique can provide useful information about the cellular content (flow cytometry), localization (confocal microscopy), subcellular distribution (CLEM) and even single-molecule distribution within the ultrastructure of the cell (STORM-CLEM).

In **chapter 1** a general introduction about bioorthogonal chemistry and its application for fluorescent analyses and imaging is presented. The general principles of bioorthogonal chemistry and metabolic labeling are introduced, and applications of bioorthogonal metabolic labeling to bacteria. Finally, the broad compatibility of bioorthogonal chemistry is illustrated by highlighting its potential application to the various analysis methods described above.

In **chapter 2** recent advancements in the field of metabolic labeling for imaging of intracellular pathogenic bacteria are reviewed. Recent results in metabolic labeling of the bacterial proteome, peptidoglycan and the mycomembrane of corynebacteria are described, and compared to another widely used chemical labeling methodology: Activity-Based Protein Profiling (ABPP). The application of both labeling approaches in imaging techniques is discussed, within the context of intracellular pathogenic bacteria.

**Chapter 3** describes that terminal alkynes and azides – two of the most widely applied bioorthogonal functionalities in metabolic labeling – are resistant to even the harshest of biochemical environments found in phagocytic cells of the immune system (dendritic cells and macrophages), while the widely used strained alkynes



BCN and DBCO quickly degrade under these conditions. In this chapter, flow cytometry was exploited to measure the fluorescence of click handle-modified beads, after attaching a fluorophore to each of the click handles by copper-catalyzed or strain-promoted Huisgen-type cycloaddition reactions (ccHc and spHc, respectively). This allowed the quantification of click handle stability, since degradation of these handles reduced the number of fluorophores per bead, thus resulting in a lower fluorescent signal. Terminal alkynes proved ideal for labeling of biological systems such as bacteria for two reasons: 1) terminal alkynes were found to be resistant to the lysosomal compartments of the phagocytes (<6% degraded) and 2) azide-containing fluorophores showed significantly lower background fluorescence compared to the alkyne-containing fluorophore, in the inverse labeling strategy.

In **chapter 4** bioorthogonal labeling is used to visualize the facultative intracellular pathogen *Salmonella enterica* serovar Typhimurium (*Stm*) within the host phagocyte, through incorporation of bioorthogonal amino acids into the proteome or cell wall of *Stm*. Optimization of label incorporation was achieved using in-gel fluorescence analysis, flow cytometry and STORM. Incorporation of either L-azidohomoalanine (Aha) or L-homopropargylglycine (Hpg) into the proteome was successful with negligible effect on bacterial viability but the alkyne-containing Hpg was preferred due to the lower background level of the azide-containing fluorophore, as discovered in chapter 3. Incorporation of D-propargylglycine (alkDala) into the peptidoglycan of the cell wall of *Stm* was also successful but proved inferior to Hpg in terms of labeling efficiency. The Hpg-labeled *Stm* were subsequently used to study their infection of dendritic cells, using flow cytometry and STORM-CLEM. Within this context, STORM-CLEM allowed for a >10-fold resolution improvement compared to confocal-CLEM, as well as providing single-molecule detection, improved signal-to-noise ratio and crisper images with more details. Some small labeled structures were detected outside of the bacterial structure, which may represent secreted *Stm* proteins, although this remains to be confirmed.

In **chapter 5** the bioorthogonal labeling strategy, described in chapter 4, is translated to a more dangerous and clinically relevant facultative intracellular pathogen, *Mycobacterium tuberculosis* (*Mtb*) which is the causative agent of tuberculosis (TB). All analysis techniques had to be customized for *Mtb* due to its excessively thick and complex mycobacterial cell wall. In-gel fluorescence, flow cytometry, on-section confocal microscopy and CLEM were used to optimize the incorporation of bioorthogonal amino acids into the bacterial proteome and cell

wall of *Mtb*. Successful triple labeling of *Mtb* was achieved by combining DsRed fluorescent protein expression with Aha-labeling of the bacterial proteins and alkDala-labeling of the cell wall.

Using these techniques, new information about the complex intracellular behavior of *Mtb* in macrophages was obtained. Most importantly, the effect of three first-line anti-tuberculosis drugs (rifampicin, isoniazid and ethambutol) on intracellular distribution and shape of the bacteria was quantified using B-CLEM. Moreover, the effect of these drugs on label retention (Aha, alkDala and DsRed) was quantified using flow cytometry. The three drugs combined had the strongest effect on intracellular distribution, relocating almost every bacterium to a large/spacious vacuole. Surprisingly, this triple drug combination did not have the strongest effect on label retention but instead an intermediate effect, suggesting some mutual drug-drug interference may occur.

## 6.2 Future prospects

Whereas the bioorthogonal CLEM (B-CLEM) method presented in this thesis has proven to be of great value to the study of pathogenic intracellular bacteria such as *Mtb*, it should be of equal value in addressing various other biological questions. For example, the degradation and further processing of non-pathogenic bacteria towards antigen presentation could be studied in more detail. Alternatively, the differences between pathogenic and non-pathogenic bacteria could be investigated, as well as the triggers that cause a non-pathogenic strain to become pathogenic. Even for *Mtb*, many questions still remain that could be answered with B-CLEM and related techniques such as bioorthogonal STORM-CLEM, flow cytometry and proteomics. Moreover, the B-CLEM approach could still be improved and expanded in several ways. Whereas B-CLEM has thus far mostly been used in combination with bioorthogonal amino acids – to study the fate of intracellular bacteria – it may also be combined with different bioorthogonal probes, such as metabolic labels for non-protein biomolecules or selective enzyme probes. Additionally, since the B-CLEM approach is based on the Tokuyasu method for cryo-sectioning, it should also be compatible with direct fluorescent probes (e.g. fluorescent enzyme probes or fixable organelle trackers), as well as immunofluorescence and immunogold labeling. This would expand the scope of potential targets and potentially increase the number of targets that can be studied simultaneously in a single sample. Another way to increase the number of targets would be to use multiple click ligation reactions that can be performed in a single sample without cross-reacting, so-called mutually orthogonal bioorthogonal

reactions. A first step towards this goal has already been illustrated in **chapter 5** where two metabolic labels, containing either an azide or an alkyne, could be reacted selectively to different fluorophores, using two sequential cChC reactions.

### 6.2.1 Application of a Highly Selective Cathepsin S Two-Step Activity-Based Probe in B-CLEM

One way in which the B-CLEM approach could be improved would be to use a highly selective Activity-Based Probe (ABP) to specifically target an enzyme of interest. Cathepsin S (Cat S) is a lysosomal cysteine protease highly expressed in immune cells such as dendritic cells, B cells and macrophages.<sup>1,2</sup> Its functions include extracellular matrix breakdown and cleavage of cell adhesion molecules to facilitate immune cell motility, as well as cleavage of the invariant chain during maturation of MHC II.<sup>3-9</sup> Cat S is a major factor in MHC II-mediated antigen presentation and there is compelling (though not yet conclusive) evidence that it also contributes to MCH I-mediated cross-presentation.<sup>6-8</sup> The identification of these diverse specific functions has brought the challenge of delineating Cat S activity with great spatial precision, relative to related enzymes and substrates.

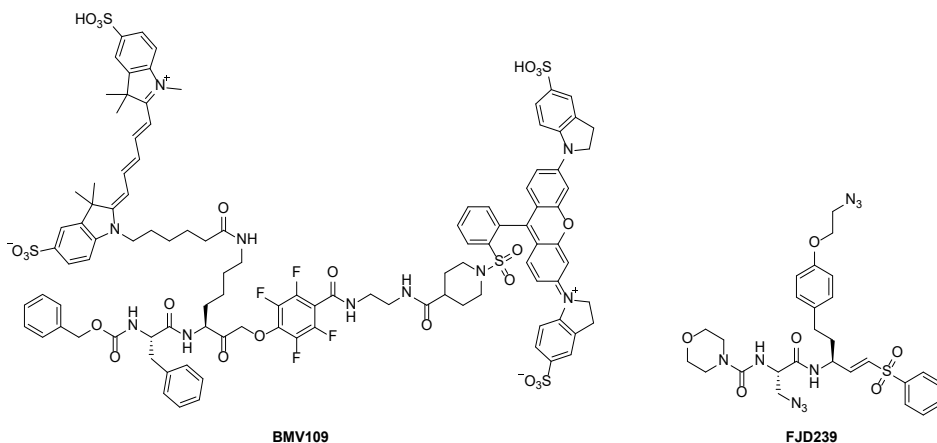


**Figure 1.** Activity-Based Probes selective for cysteine cathepsins (BMV109)<sup>10</sup> or cathepsin S only (FJD239)<sup>11</sup>.

When applying a potent and highly selective azide-containing ABP for Cat S (FJD239; **Figure 1**), confocal microscopy and B-CLEM can provide valuable information on the subcellular localization of Cat S. The broad compatibility of this technique allows for simultaneous identification of related cysteine cathepsins using a broad-spectrum ABP (BMV109), as well as a relevant bioorthogonally-labeled antigen (Hpg-*E. coli*) during degradation (**Figure 2**).

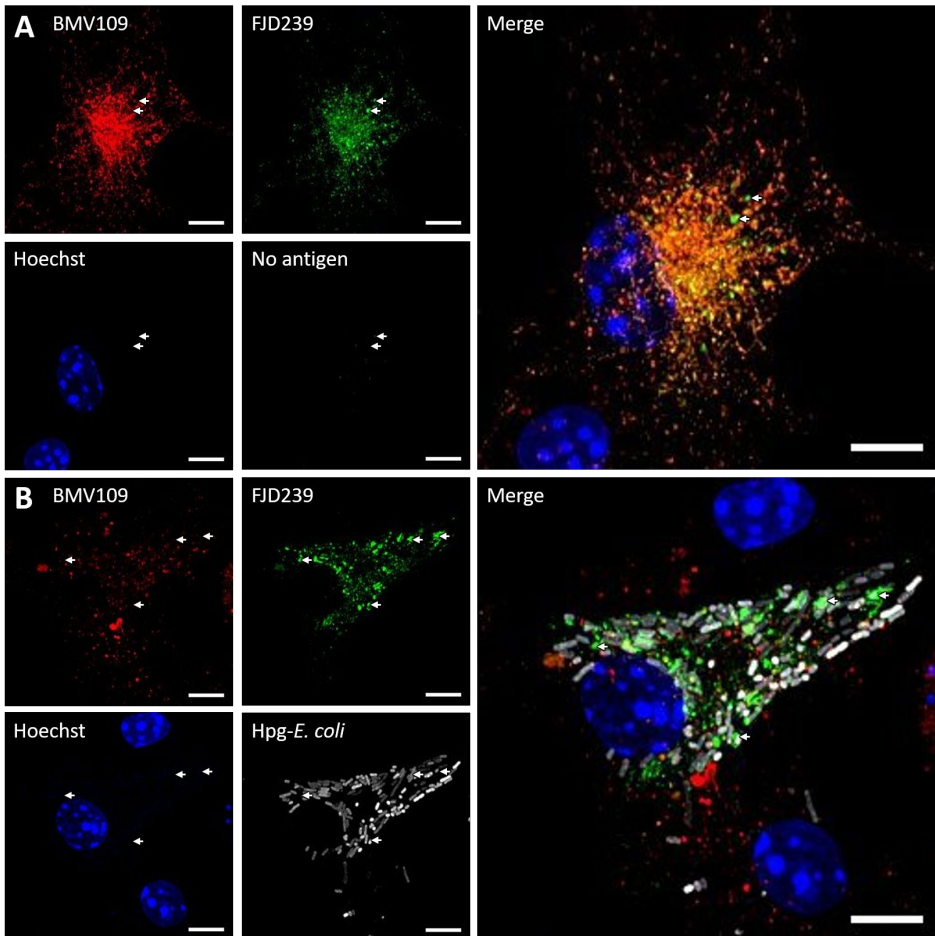


**Figure 2.** Localization of Cat S, studied by confocal microscopy. (A) Naïve BMDCs (at time point 0) were treated with FJD239 (green) for one hour and BMV109 (red) for one hour, and FJD239 was visualized through ccHC. (B) BMDCs were pulsed with Hpg-labeled *E. coli* (white) for 45 minutes, followed by treatment with FJD239 (green) for one hour and BMV109 (red) for one hour. Hpg-*E. coli* and FJD239 were visualized by dual ccHC with AFDye555-azide and AF488-alkyne. DNA was counterstained with Hoechst for reference. Vesicles containing only Cat S are annotated with white arrows. Scale bar represents 5  $\mu\text{m}$ .

Although colocalization of bacterial antigen with cathepsins was prevalent, a high variance in cathepsin activity between cells was observed (**Figure 2**). This may follow from the fact that the GM-CSF-generated BMDCs used here, form a highly heterogeneous population of monocytic cells.<sup>12</sup> It was also noted that occasionally, intact bacteria could still be observed at three hours post-infection. While most vesicles labelled positive for both Cat S activity and the broad-spectrum cathepsin probe, some vesicles can be observed that exclusively contain Cat S activity without detectable activity of the other cathepsins (**Figure 2, arrows**), which is in line with a previous observation by Bender and co-workers.<sup>10</sup> The exact function and nature of these vesicles remain elusive but would be interesting to study further.

Since the B-CLEM method is compatible with immunogold labeling, additional proteins of interest (e.g., MHC II or LAMP1) can be identified, thereby overcoming the limited number of fluorescent channels (normally 4). Ultimately, this allows for the localization of Cat S (green) relative to other cathepsins (red), antigen (magenta) and LAMP1 (15 nm gold; **Figure 3**) or MHC II (15 nm gold; **Figure 4**). The number of labeled molecules of interest in one image can be increased even more by combining various sizes of gold particles (5, 10 & 15 nm).<sup>13</sup> Alternatively, the number of fluorescent channels can be increased by adding an additional near-infrared laser, or using tandem dyes.<sup>14</sup>

The first example clearly illustrates the presence of LAMP1 on bacteria-containing phagosomes (**Figure 3**, arrow 1/2), as well as on vesicles containing both Cat S and other lysosomal cathepsins (**Figure 3**, arrow 3). Although complete colocalization of Hpg-*E. coli* with cathepsins was not observed in this example, large cathepsin-containing vesicles (**Figure 3**, arrow 3/4) are in close proximity of the phagosomes and may be in a process of fusion or exchange of contents.<sup>15,16</sup> One of the bacterial profiles is small and irregular in shape (**Figure 3**, arrow 2), suggesting partial degradation has already occurred (for more information see **chapter 5**). Although no quantification can be performed on this example alone, most of the detected Cat S activity appear in close proximity to this partially-degraded bacterium. Indeed, Cat S was shown to be actively involved with antigen presentation<sup>6</sup>, amongst various other activities.

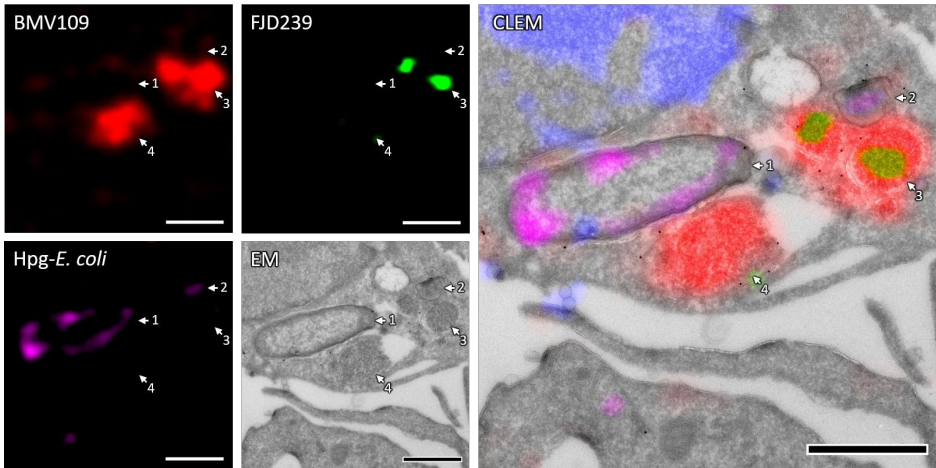


**Figure 3.** The involvement of Cat S in bacterial degradation, studied by B-CLEM. BMDCs were pulsed with Hpg-*E. coli* (magenta) for 45 minutes, followed by treatment with FJD239 (green) for one hour and BMV109 (red) for one hour. Cryo-sectioning was followed by on-section dual ccHc with AFDye555-azide and AF488-alkyne, and LAMP1 was visualized with 15 nm immunogold labelling (black dots). The nuclei were stained with DAPI (blue) and the confocal and TEM images were correlated. Scale bar represents 1  $\mu$ m.

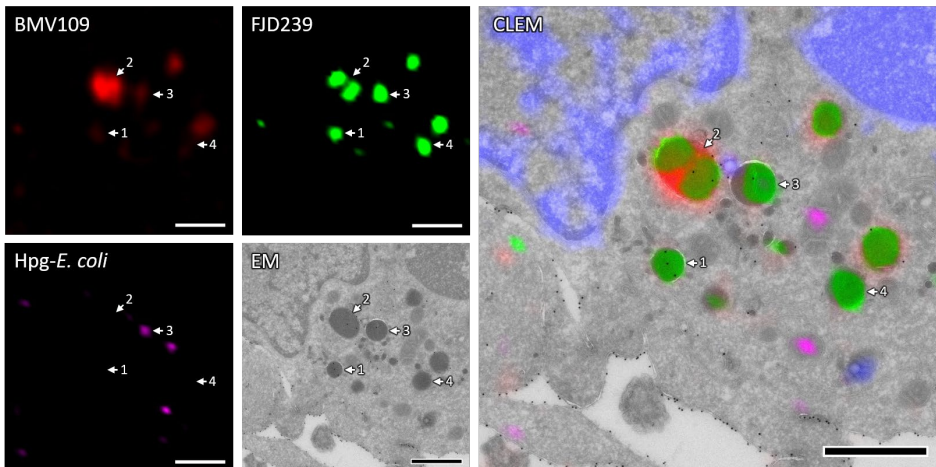


**Figure 4.** The involvement of Cat S in MHC II antigen presentation, studied by B-CLEM. BMDCs were pulsed with Hpg-*E. coli* (magenta) for 45 minutes, followed by treatment with FJD239 (green) for one hour and BMV109 (red) for one hour. Cryo-sectioning was followed by on-section dual ccHc with AFDye555-azide and AF488-alkyne, and MHC II was visualized with 15 nm immunogold labelling (black dots). The nuclei were stained with DAPI (blue) and the confocal and TEM images were correlated. Scale bar represents 1  $\mu$ m.

The second example shows the presence of MHC II both on the plasma membrane and inside several vesicles. These MHC II-positive vesicles appear to contain either (almost) exclusively Cat S (**Figure 4**, arrow 1) or a combination of Cat S and other lysosomal cathepsins (**Figure 4**, arrow 2). A vesicle that apparently contains both Cat S and bacterial digest was observed as well (**Figure 4**, arrow 3), suggesting Cat S may indeed be involved in antigen processing in this example. Another vesicle can be observed, apparently containing exclusively Cat S but no MHC II (**Figure 4**, arrow 4). The presence of MHC II on Cat S-positive vesicles clearly illustrates a role for MHC II in antigen presentation, consistent with literature.<sup>6</sup> It would be interesting to study the localization of Cat S with respect to MHC I, to potentially confirm that Cat S is involved in the production of antigenic peptides for cross-presentation.<sup>7</sup>

Although no definitive biological conclusions can be drawn from this pilot study, it clearly illustrates the potential of four color, dual bio-orthogonal fluorescence imaging in combination with CLEM and immunogold labelling. Together, this exemplifies the great applicability of FJD239 in fluorescence microscopy and state-of-the-art dual B-CLEM.

### 6.2.2 Studying the role of cathepsins in bacterial degradation and immune evasion using CLEM

B-CLEM has previously been used to study degradation of *E. coli* in dendritic cells, which showed colocalization of small Aha-positive foci, representing partially degraded bacteria, with lysosomal associated membrane protein 1 (LAMP1)-positive compartments of the host cell.<sup>17</sup> This implied that the Aha-labeled *E. coli* were degraded inside host cell lysosomes, which is in line with existing knowledge of the bacterial degradation pathway.<sup>18</sup> However, this only confirms the initial uptake and degradation of *E. coli* until the degradation products reach the late phagosomes/phagolysosomes but do not clarify the subsequent processing towards antigen presentation. Several specialized lysosomal hydrolases, including multiple cathepsins, are involved in the processing of large foreign antigens (such as bacteria) into small antigenic peptides that can be presented on Major Histocompatibility Complex (MHC) II via the classical pathway or on MHC I via so-called antigen cross-presentation.<sup>19</sup>

When applying a broad-spectrum ABP for cysteine cathepsins (BMV109; **Figure 1**), confocal microscopy and CLEM can provide valuable information on the subcellular localization of *E. coli*, with respect to enzymatically active cathepsins. Although fluorescent proteins can be inactivated during bacterial degradation, GFP was

found to remain surprisingly fluorescent and can therefore be used as a practical first step in studying the degradation process by CLEM. However, bioorthogonally-labeled *E. coli* will be more suitable to study antigen processing in more detail, since it remains detectable for longer periods of time.<sup>17</sup>

Confocal microscopy of dendritic cells, shortly after phagocytosis of the bacteria did not yet show colocalization of the lysosomal cathepsins with GFP-*E. coli* (**Figure 5**). However, in some cases large cathepsin-containing vesicles were found in close proximity to the bacterium, suggesting that fusion between phagosome and lysosomes may follow (**Figure 5**, arrows).

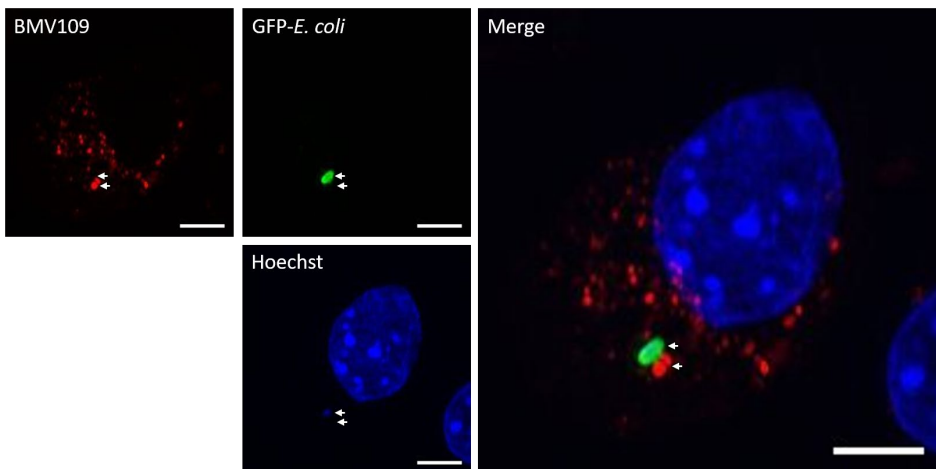


**Figure 5.** Localization of *E. coli* relative to active cathepsins, studied by confocal microscopy. DC2.4 dendritic cells were pulsed with GFP-expressing *E. coli* (green) for 45 minutes, followed by treatment with BMV109 (red) for one hour. DNA was counterstained with Hoechst for reference. Top arrow indicates an *E. coli* bacterium, bottom arrow indicates large cathepsin-containing vesicles. Scale bar represents 5  $\mu$ m.

CLEM confirmed that GFP-expressing *E. coli* (green) do not yet colocalize with active cathepsins (red) shortly after uptake (**Figure 6**) but show considerable colocalization after one hour chase in dendritic cells (**Figure 7**). As observed above, the cathepsin-containing vesicles are in close proximity to the bacteria-containing phagosomes but did not yet fuse for the earliest time point (**Figure 6**, arrows). After one hour chase, a large compartment was observed that contains a clear GFP-positive bacterial structure, surrounded by a large BMV109-positive vacuole (**Figure 7**, arrow). This compartment can be considered a classical phagolysosome due to the co-occurrence of a bacterium and the active lysosomal cathepsins.<sup>15</sup> Indeed,



some of the large bacterial antigen appears to be processed into smaller pieces that lack a recognizable structure after three hours (**Figure 8**, arrow). This smaller GFP-positive antigen seems to be localized in a multi-vesicular compartment, which is in accordance with literature, as it was found that MHC II and its associated antigens are often found in multivesicular bodies.<sup>20,21</sup>

Additional research using B-CLEM, STORM-CLEM (see **chapter 4**) and further quantification (see **chapter 5**) could shine a light on the antigen processing pathway and help to further elucidate the process of antigen (cross-)presentation. Indeed bioorthogonal model antigens have recently been used to study the effect of posttranslational modifications on antigen processing and presentation<sup>22</sup>, whereas bioorthogonal antigens have also been used to obtain chemical control over T cell activation.<sup>23,24</sup> Ideally, the entire pathway from bacterial or viral uptake until antigen (cross-)presentation can be studied using the techniques described in this thesis, in combination with other techniques such as proteomics<sup>25</sup>, to further elucidate this process and open new doors for therapeutic intervention.

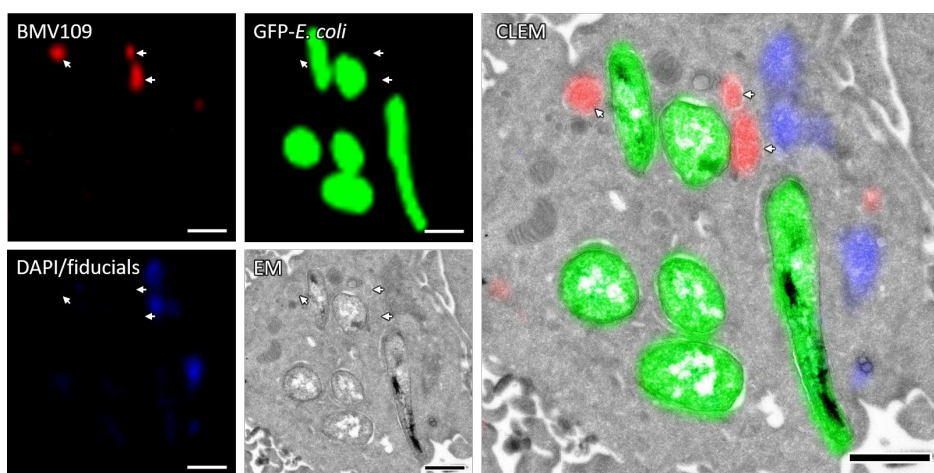


**Figure 6.** The involvement of cathepsins in bacterial degradation directly after uptake, studied by CLEM. D1 cells were pulsed with GFP-expressing *E. coli* (green) for 45 minutes, followed by treatment with BMV109 (red) for one hour. Cryo-sectioning was performed according to the Tokuyasu method. The nuclei were stained with DAPI (blue) and the confocal and TEM images were correlated. Arrows indicate BMV109-positive compartments. Scale bar represents 1  $\mu\text{m}$ .

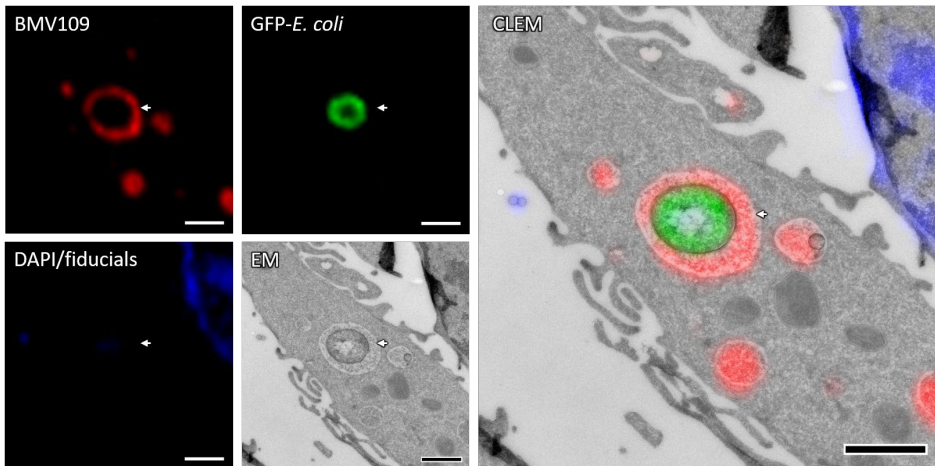


**Figure 7.** The involvement of cathepsins in bacterial degradation one hour post-uptake, studied by CLEM. D1 cells were pulsed with GFP-expressing *E. coli* (green) for 45 minutes and chased for one hour, followed by treatment with BMV109 (red) for one hour. Cryo-sectioning was performed according to the Tokuyasu method. The nuclei were stained with DAPI (blue) and the confocal and TEM images were correlated. Arrow indicates a large GFP-positive and BMV109-positive compartment. Scale bar represents 1  $\mu\text{m}$ .

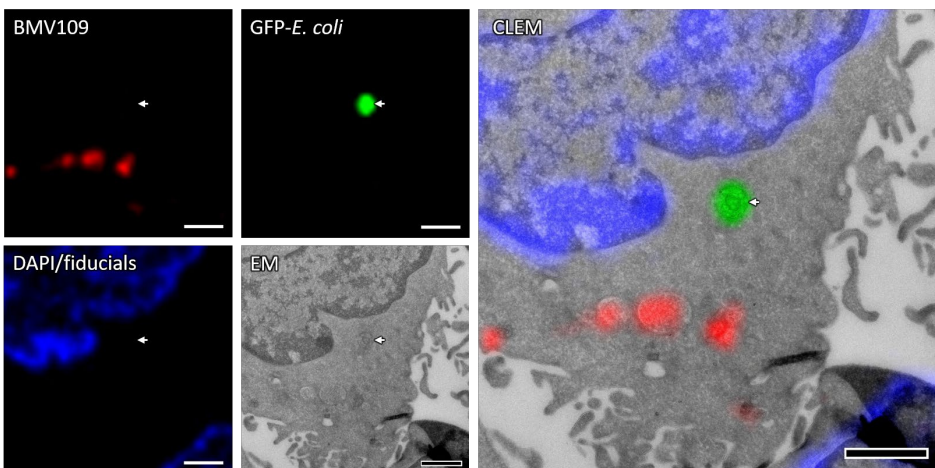


**Figure 8.** The involvement of cathepsins in bacterial degradation three hours post-uptake, studied by CLEM. D1 cells were pulsed with GFP-expressing *E. coli* (green) for 45 minutes and chased for three hours, followed by treatment with BMV109 (red) for one hour. Cryo-sectioning was performed according to the Tokuyasu method. The nuclei were stained with DAPI (blue) and the confocal and TEM images were correlated. Arrow indicates a GFP-positive multivesicular compartment. Scale bar represents 1  $\mu\text{m}$ .

Contrary to the non-pathogenic *E. coli*, intracellular pathogenic bacteria have evolved many ways to evade the host immune response, thereby allowing them to survive and often even proliferate inside host (immune) cells<sup>26</sup>. One of the survival strategies employed by *Stm* is to inhibit fusion of the *Salmonella*-containing vacuole (SCV) with lysosomes through several (secreted) effector proteins<sup>27,28</sup>, effectively avoiding exposure to acidic pH, antimicrobial peptides and hydrolytic enzymes<sup>29,30</sup>. Indeed, when DsRed-expressing *Stm* was studied by CLEM, colocalization of *Stm* with lysosomes (judged by BMV109 fluorescence) was not detected (**Figure 9**), although close encounters were observed (**Figure 10, arrow**).

Interestingly, when allowing both *E. coli* and *Stm* to infect dendritic cells simultaneously, colocalization of *Stm* with cathepsins appears to be more prevalent in cells containing both bacterial species (**Figure 11, top arrow**), suggesting an immunostimulatory effect may be elicited by the presence of *E. coli*. Cells containing only *Stm* are less likely to show colocalization of this bacterium with cathepsins (**Figure 12**). This effect must be quantified and further studied to confirm (or reject) this observation but it is interesting to speculate that immune-modulatory secreted proteins from *Stm*<sup>31</sup> may protect the bystander *E. coli* in this context.

There is a clear difference between the *Stm*-containing vacuole, which spaciouly surrounds the bacterium, and the *E. coli*-containing vacuole that is tightly wrapped around the bacterium (**Figure 11**). This allows for reliable identification of the bacterial species, even when the fluorescent protein loses fluorescence (**Figure 12, top arrow**), either due to degradation or loss of expression. Interestingly, in the small dataset presented here (n≈500 bacteria), *Stm* seems to lose DsRed fluorescence before structural integrity, while *E. coli* appears to lose its structural integrity before GFP fluorescence. Loss of DsRed fluorescence by *Stm* may either represent degradation (**Figure 11, arrow**) or loss of its expression plasmid and subsequent proliferation, resulting in fluorescent protein dilution. Loss of structure (as the result of degradation) by *E. coli* is often accompanied by the presence of small vesicles surrounding or inside the bacterial structure, as well as colocalization with cathepsins, suggesting phagolysosomal degradation is occurring (**Figure 13**).

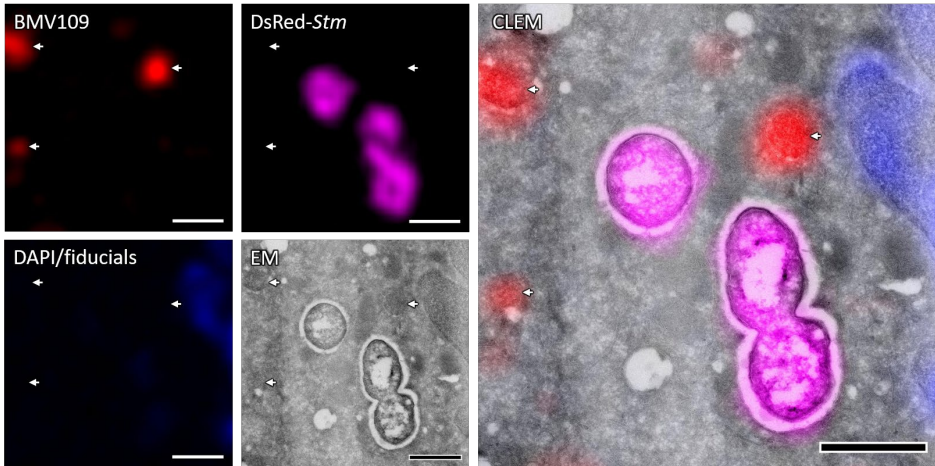


**Figure 9.** The involvement of cathepsins in Stm immune evasion, studied by CLEM (example 1). D1 cells were pulsed with DsRed-expressing Stm (magenta) for 45 minutes and chased for one hour, followed by treatment with BMV109 (red) for one hour. Cryo-sectioning was performed according to the Tokuyasu method. The nuclei were stained with DAPI (blue) and the confocal and TEM images were correlated. Arrows indicate BMV109-positive compartments. Scale bar represents 1  $\mu$ m.

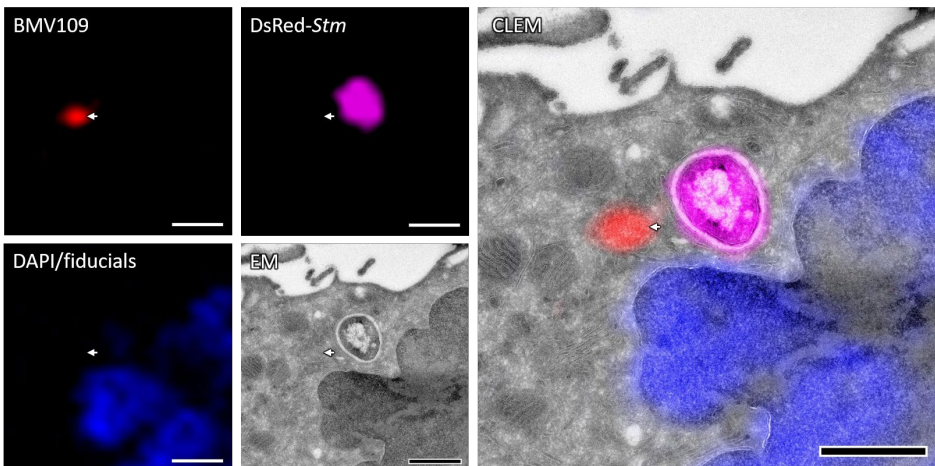


**Figure 10.** The involvement of cathepsins in Stm immune evasion, studied by CLEM (example 2). D1 cells were pulsed with DsRed-expressing Stm (magenta) for 45 minutes and chased for one hour, followed by treatment with BMV109 (red) for one hour. Cryo-sectioning was performed according to the Tokuyasu method. The nuclei were stained with DAPI (blue) and the confocal and TEM images were correlated. Arrow indicates a BMV109-positive compartment. Scale bar represents 1  $\mu$ m.



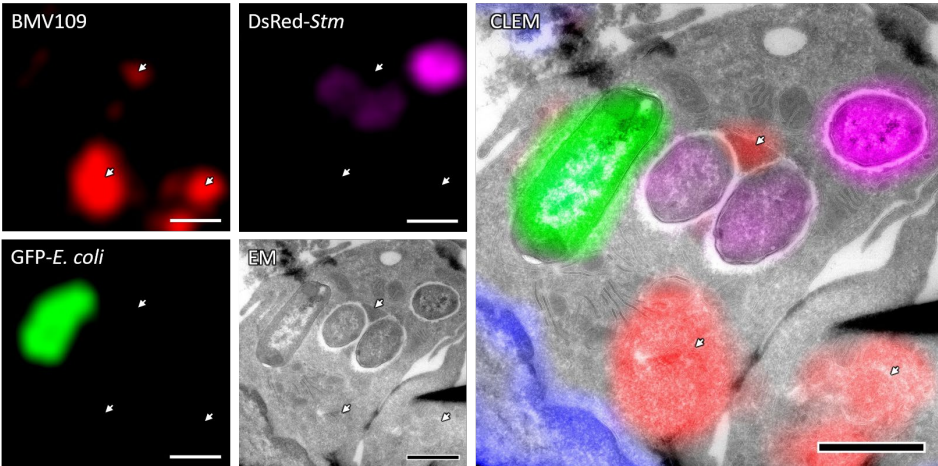


**Figure 11.** The involvement of cathepsins in bacterial degradation in a dual-infection system with *E. coli* and *Stm*, studied by CLEM (example 1). D1 cells were pulsed with GFP-expressing *E. coli* (green) and DsRed-expressing *Stm* (magenta) simultaneously for 45 minutes and chased for one hour, followed by treatment with BMV109 (red) for one hour. Cryo-sectioning was performed according to the Tokuyasu method. The nuclei were stained with DAPI (blue) and the confocal and TEM images were correlated. Arrows indicate BMV109-positive compartments. Scale bar represents 1  $\mu\text{m}$ .

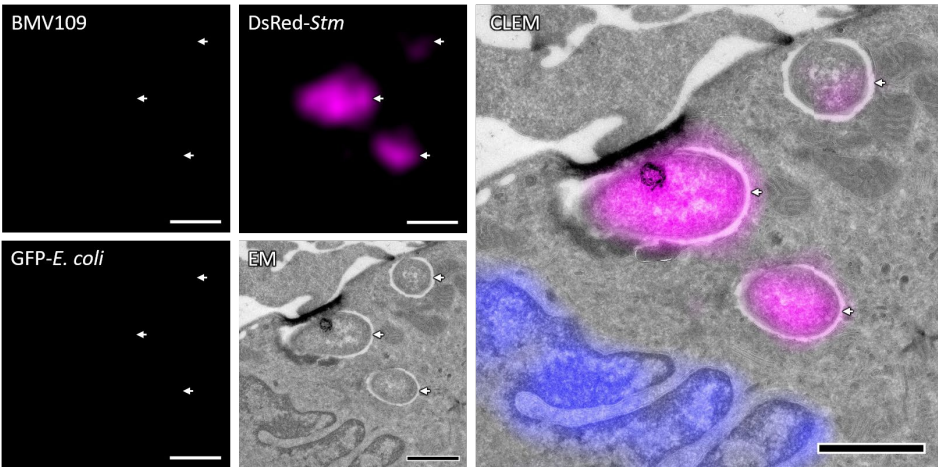


**Figure 12.** The involvement of cathepsins in bacterial degradation in a dual-infection system with *E. coli* and *Stm*, studied by CLEM (example 2). D1 cells were pulsed with GFP-expressing *E. coli* (green) and DsRed-expressing *Stm* (magenta) simultaneously for 45 minutes and chased for one hour, followed by treatment with BMV109 (red) for one hour. Cryo-sectioning was performed according to the Tokuyasu method. The nuclei were stained with DAPI (blue) and the confocal and TEM images were correlated. Arrows indicate *Stm*-containing vacuoles. Scale bar represents 1  $\mu\text{m}$ .

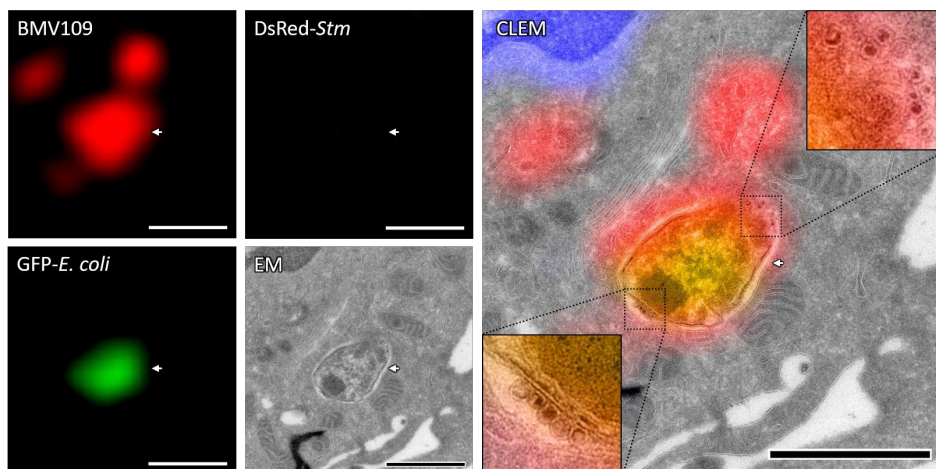


**Figure 13.** The involvement of cathepsins in bacterial degradation in a dual-infection system with *E. coli* and *Stm*, studied by CLEM (example 3). D1 cells were pulsed with GFP-expressing *E. coli* (green) and DsRed-expressing *Stm* (magenta) simultaneously for 45 minutes and chased for one hour, followed by treatment with BMV109 (red) for one hour. Cryo-sectioning was performed according to the Tokuyasu method. The nuclei were stained with DAPI (blue) and the confocal and TEM images were correlated. Arrow indicates a BMV109-positive, *E. coli*-containing compartment. Boxes show zoom-ins of the indicated regions. Scale bar represents 1  $\mu\text{m}$ .

Once again, additional research using B-CLEM, STORM-CLEM and further quantification could help to further elucidate the immune-evading strategies of *Stm*, as well as provide information on the effect of co-infection by multiple pathogenic and non-pathogenic bacteria. Moreover, it would be interesting to use B-CLEM to study pathogenic *E. coli* variants such as the enteropathogenic *E. coli* (EPEC), uropathogenic *E. coli* (UPEC) or meningitis-associated *E. coli* (MNEC), which cause enteric/diarrheal disease, urinary tract infections (UTIs) and sepsis/meningitis, respectively.<sup>32</sup>

### 6.2.3 Triple orthogonal bioorthogonal reactions for further expansion of the B-CLEM method

Using multiple bioorthogonal reactions simultaneously to selectively label more than one biomolecule in a single experiment, has been a topic of great interest to chemical biologists, ever since the discovery of the first bioorthogonal reaction.<sup>33,34</sup> Several mutually orthogonal bioorthogonal reactions have been discovered to date<sup>35</sup> and have been applied to label up to three different targets in a single sample.<sup>36–41</sup> In this thesis, it was found that even the copper-catalyzed azide-alkyne ligation can be performed in conjunction with the inversed alkyne-azide ligation in a single microscopy sample, as long as the bioorthogonal labels are incorporated

into different parts of the cell, and the reactions are performed sequentially with intermediate washing (**chapter 5**). Given the fact that several bioorthogonal reactions are mutually orthogonal (**Figure 14**), this theoretically allows for at least three different bioorthogonal ligations in one microscopy sample.

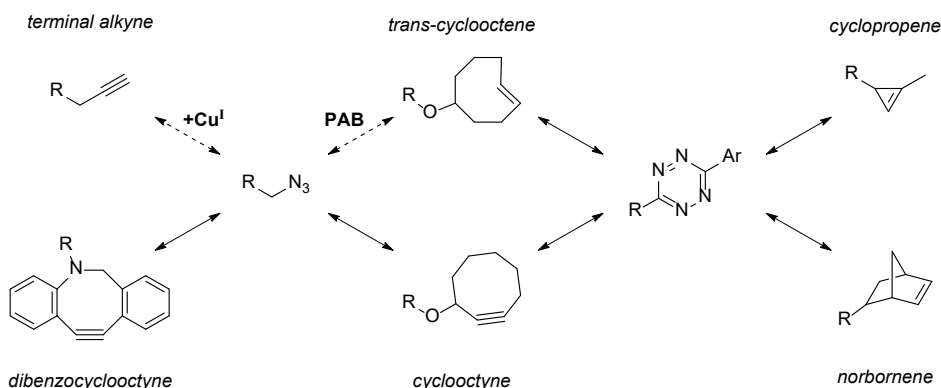


**Figure 14.** Reactivity profile of the most commonly used bioorthogonal groups. Arrows indicate reactivity between indicated groups. Dashed arrow indicates reactivity occurs exclusively under special conditions;  $+Cu^I$  = copper(I)-catalyzed conditions are required for reaction to occur<sup>42</sup>, PAB = para-azidobenzyl is required for this reaction to occur<sup>43</sup>.

A potential triple orthogonal bioorthogonal ligation (triple click) strategy could be a combination of alkyne, azide and cyclopropene metabolic labels, which are mutually unreactive in the absence of copper(I). The corresponding reporter moieties (e.g. fluorophores) can be chosen with some flexibility, depending on the nature of the sample and the analysis method. An alkyne label can only react with an azide-reporter and exclusively under copper-catalyzed conditions. An azide label can be ligated either to an alkyne-reporter under copper-catalyzed conditions or to a cyclooctyne-reporter under copper-free conditions. Since cyclooctynes react with tetrazines as well, the bulky dibenzocyclooctyne (DBCO) is the preferred reaction partner for azides, as it is sterically hindered in its reaction with aryltetrazines.<sup>35</sup> Strained cycloalkenes readily react with tetrazines but the rate of reaction heavily depends on the actual structure of both the cycloalkene and the tetrazine.<sup>44–46</sup> When prioritizing the small size of bioorthogonal label (as for the alkyne and azide groups) the cyclopropene is the obvious choice. The corresponding reporter must then contain a tetrazine but the exact structure (R and Ar groups) remains open for optimization.

When applying this triple click strategy to the metabolic labelling and imaging strategy presented in this thesis, a combination of the alkyne-containing nucleoside 5-ethynyl-2'-deoxyuridine (EdU), the azide-containing sugar 1,3,4,6-tetra-*O*-acetyl-*N*-azidoacetylmannosamine (Ac4ManNAz) and the cyclopropene-containing fatty acid sterculic acid (StA) can be used. To confirm the viability of this approach, cells were incubated with the three metabolic labels simultaneously for two hours, followed by fixation with PFA and permeabilization with Triton-X100 with intermediate washing. A sequential triple click approach was chosen, with intermediate washing steps to minimize potential cross-reactivity or interference. StA was first reacted to 5  $\mu$ M AFDye 488-tetrazine in PBS for one hour, followed by a washing step with PBS to remove excess dye. EdU was next reacted to 5  $\mu$ M AFDye 647-azide under cHc conditions, followed by a washing step with PBS to remove excess dye. Finally, Ac4ManNAz was reacted to 5  $\mu$ M AFDye 555-alkyne under cHc conditions, followed by a washing step with PBS to remove excess dye and a 30 minute wash with 1% BSA in PBS to remove any non-specifically bound dye. Indeed, the three click reactions were found to be mutually orthogonal, succeeding in selectively labelling StA, Ac4ManNAz and EdU (**Figure 15A**) without any detectable background staining (**Figure 15B**).

It would be interesting to combine this triple click approach with CLEM as it creates the possibility to study three metabolic bioorthogonal labels simultaneously, at the subcellular level. This could for example allow the study of three bacterial components (e.g., proteins, peptidoglycan and lipids) simultaneously and observe how these components are processed by the host immune cell after degradation of the bacterium. Alternatively, this approach could be reversed to study the uptake of host components by an intracellular pathogenic bacterium, in order to understand which nutrients are taken up by the pathogen under different conditions, *in situ*.

Theoretically, a fourth orthogonal group could be added for a quadruple click strategy but when considering only the bioorthogonal groups discussed here, selectivity will have to be obtained through the difference in reaction rate and/or sterics.<sup>46</sup> Hypothetically, kinetic selectivity could be obtained between the fast trans-cyclooctene (TCO) and the slow norbornene group or even an unstrained vinyl group, which has been shown to react with tetrazines, albeit slowly.<sup>47</sup> When considering steric factors, selectivity can be obtained between a TCO and a cyclopropene group, when using two different tetrazines containing either small or bulky side groups.<sup>46</sup> Alternatively, a fourth (and potentially even fifth) orthogonal group may potentially be found in the ever expanding collection of novel



bioorthogonal chemistries.<sup>41,48,49</sup> Since pure orthogonality in reactivity is difficult to obtain, special conditions may be required to obtain a fourth fully orthogonal group such as photoinduction.<sup>50</sup> It remains to be experimentally confirmed if these bioorthogonal labeling and ligation strategies can indeed be applied to a single sample, without cross-reactivity.

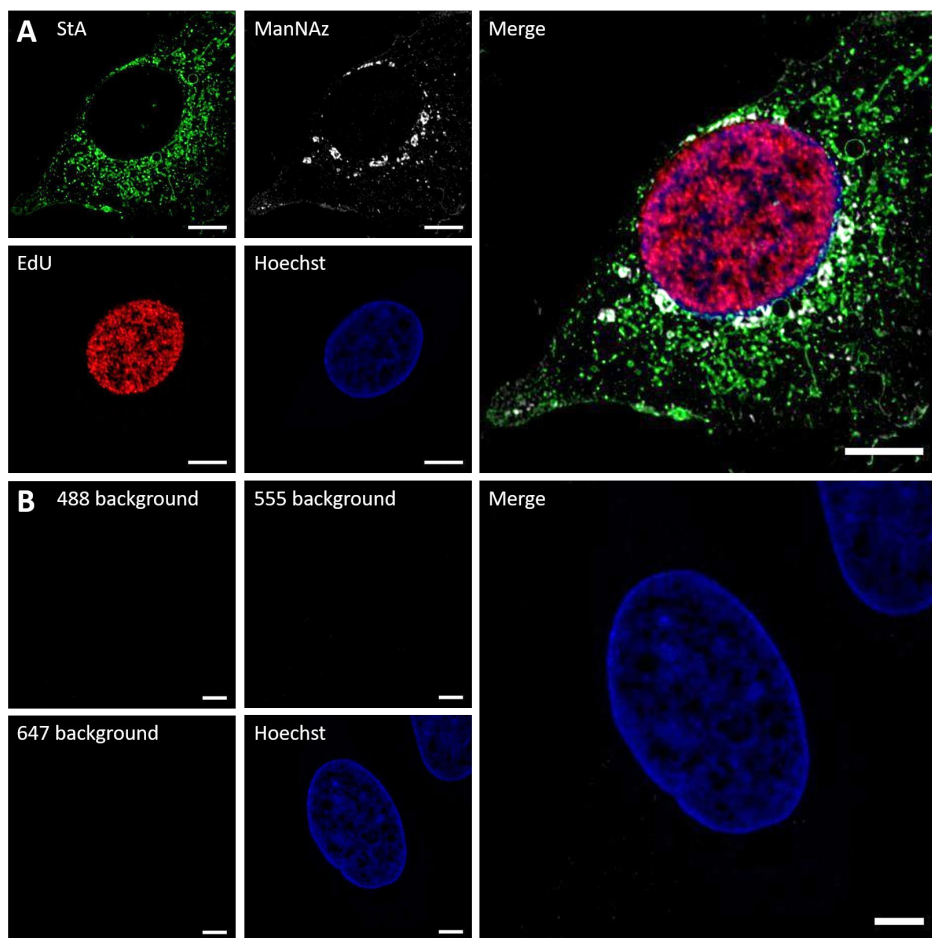


**Figure 15.** Triple orthogonal bioorthogonal labeling (triple click), studied by confocal microscopy. (A) U2OS cells were incubated with StA (green), Ac4ManNAz (gray) and EdU (red) simultaneously for two hours, and visualized through sequential triple click reactions using AFDye 488-tetrazine, AFDye 555-alkyne and AFDye 647-azide, with intermediate washing. (B) U2OS cells were incubated without labels for two hours, and background labeling was analyzed by subjecting the unlabeled cells to the same triple click treatment as above. DNA was counterstained with Hoechst for reference. Scale bar represents 5  $\mu\text{m}$ .

### 6.3 Challenges and limitations of the current B-CLEM approach

Although bioorthogonal labeling has proven to be a useful partner for various fluorescence-based analysis and imaging techniques, including CLEM, it does introduce some intrinsic challenges and limitations. First of all, the introduction of a click handle through metabolic labeling can be challenging, depending on the biomolecule and organism of interest. For example, it has been shown that while bioorthogonal analogues of mannosamine and various other sugars are readily metabolized and incorporated into cell surface glycans, analogues of galactose are not.<sup>51</sup> This hurdle could be overcome by injecting a bioorthogonal analogue of a downstream metabolite (UDP-galactose) but clearly exemplifies how a single approach cannot always be translated directly to similar biomolecules. Similarly, while bioorthogonal analogues of D-alanine are readily incorporated into the peptidoglycan of many bacteria, *Chlamydia trachomatis* does not accept D-alanine analogues.<sup>52</sup> Again, this hurdle could be overcome by using a bioorthogonal analogue of a downstream metabolite (D-alanine-D-alanine dipeptide) but it exemplifies how a potential difference between organisms.

Another challenge is the selective ligation of a fluorophore to the incorporated click handle, which starts with selecting a suitable bioorthogonal reaction. The ccHc reaction is a logical first choice, since the alkyne and azide groups are the smallest available click handles, resulting in minimal interference in the function of the labeled biomolecule. The reaction is also fast, selective (low background) and well-established. However, the copper(I)-dependency of this reaction makes it unsuitable for live cell ligation and causes several problems for copper/redox-sensitive techniques. The copper-free spHc reaction can be used to avoid this issue but at the expense of speed and selectivity. An IEDDA reaction provides a viable alternative but at the expense of click handle size, potentially causing interference in the function of the biomolecule of interest.

Performing the ligation reaction can bring challenges as well. Whereas cell surface labels can easily be reached by a fluorophore in solution, an intracellular click handle requires additional consideration. Cell permeable fluorophores are often poorly water soluble, causing additional background labeling, while water soluble fluorophores are often cell impermeable. It is therefore desirable to chemically fix and permeabilize (or section) the cells in order to allow fluorophores to freely access the intracellular environment. If live cell imaging

is required, a compatible reaction should be chosen, in combination with a cell permeable fluorophore.

Since electron microscopy requires fixation of the biological sample, all available bioorthogonal reactions should theoretically be compatible with CLEM. However, only the Tokuyasu cryo-sectioning method has thus far been proven to be compatible with on-section click reactions.<sup>17</sup> Other techniques usually involve resin embedding, for which the click handles are expected to either be degraded in the polymerization process or become unreachable for the fluorophore.<sup>53</sup> It is important to note that cryo-sectioning provides poorer contrast and preservation of ultrastructure when comparing to resin-based methods.<sup>54</sup> It would therefore be beneficial to identify a method that is compatible with bioorthogonal ligation reactions, while providing better contrast and preservation of ultrastructure. A recent publication showed that, surprisingly, immunogold labeling can still be performed on ultrathin sections of resin-embedded cells.<sup>54</sup> Therefore, if a mild resin-embedding method can be identified that is compatible with click handles, this could potentially open up new possibilities for on-section click reactions as well. Alternatively, if the bioorthogonal ligation reactions are performed on live cells, the cells could then be fixed and resin-embedded, potentially providing better contrast and preservation of ultrastructure (assuming the fluorescence is preserved).<sup>55</sup>

STORM-CLEM provides roughly 10-fold better spatial resolution in the fluorescent signal and much higher sensitivity compared to confocal-CLEM.<sup>56</sup> However, this technique introduces several additional challenges and limitations. Whereas the entire process of sample preparation, cryo-sectioning, imaging and correlation of images for CLEM is already highly laborious, the addition of STORM makes the process even more laborious and time consuming. Additionally, due to the single-molecule sensitivity of STORM, the observable background labeling of non-specifically bound fluorophores is increased significantly.<sup>57</sup> Reduction of this background is highly desirable but difficult to achieve. Finally, the high laser power required for STORM has a negative effect on the preservation of ultrastructure.<sup>57</sup> It would therefore be desirable to use an alternative super-resolution fluorescence microscopy technique that requires lower laser power, such as DNA-based point accumulation for imaging in nanoscale topography (DNA-PAINT) in combination with on-section click reactions.<sup>58</sup>

## 6.4 Conclusion and future outlook

In summary, the current B-CLEM method can be applied to many different research questions and still has a lot of room for improvements. Its broad compatibility with many labeling strategies, as well as the potential for direct translation to bioorthogonal STORM-CLEM, flow cytometry and other techniques, is a great virtue. Nevertheless, alternative strategies combining click chemistry with CLEM can be conceived, in order to overcome intrinsic limitations of the current technique.

First, 3D information could also be obtained with CLEM. To achieve this, a large series of sections must be obtained, individually correlated, and manually stacked in a retrospective manner, known as array tomography. Although not impossible, this is very difficult to achieve with Tokuyasu cryo-sections. A different approach would be to perform the click reaction(s) on live cells, followed by resin embedding and room-temperature sectioning to obtain strong, consistent sections that are more suited for array tomography.<sup>55</sup>

Second, the need for chemical fixation can be overcome by using cryo-EM. To achieve this, the click reaction(s) must be performed on live cells, after which the sample is plunge-frozen. Super-resolution cryo-CLEM can then be performed to obtain high-resolution fluorescence information within the native ultrastructure.<sup>59,60</sup>

Finally, the need for electron microscopy may be circumvented by using of expansion microscopy.<sup>61</sup> Although technically not CLEM, this technique uses physical swelling of the sample to enlarge the cells enough to obtain EM-resolution using only light microscopy.<sup>62</sup>

It is important to note that all three examples have limitations of their own, such as the need to perform the click reactions on live cells, rendering the ccHc reaction nearly impossible. Therefore, when the small size of the incorporated click handles is a priority, the current B-CLEM method is still preferred.

## 6.5 Experimental

### Safety statement

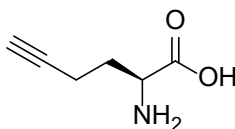
All biological experiments with *S. enterica* serovar Typhimurium described in this study were performed under strict Bio Safety Level 2 conditions. Following fixation and disinfection of the tubes, further sample preparation for CLEM was performed under normal laboratory conditions. No unexpected or unusually high safety hazards were encountered.

### Reagents

Lysogeny broth (LB) medium, methionine (Met), Dulbecco's modified Eagle medium (DMEM), Iscove's Modified Dulbecco's Medium (IMDM), GlutaMAX, pyruvate, 4-(2-hydroxyethyl)-1-piperazineethanesulfonic acid (HEPES), glycine, gelatin type A bloom 300 (gelatin), paraformaldehyde (PFA), bovine serum albumin (BSA), Copper(II) sulfate pentahydrate, (+)-sodium L-ascorbate, tris(3-hydroxypropyltriazolylmethyl)amine (THPTA), aminoguanidine hydrochloride, and IGEPAL CA-630 were purchased from Sigma-Aldrich, Zwijndrecht, The Netherlands. Non-essential amino acids (NEAA), 2-mercaptoethanol, L-glutamine, Hoechst 33342, 4',6-Diamidino-2-Phenylindole (DAPI) and Alexa Fluor 488 (AF488)-alkyne were purchased from Thermo Fisher Scientific, Bleiswijk, The Netherlands. AFDye488-tetrazine, AFDye555-alkyne and AFDye647-azide were purchased from Click Chemistry Tools, Scottsdale, USA. SelenoMet minimal medium was purchased from Molecular Dimensions, Sheffield, UK. D-propargylglycine (alkDala) was purchased from Combi-Blocks, San Diego, USA. EM-grade 8% paraformaldehyde, EM-grade 8% glutaraldehyde and BSA-c were purchased from Aurion, Wageningen, The Netherlands. Fetal calf serum (FCS) was purchased from VWR International, Amsterdam, The Netherlands. Penicillin G sodium and streptomycin sulphate were purchased from Duchefa, Haarlem, The Netherlands. Granulocyte-Macrophage Colony-Stimulating Factor (GM-CSF) was purchased from ImmunoTools, Friesoythe, Germany. BMV109 and FJD239 were kindly provided by Floris van Dalen and Dr. Martijn Verdoes.

### Organic synthesis

Synthesis of (S)-2-Aminohept-5-ynoic acid (L-homopropargylglycine; Hpg)



Hpg was synthesized according to previously described procedure by Li et al.<sup>63</sup>, adjusted to obtain the enantiomerically pure L-Hpg variant based on Chenault et al.<sup>64</sup>, Biagini et al.<sup>65</sup> and Dong et al.<sup>66</sup>

### **Chiral deprotection of *N*-acetyl-DL-homopropargylglycine (2-acetamidohex-5-ynoic acid)**

A solution of 303 mg (1.13 mmol, 1 eq.) *N*-acetyl-DL-homopropargylglycine in 20 mL H<sub>2</sub>O and adjusted to pH 7.5 using 1M NH<sub>4</sub>OH. 1 mg kidney acylase I ( $\geq 2000$  units/mg) was added and the mixture was stirred for 16 h at 37°C. The enzyme was recovered by centrifugation dialysis, using a 10kDa membrane at 4000 rpm for 35 min at 10°C. Next, the solution was acidified to pH 3 with 2M HCl and extracted with 3 x 20 mL diethyl ether. The organic layers were concentrated to retrieve the *N*-acetyl-D-homopropargylglycine. The aqueous layer was loaded on a pre-washed and regenerated Dowex 50WX8 cation exchange resin (60 mL). The column was washed with 5 x bed volume of water, maintaining a pH of 5.5 at the exit and eluted with 200 mL 1.5M NH<sub>4</sub>OH. Product was detected by TLC and the eluate was concentrated and lyophilized to yield chirally pure L-Hpg (68 mg, 0.535 mmol, 95%) as a white powder.

<sup>1</sup>H NMR (400MHz, D<sub>2</sub>O):  $\delta$  [ppm] = 4.11 (t, J = 6.4 Hz, 1H), 2.42 – 2.36 (m, 2H), 2.36 (s, 1H), 2.19 – 2.10 (m, 1H), 2.07 – 1.98 (m, 1H); <sup>13</sup>C NMR (101MHz, D<sub>2</sub>O):  $\delta$  82.28, 71.16, 52.05, 28.44, 14.16; HRMS (ESI): C<sub>6</sub>H<sub>9</sub>NO<sub>2</sub> [M+H]<sup>+</sup> 128.06, found 128.07;  $[\alpha]_{20}^D$ : +32.4 (c = 1, 1 M HCl); Ref <sup>66</sup>: +28 (c = 1, 1 M HCl).

### **Bacterial culture and metabolic labeling**

*E. coli* B834, *E. coli* B834 expressing GFP<sup>17</sup> and *Stm* SL1344 expressing DsRed<sup>67</sup> were grown overnight at 37°C in LB medium. The following day cultures were diluted 1:33 and grown at 37°C to an OD<sub>600</sub> between 0.3-0.5. In case of metabolic labeling, the bacteria were collected and resuspended in SelenoMet medium, supplemented with 4 mM Hpg and incubated for 30 min at 37°C to allow for label incorporation. The bacteria were washed (1x PBS), resuspended in PBS and their concentration was measured by OD<sub>600</sub>. Throughout culturing, the medium was supplemented with 100 µg/ml ampicillin.

### **Mammalian cell culture**

U2OS cells were cultured in DMEM, supplemented with 10% heat-inactivated FCS, 2 mM GlutaMAX, penicillin 100 I.U./mL and streptomycin 50 µg/mL.

DC2.4 and D1 cells were cultured in IMDM, supplemented with 10% heat-inactivated FCS, 2 mM GlutaMAX, 10 mM HEPES pH 7.3, 1 mM pyruvate, penicillin 100 I.U./mL and streptomycin 50 µg/mL, 50 µM 2-Mercaptoethanol and 1X non-essential amino acids. D1 cells were additionally supplemented with fibroblast supernatant from NIH/3T3 cells, collected from confluent cultures and filtered.

Mouse bone marrow-derived dendritic cells (BMDCs) were generated from B57BL/6 mice bone marrow essentially as described<sup>68</sup> with some modifications. Briefly, bone marrow was flushed from femurs and tibia and cells were cultured in IMDM supplemented with 8% heat-inactivated FCS, 2 mM L-glutamine, 20 µM 2-Mercaptoethanol, penicillin 100 I.U./mL and streptomycin 50 µg/mL in the presence of 20 ng/mL GM-CSF. Medium was replaced on day 3 and 7 of culture and the cells were used between days 10 and 13.

### **Infection with Hpg-labeled *E. coli* and incubation with Activity-Based Probes**

For confocal microscopy,  $2 \times 10^5$  BMDCs were seeded on an 8-chamber slide (Ibidi) and left to attach for 3 hours. For CLEM,  $10 \times 10^6$  BMDCs were seeded on a 10 cm dish and left to attach for 3 hours. Infection of dendritic cells was achieved by adding Hpg-labeled *E. coli* at an MOI of 50 and incubating for 45 min at 37°C, 5% CO<sub>2</sub>. Unbound/non-internalized bacteria were washed off (2x PBS) and medium was replaced for immediate analysis ( $t = 0$ ) or further incubation for 1 or 3 hours. The cells were then incubated for 1 hour with 100 nM FJD239 and washed (2x PBS). Next, the cells were additionally incubated for 1 hour with 1 µM BMV109 and washed (2x PBS).

### **Infection with *E. coli* and/or *Stm* and incubation with Activity-Based Probes**

For confocal microscopy,  $5 \times 10^4$  DC2.4 cells were seeded on an 8-chamber slide (Ibidi) and left to grow overnight. For CLEM,  $10 \times 10^6$  D1 cells were seeded on a 10 cm dish and left to attach for 3 hours. Infection of dendritic cells was achieved by adding GFP-expressing *E. coli* and/or DsRed-expressing *Stm* at an MOI of 50 and incubating for 45 min at 37°C, 5% CO<sub>2</sub>. Unbound/non-internalized bacteria were washed off (2x PBS) and medium was replaced for immediate analysis ( $t = 0$ ) or further incubation for 1 or 3 hours. The cells were then additionally incubated for 1 hour with 1 µM BMV109 and washed (2x PBS).

### **Triple bioorthogonal metabolic labeling**

For confocal microscopy,  $2 \times 10^5$  U2OS cells were seeded on an 8-chamber slide (Ibidi) and left to attach for 3 hours. A metabolic label cocktail was prepared, containing 100 µM sterculic acid (StA), 100 µM 1,3,4,6-tetra-*O*-acetyl-*N*-

azidoacetylmannosamine (Ac4ManNAz) and 10  $\mu\text{M}$  5-Ethynyl-2'-deoxyuridine (EdU) in cell medium. The cells were incubated with metabolic label cocktail for 2 hours at 37°C, 5%  $\text{CO}_2$ , additionally incubated with fresh cell medium for 15 min to allow for diffusion of non-incorporated metabolic labels and washed (2x PBS).

### **Preparation for whole cell confocal microscopy**

Following the biological experiment, the cells were fixed for 2 hours in 4% PFA at RT, then kept in 0.5% PFA at 4°C until further processing. Fixed cells were then washed with PBS and 20 mM glycine in PBS to quench potential aldehyde residues. Cells containing click handles were then permeabilized for 20 min with 0.1% Triton-X100 and washed (1x PBS).

Samples without click handles were immediately counterstained with 2  $\mu\text{g}/\text{mL}$  Hoechst 33342 in PBS for 5 min and washed once more with PBS, without additional staining.

Samples containing an azide (FJD239) and an alkyne (Hpg-*E. coli*) functionality were first reacted with 5  $\mu\text{M}$  AFDye555-azide in ccHc cocktail (0.1 M HEPES, pH 7.3, 1 mM  $\text{CuSO}_4$ , 10 mM sodium ascorbate, 1 mM THPTA ligand, 10 mM aminoguanidine) for 1 hour, washed (2x PBS) and subsequently reacted with 5  $\mu\text{M}$  AF488-alkyne in ccHc cocktail.

Samples containing a cyclopropene (StA), an azide (Ac4ManNAz) and an alkyne (EdU) functionality were first reacted with 5  $\mu\text{M}$  AFDye488-tetrazine in PBS, washed (2x PBS), then reacted with 5  $\mu\text{M}$  AFDye647-azide in ccHc cocktail, washed (2x PBS) and finally reacted with 5  $\mu\text{M}$  AFDye555-alkyne in ccHc cocktail.

After the click reactions, the cells were washed (1x PBS) and incubated for 30 min with 1% BSA in PBS to facilitate removal of non-specifically bound fluorophores, and washed (1x PBS). Nuclei were counterstained with 2  $\mu\text{g}/\text{mL}$  Hoechst 33342 for 5 min and washed once more with PBS. All samples were imaged in glycerol/DABCO solution to minimize photobleaching.

### **Preparation of dendritic cells for CLEM**

Following the biological experiment, the cells were fixed for 24 hours in 2% EM-grade PFA in 0.1M phosphate buffer pH 7.2 at RT, then kept in 0.5% EM-grade PFA at 4°C until further processing. Fixed cells were rinsed with PBS, harvested in warm 1% gelatin in PBS with cell scrapers and transferred to a 15 mL Falcon tube. The cells were collected by centrifugation, resuspended in warm 1% gelatin in PBS, transferred to a 1.5 mL Eppendorf tube, resuspended in warm 12% gelatin in PBS



and pelleted by centrifugation (3 min at 800 rcf). After jellification on ice, the sample pellet was cut off from the tube and cut in half with a razor knife. Sample cubes of approx. 1 mm<sup>2</sup> were prepared and rotated in a 2.3 M sucrose solution for 18 hours to allow for sucrose infiltration, as a cryo-protectant, followed by plunge-freezing the cubes on metal support pins.

### **Cryo-sectioning and on-section ccHc reaction**

Ultrathin (75 nm) cryo-sections were prepared according to the Tokuyasu technique<sup>69,70</sup>, using a cryo-ultramicrotome (Leica) and diamond knife (Diatome). Sections were thawed on a droplet of pickup fluid (1.15 M sucrose, 1% methylcellulose) and transferred to a Formvar/carbon-coated TEM grid (titanium, 100 square mesh, 3.05 mm, center-marked; Agar Scientific), pre-coated with blue 0.2 µm FluoSpheres (Thermo Fisher) as fiducial markers. Thawed cryo-sections attached to the TEM grid were incubated on 2% gelatin in PBS for 30 min at 37°C, followed by washing on 20 mM glycine in PBS (5x 2 min).

Samples without click handles were immediately counterstained with 0.2 µg/mL DAPI in PBS for 5 min and washed once more with PBS without additional staining.

Samples containing an azide (FJD239) and an alkyne (Hpg-*E. coli*) functionality were first reacted with 5 µM AFDye555-azide in ccHc cocktail (0.1 M HEPES, pH 7.3, 1 mM CuSO<sub>4</sub>, 10 mM sodium ascorbate, 1 mM THPTA ligand, 10 mM aminoguanidine) for 1 hour, washed (2x PBS) and subsequently reacted with 5 µM AF488-alkyne in ccHc cocktail. These samples were then incubated on 1% BSA in PBS (3x 10 min), to assist the removal of non-specifically bound fluorophores and additionally blocked on 0.1% BSA-c in PBS (2x 2 min). Immunogold staining was achieved by 1 hour incubation on anti-LAMP1 (1D4B, 1:300, eBioscience) or anti-MHC II (M5/114, 1:300, BioXCell), followed by washing (2x 0.1% BSA-c in PBS), 20 min incubation on rabbit-anti-rat (1:50, Abcam), washing (2x 0.1% BSA-c in PBS), 20 min incubation on protein-A conjugated to 15 nm gold (1:50; Aurion). These samples were then washed (2x 0.1% BSA-c in PBS and 3x PBS), followed by immobilization of the antibody complexes by incubating 5 min on 1% glutaraldehyde in PBS. The samples were then washed (3x PBS), counterstained with 0.2 µg/mL DAPI in PBS for 5 min and washed once more (3x milliQ H<sub>2</sub>O).

The fluorescently-labeled sections attached to TEM grids were mounted in water containing 30% glycerol between a microscopy slide and a coverslip, and sealed with silver Scotch tape.

### **Confocal microscopy**

All samples were imaged on an Andor Dragonfly 505 Spinning Disk Confocal (Oxford Instruments), containing an 8-line integrated laser engine, on a Leica DMI8 inverted microscope equipped with a 63X/1.40-0.60 HCX PL APO oil objective or 100X/1.47 HC PL APO TIRF-corrected oil objective. Hoechst, DAPI and FluoSpheres were excited with the 405 line and collected with the 450/50 BP emission filter, AF488 was excited with the 488 line and collected with the 525/50 BP emission filter, DsRed was excited with the 561 line and collected with the 620/60 BP emission filter and AF647 was excited with the 637 line and collected with the 700/75 BP emission filter. Images were acquired with the Zyla 2048x2048 sCMOS camera and 2x2 camera binning controlled with the integrated Fusion software. Z-series optical sections were collected with a system-optimized step-size of 0.13 microns and deconvolved using the integrated ClearView-GPU<sup>TM</sup> deconvolution software. Gamma, brightness and contrast were carefully adjusted (identically for compared image sets) using FIJI.<sup>71</sup> In case of CLEM, maximum intensity projections were made, in order to compensate for non-flat sections.

### **TEM imaging and correlation**

After acquiring the confocal fluorescence microscopy (FM) images, the TEM grids containing the sections were recovered from the microscopy slides, rinsed in milliQ water and incubated for 5 min on droplets of uranyl acetate/methylcellulose. The negatively-stained sections were then imaged on a FEI Tecnai 12 BioTwin TEM System (FEI Technologies) at 120 kV acceleration voltage. Correlation of FM to TEM images was performed in Adobe Photoshop CC 2020 (Adobe Systems). The separate fluorescence channels were imported as layers, set to overlay mode 'Lighten', then grouped and set to overlay mode 'Color', placed on top of the TEM image. Transformation of the FM image to match the TEM image was achieved by isotropic scaling with interpolation setting 'bicubic smoother', translation and rotation. Alignment at low magnification was guided by the grid bars and nuclei. Alignment at high magnification was guided by the shape of the nucleus and the position of the fiducial beads.

## 6.6 References

- (1) Jakoš, T.; Pišlar, A.; Jewett, A.; Kos, J. Cysteine Cathepsins in Tumor-Associated Immune Cells. *Frontiers in Immunology*. Frontiers Media S.A. August 28, 2019, p 2037.
- (2) Gupta, S.; Singh, R. K.; Dastidar, S.; Ray, A. *Cysteine Cathepsin S as an Immunomodulatory Target: Present and Future Trends*; Taylor & Francis, 2008; Vol. 12, pp 291–299.
- (3) Fonović, M.; Turk, B. Cysteine Cathepsins and Extracellular Matrix Degradation. *Biochimica et Biophysica Acta - General Subjects*. Elsevier August 1, 2014, pp 2560–2570.
- (4) Sevenich, L.; Bowman, R. L.; Mason, S. D.; Quail, D. F.; Rapaport, F.; Elie, B. T.; Brogi, E.; Brastianos, P. K.; Hahn, W. C.; Holsinger, L. J.; Massagué, J.; Leslie, C. S.; Joyce, J. A. Analysis of Tumour- and Stroma-Supplied Proteolytic Networks Reveals a Brain-Metastasis-Promoting Role for Cathepsin S. *Nat. Cell Biol.* **2014**, *16* (9), 876–888.
- (5) Sobotič, B.; Vizovišek, M.; Vidmar, R.; Van Damme, P.; Gocheva, V.; Joyce, J. A.; Gevaert, K.; Turk, V.; Turk, B.; Fonović, M. Proteomic Identification of Cysteine Cathepsin Substrates Shed from the Surface of Cancer Cells. *Mol. Cell. Proteomics* **2015**, *14* (8), 2213–2228.
- (6) Driessen, C.; Bryant, R. A. R.; Lennon-Duménil, A. M.; Villadangos, J. A.; Bryant, P. W.; Shi, G. P.; Chapman, H. A.; Ploegh, H. L. Cathepsin S Controls the Trafficking and Maturation of MHC Class II Molecules in Dendritic Cells. *J. Cell Biol.* **1999**, *147* (4), 775–790.
- (7) Shen, L.; Sigal, L. J.; Boes, M.; Rock, K. L. Important Role of Cathepsin S in Generating Peptides for TAP-Independent MHC Class I Crosspresentation in Vivo. *Immunity* **2004**, *21* (2), 155–165.
- (8) Bania, J.; Gatti, E.; Lelouard, H.; David, A.; Cappello, F.; Weber, E.; Camosseto, V.; Pierre, P. Human Cathepsin S, but Not Cathepsin L, Degrades Efficiently MHC Class II-Associated Invariant Chain in Nonprofessional APCs. *Proc. Natl. Acad. Sci. U. S. A.* **2003**, *100* (11), 6664–6669.
- (9) Theron, M.; Bentley, D.; Nagel, S.; Manchester, M.; Gerg, M.; Schindler, T.; Silva, A.; Ecabert, B.; Teixeira, P.; Perret, C.; Reis, B. Pharmacodynamic Monitoring of RO5459072, a Small Molecule Inhibitor of Cathepsin S. *Front. Immunol.* **2017**, *8* (JUL), 806.
- (10) Oresic Bender, K.; Ofori, L.; Van Der Linden, W. A.; Mock, E. D.; Datta, G. K.; Chowdhury, S.; Li, H.; Segal, E.; Sanchez Lopez, M.; Ellman, J. A.; Figdor, C. G.; Bogyo, M.; Verdoes, M. Design of a Highly Selective Quenched Activity-Based Probe and Its Application in Dual Color Imaging Studies of Cathepsin S Activity Localization. *J. Am. Chem. Soc.* **2015**, *137* (14), 4771–4777.
- (11) van Dalen, F. J.; Bakkum, T.; van Leeuwen, T.; Groenewold, M.; Deu, E.; Koster, A.; Van Kasteren, S. I.; Verdoes, M. Application of a Highly Selective Cathepsin S Two-Step Activity-Based Probe in Multicolour Bio-Orthogonal Correlative Light Electron Microscopy. *Front. Chem.* **2020**, *8* (628433), 1–13.
- (12) Helft, J.; Böttcher, J.; Chakravarty, P.; Zelenay, S.; Huotari, J.; Schraml, B. U.; Goubau, D.; Reis e Sousa, C. GM-CSF Mouse Bone Marrow Cultures Comprise a Heterogeneous Population of CD11c+MHCII+ Macrophages and Dendritic Cells. *Immunity* **2015**, *42* (6), 1197–1211.
- (13) Mayhew, T. M.; Lucocq, J. M. Multiple-Labeling ImmunoEM Using Different Sizes of Colloidal Gold: Alternative Approaches to Test for Differential Distribution and Colocalization in Subcellular Structures. *Histochem. Cell Biol.* **2011**, *135* (3), 317–326.
- (14) Eissing, N.; Heger, L.; Baranska, A.; Cesnjevar, R.; Büttner-Herold, M.; Söder, S.; Hartmann, A.; Heidkamp, G. F.; Dudziak, D. Easy Performance of 6-Color Confocal

- Immunofluorescence with 4-Laser Line Microscopes. *Immunol. Lett.* **2014**, *161* (1), 1–5.
- (15) Luzio, J. P.; Pryor, P. R.; Bright, N. A. Lysosomes: Fusion and Function. *Nat. Rev. Mol. Cell Biol.* **2007**, *8* (8), 622–632.
- (16) Flannagan, R. S.; Jaumouillé, V.; Grinstein, S. The Cell Biology of Phagocytosis. *Annu. Rev. Pathol. Mech. Dis.* **2012**, *7* (1), 61–98.
- (17) van Elsland, D. M.; Bos, E.; de Boer, W.; Overkleeft, H. S.; Koster, A. J.; van Kasteren, S. I. Detection of Bioorthogonal Groups by Correlative Light and Electron Microscopy Allows Imaging of Degraded Bacteria in Phagocytes. *Chem. Sci.* **2016**, *7* (1), 752–758.
- (18) Uribe-Quero, E.; Rosales, C. Control of Phagocytosis by Microbial Pathogens. *Front. Immunol.* **2017**, *8* (OCT), 1–23.
- (19) Blum, J. S.; Wearsch, P. A.; Cresswell, P. Pathways of Antigen Processing. *Annu. Rev. Immunol.* **2013**, *31* (1), 443–473.
- (20) Kleijmeer, M.; Ramm, G.; Schuurhuis, D.; Griffith, J.; Rescigno, M.; Ricciardi-Castagnoli, P.; Rudensky, A. Y.; Ossendorp, F.; Melief, C. J. M.; Stoorvogel, W.; Geuze, H. J. Reorganization of Multivesicular Bodies Regulates MHC Class II Antigen Presentation by Dendritic Cells. *J. Cell Biol.* **2001**, *155* (1), 53–63.
- (21) Bosch, B.; Berger, A. C.; Khandelwal, S.; Heipertz, E. L.; Scharf, B.; Santambrogio, L.; Roche, P. A. Disruption of Multivesicular Body Vesicles Does Not Affect Major Histocompatibility Complex (MHC) Class II-Peptide Complex Formation and Antigen Presentation by Dendritic Cells. *J. Biol. Chem.* **2013**, *288* (34), 24286–24292.
- (22) van Leeuwen, T.; Araman, C.; Pieper Pournara, L.; Kampstra, A. S. B.; Bakkum, T.; Marqvorsen, M. H. S.; Nascimento, C. R.; Groenewold, G. J. M.; van der Wulp, W.; Camps, M. G. M.; Janssen, G. M. C.; van Veelen, P. A.; van Westen, G. J. P.; Janssen, A. P. A.; Florea, B. I.; Overkleeft, H. S.; Ossendorp, F. A.; Toes, R. E. M.; van Kasteren, S. I. Bioorthogonal Protein Labelling Enables the Study of Antigen Processing of Citrullinated and Carbamylated Auto-Antigens. *RSC Chem. Biol.* **2021**.
- (23) Pawlak, J. B.; Gential, G. P. P.; Ruckwardt, T. J.; Bremmers, J. S.; Meeuwenoord, N. J.; Ossendorp, F. A.; Overkleeft, H. S.; Filippov, D. V.; Van Kasteren, S. I. Bioorthogonal Deprotection on the Dendritic Cell Surface for Chemical Control of Antigen Cross-Presentation. *Angew. Chemie - Int. Ed.* **2015**, *54* (19), 5628–5631.
- (24) van der Gracht, A. M. F.; de Geus, M. A. R.; Camps, M. G. M.; Ruckwardt, T. J.; Sarris, A. J. C.; Bremmers, J.; Maurits, E.; Pawlak, J. B.; Posthoorn, M. M.; Bongers, K. M.; Filippov, D. V.; Overkleeft, H. S.; Robillard, M. S.; Ossendorp, F.; van Kasteren, S. I. Chemical Control over T-Cell Activation In Vivo Using Deprotection of Trans-Cyclooctene-Modified Epitopes. *ACS Chem. Biol.* **2018**, acschembio.8b00155.
- (25) Bagert, J. D.; Xie, Y. J.; Sweredoski, M. J.; Qi, Y.; Hess, S.; Schuman, E. M.; Tirrell, D. A. Quantitative, Time-Resolved Proteomic Analysis by Combining Bioorthogonal Noncanonical Amino Acid Tagging and Pulsed Stable Isotope Labeling by Amino Acids in Cell Culture. *Mol. Cell. Proteomics* **2014**, *13* (5), 1352–1358.
- (26) Thakur, A.; Mikkelsen, H.; Jungersen, G. Intracellular Pathogens: Host Immunity and Microbial Persistence Strategies. *Journal of Immunology Research*. Hindawi Limited 2019.
- (27) Buchmeier, N. A.; Heffron, F. Inhibition of Macrophage Phagosome-Lysosome Fusion by Salmonella Typhimurium. *Infect. Immun.* **1991**, *59* (7), 2232–2238.
- (28) Pradhan, D.; Pradhan, J.; Mishra, A.; Karmakar, K.; Dhiman, R.; Chakravorty, D.; Negi, V. D. Immune Modulations and Survival Strategies of Evolved Hypervirulent Salmonella Typhimurium Strains. *Biochim. Biophys. Acta - Gen. Subj.* **2020**, 129627.
- (29) Gray, M. A.; Choy, C. H.; Dayam, R. M.; Ospina-Escobar, E.; Somerville, A.; Xiao, X.; Ferguson, S. M.; Botelho, R. J. Phagocytosis Enhances Lysosomal and Bactericidal Properties by Activating the Transcription Factor TFEB. *Curr. Biol.* **2016**, *26* (15), 1955–1964.

- (30) Bah, A.; Vergne, I. Macrophage Autophagy and Bacterial Infections. *Frontiers in Immunology*. Frontiers Media S.A. November 6, 2017, p 1483.
- (31) Azimi, T.; Zamirnasta, M.; Sani, M. A.; Dallal, M. M. S.; Nasser, A. Molecular Mechanisms of Salmonella Effector Proteins: A Comprehensive Review. *Infection and Drug Resistance*. Dove Medical Press Ltd. January 6, 2020, pp 11–26.
- (32) Kaper, J. B.; Nataro, J. P.; Mobley, H. L. T. Pathogenic Escherichia Coli. *Nature Reviews Microbiology*. Nature Publishing Group February 2004, pp 123–140.
- (33) Sletten, E. M.; Bertozzi, C. R. From Mechanism to Mouse; A Tale of Two Bioorthogonal Reactions. *Acc. Chem. Res.* **2011**, 44 (9), 666–676.
- (34) Saxon, E.; Bertozzi, C. R. Cell Surface Engineering by a Modified Staudinger Reaction. *Science* **2000**, 287 (5460), 2007–2010.
- (35) Patterson, D. M.; Prescher, J. A. Orthogonal Bioorthogonal Chemistries. *Curr. Opin. Chem. Biol.* **2015**, 28, 141–149.
- (36) Nguyen, S. S.; Prescher, J. A. Developing Bioorthogonal Probes to Span a Spectrum of Reactivities. *Nat. Rev. Chem.* **2020**, 4 (9), 476–489.
- (37) Willems, L. I.; Li, N.; Florea, B. I.; Ruben, M.; Van Der Marel, G. A.; Overkleeft, H. S. Triple Bioorthogonal Ligation Strategy for Simultaneous Labeling of Multiple Enzymatic Activities. *Angew. Chemie - Int. Ed.* **2012**, 51 (18), 4431–4434.
- (38) Narayanam, M. K.; Liang, Y.; Houk, K. N.; Murphy, J. M. Discovery of New Mutually Orthogonal Bioorthogonal Cycloaddition Pairs through Computational Screening. *Chem. Sci.* **2016**, 7 (2), 1257–1261.
- (39) Liang, Y.; Mackey, J. L.; Lopez, S. A.; Liu, F.; Houk, K. N. Control and Design of Mutual Orthogonality in Bioorthogonal Cycloadditions. *J. Am. Chem. Soc.* **2012**, 134 (43), 17904–17907.
- (40) Karver, M. R.; Weissleder, R.; Hilderbrand, S. A. Bioorthogonal Reaction Pairs Enable Simultaneous, Selective, Multi-Target Imaging. *Angew. Chemie - Int. Ed.* **2012**, 51 (4), 920–922.
- (41) Rahim, M. K.; Kota, R.; Haun, J. B. Enhancing Reactivity for Bioorthogonal Pretargeting by Unmasking Antibody-Conjugated Trans-Cyclooctenes. *Bioconjug. Chem.* **2015**, 26 (2), 352–360.
- (42) Worrell, B. T.; Malik, J. A.; Fokin, V. V. Direct Evidence of a Dinuclear Copper Intermediate in Cu(I)-Catalyzed Azide-Alkyne Cycloadditions. *Science (80-. )*. **2013**, 340, 457–460.
- (43) Matikonda, S. S.; Orsi, D. L.; Staudacher, V.; Jenkins, I. A.; Fiedler, F.; Chen, J.; Gamble, A. B. Bioorthogonal Prodrug Activation Driven by a Strain-Promoted 1,3-Dipolar Cycloaddition. *Chem. Sci.* **2015**, 6 (2), 1212–1218.
- (44) Oliveira, B. L.; Guo, Z.; Bernardes, G. J. L. Inverse Electron Demand Diels–Alder Reactions in Chemical Biology. *Chem. Soc. Rev.* **2017**, 46 (16), 4895–4950.
- (45) Ramil, C. P.; Lin, Q. Bioorthogonal Chemistry: Strategies and Recent Developments. *Chem. Commun.* **2013**, 49 (94), 11007–11022.
- (46) Sarris, A. J.; Hansen, T.; de Geus, M. A.; Maurits, E.; Doelman, W.; Overkleeft, H. S.; Codee, J. D.; Filippov, D.; van Kasteren, S. I. Fast and PH Independent Elimination of Trans-Cyclooctene Using Aminoethyl Functionalized Tetrazines. *Chem. - A Eur. J.* **2018**.
- (47) Rieder, U.; Luedtke, N. W. Alkene-Tetrazine Ligation for Imaging Cellular DNA. *Angew. Chemie - Int. Ed.* **2014**, 53 (35), 9168–9172.
- (48) Lang, K.; Chin, J. W. Bioorthogonal Reactions for Labeling Proteins. *ACS Chem. Biol.* **2014**, 9 (1), 16–20.
- (49) Devaraj, N. K. The Future of Bioorthogonal Chemistry. *ACS Cent. Sci.* **2018**, 4, 952–959.
- (50) Shang, X.; Lai, R.; Song, X.; Li, H.; Niu, W.; Guo, J. Improved Photoinduced Fluorogenic Alkene-Tetrazole Reaction for Protein Labeling. *Bioconjug. Chem.* **2017**, 28 (11), 2859–2864.

- (51) Daughtry, J. L.; Cao, W.; Ye, J.; Baskin, J. M. Clickable Galactose Analogues for Imaging Glycans in Developing Zebrafish. *ACS Chem. Biol.* **2020**.
- (52) Liechti, G. W.; Kuru, E.; Hall, E.; Kalinda, A.; Brun, Y. V.; Vannieuwenhze, M.; Maurelli, & A. T.; Maurelli, A. T. A New Metabolic Cell-Wall Labelling Method Reveals Peptidoglycan in Chlamydia Trachomatis. *Nature* **2014**, *506* (7489), 507–510.
- (53) van Elsland, D. M.; van Kasteren, S. I. Imaging Bioorthogonal Groups in Their Ultrastructural Context with Electron Microscopy. *Angew. Chemie - Int. Ed.* **2016**, *55* (33), 9472–9473.
- (54) Flechsler, J.; Heimerl, T.; Pickl, C.; Rachel, R.; Stierhof, Y. D.; Klingl, A. 2D and 3D Immunogold Localization on (Epoxy) Ultrathin Sections with and without Osmium Tetroxide. *Microsc. Res. Tech.* **2020**, *83* (6), 691–705.
- (55) Peters, S.; Kaiser, L.; Fink, J.; Schumacher, F.; Perschin, V.; Schlegel, J.; Sauer, M.; Stigloher, C.; Kleuser, B.; Seibel, J.; Schubert-Unkmeir, A. Click-Correlative Light and Electron Microscopy (Click-AT-CLEM) for Imaging and Tracking Azido-Functionalized Sphingolipids in Bacteria. *Sci. Rep.* **2021**, *11* (1), 4300.
- (56) van Elsland, D. M.; Pujals, S.; Bakkum, T.; Bos, E.; Oikonomeas-Koppas, N.; Berlin, I.; Neefjes, J.; Meijer, A. H.; Koster, A. J.; Albertazzi, L.; van Kasteren, S. I. Ultrastructural Imaging of Salmonella–Host Interactions Using Super-Resolution Correlative Light-Electron Microscopy of Bioorthogonal Pathogens. *ChemBioChem* **2018**, *19* (16), 1766–1770.
- (57) Adrian, T.; Bakkum, T.; van Elsland, D. M.; Bos, E.; Koster, A. J.; Albertazzi, L.; van Kasteren, S. I.; Pujals, S. Super-Resolution Correlative Light-Electron Microscopy Using a Click-Chemistry Approach for Studying Intracellular Trafficking. In *Methods in Cell Biology*; Academic Press Inc., 2021; Vol. 162, pp 303–331.
- (58) Nikić, I.; Estrada Girona, G.; Kang, J. H.; Paci, G.; Mikhaleva, S.; Koehler, C.; Shymanska, N. V.; Ventura Santos, C.; Spitz, D.; Lemke, E. A. Debugging Eukaryotic Genetic Code Expansion for Site-Specific Click-PAINT Super-Resolution Microscopy. *Angew. Chemie - Int. Ed.* **2016**, *55* (52), 16172–16176.
- (59) Tuijtel, M. W.; Koster, A. J.; Jakobs, S.; Faas, F. G. A.; Sharp, T. H. Correlative Cryo Super-Resolution Light and Electron Microscopy on Mammalian Cells Using Fluorescent Proteins. *Sci. Rep.* **2019**, *9* (1), 1369.
- (60) Moser, F.; Pražák, V.; Mordhorst, V.; Andrade, D. M.; Baker, L. A.; Hagen, C.; Grünwald, K.; Kaufmann, R. Cryo-SOFI Enabling Low-Dose Super-Resolution Correlative Light and Electron Cryo-Microscopy. *Proc. Natl. Acad. Sci.* **2019**, 201810690.
- (61) Sun, D. en; Fan, X.; Shi, Y.; Zhang, H.; Huang, Z.; Cheng, B.; Tang, Q.; Li, W.; Zhu, Y.; Bai, J.; Liu, W.; Li, Y.; Wang, X.; Lei, X.; Chen, X. Click-ExM Enables Expansion Microscopy for All Biomolecules. *Nat. Methods* **2021**, *18* (1), 107–113.
- (62) M'Saad, O.; Bewersdorf, J. Light Microscopy of Proteins in Their Ultrastructural Context. *Nat. Commun.* **2020**, *11* (1), 1–15.
- (63) Li, N.; Lim, R. K. V.; Edwardraja, S.; Lin, Q. Copper-Free Sonogashira Cross-Coupling for Functionalization of Alkyne-Encoded Proteins in Aqueous Medium and in Bacterial Cells. *J. Am. Chem. Soc.* **2011**, *133* (39), 15316–15319.
- (64) Chenault, H. K.; Dahmer, J.; Whitesides, G. M. Kinetic Resolution of Unnatural and Rarely Occurring Amino Acids: Enantioselective Hydrolysis of N-Acyl Amino Acids Catalyzed by Acylase I. *J. Am. Chem. Soc.* **1989**, *111* (16), 6354–6364.
- (65) Biagini, S. C. G.; Gibson, S. E.; Keen, S. P. Cross-Metathesis of Unsaturated Alpha-Amino Acid Derivatives. *J. Chem. Soc. Perkin Trans. 1* **1998**, *1*, 2485–2500.
- (66) Dong, S.; Merkel, L.; Moroder, L.; Budisa, N. Convenient Syntheses of Homopropargylglycine. *J. Pept. Sci.* **2008**, *14* (10), 1148–1150.
- (67) Albers, H. M. H. G.; Kuijl, C.; Bakker, J.; Hendrickx, L.; Wekker, S.; Farhou, N.; Liu, N.; Blasco-Moreno, B.; Scanu, T.; Den Hertog, J.; Celie, P.; Ovaa, H.; Neefjes, J. Integrating

- Chemical and Genetic Silencing Strategies to Identify Host Kinase-Phosphatase Inhibitor Networks That Control Bacterial Infection. *ACS Chem. Biol.* **2014**, *9* (2), 414–422.
- (68) Lutz, M. B.; Kukutsch, N.; Ogilvie, A. L. .; Rößner, S.; Koch, F.; Romani, N.; Schuler, G. An Advanced Culture Method for Generating Large Quantities of Highly Pure Dendritic Cells from Mouse Bone Marrow. *J. Immunol. Methods* **1999**, *223* (1), 77–92.
- (69) Tokuyasu, K. T. A Technique for Ultracryotomy of Cell Suspensions and Tissues. *J. Cell Biol.* **1973**, *57* (2), 551–565.
- (70) Peters, P. J.; Bos, E.; Griekspoor, A. Cryo-Immunogold Electron Microscopy. *Curr. Protoc. Cell Biol.* **2006**, *30* (1), 4.7.1-4.7.19.
- (71) Schindelin, J.; Arganda-Carreras, I.; Frise, E.; Kaynig, V.; Longair, M.; Pietzsch, T.; Preibisch, S.; Rueden, C.; Saalfeld, S.; Schmid, B.; Tinevez, J. Y.; White, D. J.; Hartenstein, V.; Eliceiri, K.; Tomancak, P.; Cardona, A. Fiji: An Open-Source Platform for Biological-Image Analysis. *Nat. Methods* **2012**, *9* (7), 676–682.





# Nederlandse Samenvatting

Bioorthogonale chemie wordt gedefinieerd als scheikundige reacties die selectief uitgevoerd kunnen worden in een levende cel, zonder de van nature voorkomende biochemische reacties te verstoren en *vice versa*. Bioorthogonale chemie wordt voornamelijk gebruikt voor het selectief koppelen van twee moleculen ten midden van het complexe mengsel aan biochemische reacties die in een cel plaatsvinden. Deze specifieke koppeling van twee moleculen wordt ook wel een klik reactie genoemd en is uitermate geschikt om een fluorescente groep aan een biomolecuul vast te maken. Om deze koppeling mogelijk te maken, moet eerst in het biomolecuul van interesse een moleculair haakje aangebracht worden, ook wel een klik handvat genoemd. Door de fluorescente groep te voorzien van een bijpassend klik handvat, kunnen de twee moleculen eenvoudig aan elkaar geklikt worden. Hierdoor wordt het mogelijk om het biomolecuul te detecteren met behulp van microscopie of andere fluorescentie technieken, waardoor de functie van biomolecuul bestudeerd kan worden. In dit proefschrift wordt bioorthogonale chemie gecombineerd met verschillende analysemethoden zoals flowcytometrie, confocale fluorescentie microscopie, super-resolutie fluorescentie microscopie en bovenal correlatieve licht en elektronenmicroscopie (CLEM), om pathogene intracellulaire bacteriën te bestuderen in hun natuurlijke omgeving, wat wil zeggen binnenin de gastheercel.

In **hoofdstuk 1** wordt beschreven hoe bioorthogonale chemie en klik reacties toegepast kunnen worden voor biologisch onderzoek. Allereerst worden de algemene principes en geschiedenis van bioorthogonale chemie en klik reacties besproken. Vervolgens wordt beschreven hoe met behulp van metabole labeling biologische bouwstenen met een klik handvat eenvoudig ingebouwd kunnen worden in grotere biomoleculen zoals eiwitten en complexe koolhydraten. Vervolgens wordt uitgelegd hoe bioorthogonale metabole labeling toegepast kan worden om intracellulaire bacteriën te bestuderen, door middel van het aanbrengen van klik handvatten in de bacteriële eiwitten of celwand, en welke analysemethoden hiervoor geschikt zijn.

In **hoofdstuk 2** wordt een overzicht geschetst van de nieuwste ontwikkelingen op het gebied van metabole labeling om de interacties tussen een pathogene bacterie en zijn gastheer te kunnen bestuderen, met behulp van geavanceerde microscopie technieken zoals CLEM. Hierbij wordt vooral gefocust op het labelen van enerzijds de bacteriële eiwitten en anderzijds de bacteriële celwand via het peptidoglycaan

of het mycomembraan, in het geval van corynebacteriën. Hierbij wordt onderscheid gemaakt tussen directe labeling met een fluorofoor en twee-staps-labeling via een klik reactie. Speciale aandacht wordt gegeven aan het labelen van *Mycobacterium tuberculosis* (*Mtb*), vanwege de complexe samenstelling van het mycomembraan van deze gevaarlijke pathogeen. Ten slotte wordt een aanvullende techniek uitgelicht, genaamd 'Activity-Based Protein Profiling' (ABPP), waarmee actieve enzym populaties specifiek gelabeld kunnen worden.

**Hoofdstuk 3** beschrijft de ontwikkeling van een techniek om de stabiliteit van klik handvatten te bestuderen in immuuncellen, ter bevestiging van de bruikbaarheid van deze chemische groepen voor het bestuderen van intracellulaire bacteriën. In dit hoofdstuk wordt met behulp van flow cytometrie bevestigd dat de terminale alkyn en azide groep langdurig stabiel blijven, terwijl de ringvormige alkyn groepen dibenzocylcooctyn (DBCO) en bicyclononyn (BCN) in grote mate afgebroken worden in de lysosomale compartimenten van immuuncellen.

**Hoofdstuk 4** beschrijft de ontwikkeling van een techniek om intracellulaire (pathogene) bacteriën te bestuderen in immuuncellen, door de hoge resolutie van 'Stochastic Optical Reconstruction Microscopy' (STORM) te combineren met de ultrastructurele informatie van transmissie elektronenmicroscopie (TEM). De resulterende techniek, genaamd STORM-CLEM, werd geoptimaliseerd met behulp van een bioorthogonaal gelabelde *Salmonella enterica* serovar Typhimurium (*Stm*). Om dit doel te bereiken, werd de labeling van *Stm* met homopropargylglycine (Hpg), azidohomoalanine (Aha) en alkyn-D-alanine (alkDala) geoptimaliseerd en gevalideerd. Ten slotte wordt een overzicht gegeven van de STORM-CLEM techniek voor het bestuderen van *Stm* in dendritische cellen.

**Hoofdstuk 5** beschrijft de ontwikkeling van drievoudig gelabelde *Mtb* bacteriën en de toepassing van bioorthogonale CLEM voor het bestuderen van de intracellulaire verdeling van *Mtb* in macrofagen, onder normale omstandigheden en onder invloed van verschillende antibiotica. Voor de drievoudige labeling van *Mtb* werd een fluorescent eiwit (DsRed) gecombineerd met bioorthogonale eiwitlabeling (Aha) en celwandlabeling (alkDala). Met behulp van deze techniek konden verschillende observaties gemaakt worden met betrekking tot de pathogeen-gastheer interacties, waarvan sommigen kwantificeerbaar en anderen zeldzaam. Door de intracellulaire verdeling van *Mtb* in de macrofaag gastheercel te kwantificeren, werd een significant verschil gedetecteerd tussen onbehandelde bacteriën, dode bacteriën en bacteriën die intracellulair behandeld werden met verschillende antibiotica. Dit patroon zou mogelijk een verband kunnen houden

met de mate van *Mtb*-doding. Kwantificatie van de vorm van de bacteriële doorsnede liet een vergelijkbaar patroon zien en zou mogelijk een verband kunnen houden met de mate van *Mtb*-afbraak. Ten slotte kon het behoud van bioorthogonale labels door *Mtb* over tijd gebruikt worden als een maat voor remming van *Mtb*-celdeling. Hiervoor werd een aparte techniek opgezet, gebaseerd op flow cytometrie, om het totale labelbehoud per bacterie accuraat te kwantificeren, na herwinnen van de intracellulaire bacteriën door selectief de gastheercel open te breken.

In **hoofdstuk 6** worden de bevindingen samengevat en worden verschillende suggesties gegeven voor het verder ontwikkelen en toepassen van de beschreven technieken, waaronder; de toepassing van bioorthogonale CLEM op het bestuderen van een cathepsin S-selectieve 'Activity-Based Probe' (ABP) en het bestuderen van de rol van cathepsins in het afbraakproces van (non-)pathogene bacteriën. Daarnaast wordt de mogelijkheid van multi-orthogonale bioorthogonale reacties beschreven, waarbij drie verschillende klik reacties op een drievoudig-bioorthogonaal gelabelde cel uitgevoerd kunnen worden. Ten slotte worden verschillende suggesties gegeven om CLEM techniek verder te verbeteren, waardoor bijvoorbeeld 3-dimensionale informatie verkregen kan worden.

Alles tezamen biedt de hier beschreven bioorthogonale CLEM techniek vele mogelijkheden voor het bestuderen van de interacties tussen pathogene bacteriën en de gastheercel, op ultrastructureel niveau. Flow cytometrie en andere op fluorescentie gebaseerde analyse methoden kunnen hierbij aanvullende informatie verschaffen, om een vollediger beeld te krijgen van de label opname en behoud over tijd, onder invloed van bijvoorbeeld antibiotica. Mogelijk kunnen deze technieken in de toekomst bijdragen aan het bestuderen van het werkingsmechanisme van nieuwe antibiotica en het ontwikkelen van nieuwe antibiotica of gastheer-gerichte therapieën.



# List of Publications – First Authorship

## **Metabolic Labeling Probes for Interrogation of the Host-Pathogen Interaction**

B.J. Ignacio\*, T. Bakkum\*, K.M. Bongers, N.I. Martin, S.I. van Kasteren

*\*These authors contributed equally to this work*

*Org. Biomol. Chem.* **2021**, 19(13): 2856–2870

DOI: 10.1039/d0ob02517h

## **Super-Resolution Correlative Light-Electron Microscopy Using a Click-Chemistry Approach for Studying Intracellular Trafficking**

T. Andrian\*, T. Bakkum\*, D.M. van Elsland, E. Bos, A.J. Koster, L. Albertazzi, S.I. van Kasteren, S. Pujals

*\*These authors contributed equally to this work*

*Methods Cell Biol.* **2021**, 162: 303–331

DOI: 10.1016/bs.mcb.2020.09.001

## **Bioorthogonal Correlative Light-Electron Microscopy of *Mycobacterium tuberculosis* in Macrophages Reveals the Effect of Antituberculosis Drugs on Subcellular Bacterial Distribution**

T. Bakkum, M.T. Heemskerk, E. Bos, G.J.M. Groenewold, N. Oikonomou-Koppas, K.V. Walburg, S. van Veen, M.J.C. van der Lienden, T. van Leeuwen, M.C. Haks, T.H.M. Ottenhoff, A.J. Koster, S.I. van Kasteren

*ACS Cent. Sci.* **2020**, 6(11): 1997–2007

DOI: 10.1021/acscentsci.0c00539

## **Quantification of Bioorthogonal Stability in Immune Phagocytes Using Flow Cytometry Reveals Rapid Degradation of Strained Alkynes**

T. Bakkum, T. van Leeuwen, A.J.C. Sarris, D.M. van Elsland, D. Poulcharidis, H.S. Overkleef, S.I. van Kasteren

*ACS Chem. Biol.* **2018**, 13(5): 1173–1179

DOI: 10.1021/acscchembio.8b00355

## **Ultrastructural Imaging of *Salmonella*–Host Interactions Using Super-Resolution Correlative Light-Electron Microscopy of Bioorthogonal Pathogens**

D.M. van Elsland\*, S. Pujals\*, T. Bakkum\*, E. Bos, N. Oikonomou-Koppas, I. Berlin, J. Neefjes, A.H. Meijer, A.J. Koster, L. Albertazzi, S.I. van Kasteren

*\*These authors contributed equally to this work*

*Chembiochem.* **2018**, 19(16): 1766–1770

DOI: 10.1002/cbic.201800230

## List of Publications – Co-authorship

### **Application of a Highly Selective Cathepsin S Two-step Activity-Based Probe in Multicolor Bio-Orthogonal Correlative Light-Electron Microscopy**

F.J. van Dalen, T. Bakkum, T. van Leeuwen, G.J.M. Groenewold, E. Deu, A.J. Koster, S.I. van Kasteren, M. Verdoes

*Front. Chem.* **2021**, 8: 628433

DOI: 10.3389/fchem.2020.628433

### **Bioorthogonal Protein Labelling Enables the Study of Antigen Processing of Citrullinated and Carbamylated Auto-Antigens**

T. van Leeuwen\*, C. Araman\*, L. Pieper-Pournara, A.S.B. Kampstra, T. Bakkum, M.H.S. Marqvorsen, C.R. Nascimento, G.J.M. Groenewold, W. van der Wulp, M.G.M. Camps, G.M.C. Janssen, P.A. van Veelen, G.J.P. van Westen, A.P.A. Janssen, B.I. Florea, H.S. Overkleeft, F.A. Ossendorp, R.E.M. Toes, S.I. van Kasteren

*\*These authors contributed equally to this work*

*RSC Chem. Biol.* **2021**, Advance Article

DOI: 10.1039/d1cb00009h

### **Magnetic-Activated Cell Sorting Using Coiled-Coil Peptides: An Alternative Strategy for Isolating Cells with High Efficiency and Specificity**

M.J. Shen, R.C.L. Olsthoorn, Y. Zeng, T. Bakkum, A. Kros, A.L. Boyle

*ACS Appl. Mater. Interfaces.* **2021**, 13(10): 11621–11630

DOI: 10.1021/acsami.0c22185

### **Olaparib-Based Photoaffinity Probes for PARP-1 Detection in Living Cells**

J. Voorneveld, B.I. Florea, T. Bakkum, R.J. Mendowicz, M.S. van der Veer, B. Gagestein, S.I. van Kasteren, M. van der Stelt, H.S. Overkleeft, D.V. Filippov

*Chembiochem.* **2020**, 21(17): 2431–2434

DOI: 10.1002/cbic.202000042

### **Synthesis and Characterization of the First Inhibitor of N-Acylphosphatidylethanolamine Phospholipase D (NAPE-PLD)**

B. Castellani, E. Diamanti, D. Pizzirani, P. Tardia, M. Maccesi, N. Realini, P. Magotti, G. Garau, T. Bakkum, S. Rivara, M. Mor, D. Piomelli

*Chem. Commun.* **2017**, 53: 12814–12817

DOI: 10.1039/c7cc07582k

## Curriculum Vitae – English

Thomas Bakkum was born on the 17<sup>th</sup> of January 1991 in Delft. He obtained his Bachelor of Science (BSc) in Life Science & Technology in 2014 at Leiden University in collaboration with Delft University of Technology. As part of this bachelor's program, he performed a research internship in the Physics of Life Processes research group at Leiden University, under supervision of dr. D. Donato and prof. dr. T. Schmidt. In this study titled "Focal adhesion localization of CAS: Can one CAS anchoring domain compensate for the other?" he contributed to the characterization of the role of the protein p130Cas in mechanosensing.

Thomas subsequently obtained his Master of Science (MSc) Summa Cum Laude in Life Science & Technology in 2016 at Leiden University. As part of this master's program, he performed two research internships. He performed his first master internship in the Bio-organic Synthesis research group at Leiden University, under supervision of dr. D.M. van Elsland, dr. M.J. van de Graaff and dr. S.I. van Kasteren. In this study titled "Assessing the stability of bioorthogonal 'click' handles for intralysosomal click reactions" he developed an assay to quantify the stability of bioorthogonal groups in lysosomal compartments of immune cells. He also obtained some experience in organic synthesis of amino acids and fluorophores. His master thesis won second place at the KNCV Golden Master Award in 2016.

He performed his second master internship in the Drug Discovery and Development research group at the IIT in Genoa, under supervision of dr. E. Diamanti, dr. B. Castellani and prof. dr. D. Piomelli. In this study titled "The search for potent and selective small-molecule inhibitors for NAPE-PLD" he contributed to the design, synthesis and validation of selective inhibitors for the enzyme NAPE-PLD.

In October of 2016, Thomas returned to the Bio-organic Synthesis research group at Leiden University as a PhD candidate, under supervision of dr. S.I. van Kasteren and prof. dr. H.S. Overkleeft. The resulting research, as described in this thesis, was partially conducted at the Infectious Diseases department of the Leiden University Medical Center (LUMC), under supervision of prof. dr. T.H.M. Ottenhoff and dr. M.C. Haks, and partially at the Cell and Chemical Biology department of the LUMC under supervision of prof. dr. ir. A.J. Koster and E. Bos, MSc. Another small part of the research was conducted at the Nanoscopy for Nanomedicine research group at the IBEC in Barcelona, under supervision of dr. L. Albertazzi, dr. S. Pujals and T. Andrian, MSc.

Parts of this PhD research were presented as a poster at conferences: CHAINS (2017, 2018, 2019), NanoBioMed (2018), Reedijk Symposium (2019) and EMBO Chemical Biology Workshop (2018; recipient of a poster award). In addition, part of this research was orally presented at the Reedijk Symposium (2019), LACDR Spring Symposium (2021) and the Bioorthogonal & Bioresponsive symposium (2021; recipient of flash presentation award).

Thomas has collaborated frequently and contentedly with several research groups, including those of prof. dr. A.H. Meijer, dr. M. Verdoes, prof. dr. G. van den Bogaart, dr. D.E. Rozen en dr. D. Finlay. In addition, he has supervised students in the form of practical courses, bachelor- and master internships, and he has trained internal and external colleagues in the application of various techniques described in this thesis.

In September 2021 Thomas started working as an Application Scientist at VitroTEM.



## Curriculum Vitae – Nederlands

Thomas Bakkum werd op 17 januari 1991 geboren te Delft. Hij heeft zijn Bachelor of Science (BSc) in Life Science & Technology behaald in 2014 aan de Universiteit Leiden in samenwerking met de Technische Universiteit Delft. Tijdens deze bacheloropleiding heeft hij stage gelopen in de vakgroep Fysica van Levensprocessen aan de Universiteit Leiden, onder begeleiding van dr. D. Donato en prof. dr. T. Schmidt. In dit onderzoek met als titel “Focal adhesion localization of CAS: Can one CAS anchoring domain compensate for the other?” heeft hij bijgedragen aan het karakteriseren van de rol van het eiwit p130Cas als mechanosensor.

Aansluitend heeft Thomas zijn Master of Science (MSc) in Life Science & Technology Summa Cum Laude afgerond in 2016 aan de Universiteit Leiden. Tijdens deze masteropleiding heeft hij twee onderzoeksstages gelopen. Zijn eerste masterstage heeft hij uitgevoerd in de vakgroep Bio-organische Synthese aan de Universiteit Leiden, onder begeleiding van dr. D.M. van Elsland, dr. M.J. van de Graaff en dr. S.I. van Kasteren. In dit onderzoek met als titel “Assessing the stability of bioorthogonal ‘click’ handles for intralysosomal click reactions” heeft hij een assay ontwikkeld om de stabiliteit van bioorthogonale groepen te kwantificeren in lysosomale compartimenten van immuuncellen. Tevens heeft hij hierbij ervaring opgedaan in de organische synthese van aminozuren en fluoroforen. Zijn masterscriptie heeft in 2016 een eervolle tweede plek gewonnen in de KNCV Golden Master Award.

Zijn tweede masterstage heeft hij uitgevoerd in de vakgroep Drug Discovery and Development aan het IIT in Genua, onder begeleiding van dr. E. Diamanti, dr. B. Castellani en prof. dr. D. Piomelli. In dit onderzoek met als titel “The search for potent and selective small-molecule inhibitors for NAPE-PLD” heeft hij bijgedragen aan het ontwerpen, synthetiseren en valideren van selectieve remmers voor het enzym NAPE-PLD.

In oktober 2016 keerde Thomas als promovendus (PhD kandidaat) terug in de vakgroep Bio-organische Synthese aan de Universiteit Leiden, onder begeleiding van dr. S.I. van Kasteren en prof. dr. H.S. Overkleeft. Het resulterende onderzoek, zoals beschreven in dit proefschrift, werd gedeeltelijk uitgevoerd bij de afdeling Infectieziekten van het Leiden Universitair Medisch Centrum (LUMC), onder begeleiding van prof. dr. T.H.M. Ottenhoff en dr. M.C. Haks, en gedeeltelijk bij de afdeling Cel en Chemische Biologie van het LUMC, onder begeleiding van prof. dr.

ir. A.J. Koster en E. Bos, MSc. Tevens is een klein deel van het onderzoek uitgevoerd bij de Nanoscopy for Nanomedicine vakgroep van het IBEC in Barcelona, onder begeleiding van dr. L. Albertazzi, dr. S. Pujals en T. Andrian, MSc.

Delen van dit promotieonderzoek zijn gepresenteerd als poster op congressen: CHAINS (2017, 2018, 2019), NanoBioMed (2018), Reedijk Symposium (2019) en EMBO Chemical Biology Workshop (2018; tevens winnaar van poster prijs). Daarnaast is een deel van dit onderzoek mondeling gepresenteerd op het Reedijk Symposium (2019), LACDR Spring Symposium (2021) en het Bioorthogonal & Bioresponsive symposium (2021; winnaar van flash presentatie prijs).

Thomas heeft veelvuldig en met veel plezier samengewerkt met verschillende onderzoeksgroepen, waaronder die van prof. dr. A.H. Meijer, dr. M. Verdoes, prof. dr. G. van den Bogaart, dr. D.E. Rozen en dr. D. Finlay. Daarnaast heeft hij studenten begeleid in de vorm van practica, bachelor- en master onderzoeksprojecten, en tevens training gegeven aan interne en externe collega's in het toepassen van de verschillende technieken beschreven in dit proefschrift.

In september 2021 is Thomas gestart als Application Scientist bij VitroTEM.

# Dankwoord

Wetenschap is niet alleen topsport, het is ook een teamsport. Dit laatste wordt naar mijn idee nog wel eens ondergewaardeerd. Daarom wil ik graag iedereen hartelijk bedanken die direct of indirect, professioneel of persoonlijk heeft bijgedragen aan het tot stand komen van dit proefschrift. Eigenlijk zijn dit teveel mensen om op te noemen maar zonder jullie had ik dit nooit voor elkaar gekregen.

Allereerst Sander, bedankt voor je aanstekelijk enthousiasme, optimisme en je eindeloze stroom aan ideeën. Bedankt dat je mij de kans hebt geboden om een PhD te doen in jouw groep en met zo'n gaaf project. Je hebt mij door dik en dun gesteund, geënthousiasmeerd en gemotiveerd, zodat we samen steeds tot prachtige resultaten konden komen. Daarnaast heb ik het altijd naar mijn zin gehad met jou in de klimhal, op het mountainbike parcours en in de kroeg. Naast een fijne mentor was je een goede vriend en ik ben je tevens enorm dankbaar voor alle connecties en samenwerkingen die je hebt geïnitieerd. Ten slotte ontzettend bedankt voor je begrip en steun toen het even minder ging. Dit geeft prachtig aan wat voor persoon je bent.

Hermen, bedankt voor je vertrouwen en waardering al tijdens mijn master. Bedankt voor je duidelijke, recht-door-zee aanwijzingen en je snelle feedback. Bedankt voor je geweldige aanbevelingsbrief die mij een prachtige stage in Italië heeft opgeleverd en bedankt voor de 10 die je mij durfde te geven voor mijn colloquium, terwijl de rest van de jury niet hoger dan een 9,5 wilde gaan. Het lijkt misschien een klein gebaar maar voor mij betekent het veel.

CLEM sensei Erik, je was als een tweede supervisor voor mij en ik heb veel van je geleerd. Je was altijd geduldig, vriendelijk, begripvol en een stabiele factor in mijn PhD. Dankjewel voor het creëren van een oase van rust, ten midden van een PhD die soms kon voelen als een zandstorm. Als ik mijzelf weer eens voorbij aan het rennen was of door de bomen het bos niet kon zien, stond jij voor mij klaar. Die biertjes hou je nog steeds van mij tegoed.

Bram en de rest van de EM afdeling, ontzettend bedankt voor de gastvrijheid in jullie EM lab en voor de fijne gesprekken in de gang. Aat, het was altijd gezellig om als eerste met jou in het lab te zijn of als laatste te vertrekken. Cristina, bedankt voor je oprechte interesse, zorgzame woorden en gezelligheid in het lab. Willem, bedankt voor je eindeloze vrolijkheid, geduld en behulpzaamheid. Dylan, thank you for the fun times in both the lab and the climbing hall.

Tom, Mariëlle en de rest van het TB lab, bedankt voor de gastvrijheid en gezelligheid op jullie afdeling. Kimberley, bedankt dat je mij wilde opleiden en dat je altijd klaar stond als er iets niet helemaal goed ging. Suzanne, Cassandra en Arthur, bedankt voor de gezelligheid die jullie altijd meenamen naar het ML3 lab. Matthias, ik heb het ontzettend naar mijn zin gehad met jou zowel in het lab als in de klimhal en bij de cursus Italiaans. Zonder jouw hulp was mijn *Mtb* artikel misschien niet eens af, laat staan gepubliceerd. Ik waardeer je enorm als collega en als vriend.

Lorenzo, Sílvia and the rest of the group, thank you so much for your hospitality and kindness in both Eindhoven and Barcelona. I had lots of fun working with you and I'm very happy with the results of our collaborations. Teodora, thanks for being both an awesome collaboration partner and a friend.

Annemarie, Michel en de rest van de groep, bedankt dat ik jullie ML2 lab mocht gebruiken en daarbij ontvangen werd als een van de groep. De gesprekken in de gang en sporadische borrels vond ik altijd erg gezellig. Saskia, bedankt dat je altijd klaar stond als er weer eens iets niet helemaal soepel ging in het lab.

Bedankt iedereen van de SvK groep, MolPhys en BioSyn voor alle gezelligheid, koffiepauzes, lunchgesprekken, feestjes en uit de hand gelopen borrels! Ondanks dat ik veel op andere locaties gewerkt heb, voelde ik mij toch altijd thuis in onze vleugel. Mirjam, als mijn langstzittende kantoorgenootje ben ik je dankbaar voor alle serieuze en minder serieuze gesprekken, het benoemen van de juiste kleuren en je eeuwige bereidheid om cellen te splitten als ik weer eens druk was op het LUMC. Larissa, Tyrza, Nick, Oscar en Menno, ontzettend bedankt voor al jullie harde werk als mijn studenten. Ik heb jullie inzet, doorzettingsvermogen en gezelligheid ontzettend gewaardeerd.

Ook de rest van het LIC/LACDR/IBL in het Gorlaeus bedankt voor het creëren van een fijne en productieve werkomgeving. Hellen en Annelies, bedankt dat jullie ons werk een stuk makkelijker hebben gemaakt. Jaap, Trudy en Matthieu†, bedankt voor het brengen van sfeer en eenheid in het instituut. Jullie professionele en persoonlijke support heb ik altijd enorm gewaardeerd.

Niet te vergeten mijn lieve vrienden en familie, zonder jullie steun was dit niet mogelijk geweest en daarvoor ben ik jullie eeuwig dankbaar. And finally Giorgia, thank you for your never ending support, optimism and everything else!